Synthetic lenses for the ageing eye: a motivation for developing the mechanical applications of Liquid Crystal Elastomers

Devesh Arvind Mistry

University of Leeds

School of Physics and Astronomy

Submitted in accordance with the requirements for the degree of

Doctor of Philosophy

June 2018

The candidate confirms that the work submitted is his own, except where work which has formed part of jointly authored publications has been included. The contribution of the candidate and the other authors to this work has been explicitly indicated below. The candidate confirms that appropriate credit has been given within the thesis where reference has been made to the work of others.

Chapter 7 includes material which has been published in the paper by Devesh Mistry, Philip B. Morgan, John H. Clamp and Helen F. Gleeson in the journal *Soft Matter* in 2018 (volume **14**, issue (8) and pages 1301-1310). All the work and the majority of the writing of this paper was performed by myself. H. F. Gleeson, P. B. Morgan and J. H. Clamp provided edits and comments to drafts of this paper.

Acknowledgements

This PhD has been fun. I have worked on a diverse and interesting project, met many inspiring people and have travelled the world to learn, discuss and share soft matter science. For this opportunity there are numerous people and organisations that I wholeheartedly thank for their support throughout my PhD and over the years.

First and foremost I thank my supervisors: Professor Helen Gleeson, Professor Phil Morgan and John Clamp without whom none of this work would have been possible. Thank you all for devising such an interesting project and for your continued support and advice throughout the past four years. Through this PhD you have provided me with the best possible platform from which I can go on and launch my own career. I would especially like to thank Helen for the mentorship, encouragement and freedom which together have led me to apply for additional funding, participate in outreach and be creative in my research. I have gotten so much more out of this PhD than I thought possible and so I cannot thank you enough! Additionally, thank you to John and UltraVision CLPL for supporting my PhD *via* a CASE award, the industrial dimension of my PhD has made it all the more informative and enjoyable.

I would also like to thank the Royal Commission for the Exhibition of 1851 for providing additional financial support and opportunities to my PhD. The resources provided through the Industrial Fellowship have truly been transformational to my PhD in allowing me to explore a wider array of research avenues and to travel to a greater number

of conferences than would otherwise have been possible. Again, your support has been a springboard for my career.

Thank you also to Drs. James Bailey, Sarabjot Kaur and Harry Milton for showing me the ropes of liquid crystals research and the various tricks of the trade which make the dark art of scientific research actually possible. The vast majority of the work of this thesis would also not have been possible without Trevor Haynes and Phil Thornton from the Mechanical and Electronic workshops in the School of Physics and Astronomy, who transformed my basic (and slightly impossible) designs and ideas of new equipment into a fully functional and bespoke piece of scientific apparatus. The surface of research possibilities using this equipment has just been scratched and so our group will continue to reap the benefits of your work for many years to come. I have also benefited hugely from numerous discussions with Professor Mark Warner. Through these discussions I have learnt about the theoretical aspects of liquid crystal elastomers and have been able to develop a theoretical insight into the surprises and puzzles thrown up by our results. I would also like to specially thank the Leeds Soft Matter group, and in particular Dan, Winke, Steve, Ben, Edgar and Glenys for welcoming me to the Leeds group (and showing me the School of Physics and Astronomy Friday "de-brief" room) following the cross-Pennine migration of liquid crystals activity. The polymeric expertise of the wider Leeds group has aided my understanding of my own subject enormously and certainly impacted the content of this thesis. Thank you also to Professor J. Cliff Jones and Dr. Mamatha Nagaraj for the useful discussions and nuggets of advice throughout my PhD.

Additionally thank you to all my co-PhDs from Manchester and Leeds: Helen, Shakhawan, David, Guanghui, Outi, Wafa, Matt, Shaj, Nikita, Sophie, Pete, Ethan, Mariam, Nina, Rowan and those mentioned

above. You have all in some way helped me along the way and have kept me relatively sane during the writing of this thesis. A special thanks goes to those of you who reminded me (numerous times...) to write my thesis — I definitely almost forgot!

Last, but most certainly, not least, thank you to Mum, Dad and Hemi for essentially everything over the past 26 years. Alongside converting me from a relatively useless small bag of bones into what I think qualifies as functioning human, you guys have never stopped supporting, advising and believing in me. I would not be a position to do the work that interests me and enjoy the life I do without the start you provided me with. As it is impossible to thank you and the rest of the family enough, I'll just say it one more time — thank you!

Abstract

This thesis describes new Liquid Crystal Elastomers (LCEs) and the study of their mechanical behaviours with the aim of designing a concept "Accommodating Intra-Ocular Lens" (AIOL) — a device which could be used to treat conditions affecting the ageing eye. In this process we discover new physics of LCEs.

Five acrylate-based LCEs with glass transition temperatures $< 15°C$ are developed from commercially available materials.

We detail the opto-mechanical properties of one of these materials — LCE A. When monodomains of LCE A are stressed perpendicular to the liquid crystal (LC) "director", we observe a new deformation mode whereby the polymer conformation deforms through a state of negative backbone order parameter, measured as $Q_B = -0.41 \pm 0.01$. This implies a negative LC order parameter. Moreover, this state coincides with the emergence of a negative Poisson's ratio of maximum magnitude -0.8. We deduce LCE A is the first example of a synthetic "molecular auxetic".

Our characterisation LCE A's mechanical anisotropy shows the initial elastic moduli varies between 4.1 ± 0.6 and 20 ± 2 MPa depending on the angle between the director and stress axis. Unexpectedly, the maximum and minimum of the elastic modulus does not correspond to stresses applied parallel and perpendicular to the director respectively. We develop an empirical model describing generalised uniaxial

deformations of LCE A which we use to predict the stress distribution within a director-patterned film of LCE A when strained.

In studying uniaxial deformations of LCE B, which becomes nematic under stress, we record a stress-optic coefficient of $(1.3 \pm 0.1) \times 10^5$ Brewsters — $\sim 50\times$ greater than that of typical polymeric materials. Upon radial deformation of LCE B we deduce a state of negative ordering for which we calculate $Q_B = -0.14 \pm 0.03$.

The promise of the AIOL concept developed as a consequence of our results and the new physics discovered is testament to LCEs currently being one of the most exciting soft materials.

Contents

List of Figures

Abbreviations

D	Dioptre (unit of optical power)
ϵ	Strain
E	Elastic (Young's) modulus
F_{el}	Elastic free energy
k_B	Boltzmann's constant
$\underline{\underline{\lambda}}$	Deformation gradient tensor
$\underline{\underline{\mathbf{l}}}$	Effective step length tensor for an anisotropic random walk
l_i	Principal components of a general biaxial $\underline{\underline{\mathbf{l}}}$
$l_\parallel$, $l_\perp$	Principal components parallel and perpendicular (respectively) to the unique direction for a uniaxial $\underline{\underline{\mathbf{l}}}$
μ	Shear elastic modulus
$\vec{n}$	Vector describing orientation of the liquid crystal director
n_s	Chemical crosslink density of an elastomer
Q_B	Backbone scalar order parameter for a polymer chain backbone
Q_N	Nematic scalar order parameter
$\vec{R}$	Polymer chain end-to-end vector
r	Step length anisotropy
σ_E	Engineering stress
σ_T	True stress
T	Temperature
$\mathrm{T_g}$	Glass transition temperature
$\mathrm{T_{NI}}$	Nematic to isotropic phase transition temperature

AIOL	Accommodating Intra-Ocular Lens
DSC	Differential Scanning Calorimetry
IOL	Intra-Ocular Lens
LC	Liquid Crystal
LCE	Liquid Crystal Elastomer
LCP	Liquid Crystal Polymer
MFT	"mechanical Fréedericksz" transition
MC	Main chain
NOP	Negative Order Parameter
px	Pixel
SC	Side chain
SSE	(Semi-)soft elasticity
W&T	Warner and Terentjev

Chapter 1

Motivation and direction

1.1 Introduction

The hypothesis behind this thesis is simple enough to be written in a single line:

A functional Accommodation Intra-Ocular Lens implant can be made from Liquid Crystal Elastomers.

While this succinct hypothesis is perhaps difficult to understand without some knowledge of both ophthalmics and soft matter science, it does illustrate the fact that the content of this thesis spans a range of disciplines which will all need to be introduced. In an effort to avoid an unwieldy introduction of both ophthalmics and soft matter science, we first provide in this chapter an outline of the fundamental problems at hand. With the aims of the thesis clearly defined, chapter 2 focuses on only the relevant elements of ophthalmics and soft matter science. While much of what is written in this chapter may appear all too brief, the relevant aspects will be expanded upon to the required level in chapter 2

Below we first illustrate the remarkable nature of Liquid Crystal Elastomers (LCEs) and the motivating problem posed by the ageing eye. We finish by providing an outline for why LCEs are interesting materials to consider for novel ophthalmic devices. This outline provides a rational for the hypothesis written above, and hence for the entirety of this thesis.

1.2 Liquid Crystal Elastomers

LCEs combine the anisotropic molecular ordering (packing) of liquid crystals (LCs) with the elasticity and form-retention of crosslinked polymer systems or "elastomers" (more simply — rubbers). This combination gives rise to an anisotropic elastic material which shares the properties of the constituent material types, for instance refractive index anisotropy from LCs, and elasticity from elastomers. However, this combination of material types also gives rise to numerous unique behaviours — a consequence of the polymer chain random walk, and hence conformation, being templated with LC order. [169]

Perhaps the most striking result of the LC-elastomer coupling is the reversible shape actuation of LCEs. Upon exposure to thermal, optical or chemical stimuli, LCEs can undergo actuations of as much as $\sim 400\%$. [3, 18] The LC-elastomer coupling also gives rise to a plethora of exciting mechanical behaviours including: elastic anisotropy, and so-called "soft elasticity". The latter of these properties relates to the fact that, under certain configurations, a LCE can be stretched by up to $\sim 100\%$ without any energy input required. [170] These mechanical behaviours are a result of the inherent anisotropy of LCEs coupled with the reconfigurability of their microstructures throughout deformations (thus reducing the deformation's energetic cost). The coupling of elastic anisotropy and structural programmability means LCEs are also highly reminiscent of biological tissues. [169] LCEs evidently have great promise for biomedical applications and bioinspired devices. However, in the forty years since the first LCE was synthesised by Finkelmann *et. al.*, no "killer" mechanical-based (or "mechano-") LCE device has been identified. Thus in the last fifteen years the focus of the LCE research community has shifted to focus on shape actuation applications. [164, 173] Without a killer mechano-LCE application to be aiming for, research in to phenomena behind the unknowns of LCE mechanical behaviours remain unexplored and hurdles preventing fabrication of mechano-LCE devices persist.

1.3 The ageing eye

Vision is a human's dominant sense — allowing us to perceive and interact with our environment. One of the most remarkable anatomical aspects of the eye is the "crystalline lens", a soft lens which enables us to change focus between near and distant objects through a process called "accommodation". [26] During accommodation, the shape of the lens is mediated by the ciliary body, an annular-shaped muscle which surrounds the crystalline lens and applies a variable radial stress to the crystalline lens *via* numerous suspensory ligaments (or "zonules"). [26] As remarkable as this opto-mechanical arrangement is, its effectiveness ubiquitously decreases with age as the crystalline lens progressively changes in ways which eventually impact our everyday experience of vision. [26, 10]

Firstly, progressive changes in the shape and elasticity of the crystalline lens reduces the degree of possible accommodation from ~ 15 Dioptres (D) in youth to typically < 2 D by mid-life — a condition termed "presbyopia" (the unit of a Dioptre is explained in appendix A). [26] For a person with perfect distance vision — an "emmetrope" — the result is an inability to focus at the close distances required for everyday tasks such as reading a book at a comfortable distance. We are left requiring aids such as reading spectacles or speciality contact lenses in order to focus up close. [6] The effects of presbyopia slightly differ for short-sighted ("myopic") or long-sighted ("hyperopic") people, however in all cases the degree of possible accommodation reduces with age and additional visual aids become necessary. For simplicity, we proceed only considering the case of emmetropes.

Later in life, we develop cataracts — a clouding of the crystalline lens which obstructs our vision. Currently the only treatment for cataracts is to remove the bulk of the crystalline lens and replace it with a synthetic lens known as an "Intra-Ocular Lens" (IOL). In the vast majority of cases, implantation of an IOL removes any accommodative ability of the eye. [10]

The current treatments for both of these conditions fall far short of restoring natural and youthful vision. [6] Spectacles or contact lenses are typically used

for treating presbyopia. Reading spectacles provide the additional optical power required for close focusing, but must be removed or replaced each time one wishes to switch focusing between near and distance objects. If one is willing to sacrifice optimal visual acuity, more convenient treatments exist in the form of bi- or multi- focal spectacles and contact lenses. Such spectacle arrangements offer "translating" correction where the user looks through the appropriate part of the lens in order to correctly focus on a given object. Most contact lenses instead offer "simultaneous" correction where light from distance and near objects is simultaneously focused onto the retina of the eye. [56] IOLs used for treating cataracts can have single focal length arrangements (requiring a patient to have additional spectacles for close focusing), bi- or multi-focal optical arrangements (which operate in similar ways to bi- or multi- focal contact lenses), or alternative optical monofocal arrangements which, for the purposes of this chapter, have equivalent modes of operation to bi- and multi-focal IOLs. As implantation of an IOL removes any accommodative ability of the eye, the functionality of a patient's vision following insertion of an IOL is worse than a presbyopic person. [56]

The ultimate goal for treatment of the ageing eye is the development of Accommodating Intra-Ocular Lenses (AIOLs) which would replace the aged crystalline lens with a synthetic lens capable of replicating the functionality of the youthful crystalline lens. [125, 6] Such a device is believed to be feasible as the ciliary body appears to maintain (or even increase) its strength with age — thus mechanical stimuli can still be applied to a switchable lens. [122] An AIOL could operate by use of one or several of following parameters which control the power of lens: [72]

- Lens curvature — The optical power of a lens has a strong dependency on the lens curvature. This is the operation mode of natural accommodation.
- Refractive index — The optical power of a lens is also strongly dependent on its refractive index.
- Lens positioning — In multi-lens optical devices, varying the distance between lens elements changes the optical power. The response of optical power to lens position is *significantly* smaller than the two modes described above.

Although the last of the above three methods offers the smallest effect, it is the easiest method to implement in a device. This is evident by the fact that essentially all camera-lens devices change optical power through the relative movement of optical elements. The current (limited) range of AIOLs approved for medical use also operate *via* the movement of optics and consequently have limited accommodative ability in comparison to the youthful crystalline lens. [6] Ideally an AIOL would provide a minimum of 3 D of functional accommodation. One reason for why current AIOLs do not use changes in lens curvature or refractive index is that typical soft materials used in biomedical implants are isotropic and homogeneous and thus lack the complexity of the natural crystalline lens — put simply, current materials are realistically incapable of forming shape- or refractive index-switchable lenses.

1.4 LCEs and AIOLs — A perfect match?

The above discussions can be reduced to two statements:

- LCEs have unique mechanical properties but real-world applications are needed to motivate further mechanical-focused research.
- AIOLs could revolutionise the way we treat presbyopia and cataracts but novel, smart materials are needed to produce functional devices.

With these two statements in mind, the rational behind the initial hypothesis and the motivation for this entire thesis becomes clear. We have identified LCEs as attractive materials for a functional AIOL as they: are optically transparent when prepared appropriately; have mechanically controllable refractive index/optical anisotropy and; have elastic anisotropy and programmability. [169, 164] The first of these properties is a fundamental requirement for any optical lens. The second of these properties offers the possibility to tune lens optical power *via* a mechanically switchable refractive index. The last of these properties offers the possibility to tune lens optical power through programmed mechanically-induced shape changes between lensing geometries — conceptually

a similar mode of operation to the natural crystalline lens.

The development of a LCE-based AIOL is a highly exciting but incredibly complex challenge, requiring not only the development of a standalone functioning lens, but also the development of a way by which the AIOL can be implanted. The first step to take to develop this proposed technology is to demonstrate the feasibility of a mechanically switchable LCE-based lens. Thus this thesis aims to answer the following questions — is a standalone, mechanically switchable LCE-based lens possible? And what might such a lens look like?

Chapter 2

Introduction

Now that an outline of the purpose and direction of this thesis has been made apparent, we now turn to explore in greater depth the eye and LCEs. In terms of the eye, we detail its anatomy, the process of accommodation, how the eye changes with age and why existing treatments fall short of society's demands. In terms of LCEs, we must first introduce their constituent parts — liquid crystals and elastomers before turning to introduce LCEs.

Appendix A provides a brief overview of the lens optics called upon in this chapter to discuss the optical components of the eye and how current ophthalmic treatments for presbyopia and cataracts work and perform. For this section it is helpful to recall the following equation which gives the focal length, f, of a lens placed in air

$$\frac{1}{f} = (n-1)\left(\frac{1}{R_1} - \frac{1}{R_2} + \frac{(n-1)}{n}\frac{t}{R_1 R_2}\right), \tag{2.1}$$

where R_1 and R_2 are the radii of curvature of each lens face, n is the lens refractive index and t is the thickness of the lens.

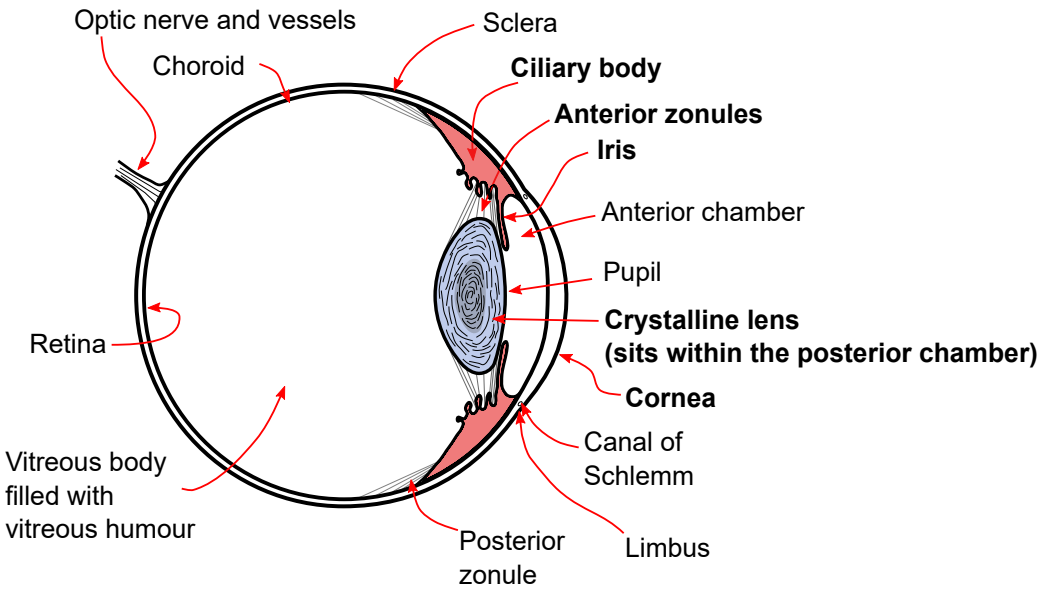

Figure 2.1: Simplified diagram of the human eye. Aspects highlighted in boldface are of particular importance to this thesis

2.1 The ageing eye

2.1.1 Anatomy of the eye

Figure 2.1 shows a simplified diagram of the human eye. The aspects highlighted by a boldface font are particularly key to the conditions of presbyopia and cataracts. The eyeball has three tunics (layers) named the "outer", "middle" and "inner". [49]

Approximately 80% of the outer tunic is formed from the sclera, a tough layer which provides shape and protection. The remaining ∼20% of the outer tunic is the cornea, a transparent lens that provides a fixed ∼70% or ∼44 D of the eye's refractive power (see appendix A for a definition of the unit of a dioptre, D). [117] The vast majority of the rest of eye's refractive power comes from the crystalline lens — the element solely responsible for changing the optical power of the eye (see section 2.1.2). [141]

The middle tunic of the eye includes the ciliary body and iris. The ciliary body

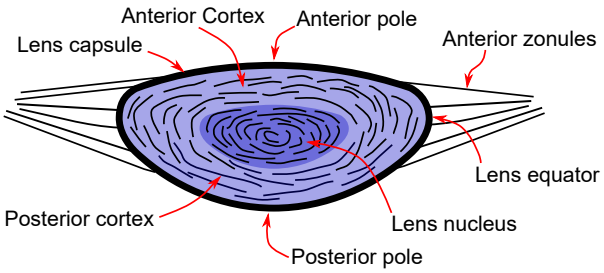

Figure 2.2: Diagram of the human crystalline lens.

is an annular ring of tissue which has two main functions. Firstly, it produces and secretes aqueous humour which fills the anterior chamber of the eye. [49] Secondly, the ciliary body provides the force required to distort the crystalline lens during accommodation (see section 2.1.3). The ciliary body is triangular in cross-section and has a series of invaginations on the anterior surface called ciliary processes [149] The main components of the ciliary body are the ciliary stroma and ciliary muscles. The ciliary stroma is vascular connective tissue that extends into the ciliary processes and is embedded with ciliary muscle [149] The ciliary muscle, which forms the majority of the ciliary body, consists of smooth muscle fibres of three different types: 'Longitudinal fibres', which are closest to the sclera, 'radial fibres', which connect the longitudinal fibres to the innermost 'circular fibres', which form a sphincter that lies close to the outer edge of the crystalline lens. [49]

The retina, which forms part of the inner tunic, is covered with photosensitive cells that detect light allowing vision. [49]

2.1.2 The crystalline lens

The crystalline lens is the only refractive component of the eye that changes optical power, a phenomena called "accommodation". [49] Figure 2.2 provides an illustration of a cross-section through the crystalline lens. The lens has a gradient in refractive index from 1.41 at the core to 1.39 in the cortex, giving the crystalline lens a slight gradient refractive index (GRIN) lens quality. [72] The

lens has biconvex shape where the posterior (rear) surface has a smaller radius of curvature compared to the anterior (front) surface. [84] The exact values for these radii of curvature change with age. [26] If the lens were studied in air, its power in the "distance vision state" would be measured as ~ 90 D. However, *in vivo* the power of the lens is reduced to ~ 15 D as the lens is surrounded by aqueous and vitreous humours which have refractive indices of $\sim$1.33 (see appendix A).

The lens is composed of transparent fibres and cells arranged in three parts: the capsule, epithelium and fibres. The capsule is composed of elastic collagen and its thickness varies across the lens. At the equator the capsule is $17-28$ μm thick while at the anterior and posterior poles it is $9-14$ μm and $2-3$ μm thick respectively. [49] Beneath the anterior portion of the capsule lies an epithelium (a layer of cells) which control the growth of new lens fibres. [9] The bulk of the crystalline lens is formed from fibres that continually form and grow throughout life. As old fibres are not removed, the size of the crystalline lens increase with age, the consequences of which are discussed in section 2.1.4. The stiffness of the lens is highly spatially inhomogeneous and also changes dramatically with age. Weeber *et. al.* tested lenses with ages between 19 and 78 years old *via* Dynamical Mechanical Analysis (DMA). [171] The authors sliced the lenses in half along their equatorial plane and measured their (compressive) shear modulus as a function of position using 0.1 Hz oscillations of the DMA probe. For the 19 year old eyes, the shear modulus increased from ~ 15 Pa at the centre of the nucleus to ~ 100 Pa at the edge of the cortex. For the 49 year old eye the modulus was ~ 1 kPa across the lens while for the 78 year old eye, the modulus instead decreased from ~ 500 kPa at the centre to ~ 1 kPa at the edge. [171] Similar results were seen by Heys *et. al.* [73]

The crystalline lens is attached to the ciliary body *via* "suspensory ligaments" or "zonules" which span from the ciliary processes to the lens capsular bag in a radial arrangement (illustrated in figures 2.1 and 2.2). These zonules fuse to form approximately 140 bundles which run to the lens and split up to fuse with the capsular bag. Larger fibres fuse with the anterior surface of the capsular bag; together these are known as the anterior zonular sheet. Smaller fibres curve

around the back of the lens where they fuse; together these as known as the posterior zonular sheet. [149]

2.1.3 Accommodation

The young, healthy human eye is able to accommodate between object placed as close to it as $\sim$ 10 cm through to distance objects located at "infinity" (near point calculated using equation A.1 with a total lens power in youth of $\sim$ 70 D and an image distance for the eye of $\sim$ 20 mm). [135] The method by which the lens accommodates is as follows.

When the ciliary body is in the relaxed state, the zonules are under their maximum tension and therefore apply the maximum radial stress to the crystalline lens. This stress causes the crystalline lens to flatten relative its preferred shape, thus adopting a shape tuned for distance vision. In this thinnest state of the lens, the anterior and posterior surfaces of the lens have their largest radii of curvatures. From equation 2.1 we can see that this correlates to the optically weakest state for the lens. [26]

To focus on closer objects the optical power of the crystalline lens must increase. A simultaneous contraction of the ciliary body's longitudinal and circular fibres respectively cause the ciliary body to pull itself forward and make the ciliary sphincter smaller. Together these contractions reduce the tension in the zonules and the stress applied to the crystalline lens. The lens is therefore able to elastically return to a more globular shape meaning the anterior and posterior radii of curvatures decrease (become more curved) which, from equation 2.1, causes the lens dioptric power to increase as required. [49]

The lens in an infant's eye is able to provide an accommodative range of approximately 14 D. As the lens ages this range decreases to approximately 4 D at age 40. [57] The typical reduction in accommodation after the age of 40, which can lead to functional difficulties with reading and other near-visual tasks, is termed 'presbyopia' and is discussed next.

2.1.4 Presbyopia

Presbyopia is the age-related decrease in the eye's accommodative amplitude which reduces its ability to focus on near objects. [56] The onset of the condition affects all without discrimination and its progression does not seem to be affected by nutrition or lifestyle factors. [27] Most researchers agree the dominant cause of presbyopia is the continued growth of the crystalline lens with age. [26] The effects of presbyopia generally become apparent at around the age of 40 when the accommodative amplitude falls below that required for everyday near visual tasks. [26] As children we are over-endowed with an accommodative amplitude which exceed our needs in everyday life. Thus the reduction in accommodative amplitude with age is only first noticed in mid-life when the eye's nearest point of focus extends beyond a working distance of approximately ∼25 cm. [26]

The review by Charman analysed studies on the causes and consequences of presbyopia. [26] The authors reported that the eye's accommodative amplitude decreases from ∼12 D at age 10 to 3 D at age 45. Past 45 years old the accommodative amplitude continues to decrease toward 0 D but at a slower rate. There are numerous physiological changes that occur within the "accommodative plant" (components of the eye related to accommodation) with age that are responsible for presbyopia. The optical properties of the lens, *i.e.* the lens surface radii of curvatures, the thickness and refractive index distribution, all change, but in a manner which still allows the eye to focus on distant objects correctly. [26, 34, 127] We reiterate that for simplicity we are only considering emmetropes — *i.e.* those with perfect distance vision.

The elastic properties of the various aspects of the crystalline lens also change. In addition to the change in shear modulus previously discussed, the lens capsule changes from being strong and extensible in youth to becoming increasingly weak and brittle with age. [88] The lens as a whole also becomes ∼ 20% thicker between ages 18 and 59. [82] Together these elastic and geometrical changes of the crystalline lens results in a reduction of one's accommodative amplitude resulting

in presbyopia.

Of particular importance to the prospects for developing a functional AIOL is how the ciliary body changes with age. Early experiments by Stieve show that the ciliary body increases in mass and therefore strengthens with age (as cited by Fisher). [48] Pardue *et. al.* suggested that while the shape of the ciliary body changes with age, it retains its ability to contract with age. [122] Atchison came to the opposite conclusion to Stieve — that the strength of the ciliary body decreases with age. Interestingly however, Atchison also concluded that this decrease in strength is unlikely to contribute to the development of presbyopia. [11] On balance the existing literature appears to suggest that the ciliary body maintains a sufficient capability to exert the forces required for accommodation, but that the changes in crystalline lens and possibly the zonules means that the accommodative effect of the contractions decreases with age. The fact that the ciliary body apparently maintains sufficient strength and functionality with age means that the ciliary body should be capable of actuating an AIOL and thus accommodation can be restored if an appropriate AIOL can be designed.

2.1.5 Cataracts

Cataracts are the clouding of the crystalline lens' nucleus and cortex which then hinders vision [10] There are several types of cataracts with the most common being age-related cataracts. The precise cause of this age-related clouding is subject to debate, however oxidative damage and long-term exposure to UV radiation are commonly proposed as causes [10, 150] The most common treatment of cataracts today is to remove the lens fibres which comprise the nucleus and cortex *via* phacoemulsification and insert a replacement fixed-focus IOL within the remaining lens capsule. The procedure involves the following: A small incision is made through the limbus (section of the eye joining the cornea and sclera — see figure 2.1) and anterior section of the lens capsule. An ultrasonic probe is then inserted which emulsifies the lens cortex and nucleus. The fragments are then removed *via* the same probe. The IOL is then inserted either into the anterior chamber between the iris and cornea or in the (now empty) capsular bag. The

latter design is much more common, however the former option may be used if, after phacoemulsification, the capsular bag is not strong enough to support an IOL. [10] Nowadays, the procedure for implanting an IOL is a routine operation most frequently does not require the patient to stay in hospital overnight. [99] An ideal AIOL could be surgically implanted *via* a similar procedure to an IOL although this desire could limit the complexity and functionality AIOLs.

2.1.6 Traditional ophthalmic treatments

Spectacles. Presbyopes can use reading spectacles as and when they require the additional optical power for close visual tasks. Bi- or vari-focal spectacles can be more convenient as their lenses have regions tuned for focusing at different distances. Therefore, instead of removing or replacing their glasses to change their focal range, a person instead looks through the appropriate region of their spectacle lens. In almost all cases, the lower portion of the spectacles has the greater optical power required for near-visual tasks — reflecting the direction our eyes typically point for tasks such as reading and eating.

Traditional contact lenses. Contact lenses for treating presbyopia exist in monovision, bifocal or multi-focal arrangements. [129] The success of each approach varies between patients. [39] Monovision contacts lenses have optical powers that correct one eye for distance vision and the other for near vision with the idea that one eye will always be able to correctly focus on a subject. [39] By contrast, bi- or multi-focal contact lenses (which are more frequently used) use regions of different optical power to simultaneously focus light from both distance and near objects (figure 2.3(a)). While bi- and multi-focal arrangements allow both the eyes of a presbyope to focus on both distant and near objects, wearers of bi- or multi-focal contact lenses must also accept a decrease in visual performance as light from a given object will always be partially defocused as shown in figure 2.3(b). [17, 39]

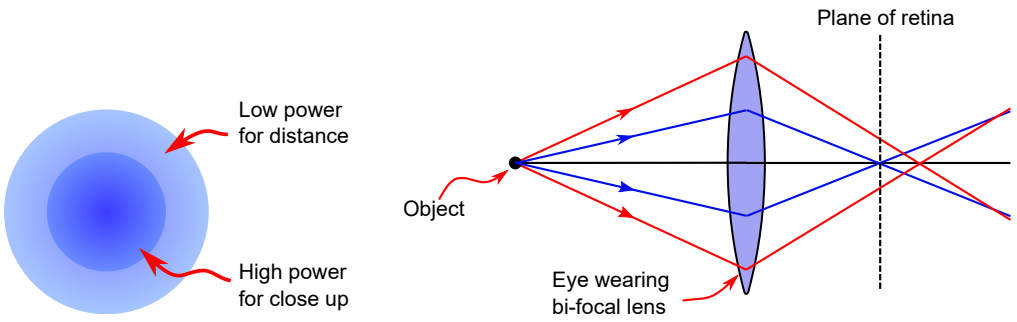

(a) (b)

Figure 2.3: a) Simplified diagram of the lens surface for a bifocal lens. Numerous other arrangements exist for instance to prevent pupillary contraction affecting the range of focus. b) Ray diagram illustrating how, while a bifocal lens enable focusing on near objects, it also partially mis-focuses light from the same object.

Liquid crystal based contact lenses. Electrically switchable liquid crystal (LC) contact lenses were first reported by Milton *et. al.* in 2014. In the current device configuration, the refractive index and hence optical power of a liquid crystal lens-shaped layer (encapsulated between two poly(methyl methacrylate) (PMMA) lenses), could be switched. [109] By selecting a high birefringence liquid crystal and carefully designing the PMMA lens curvatures, switching powers of up to 4 D could be readily achievable. [12] In the current design configuration, the contact lens only changes optical power for one polarisation of light as the switch relies on the reorientation of rod-like liquid crystal molecules which have uniaxial symmetry (see section 2.2). Thus in one of the states, the lens will essentially act as a bifocal lens as light passing through the LC layer will experience an effective birefringence. Amigó-Melchior and Finkelmann actually proposed to make use of the high birefringence of a liquid crystal in the creation of a "liquid single crystal hydrogel" bi-focal contact lens. [8] The authors suggested the material could also be used to create a bifocal IOL.

Fixed power IOL implants None of the above treatments are effective for the treatment of cataracts as they all leave the clouded crystalline lens in place. As discussed in section 2.1.5, cataracts must be treated by replacing the clouded

portion of the crystalline lens with a new lens. In the vast majority of cases, the new lens offers no accommodative ability. Like contact lenses, implanted IOLs can have, monovision or bi-focal or multi-focal arrangements and therefore they have similar compromises to contact lens treatment with the added consequence of the patient having zero accommodative ability.

2.1.7 Accommodating Intra-Ocular Lenses (AIOLs)

Accommodating intra-ocular lenses (AIOLs) aim to provide a treatment for both presbyopia and cataracts that still allows the eye to accommodate after surgery. Over the years numerous AIOL designs and modes of operation have been proposed, investigated and discarded. Both passive (mechanical based) and electrical (*e.g.* liquid-crystal based) devices have been proposed but so far only passive devices have been fully developed and approved for medical use. [6] As AIOLs concepts are continually being proposed and discarded, we base the following discussion off the two most recent reviews of AIOLs published by Pepose *et. al.* and Alió *et. al.*

What is immediately apparent from these reviews is that reports on the effectiveness of a given treatment can vary significantly. Inconsistencies can be attributed to small trial sizes, the short-term nature of the studies and different ways of determining the accommodative effect. The first two of these effects are a result of the relative youth of these new treatments meaning relatively few studies have been performed. The accommodative effect an AIOL provides can be reported based on *in vitro* experiments, subjective *in vivo* studies and objective *in vivo* studies. Of these ways of determining the real accommodative effect, only the results of objective *in vivo* tests, where the behaviour of the implanted AIOL is directly observed, have any meaning as *in vitro* tests experiments do not replicate the environment and behaviour of the eye and subjective tests are, by definition, subjective.

Alió *et. al.* reported that the four AIOLs which are currently commercially available today, have objective accommodative amplitudes of between 0 D and 2 D — far less that the $\sim$ 15 D of a young and healthy eye. [6] Additional effects,

such as lens distortions that increase the depth of focus can help to increase the perceived accommodative amplitude. [6] The failure of currently available AIOLs (and numerous similar AIOLs under development) lies in the fact that their accommodative effects rely on the translation of optical elements along the optic axis. The Crystalens, 1CU lens and Tetraflex AIOLs all feature a single lens connected to hinged "haptics'. As the lenses are placed in the capsular bag (following the removal of the lens cortex and nucleus), the haptics cause the lens to move forwards and backwards by $\lesssim 1$ mm as the ciliary body contracts and relaxes. The effect of this is extremely small and reported as being a 2 D change per mm of lens movement. [6] Appendix A shows *via* simple geometric optics why such small effects are to be expected from the translation of optical elements.

More promising AIOL devices are currently under development. The Lumina lens uses the Alvarez principle to change optical power and distortion for enhanced depth of focus. [6, 125] In this system two lenses (mounted on haptics) move relative to one another in the plane perpendicular to the optic axis. The Nulens uses a piston to transfer the force exerted by the ciliary body to a silicone gel — changing its lensing shape and thus changing the lens' optical power. While in theory the effect can offer 50–70 D of accommodative amplitude, the lens works in reverse to how the natural crystalline lens works, *i.e.* when the ciliary body is relaxed, the Nulens is at its strongest optical power. [125] As no clinical reports of this lens have been published since 2009 is is possible the Nulens is no longer under development. [125] The FluidVision AIOL features a lens filled with a silicone fluid connected to two haptics which also act as reservoirs for more silicone fluid. Forces exerted on the haptics cause fluid to move in and out of the lens region, changing its shape and hence optical power. In one trial objective measurements of accommodative amplitude ranged between 1.81 and 2.17 D. [125]

Alternative treatments for restoring accommodation have been to refill the capsular bag with a gel or soft polymer following removal of the cortex. However, historically this technique has been limited by the capsular bag post-operatively becoming opaque and/or the leakage of the injected material. These difficulties

are linked to the lack of an appropriate material which has the correct viscoelastic properties capable of providing sufficient form retention for maintaining the required lensing geometries alongside being sufficiently deformable in order to allow accommodation. [125]

2.1.8 Conclusion on current AIOLs for treating presbyopia and cataracts

While treatments for presbyopia and cataracts enable people to manage the age-related changes of the eye, none, including current AIOLs, come close to replicating the natural functionality of the youthful crystalline lens. From simple physics it is not surprising that currently available AIOLs (which modulate power *via* a movement of lens(es) of fixed optical power) fail to provide a full amplitude of accommodation. While smarter AIOLs which better replicate the behaviour of the crystalline lens may be under development, they too appear to either: not match the accommodative amplitude of the crystalline lens (in the case of the FluidVision AIOL); or be too complex to be practically realistic (as in the case of the Nulens).

Arguably the most ideal solution for treatment of presbyopia would be to replace the contents of the capsular bag with a material which allows the lens to function as it did in youth. However, approaches which have filled the capsular bag with a gel or polymer appear to have enjoyed little success as well. [125]

Perhaps where all of the currently proposed AIOLs have failed is because they have not attempted to replicate the structure and complexity of the natural crystalline lens. The crystalline lens is composed of fibres and has distinct nuclear, cortex and capsular regions. The lens is therefore structured and anisotropic. Moreover, the young, fully functioning crystalline lens has a shear modulus that is at its lowest ($\sim$ 15 Pa) in the central region, increasing with distance from the centre to its greatest at the edge ($\sim$ 100 Pa). Thus the mechanical properties of the crystalline lens are spatially inhomogeneous. As is noted below in section 2.5, LCEs can be prepared to be mechanically anisotropic and spatially structured.

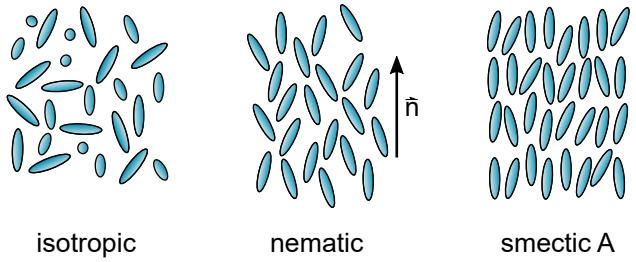

Figure 2.4: Illustration of the symmetries of how rod-like mesogenic molecules pack in the isotropic (conventional liquid) phase and in nematic and smectic LC phases.

Therefore LCEs are an exciting material to consider for use in a truly biomimetic AIOL.

2.2 Liquid crystals

2.2.1 Introduction

The term "liquid crystal" refers to a set of material phases, just like solids and liquids, that are exhibited by certain materials. As only certain chemical structures can form liquid crystalline phases, such materials are frequently referred to as being "liquid crystalline" — although they do also exhibit conventional liquid and solid phases. As is common, we will use the term "liquid crystal" (or LC) to refer to a "liquid crystal phase" or to "materials in a liquid crystalline phase".

LCs are perhaps most succinctly described as being ordered fluids. The LC molecules (or mesogens) pack with one another in a particular way which gives rise to macroscopic symmetries which in most cases are anisotropic — like many solid crystalline phases. However, as the LC molecules are also able to move past one another, LCs can also flow — like a liquid. Two types of LCs exist: "Thermotropics", where the LC phase behaviour is mediated by temperature; and "lyotropics" where the phase behaviour is mediated by the concentration of a solvent. In this thesis we are only concerned with thermotropics and so our use

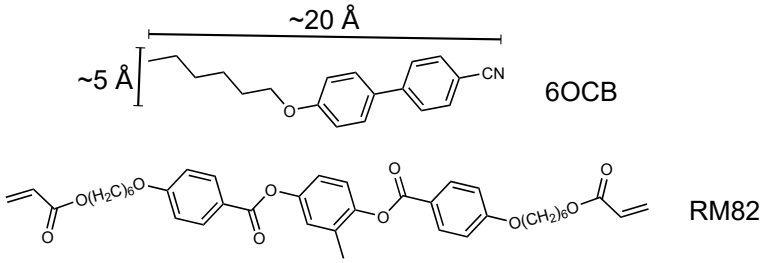

Figure 2.5: Chemical structures of mesogenic molecules which display nematic phases. These exemplars are chosen as they are used later in this thesis. The dimensions of 6OCB shown should only be taken as rough numbers indicating the length scale and shape anisotropy.

of LC will refer solely to thermotropic LCs.

Like the 270 different crystalline space groups, there are numerous LC phases each with a unique symmetry. Again, in this thesis we are, for the most part, only concerned with the simplest of these phases — the "nematic" phase. Our introduction therefore only describes the nematic phase in any detail. The (conventional) liquid phase will also be of importance and will be referred to as the "isotropic" phase to reflect its symmetry. Figure 2.4 shows a two dimensional simplified diagram of how (rod-like, or "calamitic") LC molecules are arranged in the isotropic and nematic phases. For completeness figure 2.4 also shows molecular arrangements for the the simplest of the layered (or "smectic") phases known as the "smectic A" phase as it will be referred to on occasion. However, we do not provide any further detail about the smectic A phases here.

2.2.2 Nematic and isotropic phases for calamitics

2.2.2.1 Typical chemical structure

Figure 2.5 shows chemical diagrams for two example nematic mesogens called (in short) 6OCB and RM82. The approximate dimensions of 6OCB shown are based off the chemically similar 5CB (which lacks the oxygen and has an alkyl chain of 5 carbons) and illustrates the length scale and anisotropy of mesogenic

molecules. [112] Perhaps the most key aspect of these molecules are their rigid cores, formed from the benzene rings and (for RM82) the ester groups. The rigid core of a mesogen provides a rod-like, anisotropic shape which is also highly polarisable. [62] These aspects together facilitate the formation of LC phases. The alkyl chains are also key components which facilitate the formation of low and room temperature LC phases. [62] The description provided here of the function of the core and alkyl chain should only be taken in the broadest of terms as, as Gray pointed out, it is extremely difficult to predict the LC phase behaviour from single chemical structure. [62] LCs can also be formed from mixtures of several mesogenic and non-mesogenic molecules. The exact composition of the mixtures chosen is used to modify the phase behaviour and properties of the resultant LC.

The alkyl chains of RM82 are terminated with reactive acrylate groups. These are important in the formation of LCEs as they allow the molecules to bond together to form polymeric chains (see section 2.5.6.1).

2.2.2.2 Nematic and isotropic symmetries and temperature dependencies

The nematic LC phase is the simplest LC phase possible and has the highest symmetry possible for an LC phase. Compared to the conventional liquid (isotropic) phase, a unique axes exists and the system has cylindrical symmetry. This anisotropic symmetry gives rise to anisotropy in physical properties such as refractive index (birefringence) and dielectric constant. As will be discussed in section 5.4, the birefringence of liquid crystals offers a way by which the orientation and ordering of nematic LCs can be assessed.

As the nematic phase is a thermotropic LC phase, it is only observed within a certain temperature window which is unique to each chemical structure/formulation mixture. On cooling a nematic LC, the material will eventually reach a phase transition temperature below which the material may enter either a different (*e.g.* Smectic A) LC phase or a solid (typically crystalline) phase. On heating a nematic LC, above a temperature denoted as T_{NI}, the LC will undergo a first order

phase transition to the isotropic phase. [62]

Figure 2.4 illustrated how the molecules within a nematic phase are preferentially aligned with a direction labelled by $\vec{n}$, known as the "director". The degree to which the LC molecules align parallel to the director is highly temperature dependent and can be characterised by a scalar order parameter, Q_N, which is based on the average of the cosines of the angles made between each molecule and the director. Given the symmetry of the system, the Legendre polynomials are the most natural base for the order parameter. As the nematic phase is inversion symmetric ($\vec{n} = -\vec{n}$), the odd Legendre polynomials, for instance $P_1 = \langle \cos\theta \rangle$, are zero by necessity. Consequently, the even Legendre polynomials are used as order parameters with $P_2 = {}^1\!/_2 \langle 3\cos^2\theta - 1 \rangle$ being the most commonly used to describe the magnitude of nematic order.

As $\cos\theta$ is bound by ± 1, the even Legendre polynomials and hence Q_N are bound by values of -0.5 and $+1$. The order parameter can be rewritten in integral form [115]

$$Q_N = \int_0^\pi d\theta P(\theta) \times \frac{1}{2}(3\cos^2\theta - 1)\sin\theta, \tag{2.2}$$

where θ is the angle between the LC molecular orientations and the director, which we have taken to lie along the $\hat{z}$ axis. The normalised distribution function $P(\theta)$ describes the angular distribution of the mesogens' orientation relative to the director. The director sign invariance of the nematic phase means the distribution function $P(\theta)$ is symmetric about $\theta = 90°$ and also has no dependency on the azimuthal angle about $\hat{z}$. The links between the distribution of mesogen orientations and value of the order parameter can be readily understood by considering top-hat-like forms of $P(\theta)$ which describe the allowed solid angles within which each molecule's orientation may lie. Figure 2.6 illustrates a series of solid angles within the range of $Q_N = 1$ to $Q_N = -0.5$. The central figure where $Q_N = 0$ corresponds to the isotropic phase in which there is zero correlation between the orientation of any two mesogens — *i.e.* $P(\theta) = {}^1\!/_\pi$. [115] Moving (in

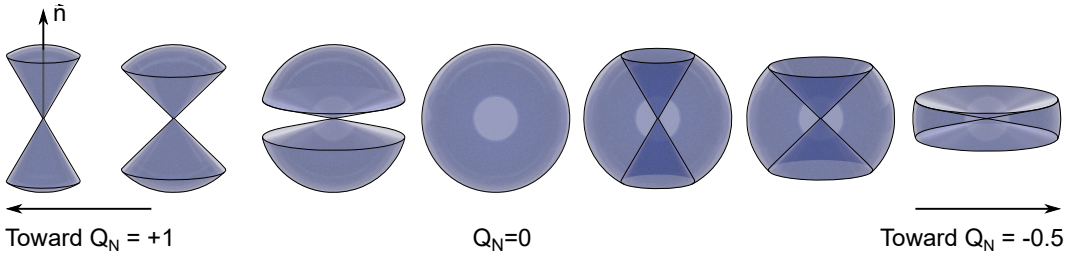

Figure 2.6: Illustration of the relationship between the LC order parameter, Q_N, and the distribution of mesogen angular orientation relative to the director. Top hat-like probability distribution functions for the allowed solid angles are shown for clarity of the illustration however the real distribution functions will be continuous in nature.

figure 2.6) to the left of the isotropic arrangement, we increase Q_N by constraining the possible orientations toward the director. If the solid angle was reduced further to the state where all the molecules aligned perfectly with the director then we would have a state of $Q_N = 1$. If however, we move to the right from the $Q_N = 0$ state and we exclude allowed orientations parallel to the director, we then have negative values of the order parameter whereby the molecules on average lie in the plane perpendicular to the director. Q_N reaches its minimum possible value of -0.5 in the extreme case where all molecules are confined to the plane defined by $\theta = \frac{\pi}{2}$. [115]

The value of Q_N for a given nematic system at a given temperature depends on the balance between the various interactions between molecules. Most important (for thermotropic LCs) are the anisotropic van der Waals and steric interactions between molecules, and the thermal energy of the molecules which allows them to vibrate and rotate. According to Maier-Saupe theory, the combination of these various interactions and energies means that each molecule experiences an anisotropic mean field potential. Using this one can account for the nematic to isotropic transition as well the orientational properties of the nematic phase. [102]

As the nematic to isotropic phase transition is a first order transition, the order parameter discontinuously jumps from $Q_N = 0$ in the isotropic phase to $Q_N > 0$ in the nematic phase. Moving the system deeper into the nematic phase

by decreasing the temperature below T_{NI} sees Q_N increase. [36]

2.3 Elastomers

Elastomers are isotropic, rubbery materials formed from amorphous polymer chains joined together through either chemical or physical crosslinks. Upon mechanical deformation, the crosslinks prevent the polymer chains slipping past one another thus meaning the chains become extended. The resultant lowering of the internal entropy results in the generation of an elastic restoring force in order to drive the system back to the preferential highest entropy state. Elastomers are characterised by their viscoelasticity, low elastic moduli (typically a few MPa), high extensibility (as high as several hundreds of percent) and glass transition temperatures that are below room temperature. [134] The combination of elasticity and dissipivity in elastomers makes them highly useful for a variety of applications including sealing gaskets, protective/disposable gloves, biomedical devices, vibration dampers and shock absorbers.

In this section we describe the physical form and elasticity of elastomers in general. Chapter 4 will consider the elasticity *via* classical rubber elasticity.

2.3.1 Chemical and physical structure of polymers and elastomers

Elastomers are made from long strands of polymer chains that are linked to one another through chemical and physical bonds. The polymeric chains of elastomers are typically between 10,000-50,000 main chain atoms long with crosslinks every spaced every 100-1,000 main chain atoms. [107, 134, 55] At this crosslinking level, crosslinked polymers display elastomeric behaviour.

Adjacent bonds along the polymer chain lie at angles to one another. As the bonds can typically rotate, these bond angles allow the polymer chains to take up a variety of different trajectories or "conformations" which can change with time *via* diffusion or in response to stimuli. The trajectory a polymer chain takes

can be viewed as a random walk. [169] In chapter 4 we will use this to derive the stress-strain behaviour of an elastomer. The overall shape of a given polymer chain will in general appear ellipsoidal at any given snapshot in time. However, as the ellipticity will continually be changing in magnitude and orientation with time, the conformation on average appears to be spherical — hence polymer chain conformations are typically illustrated by spherical conformations. [155]

The shear modulus of an elastomer is typically quoted as $\mu = n_s k_B T$ where n_s is the density of *chemical* crosslinks, k_B is the Boltzmann constant and T is the material temperature. [134] Evidently, increasing the number of crosslinks will lead to stiffer materials. However, as an increased crosslink density also increases an elastomer's glass transition temperature, increases in the crosslink density can also result in the material becoming a brittle thermoset resin instead of an elastomer. [55] Alongside chemically-bonded crosslinks, *physical* crosslinks can occur as a result of the long polymer chains entangling with one another. [55] The presence of physical crosslinks can give an elastomer a greater shear modulus than would be expected from the chemical crosslink density.

The backbone of an elastomer's polymer chains are formed from a repeating unit of atoms such as -(C)-, -(C-O)- or -(Si-O)-. Many different chemical types of elastomers exist and can differ according to the: chemical structure of the constituent monomer unit(s), crosslink density, and the chemistry and density filling particles (colloidal particles which are typically used to increase the strength of an elastomer). [55] While classical rubber elasticity quite successfully explores the mechanical behaviour of elastomers by stripping away any details of the chemical structure, the chemistry of the network still has profound effects on other properties of an elastomer such as its swelling behaviour, chemical resistance, anisotropy and glass transition temperature. [65, 169] One route to controlling the properties of elastomers is through chemically bonding pendant or "side chain" groups to the polymer backbone. [22] As we will see in section 2.5 below, the incorporation of mesogenic side chain groups can be used to produce a side chain LCE. Additionally, in chapter 6 we use a side chain group to interfere with the packing of the elastomer chains in order to lower a LCE's glass transition temperature.

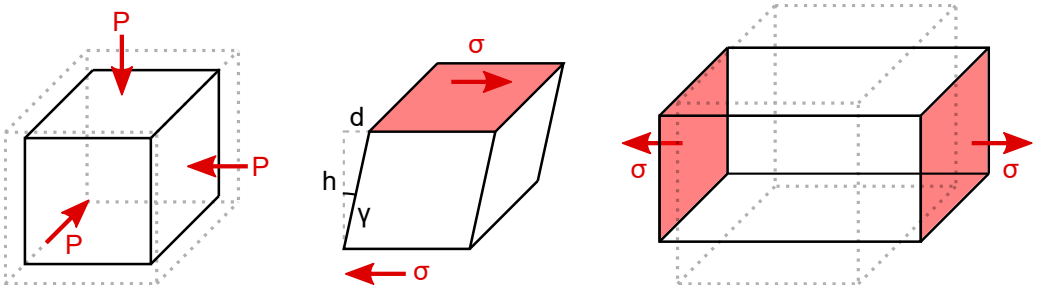

(a) (b) (c)

Figure 2.7: Three different deformation modes for an isotropic elastomer. a) Represents volume, or bulk changes, b) represents shears and, c) represents extensions. A general deformation of an elastomer can be broken down into these three components.

2.3.2 Elastomer deformation modes and elastic constants

The deformation behaviour of elastomers under loads is characterised *via* their bulk and shear moduli which respectively characterise an elastomer's resistance to changes in volume and deformations under shear (figures 2.7(a) and 2.7(b) overleaf). Applying a pressure, P, isotropically to a material, will cause a fractional volume change given by:

$$P = -K\frac{\Delta V}{V_0}, \tag{2.3}$$

where ΔV is the change in volume and V_0 is the initial volume of the body. K is the bulk modulus and for a typical elastomer has values of ∼GPa.

If a body is sheared by applying a stress, σ, over opposing surfaces as shown in figure 2.7(b), then the body will in undergo a shear characterised by the ratio of the relative movement of the surfaces in the direction of the shearing forces (d) to the initial separation of the surfaces (h). For small deformations this is equal to the angular deformation marked as γ on figure 2.7(b). σ and γ are related to one another through the shear modulus (μ):

$$\sigma = \mu\gamma. \tag{2.4}$$

Typically values of μ for an elastomer are ∼MPa — less than the bulk modulus by several orders of magnitude. Consequently, elastomers are typically assumed to essentially be incompressible and to deform at constant volume. [55, 169]

From the bulk and shear modulus, the rest of the elastic constants of an isotropic elastomer can be calculated. As typically $K >> \mu$, the expressions for these elastic constants can be somewhat simplified. For instance, the elastic modulus, which describes the resistance to a deformation of type shown in figure 2.7(c), is given by

$$E = \frac{9K\mu}{3(K+\mu)} \sim 3\mu \text{ (for } K >> \mu), \tag{2.5}$$

and Poissons ratio is given by:

$$\nu = \frac{1}{2}\left(\frac{3K-2\mu}{3K+\mu}\right) \sim \frac{1}{2} \text{ (for } K >> \mu). \tag{2.6}$$

Poisson's ratio is typically measured to be $\sim$ 0.499 for an elastomer thus confirming the assumption of incompressiblity which is frequently made. [55]

2.4 Feasibility of LCE-AIOL operation modes

Before we proceed to our full introduction of LCEs we take a moment to use what we have learnt so far in this chapter to comment on the feasibility of the LCE-AIOL operation modes identified at the end of chapter 1.

Our review of the electrically switchable liquid crystal and bifocal LCE contact lenses highlighted that the use of birefringent materials would likely give a switchable lens a bifocal characteristic — impacting the maximum visual acuity that could be expected. This makes the first idea of a mechanically switchable refractive index a less appealing concept for the LCE-AIOL and thus we will not pursue this concept any further in this thesis.

While any LCE birefringence could also impact the optical quality of a LCE-based lens designed to make use of programmed mechanical anisotropy, the effect could easily be mitigated by use of a low birefringence material. In chapter 4 we will show that the extent of the mechanical anisotropy for a LCE is related to the magnitude of the LCE order parameter, Q_N. As a high value of Q_N does not necessarily require or imply a high birefringence, it is reasonable to think that for a real device, a LCE with a suitably high Q_N (for maximal mechanical anisotropy) and low birefringence could be designed. [58]

2.5 Liquid Crystal Elastomers (LCEs)

The previous two sections have laid the foundations required for us now to consider Liquid Crystal Elastomers and understand what is unique and exciting about their physical properties. From this we will identify the challenges that must be tackled to satisfy the aims of this thesis.

2.5.1 Deeper introduction to LCEs

Before we delve deep into the physical properties and chemical structures of LCEs its worth taking the opportunity to use put together the content introduced in the previous two sections to better-define what exactly a LCE is and to provide some basic information about their physical forms. These definitions will help the understanding of the discussion of LCE properties and chemistries that follows.

In a LCE, polymer chains of the elastomer network are functionalised with mesogenic groups which are either "main chain" and directly incorporated into the polymer backbone or "side chain" and are bonded laterally (see figure 2.9 on page 31). When the density of mesogens is sufficiently high they can establish a LC phase. The inherent ordering of the LC phase constricts the orientation of the polymer chain thus increasing the backbone's persistence length either parallel (most commonly) or perpendicular to the LC director. [169] In order to maintain elasticity, and thus create a LCE, the persistence length must not be increased too much to restrict the entropic nature of the polymer backbone. [169] The polymer

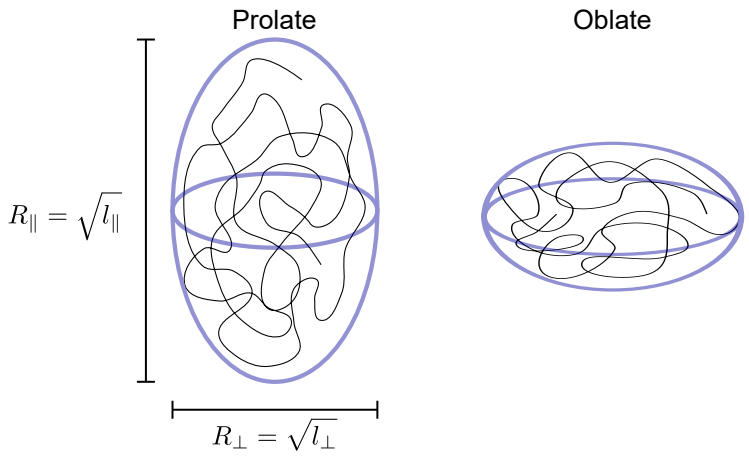

Figure 2.8: Diagrammatic representation of the prolate ($r = {}^{l_{\parallel}}/_{l_{\perp}} > 1$) and oblate ($r < 1$) ellipsoidal shapes the polymer conformation of a LCE adopts in a LC phase. The R_x represent the anisotropic polymer chain radius of gyration while the l_x represent the anisotropic effective step lengths of the polymer chain random walk. [169]

chain can now be described by an anisotropic random walk. This translates to the polymer conformation for a LCE adopting an on average (anisotropic) elliptical conformation (see figure 2.8) as opposed to the average (isotropic) spherical shape seen in conventional elastomers. [169] Essentially the LC phase is stretching the polymer chain along the LC director. This description of the physical form of a LCE network is formally expanded upon from a theoretical point of view in chapter 4.

As will become evident, the globally anisotropic polymer conformation is central to all the physical phenomena unique to LCEs. This anisotropy is quantified by the ratio of the effective step lengths of the random walk parallel ($l_{\parallel}$) and perpendicular ($l_{\perp}$) to the director (see chapter 4 for further details). This ratio, called the step length anisotropy (symbolised by r), is perhaps the most key property of LCEs as it appears in almost all theoretical descriptions of a LCE's physical behaviour. For the case of $r > 1$, the polymer conformation has a prolate ellipsoidal shape, while for $r < 1$ the polymer conformation has an oblate ellipsoidal shape (figure 2.8). LCEs with prolate polymer conformations

are more frequently reported and typically nematic LCEs with greater values of r are sought as they display greater 'magnitudes' of the LCE-specific behaviours described in section 2.5.3 and 2.5.4. This fact is an important consideration to bear in mind when designing and choosing a LCE to use for any given application.

LCEs can also be prepared in one of two geometries known as polydomains or monodomains. In a polydomain LCE the mesogens are only aligned with one another in microscopic domains. Neighbouring domains have different alignments and so light passing through a polydomain LCE is strongly scattered by domain boundaries giving an opaque appearance much like a unaligned bulk quantity of LC. Polydomain microstructures occur when during synthesis no steps are taken to instil a macroscopic direction of alignment throughout a bulk of material and thus the director cannot be defined on a macroscopic/visible length scale. By comparison monodomain LCEs have alignment of mesogens on a macroscopic/visible length scale thus they appear transparent as no scattering boundaries exist within the material. The macroscopic order within a LCE can be instilled by one of two method categories. Firstly, two-step processes where a lightly crosslinked polydomain LCE is firstly formed and converted to a monodomain by applying a mechanical stress which aligns the microscopic domains. This monodomain state is then "frozen in" by performing a second crosslinking step. [93, 176] Secondly, the monomer state can be aligned prior to polymerisation by use of LC cells (moulds for LCE polymerisation) prepared with appropriate surface treatments (see section 5.2.1) or by application of magnetic field. [157, 146] The alignment of the director in monodomain LCEs does not have to be uniform throughout a material. [164] Depending on the chemistry of a given LCE, several different methods for instilling complex director geometries exist (discussed in section 2.5.5).

Aside from their optical differences, polydomain and monodomain LCEs have very different mechanical properties and prospects as actuation devices. As we require a transparent LCE for our lens-based application we are (going forward) only concerned with monodomain LCEs.

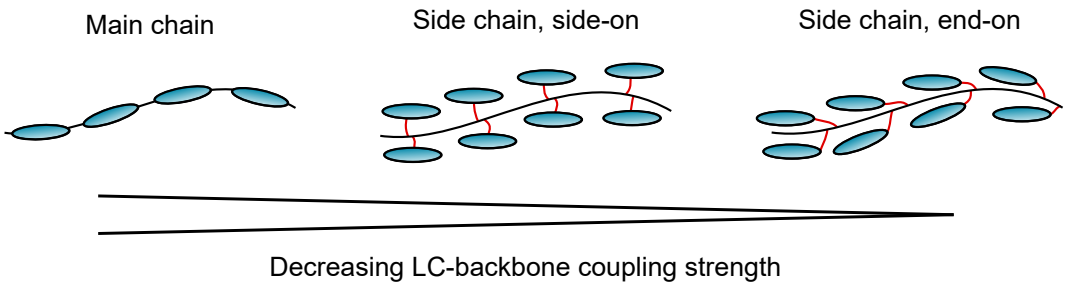

Figure 2.9: Representations of the three different ways in which rod-like LC mesogens are most commonly linked to the polymer chain backbone. Each mode has a different strength of coupling between the mesogen and the backbone which affects the magnitude of step length anisotropy possible. For side chain systems the mesogens are connected to the backbone *via* a spacer group highlighted in red.

2.5.2 LC-polymer backbone coupling modes

Figure 2.9 shows three most common ways in which LC mesogens are incorporated into a polymer backbone. For main chain (MC) configurations, mesogens can also be incorporated into the polymer backbone by their mid-points as opposed to their ends, however such configurations are rarely used.

MC LC polymers (LCPs) have the strongest coupling between the mesogens and the polymer backbone as the mesogens are directly embedded into the polymer backbones. [169] MC LCPs therefore have the largest persistence lengths of all LCP types and hence they display the largest step length anisotropies with values as large as $r \sim 60$ being reported for a nematic MC LCP by D'Allest *et. al.* [31]

Side chain (SC) LCEs have been confirmed with either prolate or oblate conformations although their characteristics are somewhat more complex than in MC LCEs as there are more parameters which can be varied. Firstly, the length of the spacer group between the polymeric backbone and the mesogenic core (highlighted in red in the relevant figures of figure 2.9) vastly alters the strength of the coupling between the ordering of the LC phase and polymer backbone and thus affects the degree of anisotropy present. Hardouin *et. al.* showed that side-on SC

LCPs have prolate chain anisotropies due to a "jacketing" effect of the polymer chain by the mesogenic molecules. [67] In general, the longer the spacer group between the polymer backbone and the mesogenic group, the weaker the jacketing effect and the lower the magnitude of r. [67, 68, 95] For instance Lecommandoux *et. al.* measured values of $r = 36$, 21 and 1.2 for three different side-on SC LCPs with identical mesogenic cores but spacer lengths of 4, 6 and 11 carbon atoms long. [95]

Many early instances of end-on SC LCPs were observed to have oblate chain conformations, a result of their smectic phases. In these "comb-like" systems the polymer chain is believed to exist primarily between the smectic layers with the mesogens hanging laterally in smectic layers. [85, 116]

Perhaps the most studied nematic SC LCE developed to date was developed by the Urayama group. [157] Using the results of Tamashima *et. al.* one can calculate $r \sim 2$ for the Urayama LCE (using the behaviour described in section 4.4.1). This comparatively low value of r for a SC end-on LCE reflects the fact that SC end-on LCEs are typically seen as having the lowest polymer chain anisotropies. [169, 22]

The length of the spacer for end-on SC LCPs is also believed to influence whether the polymer conformation is prolate or oblate. Brömmel *et. al.* report for odd (even) spacer lengths the conformation is typically prolate (oblate), a consequence of the bond angle of alkyl chains. [22] This assessment appears to be an oversimplification as examples of end-on SC LCPs with even spacer lengths and prolate polymer conformations exist. [157] In these systems reducing or increasing the spacer length by one carbon atom may result in an oblate polymer conformations.

2.5.3 Nematic order and LCE actuation

Possibly the most striking behaviour of LCEs is their reversible shape actuation response which can be triggered by thermal and optical stimuli. [169, 177, 164] This behaviour is a simple result of the coupling between the liquid crystalline

ordering (characterised by Q_N) and r (and hence the polymer conformation anisotropy). The formal link between Q_N and r is derived in chapter 4. Here we state that by lowering Q_N *via* thermal, optical or chemical means, r (for a prolate system) also reduces toward unity. Macroscopically this manifests itself as a contraction (expansion) of the LCE parallel (perpendicular) to the director. The greatest contractions of up to 80% have been observed in nematic main chain systems. [3, 172][1] By contrast side chain LCEs display actuations of around 20%. [156, 154] Smectic systems have more complicated behaviours as a result of the energies involved in the destruction and reformation of the smectic layers. Typically smectic LCEs exhibit shape memory effects with plastic deformations being reversed through heating of the LCE to the isotropic phase. [151, 124]

For thermal actuations, the temperature range over which a nematic LCE must be cycled in order to induce the full shape actuation varies dramatically between different materials and is influenced by the nature of the phase transition from the nematic to isotropic phase. In conventional LC systems the nematic-to-isotropic phase transition has a first order behaviour. However, in monodomain LCEs the presence of the polymer network and macroscopic LC ordering means the nematic to isotropic transition is instead a second-order transition where Q_N continuously changes with temperature. [168] The magnitude by which the transition departs in similarity from the first-order behaviour of conventional LCs can depend on material chemistry. For instance the inclusion of mesogenic-like crosslinking groups can completely remove the possibility of a perfectly isotropic state. [162, 165]

2.5.4 Mechanical and opto-mechanical properties of LCEs

LCEs have long being known to have interesting and unique mechanical properties. [169] Indeed it is these behaviour which led us to believe they hold promise for developing a mechanically switchable lens. However, despite the wealth of

[1] The actuation behaviour of LCEs is commonly quantified in terms of the percent extension parallel to the director as the LCE is cooled from the isotropic phase. In this case, the 80% contraction written here is equivalent to a 400% expansion.

research performed into the mechanical behaviours of LCEs, numerous inconsistencies and gaps in the community's present knowledge still exist. Below, we review the opto-mechanical properties of LCEs and identify some of the current "unknowns" of LCE opto-mechanical behaviours.

Mechanical anisotropy

Experiments have long shown that the initial moduli for stresses applied parallel to the director are typically several times greater than moduli for stresses applied perpendicular to the director. [93, 92, 105, 47] Moreover, mechanical anisotropy is also observed in the non-linearity, ultimate tensile strengths and strain-at-failures. [47, 166] Despite the above results, the initial theory of LCEs pioneered by Warner and Terentjev (W&T) predicted that the *initial* elastic moduli for monodomain LCEs stressed parallel and perpendicular to the director should be equal. [169] Modifications to the basic W&T theory which take into consideration the non-Gaussian nature of real LCE networks can account for a small degree of elastic anisotropy of around a few percent, but this anisotropy still falls short of the magnitude of anisotropy seen experimentally. [105] A pair of papers published in 2001 by Warner and co-workers investigated the elastic anisotropy of LCEs in greater detail by allowing applied stresses to deform the shape of the polymer conformation and the magnitude of the LC order parameter. Despite developing a comprehensive theoretical model the authors were unable to compare their theoretical results to experimental results as their materials studied were too far from being "ideal". [47, 126]

Considering the body of research into the stress-strain properties of LCEs as a whole it is evident that the vast majority of tests have focused on stresses applied perpendicular the the director — presumably to observe the "mechanical Fréedericksz" or (semi-)soft elastic behaviour of the LCE under consideration (these phenomena are discussed below). Comparisons of this behaviour to that observed for stresses applied parallel to the director are performed on occasion and moreover there exists only two (brief) reports of the stress-strain behaviour of a LCE stressed at a variety of angles between parallel and perpendicular to

the director. [166, 60] In order to design and develop mechano-LCE devices a much more thorough study of the stress-strain behaviour for generic angles to the director must be performed.

(Semi-)Soft elasticity and "Mechanical Fréedericksz" transitions

The optomechanical behaviour displayed by LCEs when stressed perpendicular to the director has been reported to take two forms. In both cases, the director rotates toward the stress axis — a behaviour also seen at stresses applied at a generic angle to the director. [93, 90, 76] However, beyond this similarity the two processes differ quite significantly.

Most frequently a slow and gradual rotation of the director over a range of strains is observed. This behaviour is called soft, or semi-soft elasticity (herein both behaviours are referred to as "SSE") depending on how 'ideal' the LCE under investigation is. The first observation of SSE by Küpfer and Finkelmann in 1991 triggered numerous subsequent investigations into this process. [93, 90, 29, 159] The director rotation behaviour for a SSE process is well known to be intimately linked to the shape of the tensile load curve. In the case of soft elasticity, the director begins its rotation from zero strain over which period the load curve has a gradient of zero — *i.e.* the deformation costs zero elastic energy. In the case of semi-soft elasticity material "non-idealities" (described in chapter 4) mean a threshold strain must first be overcome before the director rotation begins. The load curve over the director rotation region has a small but finite gradient. [169] The manner in which the director rotates during a SSE process can also take one of two forms: In the first, the sense of director rotation is uniform across the entire sample; however, in the second, thin strip-like counter rotating domains ("stripe" domains) are formed running parallel to the stress axis. [94, 91, 183] Zubarev *et. al.* demonstrated that stripe domains will only form when the aspect ratio of the monodomain film small enough to require the formation to stripe domains in order to avoid large shears in the vicinity of the sample clamps. However, there remains the possibility that LCE chemistry may also influence the presence of stripe domains as they have not been observed in materials developed by the

Urayama and White groups. [74, 163, 165]

The second director reorientation method is a comparatively sharp rotation of the director which occurs at a critical strain. This behaviour was dubbed a "mechanical Fréedericksz" transition (MFT) due to the similarity of director response of a conventional liquid crystal to an applied electric field. To date, MFTs have only been reported by the Mitchell group. [111, 133, 132] Surprisingly, the tensile load curve for a LCE deforming *via* a MFT has never been reported and therefore how it differs to a SSE load curve is unknown. Stripe domains have never been seen for a LCE deforming *via* a MFT, however this is perhaps not surprising given the sharpness of the director rotation.

To understand the physical behaviours of MFT and SSE in greater detail it is useful to understand the theoretical description of these behaviours provided by W&T. Additional details are therefore given in the theory chapter (4) of this thesis.

Generic deformations of monodomain LCEs

Experiments exploring the phenomena of SSE have shown that the mechanically-induced director rotation seen in LCEs is tied closely to their tensile mechanical response. Despite this, the stress-strain and director rotation response of LCEs is almost never reported together in the same paper. [93, 94, 74] Even when they are, the two properties are only known to have been recorded *simultaneously* twice. [93, 94]

The behaviour of LCEs stressed at generic angles to the director (between parallel and perpendicular) has also been largely unstudied. The rotation of the director has been studied for limited cases by Kundler *et. al.* and Hirschmann *et. al.* while the stress-strain behaviour for a range of angles has only been investigated by Ware *et. al.*. [90, 76, 166] The results of Ware *et. al.* make it clear that for smaller angles between the stress axis and the initial director, one can expect a stiffer material response along with a greater maximum stress and lower maximum strain at failure. However, the effect of the rotating director on the

shape of the load curve is unknown as the director orientation was not tracked throughout mechanical deformation.

Additionally Ware *et. al.* (and to a lesser extent Godman *et. al.*) have provided the first demonstrations of how a complexly aligned LCE mechanically deforms. These papers will be revisited and discussed in detail in chapter. 11 Here we highlight the fact that these two papers do not study the deformations presented in enough depth to allow one to begin to consider how mechano-LCE devices could be designed and how they would function.

2.5.5 Reviewing LCE chemistries

We now turn to review LCE chemistries in order to identify which of the many chemistries is most appropriate for use in this thesis. Determination of the "correct" LCE for use in this thesis is based on the following criteria which are listed in order of priority:

1. Synthesis of macroscopic (∼centimetre scale) LCE films in spatially programmed monodomain alignment geometries. The patterning of the LCE director has been identified as the way in which a mechanically switchable lens would operate thus the chemistry chosen should allow controllable patterning of the director with high resolution.

2. Ease of synthesis. The expertise and resources available exclude the possibility of creating components in-house that require specialist chemistry knowledge. Ideally the components required for the LCE pre-cursor should be commercially available such that research can be performed with a confidence in the supply of materials required.

3. Appropriate physical properties for final device.

4. Material biocompatibility.

At a first glance it may appear that the order should be almost reversed as we are proposing the development of a biomedical device. However, as some LCEs

have had their biocompatibility demonstrated and the scope of this thesis is to demonstrate the feasibility of a mechanically switchable LCE-based lens, biocompatibility is actually the lowest of our priorities. [147, 2, 176, 51]

In the near forty years since LCEs were first developed a plethora of LCEs chemistries have been created. [22, 89] The vast majority of LCE research to date has focused on LCEs of polysiloxane and acrylate chemistries. Consequently much of the fundamental physical model of LCEs was developed off the bat of observations of polysiloxane and acrylate LCEs. [169]

Despite the early popularity of polysiloxane and acrylate LCE chemistries they both have their own respective drawbacks which have motivated recent the development several new LCE chemistries aimed at combining the advantages of both chemistries while removing their limitations. [89] To review all the possible LCE chemistries that we could possibly choose to work with is beyond the scope of this introduction. For a comprehensive guide to LCE chemistries developed to date we instead refer the reader to recent reviews by Brömmel *et. al.* and Kularatne *et. al.* [22, 89]

Of all the various LCE chemistries developed over the years, polysiloxane, acrylate, amine-acrylate and thiol-acrylate chemistries were identified as being worth considering for use in this thesis. This was based on the depth of mechanical characterisation performed to date on these chemistries and the attractiveness of their properties when considering the criteria given above. Tables 2.1— 2.4 provide a succinct overview of the synthesis characteristics of each of these LCE-types.

Table 2.1: Summary of synthetic route and key properties of polysiloxane-based LCEs.

Poly-siloxane LCEs	
Pioneering group	Finkelmann [43, 44, 45, 46, 47]
Synthesis procedure	Two-step process for monodomains — a complicated procedure requiring speciality chemistry knowledge. [93]
Mesogen-backbone coupling mode(s)	Main chain, side chain side-on and side chain end-on all possible. [93, 38, 22]
Monomer commercial availability	Minimal.
Monodomains instilled by	Typically a mechanical force is applied between first and second crosslinking steps. [93] Alignment *via* strong ($\sim$ Tesla) magnetic fields has also been demonstrated. [8]
Pattern-able director geometries?	Limited ability as mechanical force or strong magnets required for alignment.
Deformation mode when stressed perpendicular to the director	Semi-soft elasticity. [93, 90]
Stripe domains observed?	Yes. [91]
Sub-room glass transition temperature?	Can be tuned over a wide range starting from below 0°C. [43]
Comment	While poly-siloxane LCEs were the first to be synthesised and their mechanical properties deeply investigated, their difficult synthesis procedure and limited prospects for patterned director geometries has seen their use decline. However, their biocompatability has been demonstrated by Agrawal *et. al.* [2]

Table 2.2: Summary of synthetic route and key properties of acrylate-based LCEs.

Acrylates	
Pioneering groups	Broer/Schennings [20, 75, 21, 37, 53] Zentel [182, 181, 121, 19, 146] Mitchell [111, 132, 133, 76] Urayama [157, 158, 159, 160, 74]
Synthesis procedure	Typically uses one-step photopolymerisation. Mitchell group LCE uses a two-step process.
Mesogen-backbone coupling mode(s)	Most frequently side chain, end-on. Side chain side-on also possible. [156, 183]
Monomer commercial availability	Numerous mono-functional and bi-functional (crosslinking) end-on monomers available. No side-on currently available.
Monodomains instilled by	Typically aligned *via* surface-alignment. Mitchell and Zentel groups have demonstrated alignment *via* magnetic fields of strength as little as $\sim$ 100 mT. [111, 146]
Pattern-able director geometries?	Yes demonstrated *via* surface (photo-) alignment and magnetic fields. [37, 146]
Deformation mode when stressed perpendicular to the director	Mitchell group reported the "mechanical Fréedericksz" transition. [111] Urayama and Finkelmann groups reported semi-soft elasticity. [74, 183]
Stripe domains observed?	No for Urayama and Mitchell LCEs. Yes for Finkelmann acrylate LCE but only for low aspect ratio samples. [183]
Sub-room glass transition temperature?	Acrylates are typically considered to have high glass transition temperatures well above room temperature. The exceptions are Thomsen and Zeng LCEs (see section 6.1.1).
Comment	Acrylate-LCEs have possibly been studied the most widely. Many different chemistries have been developed, mechanical tests performed and devices proposed.

Table 2.3: Summary of synthetic route and key properties of acrylate-amine-based LCEs.

Acrylate-amine	
Pioneering group	White/Ware [164, 163, 166]
Synthesis procedure	Michael-addition for oligermisation of polymer chains followed by photocrosslinking. [164]
Mesogen-backbone coupling mode(s)	Main chain.
Monomer commercial availability	Numerous bifunctional acrylates and primary amines available.
Monodomains instilled by	Surface-alignment and flow-alignment (for 3D printed LCEs). [164, 7, 87]
Pattern-able director geometries?	Highly complex geometries possible *via* surface (photo-) alignment. [164]
Deformation mode when stressed perpendicular to the director	Semi-soft elasticity suggested from mechanical testing but not confirmed by director rotation behaviour.
Stripe domains observed?	No, however more are studies needed. [91]
Sub-room glass transition temperature?	Tuneable from ~ 10°C upwards. [163]
Comment	This chemistry appears to be extremely promising, although to date material has only been reported by two closely related research groups. Moreover, few mechanical experiments have been performed on the materials developed.

Table 2.4: Summary of synthetic route and key properties of thiol-acrylate-based LCEs.

Thiol-acrylate	
Pioneering group	Yakacki/Bowman [176, 136, 137]
Synthesis procedure	Thiol-acrylate Michael-addition to form a lightly crosslinked network followed by second photocrosslinking step. [164]
Mesogen-backbone coupling mode(s)	Main chain.
Monomer commercial availability	Numerous bifunctional acrylates and thiols available.
Monodomains instilled by	Mechanical forces. [176]
Pattern-able director geometries?	Limited by mechanical alignment.
Deformation mode when stressed perpendicular to the director	Unknown, possibly semi-soft elastic from the appearance of the polydomain-monodomain load curve. [176]
Stripe domains observed?	Unknown. [91]
Sub-room glass transition temperature?	Tuneable from ~ 3°C upwards. [136]
Comment	Approach is scalable for the synthesis of bulk LCEs with polydomain alignment. A preliminary test demonstrating this LCE's biocompatibility has been performed. [176]

2.5.6 Choosing a LCE chemistry

From the above tables we can discount polysiloxane LCEs as, despite the wealth of the literature reporting their mechanical properties, they cannot be synthesised into films of complex direct geometries as we require. Thiol-acrylate LCEs can also be eliminated for the same reason, despite their comparative simplicity of synthesis. This leaves us with a choice between acrylates and acrylate amines.

Comparing tables 2.2 and 2.3 it would appear that the acrylate-amine LCE chemistry described by Ware *et. al.* is the most attractive to work with as

- It is made from commercially available starting materials.
- Has a practically useable T_g of 19°C.
- Its main chain nature should mean the extent of the mechanical anisotropy should far exceed that possible in LCEs formed from (the commercially available) side chain end-on acrylates. [164]

However, if we consider the fractional shape change on heating, and the shape of the semi-soft elastic plateau (low modulus region) and apply the theory described in chapter 4, (equations 4.21 and 4.40) we surprisingly calculate values of the step length anisotropy of $r = 3.5$ and $r = 3.7$ — far smaller values than would be expected for a main chain LCE. [22] Moreover, this LCE chemistry is a relatively new and has currently only been reported by two closely related research groups. Consequently, little characterisation of this type of LCE has been performed. These reasons, along with the fact that acrylate polymerisation is a simple and fast "one-pot" reaction lead us to conclude that proceeding with an acrylate LCE would be the wisest choice for this thesis. However, an appropriate material with a sub-room-temperature glass transition and made from purely commercially available monomers must first be developed.

We next outline the chemical process of acrylate polymerisation.

2.5.6.1 Acrylate polymerisation synthetic route

The generic structure of an acrylate monomer is shown at the left of figure 2.10 (overleaf). The group referred to a 'R' corresponds to a generic chemical group which, in this context, could be a rod-like mesogenic group and, in the case of crosslinking molecules, could contain additional acrylate groups. Polymerisation of acrylate monomers into a polymer chain consists of three steps: Initiation, propagation and termination.

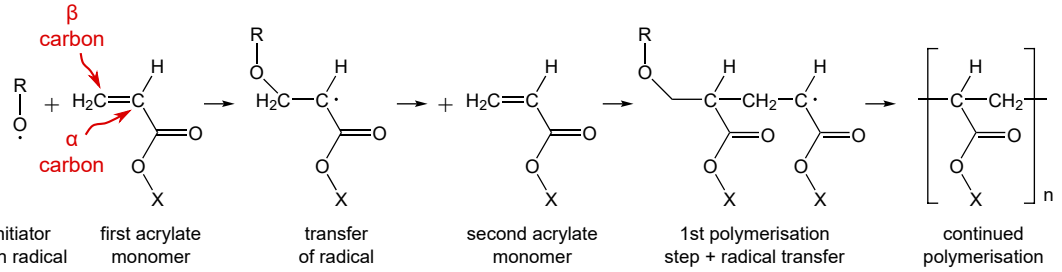

Figure 2.10: Chemical scheme of how acrylate monomers polymerise to form polymer chains.

During initiation, free radicals are typically generated by exposing a "photoinitiator" group to radiation of "sufficient" energy. This free radical attacks and bonds to the beta carbon of an acrylate group as shown in the scheme in figure 2.10. In the process the free radical is transferred to the alpha carbon. During propagation the polymer chain then grows as the free radical is passed from acrylate group to acrylate group. Termination occurs when chain meets another chain containing a free radical. The two free radical containing groups can react either through combination where both free radicals are lost and the chains join together, or through disproportionation where one free radical is lost but the chains do not bond together.

Continual exposure of the polymerising mixture to radical-generating radiation is required to allow polymerisation to continue until the desired polymerisation conversion is achieved. Typically a ∼30 minutes exposure time is used for cells ≤ 100 μm thick using a light source with an intensity of ∼100 mW cm^{-2} at the sample.

2.6 Conclusion

Alongside introducing in greater detail the challenges facing the ageing eye and what LCEs really are, this introduction has also allowed us to shape the scope of this thesis and the challenges that need to be tackled. Below the key considerations of this chapter are summarised.

Firstly, it is evident that the concept of a mechanically switchable lens for use as an AIOL is a highly novel idea which aims to truly mimic the natural crystalline lens. If a lens can be proven to be feasible, and indeed developed in work beyond this thesis, many further challenges would still exist such as how such a lens could be installed within the eye.

Given the scale of the overall research challenge of developing a LCE-AIOL, and the numerous unknowns still surrounding the mechanical properties of LCEs, this scope of this thesis is to demonstrate in principle the feasibility of such a device which can be used to justify further research into the technology.

The challenges and mechanical unknowns of LCEs are numerous. Perhaps the biggest hurdle to the development of a device is devising a way in which a "thick" LCE with quality and complex alignment could be produced. The recent development of LCE 3D printing technologies demonstrates that significant progress is being made toward this end. [7, 87] Other unknowns are more closely related to the fundamental physical behaviours of LCEs. For instance, the factors that govern whether a LCE displays MFTs or SSE when stressed perpendicular to the director are completely unknown. A deeper characterisation of what governs the presence of stripe domains may also be useful to the community. More importantly than these unknowns (in the context of this thesis) is the fact that a full characterisation of the mechanical anisotropy of LCEs, including the response of the director, to generic stresses has never been performed. Results of this type of characterisation are crucial to the design and development of mechano-LCE devices and thus a characterisation of this type is a main aim of this thesis.

When reviewing the literature surrounding the mechanical properties of LCEs it is evident that in order to understand the behaviours to the depth required, one must have a way by which the evolution of the LC director and polymer conformation (together — the "microstructure") respond to applied stresses. Surprisingly, simultaneous monitoring of a LCE's microstructure during a mechanical test has only ever being done twice before in the past — in the seminal papers by Küpfer and Finkelmann which described monodomain LCEs for the first time. [93, 94]

Evidently there are many fundamental physical, engineering and biomedical challenges which face the development of a LCE-AIOL. Considering the few AIOLs that have made it to market to date, it is worth noting that even if the work of the this thesis can justify further research into a LCE-AIOL, one of the later challenges down the line may render technology infeasible. Despite this, the concept of a LCE-AIOL is a fantastic motivator for the understanding of how LCEs could be applied to bioinspired mechanical devices as the properties of LCEs are not only unique, but are also highly bioreminescent. Thus, even if a LCE-AIOL ultimately cannot be developed, we anticipate the research of this thesis to have translational impacts on the development of other mechano-LCE devices.

Chapter 3

Thesis roadmap

The structure for the remainder of this thesis is structured as follows.

Chapter 4 builds upon the previous introduction to detail theoretical descriptions of isotropic elastomers and nematic LCEs behaviours using Gaussian rubber elasticity. The theoretical models to describe LCEs was developed by Warner and Terentjev (W&T) and the results of which are used throughout this thesis.

Chapter 5 describes the experimental methods used in this thesis. Alongside details of standard polymer physics techniques, the chapter describes the development of bespoke opto-mechanical testing apparatus and methods designed such that the evolution of a LCE's microstructure could be monitored throughout mechanical tests. This novel equipment allows us to build a complete picture of the mechanical anisotropy of one of the LCEs developed.

Chapter 6 details the steps taken to develop new acrylate-based LCEs satisfying the material requirements identified in the previous chapter. Specifically the key material developed (named "LCE A") is facile to synthesise in complex director geometries from entirely commercially available monomers. All materials developed also have sub-room glass transition temperatures and thus challenge the commonly held view on the practicality of acrylate-based LCEs.

Chapter 7 provides an initial mechanical characterisation of LCE A by considering stresses applied parallel and perpendicular to the director. Although these tests are of "standard" LCE geometries, we observe the surprising results of a mechanically-induced state of negative LC order parameter. Moreover, the results suggest more intimate links between the phenomena of "mechanical Fréedericksz" transitions and semi-soft elasticity.

Chapter 8 continues the basic mechanical characterisation of LCE A by considering the geometrical shape changes of LCE A stressed perpendicular to the director. We demonstrate for the first time "molecular auxeticity", *i.e.* we observe a negative Poisson's ratio and deduce it is a bulk material property as opposed to being generated by an auxetic-inducing porous geometry. Such a material has been a long-standing goal of the auxetics community.

Chapter 9 summarises the new phenomena observed, and new questions opened by the results of chapters 7 and 8 before detailing the structure of the second half of this thesis.

Briefly, chapters 10 and 11 develop a complete picture of the general anisotropy of LCE A and demonstrates how spatial programming of the LC director enables the mechanical generation of complex shapes. Chapter 12 then considers radial deformations of a second key LCE developed in chapter 6 — LCE B, which is an isotropic material with a mechanically-induced nematic phase. Chapter 13 then uses the results of chapters 7 – 12 together to develop concepts for how complex shape profiles can be mechanically induced in patterned LCE systems before devising a concept for a mechanically switchable LCE-AIOL.

This thesis concludes with chapter 14 which considers the successes of this thesis toward the ultimate goal of a truly functional AIOL. We also summarise the additional tangential successes achieved through the equipment, methods and materials developed and the results presented. The conclusion finishes with suggestions for next research steps to further explore the LCE-AIOL concept and understand the new LCE phenomena discovered.

Chapter 4

Theory

4.1 Introduction

In this thesis results are frequently compared to, or analysed using, theory pioneered by Warner and Terentjev (W&T). [169] This "neo-classical" approach adapts classical (isotropic) rubber elasticity by taking into consideration the anisotropy of the polymer chain conformation by modelling it as a random walk with anisotropic step lengths. As with classical rubber elasticity, the chemical composition of the polymer chains can be ignored as the chains are simply viewed as freely joined segments which have zero orientational correlation with one another. Continuum elasticity approaches, which remove all structure from the elastic bodies, instead viewing them a continuous bodies of material, have also been developed to describe the behaviour of LCEs. We choose here to use the neo-classical theory of W&T as we are interested in relating the macroscopic phenomena to the microstructure of the LCEs developed. Additionally, the neo-classical approach is most frequently used to study the experimental behaviour of LCEs. Therefore by applying the neo-classical theory to our observations, we can compare results with those previously reported.

We start this chapter by outlining the classical theory of rubber elasticity before describing how this can be modified for studying LCEs through the so called "trace formula" of W&T theory, which constitutes our toolbox for studying the physical behaviours of LCEs. We then summarise the existing predictions

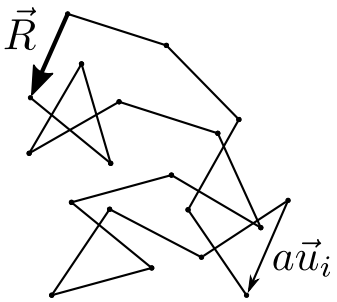

Figure 4.1: An illustration of a two dimensional random walk like that used to model the behaviour of a 3D polymer chain. The polymer chain (light lines) is made up of a series of steps $a\vec{u}_i$ which sum together to give the end-to-end vector $\vec{R}$ (heavy line). The length, a, of each step represents the minimum number of atoms along the polymer backbone for which the orientation between steps is uncorrelated.

W&T made using their theory to relate the shape actuation and opto-mechanical behaviour of LCEs to their microstructure. The theoretical results from these predictions will be applied throughout this thesis to our results.

The theory outlined in this chapter is a simplified account of the theory described in the book by Warner and Terentjev. [169] This book (and the papers of Warner and Terentjev and co-workers referenced within) is a citation for the entirety of this chapter. We mention this here to acknowledge that all of the content from this chapter is based upon content from the book by Warner and Terentjev. Additional references, where relevant, are cited as appropriate.

4.2 Isotropic classical rubber elasticity

A polymer backbone is made up of repeat units chemically bonded together. Although the angle between adjacent bonds is constrained, we assume in classical rubber elasticity that the polymer backbone can be modelled as a series of steps some number of atoms long such that the polymer backbone appears as a random walk. For these chains to be Gaussian, the length of each step, a, must be much smaller than the contour length of the chain, L (definition of L formalised below).

Figure 4.1 shows a (2D) diagram of the how the polymer chain is viewed in the classical theory of rubber elasticity. The chain is made up of a series of steps, $a\vec{u}_i$ where the set $\{\vec{u}_i\}$ are unit vectors giving the direction of each step. The vector between the start and end of the chain is denoted by $\vec{R} = a\sum_i \vec{u}_i$. If the chain has N steps, the contour length of the chain is

$$L = Na.$$

As the chain is a random walk, there are no correlations between any pair of steps $\vec{u}_i$ and $\vec{u}_j$, *i.e.*

$$\langle \vec{u}_i \cdot \vec{u}_j \rangle = \delta_{ij}, \tag{4.1}$$

δ_{ij} is the Kronecker delta. As the chain is viewed as a random walk we have the averages of

$$\langle \vec{R} \rangle = 0 \text{ and } \langle \vec{R}^2 \rangle = Na^2 = La. \tag{4.2}$$

Furthermore, as the random walk is three dimensional and isotropic we have that

$$\langle \vec{R}^2 \rangle = \langle \vec{R}_x^2 + \vec{R}_y^2 + \vec{R}_z^2 \rangle = \langle \vec{R}_x^2 \rangle + \langle \vec{R}_y^2 \rangle + \langle \vec{R}_z^2 \rangle, \tag{4.3}$$

$$\implies \langle \vec{R}_x^2 \rangle = \langle \vec{R}_y^2 \rangle = \langle \vec{R}_z^2 \rangle = \frac{1}{3}\langle \vec{R}^2 \rangle = \frac{1}{3}La, \tag{4.4}$$

where $\vec{R}_i$ is the 1D random walk along each of the principal axes.

Each polymer chain could adopt values of $0 \leq |\vec{R}| \leq L$. $|\vec{R}| = 0$ corresponds to the most likely configuration. By comparison, chains satisfying $|\vec{R}| = L$ correspond to the least likely as they all require all chain segments to lie parallel to one another which entropically is the least favoured configuration. For each $\vec{R}$, there are a number of different possible configurations of the chain random walk (microstates). By the central limit theorem, the fraction of all microstates corresponding to a given end-to-end vector, $p(\vec{R})$, is given by the normal distribution

$$p(\vec{R}) = p(R_x)p(R_y)p(R_z) = \left(\frac{3}{2\pi La}\right)^{3/2} \exp\left(-\frac{3\vec{R}^2}{2La}\right), \tag{4.5}$$

where $p(R_i)$ is the probability distribution for the projection of R along the i^{th} axis. $p(\vec{R})$ is a partition function from which we can calculate the free energy, f_s, for a single network strand of the elastomer network with a given end-to-end vector of $\vec{R}$

$$f_s(\vec{R}) = -k_B T \ln\left[p(\vec{R})\right] = \frac{3k_B T \vec{R}^2}{2La} + C, \tag{4.6}$$

where k_B is the Boltzmann constant, T is the system temperature and C is an arbitrary constant which has no $\vec{R}$ dependency.

The entirety of the elastomer has a polymer chain density of n_s strands per cubic meter, which we assume each to have the same contour length of L. At the point of network formation (where the elastomer is unstrained), each chain has a particular value of $\vec{R}$ with $\langle\vec{R}\rangle = 0$. Therefore the distribution of end-to-end vectors will described by the same partition function of equation 4.5. If the elastomer is subjected to an affine deformation (same deformation for every chain of the system), described by the deformation gradient tensor $\underline{\underline{\lambda}}$, then each chain of the end-to-end vector, $\vec{R}$ is deformed to

$$\vec{R}^d = \underline{\underline{\lambda}} \cdot \vec{R}. \tag{4.7}$$

The free energy, $f_s'(\vec{R})$, of this deformed strand is then given by

$$f_s'(\vec{R}) = \frac{3k_B T}{2La} \vec{R}^d \cdot \vec{R}^d \tag{4.8}$$

$$= \frac{3k_B T}{2La}\ \vec{R} \cdot \underline{\underline{\lambda}}^{\mathrm{T}} \cdot \underline{\underline{\lambda}} \cdot \vec{R}. \tag{4.9}$$

The free energy density of the system is then calculated by averaging the energy of each strand over the initial chain probability distribution (as we do not know the final probability distribution) and multiplying the result by the strand density. The average strand free energy is given by

$$\langle f_s'(\vec{R})\rangle = \frac{3k_B T}{2La}\ \langle R_i \lambda_{ik} \lambda_{kj} R_j\rangle, \tag{4.10}$$

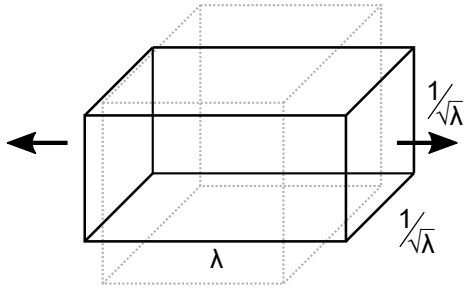

Figure 4.2: An illustration of a shear-free deformation of an isotropic material. An extension of λ applied along one axis of a unit cube of material (dotted line) will undergo transverse contractions of equal magnitude $1/\sqrt{\lambda}$ (equal for isotropy). Volume is conserved by the fact that $\lambda \times 1/\sqrt{\lambda} \times 1/\sqrt{\lambda} = 1$.

where the indices imply summation. As $\underline{\underline{\lambda}}$ is constant for all polymer chains, the averaging is only performed over $\langle R_i R_j \rangle$. Using equation 4.1 and 4.4 we find the total elastic free energy density, F_{el} to be

$$F_{el} = \frac{3n_s k_B T}{2La} \frac{1}{3} La\, \delta_{ij} \lambda_{ik} \lambda_{kj}, \tag{4.11}$$

$$= \frac{\mu}{2}\, \mathrm{Tr}(\underline{\underline{\lambda}}^{\mathrm{T}} \cdot \underline{\underline{\lambda}}), \tag{4.12}$$

where $\mu = n_s k_B T$ is the elastic shear modulus for an isotropic material. [134]

4.2.0.1 Shear-free deformation of isotropic elastomers

A shear-free deformation in the principal frame is given by $\underline{\underline{\lambda}} = \mathrm{Diag}(\lambda_x, \lambda_y, \lambda_z)$. In the case of a deformation λ applied along the x axis of an isotropic and volume conserving elastomer (as described by figure 4.2), the deformation tensor simplifies to $\underline{\underline{\lambda}} = \mathrm{Diag}(\lambda, 1/\sqrt{\lambda}, 1/\sqrt{\lambda})$. Hence the free energy of equation 4.12 is given by

$$F_{el} = \frac{\mu}{2}\left(\lambda^2 + \frac{2}{\lambda}\right). \tag{4.13}$$

Differentiating this with respect to λ gives us the engineering stress

$$\sigma_E = \mu \left(\lambda - \frac{1}{\lambda^2} \right), \tag{4.14}$$

which describes the stress based on the *initial* cross-sectional area of the deformed rubber and does not account for the change in cross-sectional area. While the engineering stress does not accurately describe the actual stress within the material, it is a useful metric when considering devices as it relates to the known quantities of the initial cross-sectional area and the force applied. The actual stress present within a material is known as the true stress, σ_T, and can be determined by recognising the fact that a (constant volume) deformation, λ, applied to a sample causes a decrease in the transverse cross-sectional area by factor of λ (figure 4.2). Therefore the true stress is found by multiplying the engineering stress by λ

$$\sigma_T = \lambda \sigma_E = \mu \left(\lambda^2 - \frac{1}{\lambda} \right). \tag{4.15}$$

For small deformations, *i.e.* λ close to unity, the true and engineering stresses are approximately equal, however for the typical scale of rubber deformations distinguishing between the two is important. Engineering and true elastic moduli can be calculated by differentiating each of σ_E and σ_T with respect to λ. In both cases, the initial elastic moduli (at $\lambda = 1$) is equal to $E = 3\mu$, a result which should be expected for isotropic and volume conserving elastomers. [54]

Equations 4.14 and 4.15 will be useful in chapter 12 and the relationship between engineering and true stress will be frequently drawn upon throughout this thesis.

4.3 Nematic rubber elasticity

We now describe the W&T extensions to classical rubber elasticity in order to derive the "trace formula" which will be applied to results throughout this thesis.

The random walk for a nematic polymer is anisotropic meaning that the effective length of each step is directionally dependent. Along the three principal

axes we, in general, will have step lengths of l_1, l_2 and l_3. This anisotropy in step lengths can therefore be encapsulated by an effective step length tensor, $\underline{\underline{\mathbf{l}}}$, which, in the diagonal frame, is given by $\mathrm{Diag}(l_1, l_2, l_3)$. Above, in section 4.2, we assumed that the step length and symmetry of the isotropic elastomer remain constant throughout a mechanical deformation. However, when considering LCEs, this cannot generally be assumed. We therefore denote $\underline{\underline{\mathbf{l}}}^{\mathbf{0}}$ as the step length tensor for the undeformed state and $\underline{\underline{\mathbf{l}}}$ as the step length tensor in the deformed state.

Appendix B follows a similar procedure performed in section 4.2 in order to derive the "trace formula"

$$F_{el} = \frac{\mu}{2}\left[\mathrm{Tr}\left(\underline{\underline{\mathbf{l}}}^{\mathbf{0}} \cdot \underline{\underline{\lambda}}^{\mathrm{T}} \cdot \underline{\underline{\mathbf{l}}}^{-\mathbf{1}} \cdot \underline{\underline{\lambda}}\right) + \ln\left(\frac{\mathrm{Det}(\underline{\underline{\mathbf{l}}})}{\mathrm{Det}(\underline{\underline{\mathbf{l}}}^{\mathbf{0}})}\right)\right], \tag{4.16}$$

which is an equivalent free energy density to equation 4.12 but for LCEs. Equation 4.16, developed by Warner and Terentjev, can be used to explore the physical behaviour of LCEs. In the following section we detail a few applications of the trace formula that are relevant to the results of this thesis.

Before we proceed we must make a few comments on the use the trace formula to investigate the various phenomena observed in LCEs. Firstly, the total free energy of the LCE system is actually the sum of the elastic and nematic free energies, (F_{el} and F_{nem} respectively). However, the applications of the trace formula in the following section describe situations in which F_{nem} can be neglected or assumed to be constant and therefore irrelevant when the F_{el} is minimised. Secondly, in the following section we consider states of uniaxial nematic order. Thus the step length tensor is given by rotations of $\underline{\underline{\mathbf{l}}} = \mathrm{Diag}(l_{\parallel}, l_{\perp}, l_{\perp})$. We will see in the following section that ratio, $r = {}^{l_{\parallel}}/_{l_{\perp}}$, known as the step length anisotropy, is the most key parameter of a LCE as the unique physical properties of LCEs are all intrinsically linked to the fact that r is greater than unity. The magnitude of r is also important and so in the applications of the trace formula below, we describe the ways in which a value for r can be determined from physical observables. Lastly, the ln() term of the trace formula is related to changes in the nematic order parameter. If the order parameter remains constant in a process

(as is generally assumed for mechanical deformations of LCEs), then the ln() term equals zero and is therefore irrelevant. This term may also become irrelevant even if there is a change in the magnitude of the order parameter if the eigenvalues of $\underline{\underline{\mathbf{l}}}$ have no dependency on $\underline{\underline{\lambda}}$. In these cases, in minimisation of equation 4.16 with respect to a deformation, the ln() term vanishes.

4.4 Applications of the "trace formula"

4.4.1 Thermal induced length changes

An ideal nematic LCE can be heated to an isotropic phase. This process causes the uniaxial LC order parameter tensor to become spherical, a change which is reflected in the step length tensor for the isotropic phase. Experimentally, we know this microscopic change manifests itself on the macroscopic scale as a contraction of the sample parallel to the director (for an initially prolate polymer conformation) and expansion of the sample in directions perpendicular to the director. If instead we consider starting in the isotropic phase and cooling to a nematic phase, we will have

$$\underline{\underline{\mathbf{l}}}^{\mathbf{0}} = \underline{\underline{\delta}} \text{ and } \underline{\underline{\mathbf{l}}}^{-\mathbf{1}} = \text{Diag}(l_{\parallel}^{-1}, l_{\perp}^{-1}, l_{\perp}^{-1}), \tag{4.17}$$

where we have chosen the director to emerge along the x axis (thus the components of $\underline{\underline{\mathbf{l}}}$ along the y and z axes are equal). The deformation gradient tensor for this process is given by

$$\underline{\underline{\lambda}}_{\mathbf{m}} = \text{Diag}(\lambda_m, {}^{1}/\sqrt{\lambda_m}, {}^{1}/\sqrt{\lambda_m}), \tag{4.18}$$

where λ_m is the sample extension ratio along the x axis between the nematic and isotropic state. The y and z components are equal by symmetry and have values which ensure the sample deforms at constant volume. Inserting this into the trace formula (equation 4.16) yields

$$F_{el} = \frac{\mu}{2}\left(\frac{\lambda_m^2}{l_\parallel} + \frac{2}{l_\perp \lambda_m}\right) + C, \tag{4.19}$$

$$= \frac{\mu}{2l_\parallel}\left(\lambda_m^2 + \frac{2r}{\lambda_m}\right) + C, \tag{4.20}$$

where we have absorbed the ln() terms into the constant C as they have no dependency on λ_m. We can safely neglect the effects of F_{nem} in this case as by definition it will be adopting its minimal value in the isotropic and nematic states under consideration. We can extract a prediction of how the deformation λ_m is related to r by minimising equation 4.19 with respect to λ_m. Doing so gives the result

$$\lambda_m = r^{1/3}. \tag{4.21}$$

Equation 4.21 can therefore be used to extract a value for a LCE's step length anisotropy based on the thermally-induced shape change. Additionally equation 4.21 shows that LCEs with a greater step length anisotropy, r, will undergo more dramatic shape actuations on heating to the isotropic phase. We use equation 4.21 in chapter 7 to determine a value of r for one of the LCEs developed in chapter 6.

4.4.2 "Mechanical Fréedericksz" transition

As we highlighted in chapter 2, the mechanical behaviour of LCEs is at its most interesting and bizarre when one considers stresses applied perpendicular to the director. In the literature two types deformation processes have been reported — "mechanical Fréedericksz" transitions (MFT) and (semi-)soft elasticity (SSE). Whilst the latter of these is the most frequently observed, it is constructive to first consider MFTs.

Experimentally, it is well known that a stress applied perpendicular to the director orientation in a film of LCE will eventually cause the director to rotate by 90° to lie parallel to the stress axis. [111, 90, 132, 153, 159] In a MFT, the director remains perpendicular to the stress axis until a critical strain at which

it sharply rotates by 90° to lie parallel to the stress axis. Using the trace formula we can calculate and compare the free energy dependencies on the applied deformation $\underline{\underline{\lambda}}$ for the cases of no director rotation and director rotation (*i.e.* before and after the transition). Here we follow the arguments of W&T and assume the LC order parameter is constant throughout the process. The discussion of results presented in chapters 7 and 8 cast doubt on the validity of this assumption.

To study the MFT process, we start with a system where the director is aligned along the y axis, *i.e.* $\underline{\underline{\mathbf{l}}}^{\mathbf{0}} = \mathrm{Diag}(l_\perp, l_\parallel, l_\perp)$. As there is a constant LC order parameter and no director rotation prior to the transition, the free energy will be calculated using $\underline{\underline{\mathbf{l}}} = \underline{\underline{\mathbf{l}}}^{\mathbf{0}}$. After the transition, we calculate the free energy using $\underline{\underline{\mathbf{l}}} = \mathrm{Diag}(l_\parallel, l_\perp, l_\perp)$. The condition of a constant LC order parameter is enforced by a constant magnitude of $r = {}^{l_\parallel}/_{l_\perp}$ throughout both deformations. Using a deformation at constant volume applied along the x axis of $\underline{\underline{\lambda}} = \mathrm{Diag}(\lambda_x, \lambda_y, {}^{1}/_{\lambda_x\lambda_y})$, we find using the trace formula the free energies, F_{el}^A and F_{el}^B before and after the transition respectively

$$F_{el}^A = \frac{\mu}{2}\left(\lambda_x^2 + \lambda_y^2 + \frac{1}{(\lambda_x\lambda_y)^2}\right), \tag{4.22}$$

$$F_{el}^B = \frac{\mu}{2}\left(\frac{l_\perp}{l_\parallel}\lambda_x^2 + \frac{l_\parallel}{l_\perp}\lambda_y^2 + \frac{1}{(\lambda_x\lambda_y)^2}\right). \tag{4.23}$$

By first minimising these with respect to λ_y to obtain $\lambda_y(\lambda_x)$ and inserting the results into equations 4.22 and 4.23, we obtain

$$F_{el}^A = \frac{\mu}{2}\left(\lambda_x^2 + \frac{2}{\lambda_x}\right), \tag{4.24}$$

$$F_{el}^B = \frac{\mu}{2}\left(\left(\frac{\lambda_x}{\sqrt{r}}\right)^2 + \frac{2\sqrt{r}}{\lambda_x}\right). \tag{4.25}$$

These, very similar looking, free energies are plotted in figure 4.3. The two free energies meet at a deformation $\lambda_x = \lambda_c$ which can be calculated by equating equations 4.24 and 4.25 and solving for λ_c

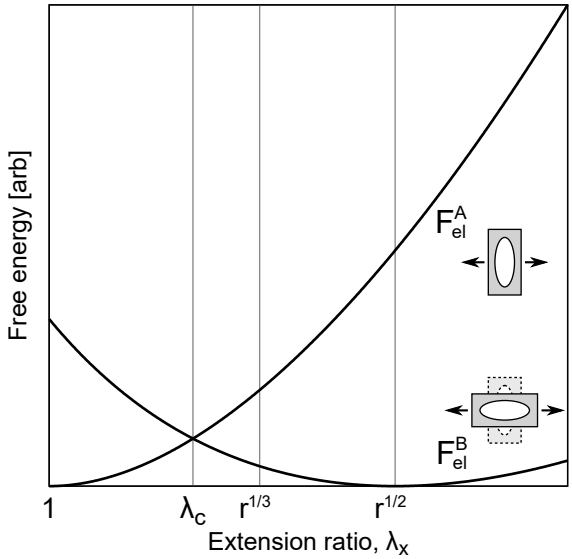

Figure 4.3: The free energy landscape for the two deformation modes for a "mechanical Fréedericksz" transition given by equations 4.24 and 4.25. F_{el}^A gives the free energy as a function of λ_x for the case of director orientation remaining constant while F_{el}^B gives the free energy for the case of the director having rotating by 90°.

$$\lambda_c = \left(\frac{2r}{\sqrt{r}+1} \right)^{1/3}. \tag{4.26}$$

According to W&T, while λ_c may be the point at which the rotated director state given by F_{el}^B becomes energetically favourable, the F_{el}^A state will still be metastable for small deformations above λ_c. W&T give $\lambda_x = \lambda_m = r^{1/3}$ as the limit for the stability for the F_{el}^A branch and therefore the latest deformation by which the MFT will occur. [169, 15] A range of values for the step length anisotropy, r, can therefore be deduced from

$$2r - \lambda_c^3\sqrt{r} - \lambda_c^3 = 0 \tag{4.27}$$

$$\text{and} \quad r = \lambda_m^3. \tag{4.28}$$

In the works of Mitchell and co-workers (the only group to have reported MFT to date), the latter of these values, which actually gives the smaller value

of r, was used to determine values for r. This value was consistent with a value measured using Small Angle Neutron Scattering (SANS). [111] Despite the consistency between values of r calculated by Mitchell *et. al.*, we do note that the process described in this chapter is quite unphysical as the jump in director angle by 90° at the transition would require an immediate increase in the sample length by a factor of $\sqrt{r}$ along the stress axis which in turn would result in a buckling on the film.

4.4.3 (Semi-)soft elasticity

In section 2.5.4 we discussed the observations, first made by Küpfer and Finkelmann, of LCEs displaying plateau-like regions of their stress-strain load curves. [93, 94] This behaviour, which has since been dubbed "(semi-) soft elasticity", physically corresponds to little or no increase in the free energy of the system throughout a region of the deformation (the prefix "semi-" is relevant to real-world LCEs which are never theoretically perfect). Along the length of the plateau, the deformation is accompanied by a rotation of the nematic director. [94, 90, 91] This process offers a second route by which a 90° rotation of the director can be mechanically induced for a LCE under strain. In contrast to the MFT described above, the director rotation in a (semi-)soft elastic deformation is gradual. In similarity to theory describing the MFT, the W&T theory describing SSE also assumes a constant nematic order parameter throughout the deformation.

An insight into how SSE behaviour is possible by considering the deformation gradient tensor proposed by Olmsted [120]

$$\underline{\underline{\lambda}} = \underline{\underline{\mathbf{l}}}^{\mathbf{1/2}} \cdot \underline{\underline{\mathbf{W}}}_{\alpha} \cdot \underline{\underline{\mathbf{l}}}_{\mathbf{0}}^{\mathbf{-1/2}}, \tag{4.29}$$

where $\underline{\underline{\mathbf{W}}}_{\alpha}$ is an arbitrary body rotation by an angle α along any axis. Inserting this into the trace formula yields $F_{el} = {}^{3\mu}/_{2}$, which is the same free energy as the undeformed sample. Therefore deformations of the type shown in equation 4.29 do not cost energy.

To see the significance of the deformation we first neglect $\underline{\underline{\mathbf{W}}}_\alpha$ as arbitrary and consider $\underline{\underline{\mathbf{l}}}_{\mathbf{0}}^{-1/2}$ in its principle frame

$$\underline{\underline{\mathbf{l}}}_{\mathbf{0}}^{-1/2} = \mathrm{Diag}(l_{\parallel}^{-1/2}, l_{\perp}^{-1/2}, l_{\perp}^{-1/2}), \tag{4.30}$$

$$= l_{\perp}^{-1/2} r^{-1/6}\, \mathrm{Diag}(r^{-1/3}, r^{1/6}, r^{1/6}), \tag{4.31}$$

$$= l_{\perp}^{-1/2} r^{-1/6} \underline{\underline{\lambda}}_{\mathbf{m}}^{-\mathbf{1}}, \tag{4.32}$$

where $\underline{\underline{\lambda}}_{\mathbf{m}}^{-\mathbf{1}}$ is the inverse of the deformation given in equation 4.18 (into which we have substituted the result of equation 4.21). Therefore the $\underline{\underline{\mathbf{l}}}_{\mathbf{0}}^{-1/2}$ term of equation 4.29 is proportional to the inverse of the elongation seen when a nematic LCE is cooled from the isotropic phase, *i.e.* it is a deformation which takes the system from a nematic to an isotropic polymer conformation. If we now take $\underline{\underline{\mathbf{l}}}^{1/2}$ as a rotation of $\underline{\underline{\mathbf{l}}}_{\mathbf{0}}^{1/2}$ described by $\underline{\underline{\mathbf{U}}}$ we find

$$\underline{\underline{\mathbf{l}}}^{1/2} = \underline{\underline{\mathbf{U}}}^{\mathrm{T}} \cdot \underline{\underline{\mathbf{l}}}_{\mathbf{0}}^{1/2} \cdot \underline{\underline{\mathbf{U}}}, \tag{4.33}$$

$$= l_{\perp}^{1/2} r^{1/6} \underline{\underline{\mathbf{U}}}^{\mathrm{T}} \cdot \underline{\underline{\lambda}}_{\mathbf{m}} \cdot \underline{\underline{\mathbf{U}}}, \tag{4.34}$$

i.e. a deformation proportional to $\underline{\underline{\lambda}}_{\mathbf{m}}$ along an arbitrary axis. This term of the deformation is proportional to the deformation given in equation 4.18 and therefore takes the system back from the isotropic polymer conformation to the original nematic polymer conformation, but now rotated from its original orientation.

Putting the deformation back together we find

$$\underline{\underline{\mathbf{l}}}^{1/2} \cdot \underline{\underline{\mathbf{l}}}_{\mathbf{0}}^{-1/2} = \underline{\underline{\mathbf{U}}}^{\mathrm{T}} \cdot \underline{\underline{\lambda}}_{\mathbf{m}} \cdot \underline{\underline{\mathbf{U}}} \cdot \underline{\underline{\lambda}}_{\mathbf{m}}^{-\mathbf{1}}. \tag{4.35}$$

This deformation describes a rotation of the polymer conformation toward a stress axis and shows that such a process can be performed at no cost to the free energy of the system. What the above decomposition of the deformation has shown is that this process requires the system to be able to adopt an isotropic reference frame. In reality, non-idealities of a LCE can prevent such a state from

actually been achievable and therefore modifications to soft elasticity must be made in order to describe the behaviour seen in real system. Verwey and Warner suggested departures from ideality may be a result of "compositional fluctuations", (*i.e.* the LCE containing chains of different lengths or different values of r) and/or the presence of rod like crosslinks. [161, 162] Modification to soft elasticity to account for these non-idealities resulted in the theory of semi-soft elasticity, the key features of which are shown below. We do not derive these results here and instead direct the reader to the book by Warner and Terentjev. [169]

For the case of stresses applied perpendicular to the initial director, semi-softness has two effects. Firstly, it introduces a threshold strain above which the soft-elastic response begins. Secondly, it means that the soft elastic plateau is not completely flat, but has a finite gradient therefore meaning the reorientation of the polymer conformation costs a finite amount of energy. The semi-soft elastic load curve is divided into three regions

$$\sigma_A = \mu\left[\lambda^2 - \frac{1}{\lambda}\right] \qquad \text{for } 0 < \lambda < \lambda_1, \tag{4.36}$$

$$\sigma_B = \mu\lambda^2\left[1 - \frac{1}{\lambda_1^3}\right] \qquad \text{for } \lambda_1 < \lambda < \lambda_2, \tag{4.37}$$

$$\sigma_C = \mu\left[\lambda^2\left(1 - \frac{r-1}{\lambda_1^3 r}\right) - \frac{\sqrt{r}}{\lambda}\right] \qquad \text{for } \lambda_2 < \lambda, \tag{4.38}$$

where σ_A, σ_B and σ_C are the engineering stresses in each region, λ_1 is the threshold deformation at which the polymer conformation (and hence) director begins to rotate toward the applied stress axis and $\lambda_2 = \lambda_1\sqrt{r}$ is the deformation at which the director has completely rotated to lie parallel to the stress axis. Evidently, LCEs with larger r will have longer semi-soft elastic plateaus. The director rotation across the semi-soft elastic plateau region (described by equation 4.37) is predicted to take the form of

$$\theta = \sin^{-1}\sqrt{\frac{r}{r-1}\frac{\lambda^2 - \lambda_1^2}{\lambda^2}}. \tag{4.39}$$

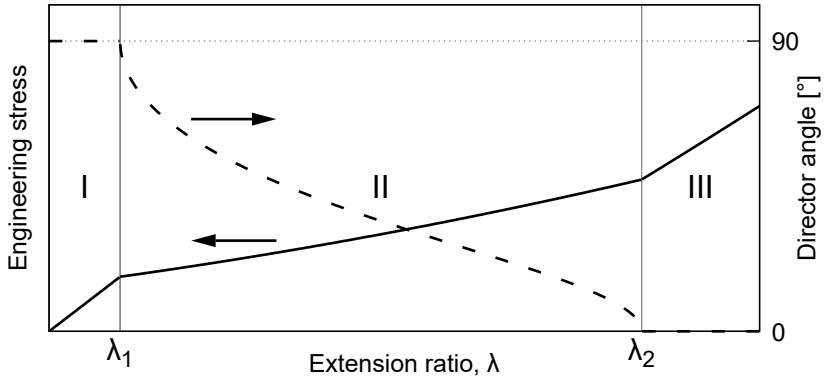

Figure 4.4: The theoretically expected tensile load curve and director rotation behaviour for a LCE stressed perpendicular to the director undergoing a SSE deformation. Plotted functions are given by equations 4.36–4.39.

Figure 4.4 plots, using equations 4.36–4.39, the expected semi-soft elastic load curve and director response for a LCE deformed perpendicular to the initial director. The plot clearly shows the three regions of the deformation: (**I**) before any director rotation takes place, (**II**) during director rotation, and (**III**) after the director has completed its full 90° rotation toward the stress axis. As figure 4.4 shows that it is easy to identify λ_1 and λ_2 from the shape of the load curve, it is therefore easy to calculate a value for r from the load curve of a LCE which displays SSE behaviour *via*

$$r = \left(\frac{\lambda_2}{\lambda_1}\right)^2 . \tag{4.40}$$

In chapter 7 this result is applied to a semi-soft-like load curve observed for one of the LCEs developed.

4.4.4 Relationship between r and scalar backbone order parameter, Q_B

We finish this section by showing how the anisotropy of the step length tensor can be linked to an order parameter, Q_B, which describes the magnitude of ordering of the elastomer backbone which in turn can be linked to the nematic LC order

parameter.

If we let the length of each "step" of the polymer chain be equal to the average step length, $\bar{l}$, and allow each step to take any orientation given by the vectors $\vec{u}_\alpha$, then the end to end vector of a polymer chain will be given by

$$\vec{R} = \bar{l} \sum_\alpha \vec{u}_\alpha. \tag{4.41}$$

Note, that in the nematic phase, the orientations of these steps will be biased toward the orientation of the LC director. Rearranging equation B.3 and inserting the above gives

$$\underline{\underline{\mathbf{l}}} = \frac{3\bar{l}^2}{L} \sum_{\alpha,\beta} \langle \vec{u}_\alpha \vec{u}_\beta \rangle. \tag{4.42}$$

As each step of the polymer chain will only be correlated with itself, equation 4.42 simplifies to

$$\underline{\underline{\mathbf{l}}} = \frac{3N\bar{l}^2}{L} \langle \vec{u}_\alpha \vec{u}_\alpha \rangle = 3\bar{l} \langle \vec{u}_\alpha \vec{u}_\alpha \rangle, \tag{4.43}$$

where in the last step we have used that the arc length $L = N\bar{l}$. If we consider being in the principle frame of the polymer conformation, with the director lying along z, then we have that $\underline{\underline{\mathbf{l}}} = \mathrm{Diag}(l_\perp, l_\perp, l_\parallel)$. Writing $\vec{u}_\alpha$ in spherical polar coordinates (the most natural coordinate set for nematic-like ordering) and inserting it into equation 4.43 gives

$$\underline{\underline{\mathbf{l}}} = 3\bar{l} \begin{pmatrix} \langle \sin^2\theta \rangle \langle \cos^2\phi \rangle & & \\ & \langle \sin^2\theta \rangle \langle \sin^2\phi \rangle & \\ & & \langle \cos^2\theta \rangle \end{pmatrix}, \tag{4.44}$$

where all off-diagonal terms are zero as uniaxial nematic order has an even symmetry and the diagonal terms include $\langle \sin\theta\cos\theta \rangle$ or $\langle \sin\phi\cos\phi \rangle$ which are both odd functions. Given the azimuthal symmetry of the uniaxial nematic phase, we have that $\langle \sin^2\phi \rangle = \langle \cos^2\phi \rangle = 1/2$. If we now assign the polymer backbone a scalar order parameter, $Q_B = 3/2\langle \cos^2\theta \rangle - 1/2$, we have that

$$\underline{\underline{\mathbf{l}}} = \bar{l} \begin{pmatrix} 1-Q_B & & \\ & 1-Q_B & \\ & & 1+2Q_B \end{pmatrix} = \bar{l} \begin{pmatrix} l_\perp & & \\ & l_\perp & \\ & & l_\parallel \end{pmatrix}, \tag{4.45}$$

$$\implies \quad r = \frac{l_\parallel}{l_\perp} = \frac{1+2Q_B}{1-Q_B}. \tag{4.46}$$

We draw upon this result in chapters 8 and 12.

For a purely main chain LC polymer/elastomer the nematic LC order parameter, $Q_N = Q_B$ since the LC molecules are directly incorporated in the polymer backbone. [169] By contrast, for side chain LCEs, Finkelmann *et. al.* showed $Q_N \propto Q_B$. [47] The constant of proportionality depends on the composition of the LCE with Finkelmann *et. al.* reporting a value of 1.28 for their polysiloxane-based LCE while Tsuchitani *et. al.* reported larger values of 1.58, 1.78 and 2.08 for a range of acrylate-based LCEs.

4.5 Conclusion

This chapter has outlined the fundamentals of classical rubber elasticity for isotropic elastomers and its modification, developed by Warner and Terentjev for nematic elastomers. We concentrated on the fundamentals in this chapter as they provide insight into how the behaviours of LCEs can be rationalised by thinking about the anisotropy in the shape of the polymer conformation, and its links to the nematic order parameter.

We then focused on some key examples of how W&T's trace formula accounts for the observed phenomena of LCEs and how it provides predictions for values of the step length anisotropy, r. The equations relating r to physical observables shown in this chapter, along with others derived in later chapters, will be used in chapters 7, 8 and 12 to calculate and discuss values of r. Commonly, we will find either inconsistencies between calculated values of r or unphysical deductions of Q_N. We will conclude these to be a consequence of the assumption that the

nematic order parameter can either be neglected or taken as constant throughout deformation processes. The full derivations of the phenomena described here can be found in the book by Warner and Terentjev, which also details additional considerations such as the effect of non-Gaussian chains. Although non-Gaussian chains are likely to exist in the LCEs studied in this thesis, the magnitude of the described corrections are too small to account for the inconsistent rs and unphysical Q_Ns. The, rather complex, modifications to the theory to include non-Gaussian chains are therefore not shown or discussed in this thesis. [169, 105]

A note worth finishing this chapter on is that the "magnitude" of LCE-specific behaviour, for instance the percentage length change on heating and the length of the semi-soft elastic plateau, is intimately tied to the magnitude of r. This simple fact has driven the research community to seek LCEs with high values of r. In turn this has contributed to side chain LCEs (such as traditional acrylate-based LCEs) falling out of favour with many researchers as the coupling factors between Q_N and Q_B limits the values of r attainable in these systems. Having said this, we will demonstrate in chapters 7 and 8 an acrylate LCE with a step length anisotropy several times greater than that previously reported — challenging the current consensus of the LCE research community.

Chapter 5

Experimental Methods

5.1 Introduction

A number of experimental methods were used in the work of this thesis, however many of them were only used on occasion and are therefore only relevant to the results of a given chapter. The core methods, techniques and equipment used in this thesis are described in this chapter while details pertaining to the less frequently used methods are introduced in later chapters as appropriate. Additionally, in some chapters the techniques described in this chapter are used but with small adaptations. Those modifications are described in the relevant chapters.

5.2 LCE production

5.2.1 Cell fabrication

Films of LCE were created by polymerising LCE precursor mixtures inside devices known as "cells" by the procedure described in section 5.2.2 below. Figure 5.1 (overleaf) gives a simplified diagram of the construction and geometry of the cells used in this thesis. The purpose of the cells is essentially to provide a mould for the creation of films of LCE of uniform and controlled thicknesses. Additionally, treatments applied to the internal surfaces of the cell substrates are used to instil macroscopic alignment of the LC molecules when in the nematic phase. The

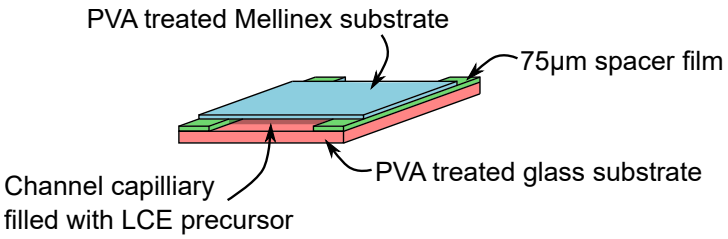

Figure 5.1: Diagram of the cell constructions used in this thesis as a mould for the alignment of and polymerisation of monodomain LCEs.

molecules at the substrate interfaces align with the preferential direction of the cell substrate. For cells with cell gaps (thickness of the cell channel shown in figure 5.1) of up to ~ 150 μm, this alignment propagates throughout the whole of the LC material and persists throughout polymerisation of the final network thus creating monodomain LCEs. Cells were constructed according to the following procedure:

Cells were made with one glass substrate and one 100 μm thick Melinex® (DuPont Teijin Films) substrate. A Melinex substrate was used as its flexible nature meant that following polymerisation, it was easily peeled away from the polymerised film of LCE.

Glass microscope slides, 25×75 mm were used for the glass substrates. These were cleaned by:

- Sonicating for 20 minutes in deionized (DI) water + soap,
- Rinsing several times in DI water,
- Sonicating in DI water for 20 minutes,
- Drying using an air gun,
- Sonicating in acetone for 20 minutes,
- Drying using an air gun.

Melinex substrates (cut to 60x15 mm), being plastic, were more easily scratched than the glass substrates and so were gently cleaned by immersing in methanol for 5 minutes and then dried using an air gun.

Cleaned substrates were then spin coated with a (filtered) LC alignment layer composed of 0.5% by wt. poly(vinyl alcohol) (PVA — molecular weight $\sim 10^5$) dissolved in DI water. The PVA solution was placed on the substrates with care to ensure the whole of the surface was covered and was left for 30 seconds prior to spinning to aid the wetting of the surfaces. The spin speed was then gradually increased to 1500 rpm, then increased to 4000 rpm for 30 seconds. This was enough to coat and dry the substrates.

The alignment layers were then rubbed uniaxially at the desired angle using an in-house rubbing machine. Briefly, the rubbing machine consists of a vacuum plate which holds the samples and moves under rolling drum covered in a velvet cloth. The rubbing of polymeric alignment layers is well known to provide macroscopic and uniform alignment of LC molecules. [52, 139]

Strips of 75 μm thick Melinex film, used as spacers to separate the substrates as shown in figure 5.1, were cut and cleaned. The cells were then constructed by placing the PVA-coated Melinex films on steel blocks (PVA side up) and applying thin lines of (UV curable) Norland Optical Adhesive NOA61 down each side of the substrate. The 75 μm spacers were placed on top of the lines of glue and additional lines of glue were placed on top of the spacers. The glass substrate was then placed to on top (PVA side down), being careful to align the rubbing directions accurately in an antiparallel fashion. Strong neodymium magnets (KJ Magnetics) were placed evenly spaced along the length of the cells over the central void. The attraction of the strong magnets to the steel block beneath compresses the glue with an even and consistent pressure. The cells were then placed under a low-intensity (2.5 mW cm^{-2}) fluorescent UV source for 30 minutes for the glue to cure resulting in the final cells.

5.2.2 LCE synthesis

LCEs were synthesised from a variety of precursor materials (described in chapter 6) which contained the following acrylate-functionalised monomeric groups, liquid crystalline groups and photoinitiator group:

- 2-Ethylhexyl acrylate (EHA) — monofunctional non-LC acrylate monomer.
- 1,6-Hexanediol diacrylate (HDDA) — bifunctional non-LC acrylate monomer.
- 6-(4-Cyano-biphenyl-4'-yloxy)hexyl acrylate (A6OCB) — monofunctional LC acrylate group.
- 1,4-Bis-[4-(6-acryloyloxyhexyloxy)benzoyloxy]-2-methylbenzene (RM82) — bifunctional LC acrylate group.
- 4-Cyano-4- hexyloxybiphenyl (6OCB) — LC group (non-acrylate).
- Methyl benzoylformate (MBF) — UV photoinitiator.

EHA, HDDA and MBF were purchased from Sigma Aldrich. A6OCB, 6OCB and RM82 were purchased from Synthon Chemical GmbH. The function and purpose of each group is discussed in the following chapter.

Using a balance with an accuracy of 0.3 mg, the solid materials (A6OCB, 6OCB and RM82) were measured into a 4 ml amber glass vial containing a small magnetic stirring bead. This was then heated to 120°C on a hotplate until all components had melted and an isotropic mixture formed. The vial and contained mixture was then cooled to approximately at room temperature and the liquid materials (EHA, HDDA and MBF) were added using Eppendorf pipettes. The vial screw caps were then replaced and the vial placed on a magnetic stirring plate set to 40°C and 60 rpm for 5 minutes. At this temperature the materials were always in their isotropic phase which aided the mixing of a homogeneous material. A stirring time of 5 minutes was chosen to minimise the evaporation and loss of EHA and HDDA which are both volatile materials.

The final mixtures were then filled at 40°C (in the isotropic phase) into the previously prepared cells *via* capillary action. The cells were then cooled to room temperature and, where appropriate, left for half an hour for the LC director to align with the rubbing direction of the cells (not all materials exhibited nematic phases — see table 6.1). Such a long time was required to allow complete annihilation of the LC defect threads within the relatively thick cells used in this work. The cells were then placed under a low intensity fluorescent UV light source (intensity of 2.5 mW cm^{-2}) for two hours to polymerise. Upon exposure of the precursor to UV light, the photoinitiator, MBF, generates free radicals which trigger polymerisation (see figure 2.10). Although radical polymerisation is a fast process for thin films of material, we used an exposure time of 2 hours to ensure complete polymerisation. After curing, the cells were opened by carefully prising away the Melinex substrate using a scalpel. In all cases the polymerised sample remained on the glass substrate. A sharp blade was then used to trim approximately 0.5 mm from the edges of each film and the spacers were removed using the scalpel. By placing the glass substrate with exposed sample in a petri dish containing methanol, the sample began to swell slightly and delaminate at the edges. For small samples, the sample could be left to lift away from the glass, however for larger samples the film had to be carefully prised away using large flat tipped tweezers to avoid the film tearing itself apart. Once separated, the film was washed in dicholormethane (DCM) to remove the 6OCB by slowly adding DCM stepwise to about 30% concentration. Solvents were exchanged several times to ensure as much of the unwanted components as possible were removed before the LCE films were de-swollen by adding methanol stepwise. This process took 8 hours to prevent swelling or deswelling the film too fast which again risked causing the film to tear itself apart. Finally the films were left to dry fully overnight at 40°C.

5.3 Glass transition temperature from Differential Scanning Calorimetry (DSC)

DSC is a powerful technique for the study of a material's thermal behaviour including glass transitions, oxidations, polymerisations and phase transitions. [78] Here we limit our discussion to the endothermic processes of the glass transition and the nematic to isotropic transitions which are relevant to the work of this thesis.

DSC works by heating two "pans", one containing the material of interest (sample pan) and one empty (reference pan), over a set temperature range and measuring the difference in heat required to raise the temperature of the pans. The difference in heat required is a result of the sample's heat capacity which can be measured in the process. [78] The heat flow required to change the temperature of a material can change with temperature as a result of phase transitions or changes in the material's heat capacity, thus the shape of a DSC trace and the position of features can be used to identify the nature of thermal processes and at what temperature they occur. [78] A DSC trace is centred on a "baseline" which reflects the heat capacity of the material studied. Exothermic and endothermic processes appear as peaks or troughs relative to the baseline. For a given DSC trace, whether an exothermic process appears as a peak or trough is down one's own choice. [50] However, the exothermic processes and endothermic processes will always deviate from the baseline in opposite directions. For the "heat flow" plots shown in this thesis, exothermic processes will always appear as features above the baseline of the DSC trace.

The temperature at which, say a phase transition, appears to occur on a DSC trace is highly dependent on the heating rate (defined in $^{\circ}$C min^{-1}) used. Due to the effects of thermal lag, *i.e.* the finite time taken for the sample temperature to equilibrate, endothermic thermal events will always appear to occur at a temperature offset higher than the true value. [78] Moreover, scans performed at greater heating rates will have greater thermal lag effects and thus greater offsets.

The glass transition of a polymeric material appears as a step change of the baseline of a DSC curve. [78, 50] Below a glass transition, polymeric materials are brittle while above a glass transition they are comparatively soft or rubbery. [50] On the DSC traces shown in this thesis, the glass transitions appears as a step lowering of the baseline. As the glass transition temperature is actually a glass transition region there are several ways of assigning a value to T_g. From DSC curves measured we determine T_g as the inflection point of the step change of the baseline as determined using the fitting function of TA Universal Analysis 2000 (TA Instruments).

For the accurate determination of T_g for the LCEs studied in detail in this thesis we follow the example of Donnio *et. al.* in calculating the glass transition based on the inflection point extrapolated to a heating rate of 0°C min^{-1}. [38] This method is used in section 6.3.2 for accurate determination of the T_g values for the final LCEs developed. Elsewhere in chapter 6 we quote, for comparison with one another, values for T_g based on the inflection point from experiments performed at a heating rate of 20°C min^{-1}. In all cases, the relevant heating rates are given alongside the results for clarity.

Although the nematic to isotropic phase transition temperature (T_{NI}) can also be determined *via* DSC (since it is a first order phase transition requiring latent heat), the DSC peak for the transition is instead smeared out in LC mixtures making it impossible to assign a single value for T_{NI}. For simplicity we therefore chose to determine T_{NI} *via* polarising microscopy. As this method was only relevant to the results of chapter 6 the method is detailed in section 6.2.1.

For determination of T_g, all DSC scans were performed using a TA Instruments Q20 DSC. In each case sample masses of approximately 6 mg were placed inside hermetically sealed TA instruments T-Zero® aluminium sample pans with an empty pan used as the reference pan. Initial scans were performed to first identify an approximate value for T_g. These were used to identify an appropriate temperature range for the measurement scans to be performed over. In all cases, prior to execution of the desired DSC testing sequences the samples

were first thrice cycled over the chosen temperature range at 20°C min^{-1} to ensure good sample contact with the base of the pan and repeatability of the DSC traces. Temperature ranges scanned over and rates used are given alongside the presented results.

5.4 Material study *via* crossed polarisers

While DSC can readily identify the temperature at which phase transition occur for a given material and the nature of those transitions (*i.e.* first or second order), other techniques are required in order to determine the precise nature and symmetries of each phase. The birefringent nature of LCs means the nature of their phases are, in general, easily studied by viewing thin films of material between crossed polarisers. In this thesis we are exclusively concerned with nematic and isotropic phases and use crossed polariser techniques to determine the microstructure of our LCEs and its evolution with mechanical deformation.

In this section we first outline fundamental principles of optical anisotropy before describing a typical crossed polariser experimental arrangement and providing an outline of the physics behind observations made with crossed polarisers.

5.4.1 Optical anisotropy

The refractive index of optically anisotropic (birefringent) materials differs along the principal axes of the material. If we align our coordinate set with the principal axes of an anisotropic material, then the refractive index can be represented by the tensor $\underline{\underline{\mathbf{n}}} = \mathrm{Diag}(n_1, n_2, n_3)$. In the simplifying case of a uniaxially birefringent material $n_1 = n_e$ and $n_2 = n_3 = n_o$, where n_e denotes the *extraordinary* refractive index and n_o denotes the *ordinary* refractive index. Diagrammatically, the refractive index tensor can be represented by the index ellipsoid, or indicatrix (figure 5.2).

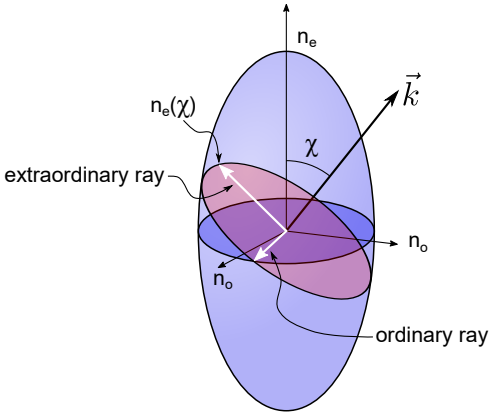

Figure 5.2: The index ellipsoid for a uniaxial anisotropic material. A general electromagnetic wave propagating along $\vec{k}$ can be split up into two polarised components with electric field vectors parallel to the principal axes of the ellipse shown (formed from the intersection of the index ellipsoid with the plane perpendicular to $\vec{k}$). The "extraordinary ray" experiences $n_e(\chi)$ while the "ordinary ray" experiences n_o.

Electromagnetic radiation passing through a transparent anisotropic material experiences different refractive indices for the linearly polarised components of the electric field resolved along the *effective* principal directions of the optically anisotropic material. We write "effective" principal directions as the electric field of the incident light experiences an optically anisotropic environment of refractive indices $n_e(\chi)$ and n_o — defined by the projection of the indicatrix on the plane perpendicular to the wavevector, $\vec{k}$, of the incident light (figure 5.2). $n_e(\chi)$ is given by

$$\frac{1}{n_e^2(\chi)} = \frac{\cos^2(\chi)}{n_e^2} + \frac{\sin^2(\chi)}{n_o^2}, \tag{5.1}$$

where χ is the angle between the wavevector $\vec{k}$ and the axis of the extraordinary refractive index. We highlight several special cases of equation 5.1. Firstly, when $\chi = 0°$, such that the light is propagating is parallel to the extraordinary axis, $n_e(\chi) = n_o$ and hence the electric field of the propagating light experiences an optically isotropic material — independent of the polarisation direction. For

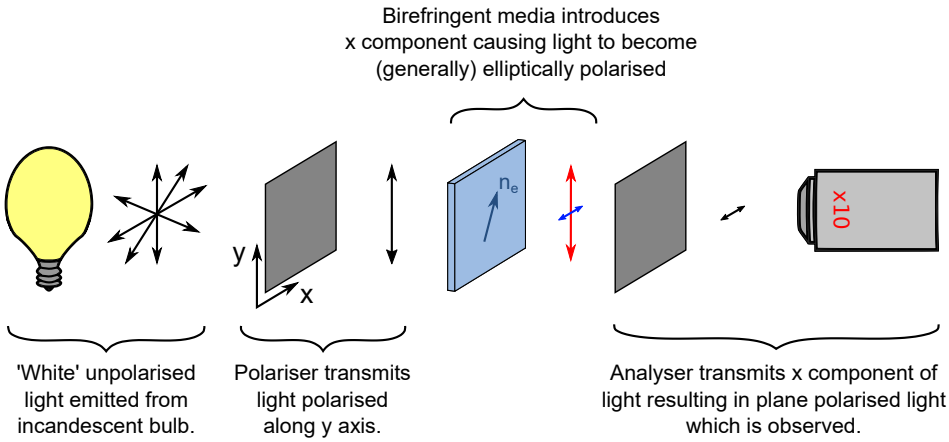

Figure 5.3: A simplified diagram of the key components of crossed polariser experimental arrangement and how the incident light is affected by each element.

a LC material, such a geometry typically corresponds to a "homeotropic" geometry where the LC molecules are aligned perpendicular to the planes of the cell substrates. Secondly, when $\chi = 90°$, $n_e(\chi) = n_e$ and the birefringence experience by the electric field of light, $\Delta n = n_e - n_o$ is at its maximum magnitude. For the geometries considered in this thesis, we will always have the case of $n_e(\chi) = n_e$.

5.4.2 Experimental arrangement

Figure 5.3 gives a diagram of the key components of a crossed polariser-based experiment along with a simplified illustration of how the incident light is affected by each optical element. The light source, typically an incandescent or LED bulb, provides unpolarised "white" light. The actual spectrum of "white" light will vary between the type of light source used and will affect the final appearance of the sample when viewed by eye or captured by a camera. Two linear polarisers are arranged at 90° with respect to one another such that if nothing (or an isotropic material) is placed between them, then no light will be transmitted by the second polariser (the analyser). Between the polarisers a birefringent sample is placed which, in general, will cause the linearly polarised light transmitted by the first polariser to become elliptically polarised. This occurs as the components of the linearly polarised light, when resolved along the effective principal axes

of the birefringent media, will experience the different refractive indices, $n_e(\chi)$ and n_o, described in the previous section. The components of light will therefore travel at different speeds through the birefringent material and will therefore emerge with a relative phase difference, or retardance, resulting in (generally) elliptically polarised light. We say "generally" as in special cases the emergent light may actually be circularly or linearly polarised. A component of light is then transmitted by the analyser as the light emerging from the birefringence media now has a component perpendicular to the initial polarisation direction. This can then be detected by a detector, camera or the eye. This brief qualitative description of the light transmitted by the analyser is formalised in the following section.

5.4.3 Mathematics behind observations

It can be shown that for light of intensity I_0 transmitted by the first polariser, that the light transmitted by the analyser depends on the thickness of the anisotropic material, d, the birefringence $\Delta n = n_e(\chi) - n_o$ the and the angle, θ, between the transmission axis of the polariser and the extraordinary principal axis of the birefringent material. The light transmitted by the analyser is given by

$$\frac{I}{I_0} = \sin^2(2\theta) \times \sin^2\left(\frac{\pi \times \Delta n \times d}{\lambda}\right), \tag{5.2}$$

where lambda is the wavelength of light. What is immediately noticeable from equation 5.2 is the fact that when a transparent isotropic material is placed between crossed polarisers, no light will be transmitted by the analyser and the material will appear black as $\Delta n = 0$ for an isotropic material.

It is important to note that equation 5.2 is valid for a single wavelength of light and not for the spectrum of light outputted by a given white light source. For white light the overall transmitted intensity would be calculated from the integral of equation 5.2 with respect to λ where a normalised distribution function $f(\lambda)$ must also be included to reflect the spectrum of white light used.

The λ dependency of equation 5.2 also affects the colour of the light transmitted by the analyser. In this thesis, the colour of transmitted light is frequently used to qualitatively deduce the magnitude of the liquid crystal ordering and so we here discuss in detail how the retardance and transmitted colour are related.

Figure 5.4 shows the transmitted intensities for a variety of wavelengths of light (colour coded appropriately) against the retardance $\Delta n \times d$. Also shown in black is the average of the coloured curves plotted. The black line shows how the overall intensity is expected to be at its brightest at low retardances before generally decreasing. While the intensities of the different wavelengths are initially in phase with one another, they quickly lose synchronisation giving different positions of intensity maxima for each wavelength of light hence causing a mixing of colours. Figure 5.4(b) shows a photograph of a film of nematic LC across a region where the thickness, and therefore the retardance, increases from 0. The effect of the retardance-dependent mixing of wavelengths on the transmitted colour is clearly evident. The appearance of the sample is reminiscent of a Michel-Levy colour chart which links the retardance of a birefringent material to its apparent colour when viewed between crossed polarisers. Important to note from figure 5.4(b) is the fact that as the retardance increases, the mixing of the various wavelengths of light shown in figure 5.4(a) causes a lowering of the perceived *saturation* of the transmitted colours. The colour mixing continues to increase with retardance such that at high retardances, birefringent materials essentially appear grey in colour. It is also evident from figure 5.4(b) that the overall intensity of transmitted light decreases with retardance as expected by the black curve of figure 5.4(a).

The symmetry of LC systems means that, for a given material, there is a close relationship between the level of birefringence and magnitude of the LC order parameter, Q_N. This relationship — and in particular the fact that when $Q_N = 0$, $\Delta n = 0$ always — means that the *evolution* of the birefringence colours for a given LC system can be used tell us a great deal about the changes in the magnitude of the order parameter. However, care must be taken in such

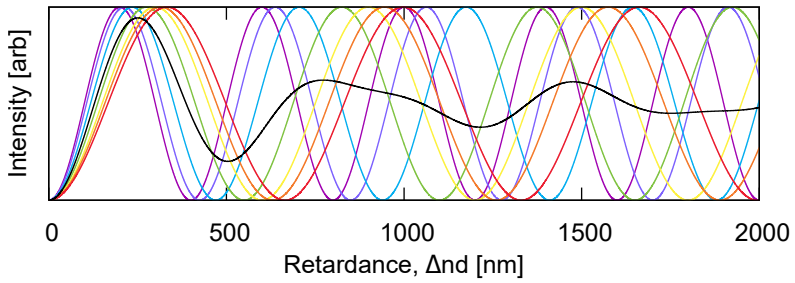

(a)

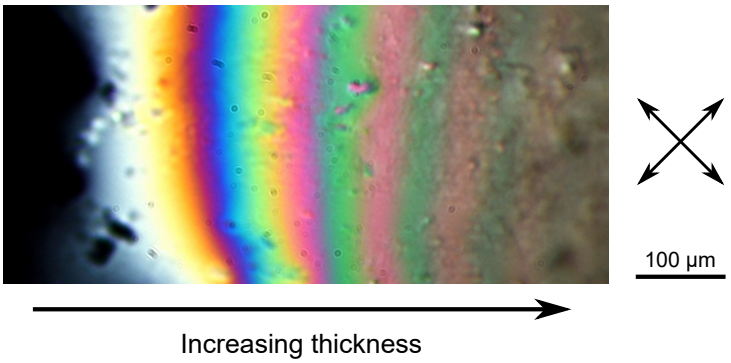

(b)

Figure 5.4: a) The intensity of light transmitted by crossed polarisers against increasing retardance. The colour of curves shown reflects the wavelength region of visible light that each curve corresponds to. The black line represents the average intensity of the coloured lines plotted. b) A photograph of the birefringence colours of a liquid crystal sample of non-uniform thickness viewed between crossed polarisers using a 20× microscope objective.

interpretations as the birefringence of a material is also strongly influenced by the molecular structure so by itself, a high birefringence does not necessarily imply a given material has a high Q_N.

The above discussion of transmitted colour relates to the second $\sin^2$ component of equation 5.2. This component has no dependence on θ, the relative angle between the polariser and extraordinary axes whereas the first component of equation 5.2 does. The θ dependency of the first $\sin^2$ component of equation 5.2

shows that the transmitted intensity will oscillate as a birefringent sample is rotated with respect to the polarisers. However, the fact that this term has no λ dependence means that the transmitted colour remains constant as the sample is rotated. The frequency of the first $\sin^2$ component means that per 360° rotation of the sample there are four maxima and four minima in transmitted intensity. Additionally, as the polariser and analyser are oriented at 90° with respect to one another and a birefringent material's ordinary and extraordinary axes are 90° apart, the appearance of zero transmitted intensity for a material of finite retardance means that the extraordinary axis is aligned parallel with *either* the polariser or the analyser. Without any other information about the sample (and without additional optical elements such as a birefringent waveplate) it is impossible to determine which of the polariser or analyser the extraordinary axis is aligned parallel to.

5.5 Opto-mechanical testing and analysis

5.5.1 The Microscope Elastomer Stress Strain Enclosure (MESSE)

Motivation

In chapter 2 we saw that while the optomechanical properties of LCEs have been investigated a great deal over the past 30 years, there are still numerous apparent inconsistencies between phenomena observed in different experiments. For instance, when a monodomain LCE is stressed perpendicular to the director, two director rotation behaviours, SSE and MFTs, have been observed. Currently the factors influencing whether a given LCE will exhibit one type of behaviour over another remains unknown and is in fact *unstudied*. Given the unique mechanical behaviours seen in LCEs are inherently linked to the state of LC order within the material and the orientational response of the director to the applied strains, it is remarkable that there are only two known reports of the mechanical *and* optical properties of LCEs being simultaneously studied. [93, 94] In one other case, separate mechanical and infra-red dichroism tests were performed on the

same type of LCE and their results compared. [74] However, as the authors used separate tests there remains the possibility that the behaviour displayed in each of the tests may differ as test parameters (for instance the strain rate, sample geometry and/or sample temperature relative to both T_g and T_{NI}) may have been changed between tests. The importance of maintaining consistent sample testing parameters was highlighted by Talroze *et. al.* and Zubarev *et. al.* who showed that the appearance of stripe domains is highly sensitive to the aspect ratio of the sample mechanically tested. [153, 183]

Bearing the above in mind, for the work of this thesis we sought to develop bespoke mechanical testing equipment which enabled the study of a LCE's microstructure throughout a mechanical test. In doing so we would be able to confidently link the evolution of the microscopic behaviour of our LCEs to the macroscopic mechanical response. Linking these behaviours was especially important for the work of this thesis where we sought to use the mechanical anisotropy of LCEs to design programmable deformations for the design of the target AIOL device. Therefore an intimate knowledge of how the director orientation affects the macroscopic mechanical behaviour of the studied LCEs was crucial to the success of the research performed.

Defining the equipment specification

Although based on the above our equipment specification appears simple, it was first important to decide which method to use to study the evolution of the LCE microstructure during mechanical testing. Three options were identified:

- X-ray diffraction (XRD),
- Infra-Red (IR) dichroism,
- Polarising microscopy.

The most commonly used techniques to date have been XRD and IR dichroism. [142, 94, 90, 183, 153, 76, 74] While these techniques can be used to quantitatively determine the director orientation and the level of ordering within the sample, it can be difficult to determine exactly what "ordering" has been measured as both techniques determine the average order parameter over any

structures present within the measurement area which typically is larger than 100×100 μm. [183, 133, 74] For example, in the experiments of Talroze *et. al.* and Zubarev *et. al.*, the sample area measured over using X-rays ($\sim 800 \times 800$ μm) contained stripe domains of width ~ 20 μm and so the diffraction patterns showed a superposition of nematic diffraction patterns corresponding to the domains of counter-rotating director orientations. [183, 153] The consequences of spatially inhomogeneous ordering can be further seen by considering the results of two papers by Roberts *et. al.* from 1997. Between the two papers the authors presented conflicting results showing constant and non-constant order parameters during a "mechanical Fréedericksz" process. In one of the papers the difference was seen to be a result of the presence of domains of constant order parameter giving the *appearance* of a reduction in the nematic order parameter when the diffracted X-rays averaged over these domains. [132]

In comparison to XRD and IR dichroism, viewing a LC material *via* polarising microscopy allows one to readily tell the difference between disordered domains of constant order parameter (which scatter light causing a sample to appear opaque) and changes in the order parameter (which cause a change in the observed birefringence colour or measured retardance). While polarising microscopy can only be used to make qualitative assessments of the LC order parameter of a sample, such assessments can be performed, along with quantitative assessments of the local director orientation, across an entire sample at once. By comparison, in order to assess the order parameter across a sample using XRD and IR dichroism, individual measurements would need to be performed at every location of interest. Moreover, polarising microscopy is a comparatively low-cost and simple experimental technique. Based on the above discussion, we decided to develop our equipment which would allow us to view the sample *via* polarising microscopy during mechanical testing.

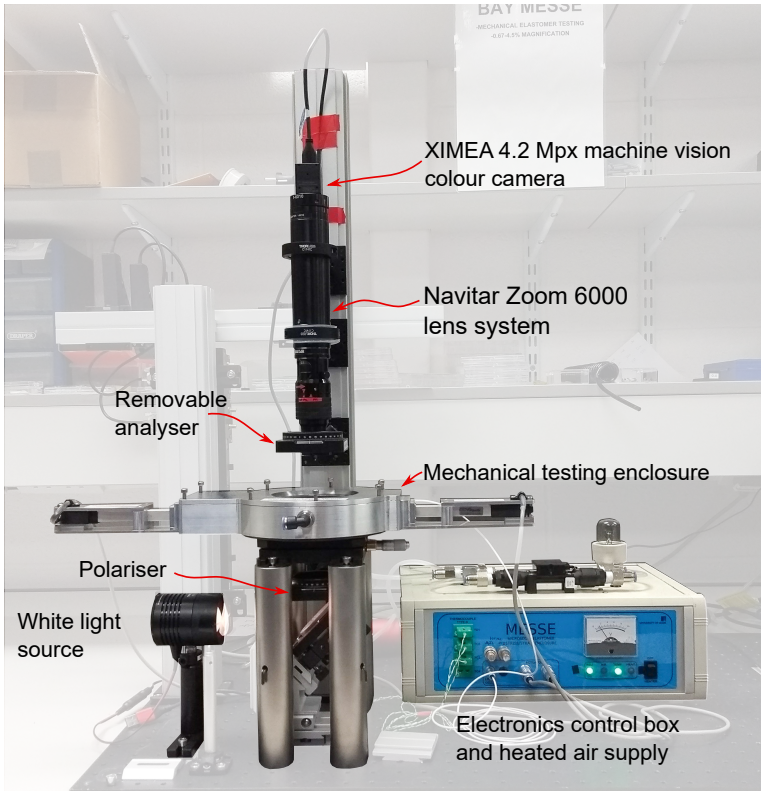

(a)

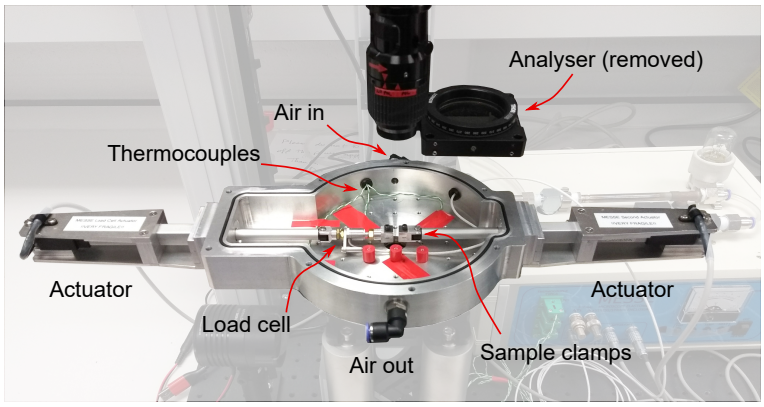

(b)

Figure 5.5: a) Photograph of the bespoke mechanical testing equipment — MESSE. b) Detailed photograph of the testing enclosure with the lid removed

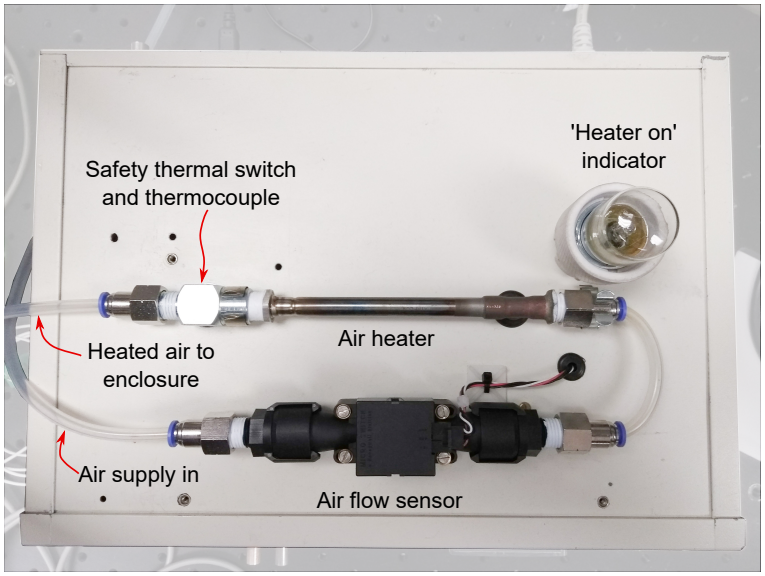

(a)

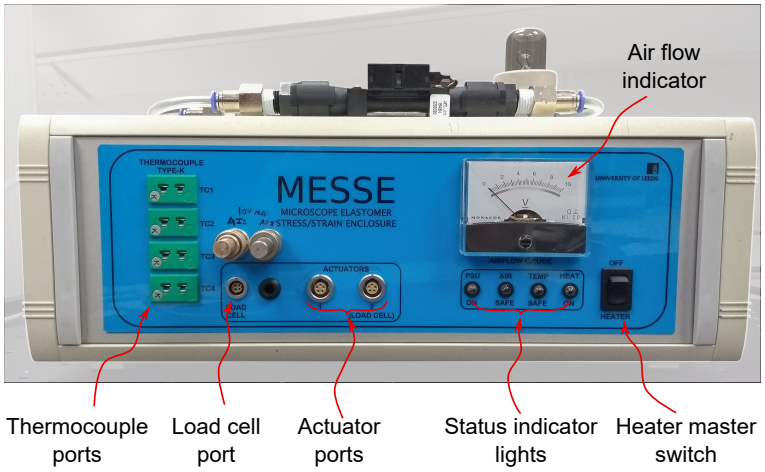

(b)

Figure 5.6: a) Photograph of the top of the electronics control box showing the components responsible for the supply of heated air to the enclosure. The thermocouple contained inside metal block shown allows the heater temperature to be monitored while the bimetallic switch automatically removes power supplied to heater if the air temperature exceeds 80°C. b) View of the front panel of the electronics control box, the air flow must exceed "6" on the indicator to enable the heater.

Given the above, the design specification of the equipment was as follows:

- Must have actuators capable of applying strains to films of LCE with minimal incremental steps of ~ 1 mm.
- Must be able to record the force applied to the samples by the actuators.
- Must be able to view the sample using a camera *via* white light illumination and *via* crossed polarisers.
- Must be capable of viewing the sample on "macroscopic" length scales but with high enough resolution to discern microscopic features.
- Must be able to maintain the whole of the sample at a uniform and constant temperature, ideally up to as high as ~ 30°C.

Details and capabilities of equipment produced

Figures 5.5 and 5.6 show photographs of the final equipment developed. In this section we first describe the various components of the equipment before describing the overall capabilities. The aluminium testing enclosure described below was machined by Mr. Trevor Haynes in the School Mechanical workshop, while the electronic control box was assembled, and custom circuit boards created by Mr. Philip Thornton in the School Electronics workshop.

The design of the equipment shown in figures 5.5 and 5.6 centres on the aluminium mechanical testing enclosure which is shown in detail in figure 5.5(b). The enclosure itself provides a testing environment within which the sample under test can be maintained at a constant temperature *via* the supply of heated air. Three thermocouples spaced evenly around the sample monitor the temperature distribution around the sample. The average temperature reading from the three (type K) thermocouples is used to control the temperature of the enclosure *via* a PID control loop (detailed below). The temperature variation between the locations of the three thermocouples was never more than 1°C. Mounted on the enclosure are two opposing Firgelli (now Actuonix) L12 Micro Linear Actuators which apply strains to the samples under test. The actuators have a minimum step size of 0.2 mm and can apply a maximum force of 80 N. Attached in series

to one of the actuators is a calibrated Measurement Specialties (now TE Connectivity) XFTC 300 load cell which is capable of recording loads of up to 5 N in either tension or compression. This low maximum recordable force offers a high resolution in the minimum detectable force which, when coupled with the voltage datalogger (Pico TC-08, discussed below), means the error from the load cell measurements is negligible compared to other experimental errors measurements performed. Large 18 mm diameter glass windows in the base and lid of the aluminium enclosure allow for sample observation *via* transmitted light.

The aluminium enclosure can be mounted on the bespoke illumination stand shown in figure 5.5(a) (components from Thorlabs) or on the sample stage of a polarising microscope. Both arrangements offer the ability to view the sample *via* white light and between crossed polarisers. The bespoke stage allows wide-field view of the sample using a 0.7—4.5× lens system (extendible to 9× with an additional 2× magnifying adapter) while the microscope offers the ability to view the sample *via* higher power microscope objectives and further allows the use of additional optical components such as waveplate retarders or Berek compensators (see section 7.2.2). In the arrangement shown in figure 5.5(a), the polariser and analyser are mounted in rotation optical mounts which have angular scales with 2° divisions. Using these polarisers, photographs of the sample can be easily captured with the crossed polarisers oriented at various angles relative to the sample. Doing so provides data which can be used to determine and map the localised director orientation as explained in section 5.5.2. The camera chosen has a 11.27×11.27 mm (1" diagonal) sensor and a 2048×2048 px resolution. The camera can be mounted on either the lens of the wide-field sample stage or the photoport of a microscope. When mounted on the former, the maximum field of view is 16.1 × 16.1 mm when the lens is set to the lowest magnification (0.7×). Unless specifically mentioned otherwise all photographs taken using MESSE are taken with the lens set at 0.7× magnification.

The electronics control box shown in figure 5.6 contains the following electronic components with the specified functions:

- Firgelli LAC actuator control boards — Controls the position of the actuators and feeds back the actuator positions to the control software.
- Pico technology USB TC-08 — Thermocouple and voltage datalogger used to read temperature from the type K thermocouples (three in the sample chamber and one at the output of the air heater) with overall $\pm 2°C$ absolute accuracy. Unit also reads the voltage signal from the load cell.
- Omega In-line Air and Gas Heater — Heats the supplied compressed air for controlling the temperature inside the testing enclosure.
- Honeywell AWM5104VN Mass Air Flow Sensor — Measures the flow rate of the supplied compressed air ensuring a minimum flow rate passes through the air heater (heating and safety elements controlled by a custom built circuit board).
- Arduino Uno and AC Phase Control Circuit (Triac board) — Together control the power delivered to the air heater based on software input.

The Pico USB TC-08, Firgelli LAC control boards and Arduino Uno are all connected to a internal USB hub through which all components are connected to a computer *via* a single USB cable.

Control software

The camera shown in figure 5.5(a) and equipment of the electronics control box are connected to a laptop computer running custom control software developed in LabVIEW 2013 (National Instruments). The software has two purposes.

Firstly, it controls the temperature of the enclosure *via* a PID control loop. The user sets the desired temperature and the software controls the power supplied to the heater such that the chamber temperature, as measured by the average of the three thermocouple readings, is increased or decreased to the set temperature. The use of a PID control loop means temperature changes are gradual thus minimising overshooting and oscillating about the set point. As the

heater is incapable of actively cooling air flowing through it, the minimum chamber temperature is limited by the temperature of the supplied compressed air. The maximum chamber temperature is limited primarily by the maximum temperature the heater is allowed to reach (80°C) before power is cut to the heater and heat loses as the air is transferred to the enclosure. Practically, a maximum chamber temperature of $\sim 35 \pm 2$°C is achievable.

Secondly, the software developed controls the actuators and camera. Mechanical testing sequences can be created which will extend the sample under test in discrete extension steps with a practical minimum step size of 0.5 mm. The user can define the time between successive steps to allow varying degrees of sample stress relaxation and also to allow measurements to be performed on the sample under test. For instance, the user can take photographs of the sample using white light and/or crossed polarisers.

5.5.2 Data analysis

The two most important aspects of data analysis used in this thesis relate to the determination of mechanically induced strains parallel and perpendicular to the applied stress axis of tested samples and the localised determination of the LC director orientation. For the majority of tests in this thesis, localised strains are determined from photographs of the samples taken at each strain step under white light illumination using the methods described below. For determination of the localised director orientation crossed polarising photographs of the sample were required for various orientations of the crossed polarisers relative to the sample. For this analysis, 36 such photographs of the sample were captured, in between which the polariser and analyser were rotated by 10°. The localised director orientation was extracted from these photographs using the method described below.

Measuring localised deformations

In order to measure the tensile load curves and quantify the geometrical deformations of films studied, the sample strains parallel and perpendicular to the

applied stress axis of each test had to be determined.

Strains parallel to the stress axis were most frequently determined using a particle tracking python package called *trackpy*. As discussed in section 6.3.2, the samples of LCEs studied in this thesis are unintentionally embedded with small crystallites. These crystallites move with the samples as they are strained and are visible in white light photographs taken of the samples at each strain step. *trackpy* generates localised deformation trajectories of the sample from the position of these crystallites at each strain step by the following process.

Firstly, a sequence of photographs, or "frames", are loaded. As the "particles" appear dark relative to the background, the images are inverted so the particles are brighter than the background. *trackpy* then analyses each frame to identify the pixel locations of the particles. The features identified as particles depends on the user specified "size" and "mass". The size refers to an estimate of the typical particle pixel size while the mass refers to the total brightness of the feature. After the particles within each frame are identified, trajectories are formed by linking the positions of particles between frames. The user defines a search window size and *trackpy* searches this window, centred on each particle location in each frame, for the position of the particle in the subseqent frame. The size of the search window is kept as small as possible to minimise the time taken for the script to run. The standard *trackpy* linking function assumes the particles move in a random walk-like manner. However as this is certainly not the case for the particles embedded in the mechanically deformed materials, the predictive linking *trackpy* function was instead used. The predictive linking biases the particle searching to the direction the particle moved between the previous frames. This enables a larger search window to be used which was particularly helpful in our application. Of the trajectories identified, only those which link a single particle's movement through all frames were kept. The accuracy of each trajectory was monitored by assessing outputted photographs of the trajectories overlaid on top of the photographs of the samples at each strain step. Occasionally, when a trajectory linked the wrong particle between frames, the position of the particle in the mis-linked frame(s) was corrected by measuring the particle

position manually using Image J (National Institute of Health, USA). [144, 145]

The strain parallel to the stress axis (chosen always to be the x axis) is then determined from a selected a pair of tracked particles located near the centre of the deformation and at approximately the same position along the width of the sample. The strain at each extension step is then calculated from the changing particle separations determined from the difference in x coordinates of the tracked positions.

Strains along y were determined using a custom *python* script which analysed cropped photographs of the central portion of the LCEs under test. The script located the pixel rows corresponding to the top and bottom edges of the film, the difference of which gave the pixel width of the film. This was readily converted into millimetres using a pixel calibration. Additionally, from the pixel widths the strain along y were easily calculated.

Determination of director orientation

In section 5.4.3 we saw that for the case of the extraordinary axis of a birefringent material being aligned with either the polariser or the analyser, the intensity of light transmitted by the analyser it at its minimum. As the extraordinary axis for a nematic liquid crystal is parallel to the director, the orientation of the director can be determined from the angular position of the transmitted intensity.

From the sample polarising microscopy images taken at 10° intervals, we can measure the transmitted intensity as a function of sample orientation with respect to the polarisers by taking the average RGB pixel intensities over a small region of interest (typically $< 100 \times 100$ px in size). Given the $\sin^2$ form of equation 5.2, the transmitted intensity calculated from each photograph is expected to fit to the function

$$I = I_0 \sin^2\left(\frac{b\pi \times (\theta - c)}{180}\right) + d, \tag{5.3}$$

where θ is the angle between the polariser and the director orientation and I_0, b, c, and d are fitting parameters. In this thesis we define $\theta = 0$ as being parallel to the applied stress axis. The wavelength and colour dependencies discussed in section 5.4.3 are incorporated in to the parameter I_0. In equation 5.3 we have a zero offset term, d, which is not present in equation 5.2. This parameter reflects the fact that a background intensity, caused be imperfect polarisers and camera settings, exists practically.

By fitting the intensity, I, measured at each 10° rotation step to the function in equation 5.3 we find c, which corresponds to a possible orientation for the director relative to the strain axis (given the four minima in equation 5.3 for a 360° rotation). As for a nematic LC $\vec{n} = -\vec{n}$, there are two possible director orientations, c and $c+90°$. The correct value is determined by knowing the initial director orientation based on the rubbing direction of the cell used.

5.6 Conclusion

In this chapter we have described the relevant aspects of experimental methods used frequently in this thesis. Other techniques used on occasion are described later in the appropriate chapters.

The latter part of this chapter has described in detail the capabilities of bespoke equipment designed and created to allow us to study the evolution of a LCE's microstructure during mechanical tests. By choosing to study the samples *via* crossed polarisers as opposed to *via* XRD or IR dichroism we can not only deduce the difference in levels of order on molecular and microscopic length scales, but we can also easily analyse any part of the sample captured in each photograph during post-experiment analysis. This will be of exceptional use in chapter 11 where we study the spatial variation of the LC director across a sample during a mechanical test. Such a test would be prohibitively difficult using XRD or IR dichroism approaches. The trade-off we accept by using crossed polarisers is that we cannot perform quantitative measurements of the LC order parameter.

However, given the depth and range of the experimental characterisation our bespoke equipment allows (seen in chapters 7 – 11), our acceptance of this trade-off is wholly justified.

In our description of the components of MESSE we have, in parts, not provided details of the accuracies of measurements which can be performed. For instance, we have not detailed the accuracy of force or strain measurements possible for mechanically tested samples. In these cases the accuracy of such measurements is also dependent on the parameters of each particular experiment. Therefore we describe the factors affecting the accuracy of these measurements in the relevant chapters alongside the descriptions of the experimental parameters.

Chapter 6

Designing acrylate-based LCEs with low glass transition temperatures

6.1 Introduction

6.1.1 The state of existing acrylate LCEs

We now turn to the development of the acrylate-based LCEs which we will use and study in this thesis. In chapter 2 we identified acrylate LCEs to be the most suitable class of LCEs for our work — a conclusion based on the balance between the fact that they can be prepared in complex director geometries, they have a quick and simple synthetic route, and there is a vast array of commercially available starting materials that can be used their synthesis. However, acrylate LCE have historically been limited by the fact that their glass transition temperatures (T_gs) are typically above room temperature which means that at ambient temperatures they are brittle. [169, 22] Thus acrylate LCEs have in general been difficult to work with as they must be studied, and in some cases must be also be polymerised, at elevated temperatures. [157, 156, 74, 183]

To date, two acrylate LCEs are known to have sub-room temperature T_gs. Thomsen *et. al.* reported in 2001 a side chain side-on LCE with a T_g of

18.8°C. [156] More recently, in 2017 Zeng *et. al.* reported a side chain end-on LCE with a T_g of $\sim$ 13°C. [180] Despite these seemingly attractive values of T_g, these LCEs have limitations which make them inappropriate for our use. Firstly, the mesogenic monomers of the Thomsen LCE are not commercially available, which would significantly limit the quantity of materials we could produce. [156] Secondly, 4% by mol. of the Zeng LCE is composed of a non-polymeric photo-reactive group which is used to for the isothermal photo-switching of the their devices. [180] The inclusion of this photo-reactive component is likely to have reduced the T_g for the final material and further, as it is also a dye, it caused the resultant LCE to have a strong red colour. [28, 180] As we are not concerned with the photo-switching of LCEs, the Zeng LCE is also not appropriate for our studies. We are left needing to develop our own acrylate-based LCE with a low T_g.

In this chapter we detail our development of bespoke acrylate LCEs with glass transition temperatures below room temperature. We first present and justify our choice of a starting LCE which to adapt. We then outline our approach to modifying this LCE to develop our own materials. Next, we detail techniques used to characterise the basic phase properties of the materials developed. Finally we present our results and justify our choice of the two LCEs studied in this thesis.

6.1.2 Our starting point — the Urayama LCE

Possibly the single most studied acrylate-LCE is the material first reported in 2005 by Urayama. [157] Although this LCE has a high T_g of 50°C a great deal is known about its mechanical properties (both experimentally and theoretically) and so it is a suitable material from which to develop our own low T_g LCE. [157, 159, 74] The Urayama LCE is synthesised using the following materials:

- 6-(4-Cyano-biphenyl-4'-yloxy)hexyl acrylate (A6OCB),
- 1,6-Hexanediol di-acrylate (HDDA),
- Irgacure 784 (visible light photoinitiator) and,
- 4-Cyano-4'- hexyloxybiphenyl (6OCB).

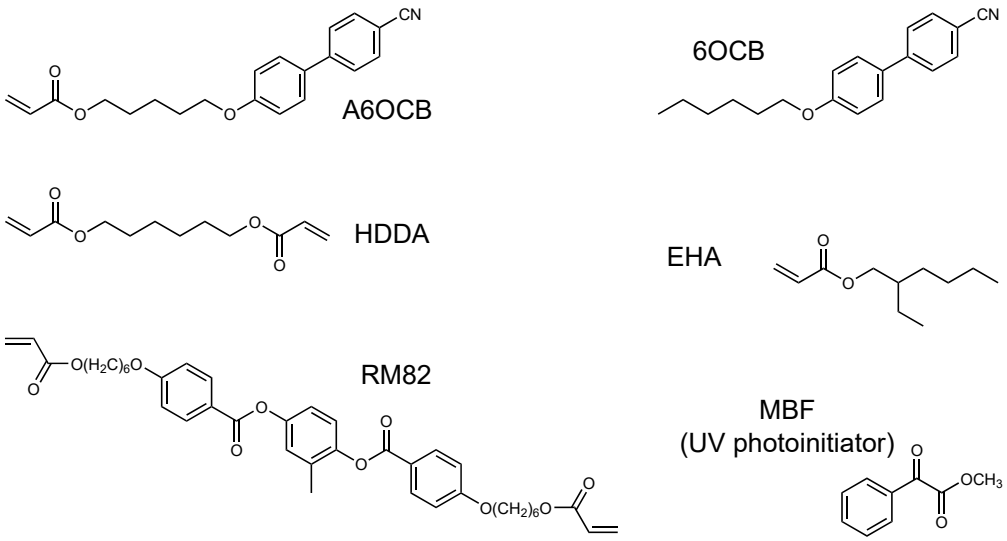

Figure 6.1: Chemical structures of components used to synthesise the Urayama LCE (A6OCB, 6OCB and HDDA) and the components we have added to create new LCEs (EHA and RM82). MBF is the UV photointitator we chose to use in this thesis.

The structures of A6OCB, 6OCB and HDDA are given in figure 6.1. A6OCB is a monofunctional reactive mesogen which forms side chain end-on liquid crystal (LC) polymer chains (refer to figure 2.9 on page 31). HDDA is a non-mesogenic crosslinking group used to crosslink the polymerised chains of A6OCB together. Finally Irgacure 784 is a visible light photoinitiator used to trigger the polymerisation of the network. 6OCB is non-reactive mesogenic group used to give the LCE precursor the phase behaviour required for forming monodomain LCEs. By itself A6OCB only displays a very narrow (~ 2°C wide) monotropic nematic phase on cooling from the isotropic phase. [160] The addition of 6OCB, which is miscible with A6OCB, broadens the nematic phase such that polymerisation can be performed in an aligned nematic state. As the alignment persists through polymerisation, monodomain LCEs can be formed.

The full synthesis used by the Urayama group to produce monomdomain LCEs is as follows. A LCE precursor is formed from: A6OCB (46.5 mol%), 6OCB (46.5 mol%), HDDA (7 mol%) and Irgacure 784 (3 mol%). The LCE

precursor has a T_{NI} of $\sim 50°C$ and so upon filling into a cell, polymerisation is typically performed at 45°C. [160] Following polymerisation, the cell is carefully opened and the polymerised film separated from the cell substrates. To form the final LCE, 6OCB is washed from the LCE and the final LCE dried *via* the same procedure described in section 5.2.2.

6.1.3 Modifying the Urayama LCE to develop the "ideal" LCE

Reducing the glass transition temperature of the Urayama LCE requires introducing additional monomeric units which will increase the flexibility and mobility of the polymer backbone. While it is difficult to accurately predict the T_g of a polymer based on the structure of the constituent monomers alone, numerous semi-empirical models have been developed over the years which can give accurate predictions of a copolymer's T_g temperature. [174, 83, 23] These models are based on the polymer's composition and the (experimentally measured) T_g of the constituent polymers. We do not go into the detail of these models as we are not concerned the accurate prediction of the T_g of our new LCE compositions. Instead we use a common feature of these models to inform how we should go about modifying the Urayama LCE in order to reduce its T_g from 50°C. From these models one can say that, in general, for a polymeric system of $T_g = {T_g}^a$, one can form a copolymer of $T_g < {T_g}^a$ by introducing monomers which by themselves would form a polymer of ${T_g}^b < {T_g}^a$. [174, 83, 23] Evidently in order to reduce the T_g of our LCE below room temperature we should choose a monomer whose polymer has a T_g below room temperature. A second consideration for choosing a co-monomer is that the co-monomer must be sufficiently miscible with the existing components of the LCE to prevent phase separation of the components prior to or during polymerisation.

Based on the above considerations, the monomer 2-ethylhexyl acrylate (EHA) was chosen for adding to the Urayama LCE. The structure of EHA is given in figure 6.1. Poly(EHA) has a glass transition temperature of −65°C and so its inclusion was expected to have a pronounced effect on the T_g of the Urayama

LCE. [64] Additionally from the chemical structure of EHA, we see that the main alkyl chain of EHA has the same length (6 carbons) as the alkyl chains of A6OCB and 6OCB — thus EHA was expected to be highly miscible with the existing Urayama LCE precursor.

Alongside reducing T_g, the inclusion of EHA was expected to cause a lowering of the LCE precursor's T_{NI} — a result of EHA's non-mesogenic nature. This was a concern as in order to create monodomain LCEs, polymerisation must be performed below the T_{NI} of the LCE precursor. Additionally, for reasons described below, we needed to be able to polymerise the LCE at room temperature. Therefore it was essential that we were able to maintain an above room temperature T_{NI} for our LCE precursor as well as lowering the material's T_g through the addition of EHA, *i.e.* we wanted a degree of independent control over the precursor T_{NI} and the final LCEs T_g.

We required the ability to polymerise our LCE at room temperature for the following reasons. Firstly, we aim to produce LCEs with complex director geometries which we will be studied at room temperature. As there are many examples of LCEs undergoing thermally-induced complex shape changes from planar films to 3D geometries, it is evident that if such a LCE was polymerised at a temperature above or below ambient temperature, then it would adopt a 3D geometry when returned to room temperature following polymerisation. Secondly we wanted to be able to produce large films of LCE. If polymerisation was not performed at ambient temperature then polymerisation of large films would require a method by which the entirety of the cell could be uniformly heated or cooled to the required temperature.

While the Urayama group polymerise their LCE 5°C below the T_{NI} of their LCE precursor, we ideally would like to polymerise our LCE at a temperature deep in the nematic phase which would minimise the sensitivity of the nematic order parameter to fluctuations in ambient temperature. Therefore we set the target T_{NI} of the LCE precursor as ~ 35°C.

Decreases in the precursor T_{NI} caused by the inclusion of EHA could have been countered by increasing in the precursor's mol. fraction of 6OCB — essentially diluting the added EHA. However, this would have been inefficient as it would also dilute the monomeric content of the precursor, thus increasing the volume of material lost as the polymerised LCE was washed. Another monomeric component was therefore required which would, together with the rest of the components, provide the desired control over T_{NI} and T_g.

Based on the above discussion we chose our second additional LCE component to be the commonly used mesogenic crosslinking group RM82 (chemical structure given in figure 6.1). RM82 was chosen for the following reasons. Firstly, RM82 has a large (rod-like) mesogenic core consisting of three benzene rings joined by ester groups. This structure is conducive to liquid crystalline ordering and therefore could be expected to increase T_{NI} for the LCE precursor — especially if RM82 was introduced at the expense of the non-mesogenic HDDA. Secondly, RM82 features alkyl chains that are 6 carbon atoms long, and thus was expected to at least be moderately miscible with the other groups of the LCE precursor.

6.2 Methods

In chapter 5 we described how our LCEs are synthesised and how their T_gs were determined. This section contains details of additional experimental techniques used in this chapter.

6.2.1 Determining the nematic to isotropic transition temperature *via* polarising microscopy

The technique of polarising microscopy was described in the previous chapter along with descriptions of what one expects to see when studying optically anisotropic and isotropic materials. The technique can be used to identify the nematic to isotropic transition temperature (T_{NI}) of the LCE precursors by heating the materials from the nematic phase and identifying the temperature at which

the sample turns black for all sample rotations with respect to the crossed polarisers. Practically speaking, on heating the material in the vicinity of T_{NI}, one typically observes a progression of the birefringence colours from $\sim 2^{nd}$ toward 0^{th}order as seen on a Michel-Levy chart (*i.e.* colours progressing from right to left as seen in figure 5.4(b)). In this thesis we define T_{NI} as the first temperature at which a "hard boundary" between the nematic phase, where a birefringence colour is seen, and the isotropic phase, which appears black. The fact that a hard boundary is seen reflects the first order nature of the nematic to isotropic transition. In reality, for a LC mixture the nematic to isotropic phase transition occurs over a range of temperatures and so no single value for T_{NI} can accurately be attributed.

The accuracy of the T_{NI} values recorded using the microscope hotstages available were affected by the following:

- The calibration accuracy of the hotstage platinum resistance thermometers.
- The microscopy hostages used to heat the sample have holes through their centres to allow the transmission of light through the sample enabling its observation. Thus there exists a temperature gradient across the observed portion of the samples with the edges being the hottest.
- The rate at which the temperature is increased. As with DSC, a finite heating rate will always result in a thermal lag between the temperature recorded by the thermocouple and the actual temperature of the sample.

A Linkam PE 120 hotstage (Linkam Scientific Instruments) was used to heat the LCE precursors for determining their respective T_{NI}s. As well as being able to heat the samples studied above room temperature, this hotstage was capable of cooling the sample below room temperature *via* a Peltier cooling element thus enabling T_{NI}s as low as 0°C to be determined. For each test a small amount of the LCE precursor was placed between glass coverslips treated with an unrubbed PVA alignment layer. This was then placed on the hotstage and studied using a polarising microscope. Due to the temperature gradient across the observed

Table 6.1: Compositions and physical properties of the investigated and the Urayama LCEs. In each case compositions are given for the LCE precursor and the final LCE. ‡Urayama group instead used the visible light photoinitiator Irgacure 784, although MBF can also be used.

		Molecular fraction [mol%]					
	Chemical	Urayama	LCE A	LCE B	LCE C	LCE D	LCE E
LCE precursor	A6OCB	45.0	14.6 ± 0.2	27.4 ± 0.2	24.5 ± 0.6	16.5 ± 0.6	18.2 ± 0.6
	6OCB	45.0	55.9 ± 0.4	35.3 ± 0.3	37.9 ± 0.8	56.9 ± 1.0	54.7 ± 1.0
	HDDA	7.0		10.2 ± 0.3	3.8 ± 0.1		
	EHA	0.0	20.9 ± 0.2	25.6 ± 0.6	32.3 ± 0.9	21.5 ± 0.6	20.1 ± 0.5
	RM82	0.0	7.1 ± 0.1			3.6 ± 0.3	5.5 ± 0.3
	MBF	3‡	1.56 ± 0.01	1.51 ± 0.05	1.56 ± 0.15	1.58 ± 0.15	1.49 ± 0.14
Final LCE	A6OCB	81.8	33.1 ± 0.3	42.3 ± 1.3	39.4 ± 1.3	38.1 ± 1.9	40.2 ± 1.9
	6OCB						
	HDDA	12.7		15.8 ± 0.3	6.1 ± 0.2		
	EHA		47.3 ± 0.2	39.6 ± 1.3	52.0 ± 1.5	49.8 ± 2.1	44.4 ± 1.9
	RM82		16.1 ± 0.1			8.3 ± 0.8	12.1 ± 0.7
	MBF	5.5	3.53 ± 0.01	2.33 ± 0.01	2.51 ± 0.01	3.66 ± 0.01	3.29 ± 0.01
LCE precursor T_{NI} [±1°C]		~ 50 [160]	36.6	n/a	n/a	22.0	32.0
Final LCE T_g [±1°C]		50 [159]	19.0	15.1	1.9	10.2	18.7

sample portions and the fact that no single transition temperature exits for a LC mixture, we here defined T_{NI} by the first temperature at which the edges of the observed sample began to transition to the isotropic phase. In determining T_{NI}, a temperature sweep was first performed at 10°C min^{-1} to identify an initial, but imprecise, value for T_{NI} (imprecise due to the above mentioned thermal lag effects). Subsequent temperature sweeps were performed at 5°C min^{-1} and 2°C min^{-1} over narrower temperature ranges in the vicinity of T_{NI} to reduce the effects of the thermal lag and therefore improving the precision of the measured T_{NI}. Despite these steps taken to improve the precision of recorded T_{NI} values, the error on each value remains at ±1°C due to the typical calibration accuracy of the hotstage platinum resistance thermometer.

6.3 Results

6.3.1 Trends in material properties

Table 6.1 gives the compositions and properties of several key LCEs created through adaptations to the Urayama LCE. For comparison, the first column gives the composition and properties of the Urayama LCE. Table 6.1 is split into three sections. The top portion gives the mol% fractions of each component in the LCE precursor — important for understanding how the T_{NI} of the LCE precursor can be controlled. The second portion gives the mol% fractions of components forming the final LCE networks. Here we assume all monomers have been incorporated into the final network and that the washing process has completely removed all of the 6OCB and MBF. Under these assumptions we can compare the final LCE compositions against one another to see how changes in composition affects the T_g of the LCEs developed. The final section of table 6.1 gives the measured values for each LCE precursor's T_{NI} (if appropriate) and the T_g of the final LCE. Values for T_g shown here are calculated from the inflection point of the baseline step changes from heating runs performed at 20°C min^{-1} (see section 5.3). Thermal lag effects mean that these values quoted will be offset above the true value for the T_g of each LCE, and so they are only used here for comparing to one another.

By comparing columns of data presented in table 6.1 to one another we can learn a great deal about how the T_g and T_{NI} of each LCE and LCE precursor respectively are influenced by the molecular composition used. First and foremost we see that all of LCEs A-E have sub-room temperature T_gs which are all significantly lower T_g than the Urayama LCE. There is a clear trend that LCEs containing higher concentrations of EHA have lower T_gs. Additionally, by comparing LCEs A and B, we see that the introduction of RM82 causes T_g to increase.

The following discussion uses the findings of preliminary tests, the results of which are not shown.

The T_{NI} values for LCEs B and C have been denoted as n/a as for each LCE precursor, no nematic phase was detected down to 0°C. In these materials, the amount of EHA introduced has either suppressed T_{NI} to below 0°C or has completely destroyed the nematic phase, an effect anticipated for compositions which did not include the mesogenic crosslinker RM82. This loss of a room temperature nematic phase could also have in part been a result of the comparatively lower concentrations of 6OCB in the LCE precursors of LCEs B and C. However, such lower concentrations were required as higher concentrations led to a phase separations of the LCE precursor. The loss of a room temperature nematic phase in LCEs B and C also extended to to the final LCEs as each of the materials showed no optical anisotropy when studied *via* polarising microscopy. This is explored in greater detail for LCE B in the following section. While both of these materials are essentially isotropic elastomers, preliminary mechanical tests showed a strong and immediate increase in birefringence colours for these materials when mechanically stretched. This is an interesting phenomenon which is explored, for LCE B, in chapter 12. LCE B was chosen for further studying as although it had a greater T_g than LCE C, preliminary tests (not shown) indicated that LCE B could sustain greater strains than LCE C, most likely due to its greater crosslinker concentration, and was therefore more suitable for studying further. In section 6.3.2 below, the T_g of LCE B is determined more accurately (using the full method described in section 5.3) and its optical isotropy is demonstrated.

Turning back to table 6.1 and considering LCEs A, D and E we see that the introduction of RM82 in place of HDDA has resulted the maintenance of an above room temperature T_{NI}. Each LCE precursor has a comparable mol% fraction of EHA and 6OCB with the balance between A6OCB and RM82 being the primary difference. We can clearly see that the greater the concentration ratio of [RM82]:[A6OCB], the higher the T_{NI} of the LCE precursor. Additionally when comparing the final LCEs, we can see that generally, greater concentrations of RM82 (crosslinkers) results in greater values of T_g. Of the three materials, LCE A is the most attractive material for further study as it has the highest value of T_{NI} for its LCE precursor (36.6 ± 1.0°C) which is also above the target of T_{NI}= 35°C set in section 6.1.3. While the T_g of LCE A is also the greatest of all

prepared materials, the actual T_g of LCE A will be lower than the 19.0 ± 1.0°C shown in table 6.1 when thermal lag is taken into account and so will still be comfortably below room temperature.

6.3.2 Final materials for this thesis

From the above discussion we have identified LCEs A and B as promising materials for further study in this thesis. In the following chapters of this thesis the mechanical behaviours of these materials are studied in detail. Here we perform a basic characterisation of the state of order and optical appearance of both materials. Firstly, we determine accurate values for their T_g by extrapolating measured values of the inflection point to a heating rate of 0°C min^{-1} (as described in section 5.3). We then show photographs of each material demonstrating their transparency and optical quality — properties important for the production of optical devices. Lastly we study their textures *via* polarising microscopy. For LCE A we are interested in the achievable quality of monodomain alignment as this both affects the optical properties and the mechanical properties (see chapter 2). For LCE B we demonstrate the material's optical isotropy. The results presented in this section are representative of all samples of LCE A and LCE B produced and used in this thesis.

DSC for accurate T_g

Figure 6.2 (overleaf) shows DSC traces for LCEs A and B. For both samples, temperature sweeps were performed at 5, 10 and 20°C min^{-1} and in each case the marked inflection points of the glass transitions occurred at lower temperatures for scans performed at slower speeds. Following the fitting and extrapolation method described in section 5.3, final values for T_g for LCEs A and B were determined to be 14.0 ± 1.0°C and 9.4 ± 1.0°C respectively, both significantly lower than room temperature.

Photographs

Figure 6.3 (overleaf) shows photographs of films of LCEs A and B. For LCE A, the displayed film was prepared in a monodomain geometry. The photographs

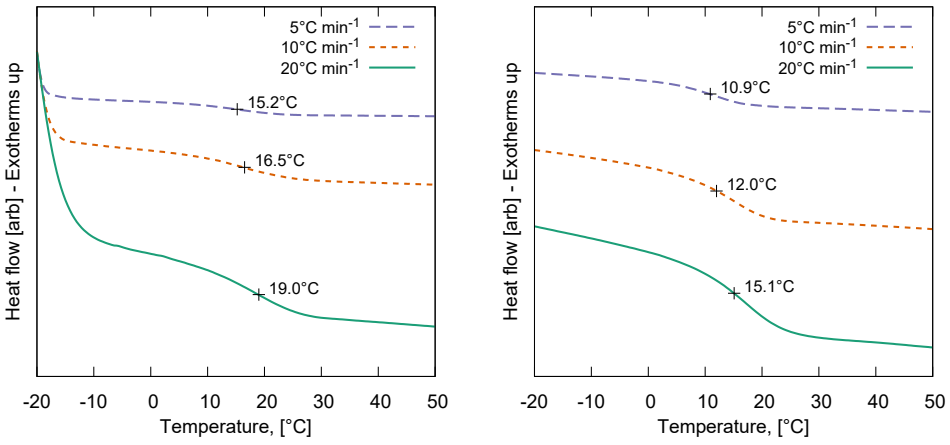

(a) (b)

Figure 6.2: DSC traces of the glass transition of a) LCE A and b) LCE B performed at 20, 10 and 5°C min^{-1}. The inflection point of each glass transition is marked on each curve. In a) the scans were performed between −20°C and +120°C. In b) the scans were performed between −50°C and +80°C.

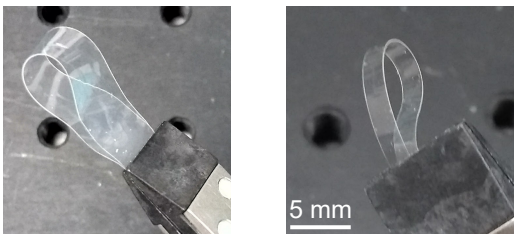

(a) (b)

Figure 6.3: Photographs of films of a) LCE A and b) LCE B held between tweezers.

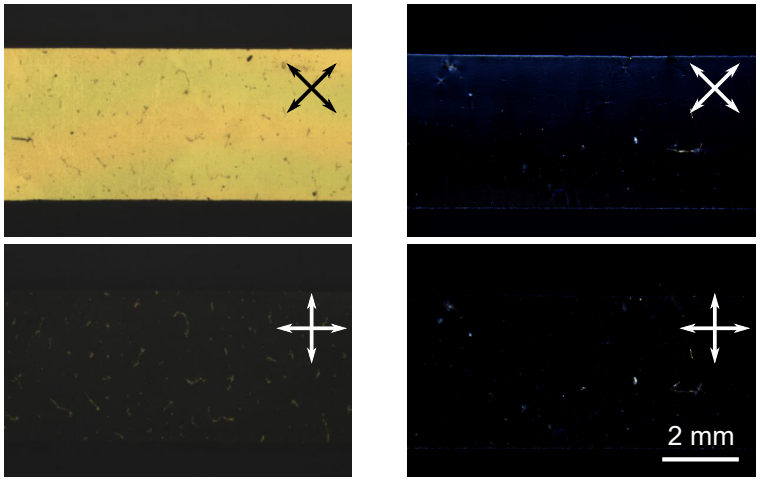

(a) (b)

Figure 6.4: Polarising microscopy photographs of a) a 95 ± 1 μm thick film of LCE A and b) a 109 ± 5 μm thick film of LCE B. Between photographs for each sample the polarisers were rotated by 45°.

show the flexibility of each material and their homogeneity. Moreover, the transparency demonstrates both materials have a high optical quality and that they do not have any porosity on length scales down to (approximately) the wavelength of light, *i.e.* ~ 400 nm, as no scattering of light is evident. This is an important point which will be revisited in chapter 8.

Polarising microscopy

Figure 6.4(a) shows a 95 ± 1 μm thick monodomain sample of LCE A prepared with the director oriented perpendicular to the long edges of the film visible. In the top and bottom images the director is respectively oriented at 45°C and 0°C relative to the polariser. The high quality of monodomain alignment achieved is demonstrated by the high contrast in transmitted light between the two images, together with the evident uniformity of the sample's appearance in both photographs. Small crystallites embedded within the LCE are visible in figure 6.4(a) and appear similar to those seen in the Urayama LCEs. [74] The precise origin of these (unintended) crystallites is unclear, however as they were present in the

un-cured monomer mixtures it seems plausible that they are caused by impurities acting as nucleation points for crystallisation of the LC monomers. Importantly, as the crystallites were present in the monomer mixtures we can assume that they do not act as physical crosslinking points of the final LCEs. The scale of these crystallites means they are not seen in the film photographs shown in figure 6.3(a) and so we assume they have a negligible effect on the optical quality of LCE A. Additionally, throughout this thesis, no detrimental effects of the crystallites on the mechanical properties of LCE are seen and they in fact prove useful for tracking localised mechanical deformations *via trackpy*.

In both of the polarising microscopy images of LCE B (figure 6.4(b)) the sample (which is 80 ± 1 μm thick) appears almost entirely black. As the polariser and analyser have been rotated by 45° between the photographs, the black appearance means that LCE B is optically isotropic. The alternative explanation of LCE B actually being nematic but with a director homeotropically aligned (*i.e.* perpendicular to the plane of the sample seen) can be discounted as a planar alignment agent was applied to the substrates of the cell used to prepare the sample. The act of placing the film of LCE B flat on a microscope slide for taking the photographs shown in figure 6.4(b) caused a slight mechanical strain to be applied to the film. In turn this caused a low level of mechanically-induced ordering and the appearance low birefringence colours. By heating the sample using a heat gun, the material was allowed to relax and the majority of the mechanically-induced ordering was removed. The remaining birefringence is seen along the top edge of the film in figure 6.4(b). In chapter 12 we explore this mechanically-induced ordering in greater detail and demonstrate that the film is essentially isotropic with the slight birefringence colours observed here being a result of localised regions of unavoidable strain.

6.4 Conclusion

In this chapter we have successfully developed a promising system of acrylate-based LCEs with sub room temperature T_gs from which we selected LCEs A and B for further study.

LCE A is a nematic LCE with a sub room glass transition and which can be synthesised in high quality monodomain geometries. This LCE thus matches all of our material requirements specified in chapter 2 and is therefore suitable for studying in this thesis.

LCE B, like LCE A, contains mesogenic components but is instead optically isotropic. From symmetry arguments we can infer than LCE B will also display isotropic mechanical properties. Indeed, LCE B is more appropriately described as an isotropic rubber rather than an LCE. However, for simplicity we will continue to refer to it as LCE B. While LCE A is of most interest to the aims of this thesis, we will also find LCE B useful in chapter 12 for exploring the potential challenges of two dimensional deformations applied to LCEs.

Considering the results of table 6.1 together, we believe that our work in this chapter is highly significant to the wider field of LCEs. While acrylate LCEs have typically been dismissed as having "high" glass transition temperatures and therefore brittle at room temperature and practically infeasible for most applications, we have shown that it is in fact relatively simple to develop a range of LCEs of varying properties, all with T_gs below room temperature. While Thomsen *et. al.* and Zeng *et. al.* have reported acrylate-based LCEs with sub-room T_gs before, the materials presented here are formed completely from commercially available starting materials and do not contain any significant concentration of non-mesogenic components in the final state. Given we have here only considered modifying the Urayama LCE with two components, we believe that by exploring combinations of the numerous other mesogenic and non-mesogenic monomers, a great variety of simple to produce, low T_g LCEs could realistically be developed. While, these materials would always be side chain end-on LCEs and therefore would not be expected to have particularly high values of the step length anisotropy, r, (see chapter 2), they would be even easier to synthesise than the acrylate-amine and thiol-acrylate LCEs developed by Ware *et. al.* and Yakacki *et. al.* [164, 176]

6. DESIGNING ACRYLATE-BASED LCES WITH LOW GLASS TRANSITION TEMPERATURES

Chapter 7

Mechanical deformations parallel and perpendicular to the director

7.1 Introduction

In the previous chapter two LCEs were identified as "interesting" from the point of view of this thesis. In particular we saw that LCE A is a nematic LCE with a T_g of $14 \pm 1°C$ and could be produced in high quality nematic monodomain geometries. However, as LCE A is a new material we must first perform a "basic" material characterisation in order to assess:

- What type of optomechanical phenomena does LCE A display?
- What is the value of the step length anisotropy, r, and how does this compare to previously reported LCEs?
- Do the basic mechanical properties of LCE A confirm its suitability for the research aims of this thesis thus justifying further research on this material?

In this chapter we use the Microscope Elastomer Stress Strain Enclosure (MESSE), detailed in chapter 5, to investigate the opto-mechanical behaviour of LCE A. By performing stress-strain experiments on strips of monodomain samples prepared with director orientations parallel and perpendicular to the applied stress axis we can assess the extent of LCE A's mechanical anisotropy. Moreover,

as we have seen in chapters 2 and 4, stressing LCEs perpendicular to the director results in highly non-linear behaviour which has previously been described by either of the the W&T theories of SSE or MFTs.

The results of this chapter will demonstrate two surprises for LCEs stressed perpendicular to the director. Firstly, we show that, paradoxically, LCE A displays hallmarks of both SSE and MFT behaviour. Secondly, we show that during mechanical deformation, LCE A passes through a state of negative LC order parameter (NOP), a highly unusual phenomena discussed in chapter 2 and which has only recently been observed and reported in LCEs. [1]

By applying both theories of SSE and MFT to our observations we determine values for the step length anisotropy, r, which we compare to a value determined from thermo-mechanical testing. The discussion section of this chapter assesses the validity of the values of r calculated and compares them to values previously reported for a range of LCEs. We also discuss the implications of the observed mechanical behaviour on the aims of this thesis and perhaps more importantly, the implications of the surprising results on the wider field of LCEs.

The contents of this chapter have been published in the paper D. Mistry *et. al.* Soft Matter (2018) **14**(8) 1301-1310. All the work of the paper was performed by myself and so this paper has largely been reproduced in this chapter.

7.2 Experimental

7.2.1 Sample preparation

Monodomain samples of LCE A were prepared in $\sim 20\times60$ mm and 100 μm thick geometries as described in Chapter 6. For mechanical testing strips were cut with 2×25 mm dimensions with length at angles of $2 \pm 1^\circ$ and $89 \pm 1^\circ$ to the director (the aim was to have samples with their long axes either effectively parallel or perpendicular to the director). The unstressed sample thicknesses were measured using a micrometer with 1 μm accuracy.

7.2.1.1 Optomechanical testing

Each sample was mechanically tested using MESSE by sequentially imposing extension steps of 5% of the LCE strips initial length and measuring the load across the sample, until failure. For both tests the sample chamber was maintained at 23 ± 2°C. At each step, photographs were taken under white light illumination along with 36 photographs taken using a crossed polariser arrangement, with the polariser and analyser rotated by 10° between each photograph. From these photographs the director angle could be determined following the procedure described in section 5.5.2. As the polarisers had to be rotated manually, the overall time taken to take a set of photos at each strain step was typically 6 minutes. During preliminary mechanical tests we observed that as one would expect, the sample stress relaxed between successive extensions. At some strain steps the stress relaxation was accompanied by a relaxation or slow change in appearance of the polarising microscopy texture. Thus for accurate measurement of the director angle, to was important to acquire the polarising microscopy photographs when the LCE was sufficiently close to stress equilibrium therefore meaning the director angle would be constant over the 6 minute window required to take all the photographs. We therefore chose to allow the sample to stress relax for two minutes following each extension before any photographs were taken. A load cell reading was taken each second during the stress relaxation phase and also when each photograph was taken.

Figure 7.1 (overleaf) shows the resultant stress relaxation curves generated from data taken at several strain steps of the 89° sample. Each curve shows an exponential-like decay in the force recorded. After two minutes the curves have somewhat plateaued indicating minimal stress relaxation. Figure 7.1(b) shows a magnified portion of the last strain step for the 89° sample during the period over which the photographs were recorded. The figure shows that the measured load across the sample is still decreasing over during the time over which photographs were taken indicating stress relaxation was still occurring. The total change over this period is ~ 0.015 N which is only 4% of the total force (~ 0.35 N) decrease shown in figure 7.1(a). While waiting longer than two minutes before

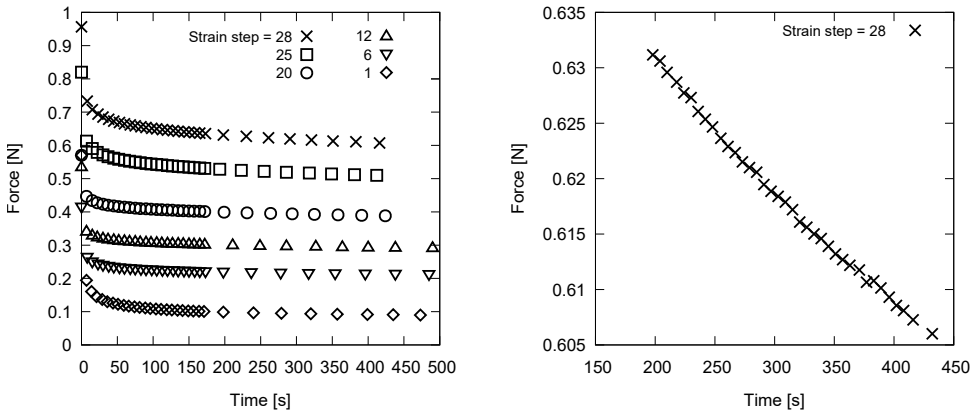

(a) (b)

Figure 7.1: a) Stress relaxation between successive extensions for selected strain steps of the 89° sample of LCE A. For clarity every five points recorded have been plotted. b) Magnified view of the stress relaxation for the last strain step (number 28) over the time period for when the polarising microscopy photographs were taken.

taking photographs would allow the gradients to further flatten, this would have been impractical from an experimental point of view because of the total time this would have added to the experiment. Therefore the gradient observed after two minutes of stress relaxation was taken as being *sufficiently* shallow to mean the sample was close enough to equilibrium to allow the polarising microscopy photographs to be recorded.

Stress-extension curves were calculated using the last load cell reading taken at each step and the photographs taken under white light illumination. The localised strain in the central portion of the films was measured using the particle tracking method described in section 5.5.2. Figure 7.2 plots the particle trajectories measured using *trackpy* on the 89° sample for unstrained and maximally strained states and demonstrates the effectiveness of the technique. In each figure the trajectories have been offset from the actual particle locations by $\sim$ 10 px such that the tracked particles can be seen. Some of the particles have been high-

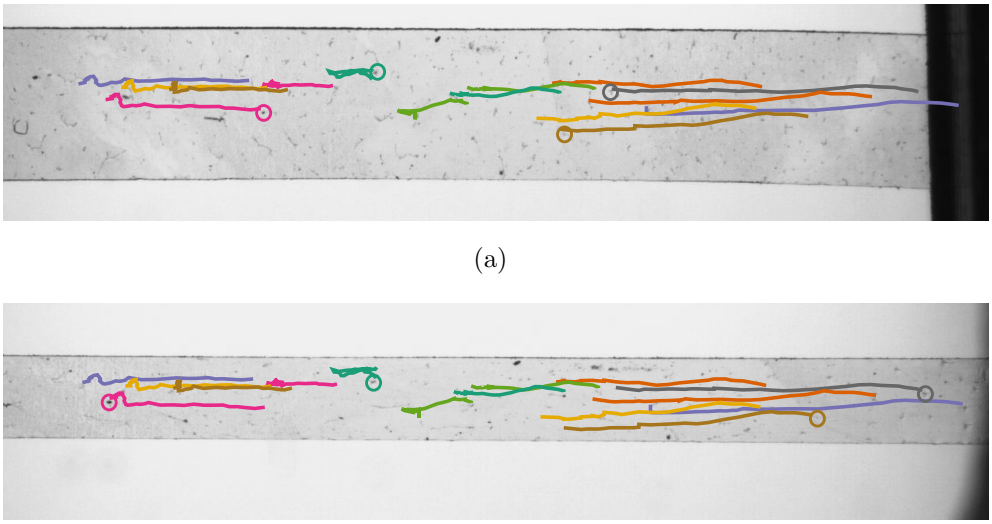

(a)

(b)

Figure 7.2: Example particle tracking trajectories measured using *trackpy* from the 89° sample. Trajectories have been overlaid onto photographs of the sample in a) unstrained and b) maximally strained states. So that the tracked particles can be seen, the trajectories have been displaced from the particles by $\sim$ 10 pixels. Selected tracked particles have been highlighted with rings.

lighted for clarity. The engineering stress was calculated at each strain step by dividing the force measured by the load cell by the initial sample cross-sectional area in the plane perpendicular to the applied stress axis.

7.2.2 Thermo-mechanical testing

Temperature-dependent changes in the sample length and birefringence were measured using a Leica DM2700 P polarising microscope equipped with a Berek compensator, a Linkam THMS600 hot stage (1°C practical accuracy) and a Nikon D7100 DSLR camera (figure 7.3 overleaf). Photographs taken were analysed using the software ImageJ (National Institutes of Health, USA). [145, 144]

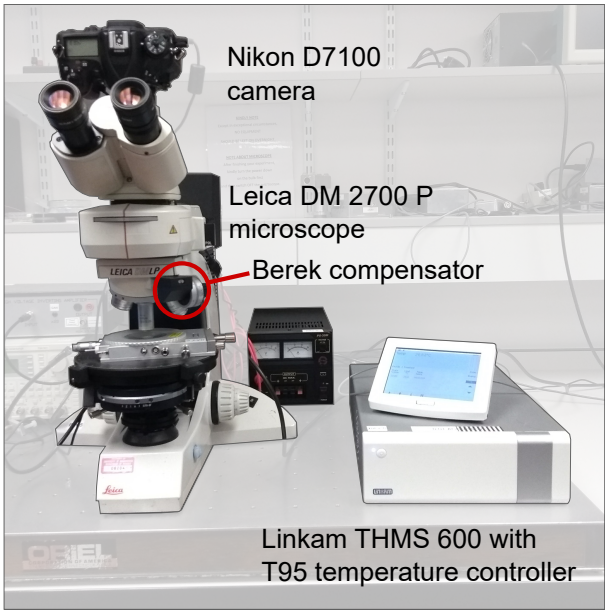

(a)

(b)

Figure 7.3: a) Polarising microscope with temperature stage and Berek compensator used for thermo-mechanical testing. b) Berek compensator use to measure optical retardance. Rutile has a negative uniaxial birefringence ($n_o > n_e$) and the crystal is cleaved with the extraordinary axis perpendicular to the exposed face seen in the picture. Rotating the dial changes the effective birefringence introduced by the crystal into the optical path of the microscope.

A Berek compensator (figure 7.3(b)) allows measurement of the optical retardance of a birefringent sample by use of a negative uniaxial birefringent sheet of crystal, in our case rutile (TiO_2), of known thickness. The rutile is cleaved with the extraordinary axis perpendicular to the face of the cleaved sheet thus under normal illumination the material appears isotropic. By rotating the dial, which tilts the crystal about the dotted axis shown in figure 7.3(b), birefringence is introduced with the fast axis parallel to the tilt axis of the crystal. By placing the Berek compensator between the crossed polarisers at 45° relative to the polariser and at 90° relative to the LCE director (if $n_e > n_o$ for the LCE), the birefringence induced by the compensator opposes that of the LCE film. The crystal is then

rotated in one direction, increasing the tilt angle, until a particular angle, α_1, is reached where the retardance induced by the rutile crystal is equal to that of the sample and a black fringe is observed by through the microscope eyepiece. By tilting the rutile sheet in the opposite direction a second black fringe at α_2 can be found. For measuring high retardances, the use of quasi-monochromatic light is recommended to aid the location of the black fringes.

The retardance of the sample $\Gamma = \Delta n \times d$ (where Δn is the birefringence of the LCE and d is the sample thickness) is then calculated from the average angle α_{avg} of α_1 and α_2 using

$$\Gamma = n_{Xo} d_X \times \left(\sqrt{1 - \frac{\sin^2(\alpha_{avg})}{n_{Xo}^2}} - \sqrt{1 - \frac{\sin^2(\alpha_{avg})}{n_{Xe}^2}} \right), \tag{7.1}$$

where n_{Xo} and n_{Xe} are the ordinary and extraordinary refractive indices of the rutile sheet for the central wavelength of light used and d_X is the thickness of the rutile sheet. All three of these quantities are taken from the compensator data sheet.

Dividing the retardance by sample thickness gave the LCE birefringence which in turn is related to the LC order parameter. Prior to thermal testing, the sample thickness was measured using a micrometer with 1 μm accuracy. The thickness at each temperature step was deduced by dividing the initial thickness by the fractional changes in sample length and width (measured in ImageJ), assuming a constant sample volume. [169]

7.3 Theory

We recall from chapters 2 and 4 that the step length anisotropy, r, is possibly the most important characteristic quantity of LCEs. Therefore determining the value of r for LCE A is the natural place from which to centre our characterisation. From the results of tensile mechanical testing performed in this chapter we will see that the mechanical behaviour shows hallmarks of both SSE and MFT, a paradox discussed in section 7.5. We therefore can use equations derived in chapter 4 to

determine values for r from both theories of SSE and MFT in addition to the theory behind the thermo-mechanical behaviour of LCEs.

Semi-soft elasticity. From the theory of SSE we recall from equation 4.40 that r can be determined from the ratio of the two critical strains, λ_1 and λ_2 present in a SSE load curve (figure 4.4 on page 63), [169]

$$r = \left(\frac{\lambda_2}{\lambda_1}\right)^2. \qquad \text{(4.40 revisited)}$$

We also recall that a second characteristic of SSE is that in the plateau-like region of the load curve (region II of figure 4.4 on page 63) the director gradually rotates from being perpendicular to parallel to the stress axis.

"Mechanical Fréedericksz transition" According to the theory of MFTs the director, by contrast, remains perpendicular to the stress axis until a single critical deformation, λ_c at which it suddenly rotates to be parallel to the stress axis. Recalling equations 4.27 and 4.28 we can determine upper and lower bounds on values of r from this critical deformation [169]

$$2r - \lambda_c^3\sqrt{r} - \lambda_c^3 = 0, \qquad \text{(4.27 revisited)}$$

or, at the very latest by [15]

$$r = \lambda_m^3. \qquad \text{(4.28 revisited)}$$

We note here that the theory of MFTs (as with the theory of SSE) assumes a constant LC order parameter throughout the deformation process.

Thermo-mechanical deformation. We also saw in chapter 4 that the thermally-induced length change of a LCE can also be used to determine r. Briefly, on heating from the nematic to the isotropic phase, a LCE with a prolate polymer conformation contracts along its director from its initial length L_0 to its final length $L = {}^{L_0}/_{\lambda_m}$. [169] In the isotropic phase $\underline{\underline{\mathbf{l}}} = \underline{\underline{\boldsymbol{\delta}}}$, the Kronecker delta, and hence $r = 1$. Using this, one can derive 4.21 which shows [169]

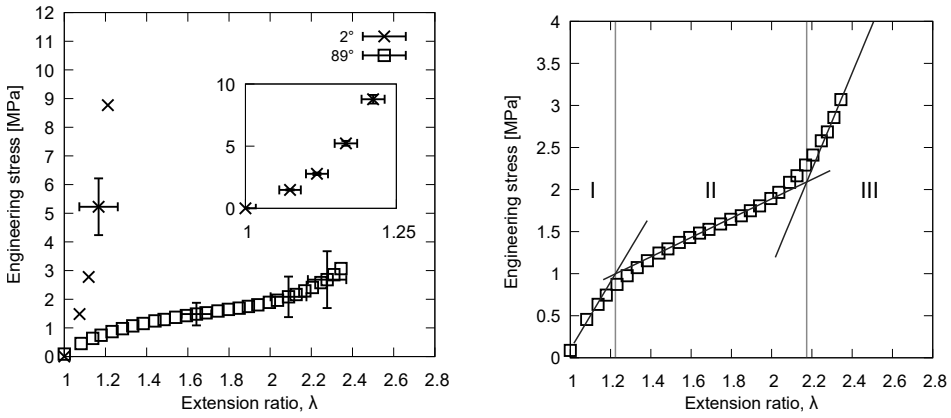

(a) (b)

Figure 7.4: a) Tensile load data for LCE A stressed at 89° and 2° to the director. In the main figure the representative error bars have been enlarged by a factor of 5 for clarity. The inset reproduces the data for the 2° sample (with unscaled error bars) to highlight the non-linearity of the data. b) 89° curve is replotted showing the SSE-like non-linearity of the curve. The extensions at which the fitted lines cross can be used to calculate a value of r from the theory of SSE.

$$r = \lambda_m^3. \qquad \text{(4.21 revisited)}$$

This last method for determining r is the simplest from a theoretical point of view and so arguably gives the most robust value of r.

7.4 Results

In order to better discuss the results of mechanical tests in context with one another, we first present the data and then move to a detailed discussion.

7.4.1 Tensile load testing

Figure 7.4 shows the load curves for the LCE stressed at 2° and 89° to the director. The significantly different shape of the two load curves clearly demonstrates the mechanical anisotropy of the LCE. The initial moduli (from linear curves fitted

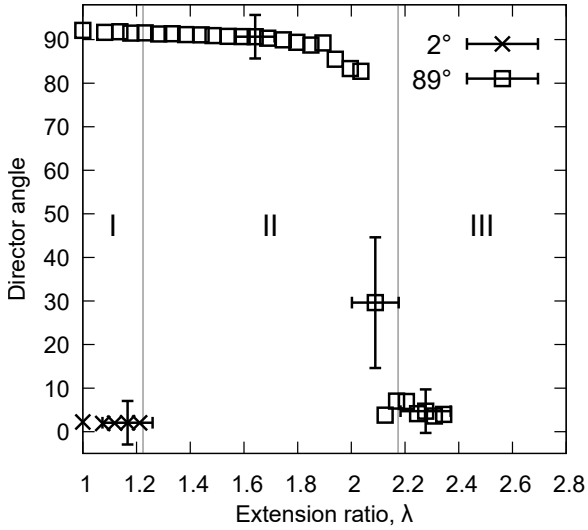

Figure 7.5: Director angle measurements for each sample at each strain step. Representation error bars have been enlarged by a factor of 5 for clarity. The vertical lines correspond to the critical extensions deduced from figure 7.4(b).

to low strain data) and extension-at-failure were measured to be 23 ± 2 MPa and 1.21 respectively for the 2° sample and 4.0 ± 0.2 MPa and 2.34 for the 89° sample. The inset of figure 7.4(a) shows, perhaps surprisingly, that the 2° load curve is somewhat non-linear. Over this relatively small extension ratio we had expected to observe a linear load curve. This was because the stress was applied at close to parallel to the long axis of the polymer conformation and so the non-linear effects of polymer conformation rotation should be minimal. Therefore the material was expected to have an isotropic response. We are left to conclude that 2° offset from perfectly parallel orientation is sufficient to cause the small non-linearity observed.

The 89° load curve has been replotted in figure 7.4(b) to clearly show its highly non-linear shape. The three distinct regions of moduli of 4.0, 1.2 and 5.7 MPa gives the load curve the typical shape of SSE. [169] The intercepts of the fitted lines gives the two critical extension ratios, $\lambda_1 = 1.22 \pm 0.03$ and $\lambda_2 = 2.17 \pm 0.10$. Using equation 4.40 we find a step length anisotropy of, $r = 3.2 \pm 0.4$.

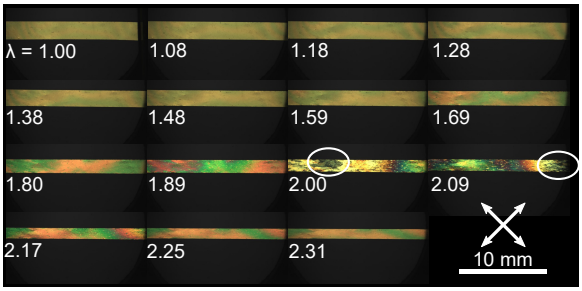

Figure 7.6: Polarising microscopy images of the 89° sample for various deformations. Circled regions in the $\lambda = 2.00$ and 2.09 highlight regions of near-zero retardance.

7.4.2 Optical tracking of the director

Figure 7.5 shows the director angle at each strain step as determined from the polarising microscopy photographs for both the 2° and 89° samples. The sample initially at 89° maintains a relatively constant director angle until $\lambda \sim 1.9$ at which point it begins to rotate before sharply rotating at $\lambda_c = 2.1$ to an orientation almost parallel to the stress axis. Such behaviour is indicative of the MFT behaviour reported by Mitchell, Roberts and co-workers. [111, 132, 133] Inserting the critical value of $\lambda_c = 2.1$ into equations 4.27 and 4.28 gives another set of possible values for the upper and lower bounds on the value of the step length anisotropy: $9.3 < r < 30$. It should be noted that equation 4.27 gives two roots for the value of r, 0.7 and 30. The solution of $r = 0.7$ is discarded as the LCE contracts parallel to the director on heating (shown later in figure 7.8 on page 121) and so the polymer conformation must be prolate and hence $r > 1$.

7.4.3 Qualitative determination of the nematic order

Figure 7.6 shows polarising microscopy images of the 89° sample during mechanical testing. The sequence shows a significant change in the birefringence colours as the imposed extension was increased. For the first of the photographs ($\lambda = 1.00$), it is known that the sample was 99 μm thick with a birefringence of 0.12 and hence a retardance of 11,880nm (approximately 20^{th} order). The increasing saturation of birefringence colours as the sample is strained indicates

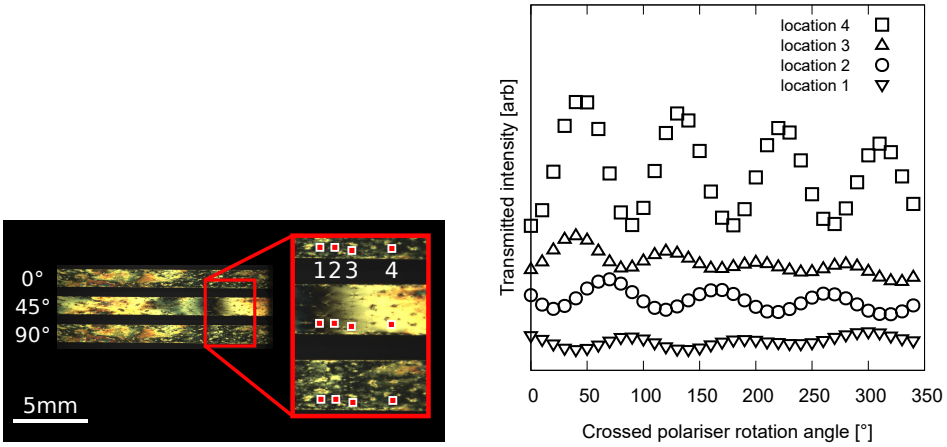

(a) (b)

Figure 7.7: a) Polarising microscopy images from the sample at $\lambda = 2.04$ with the polariser at 0°, 45° and 90° to stress axis. The transmitted intensity as a function of polariser rotation angle is plotted in b) for the four shaded 30×30 regions shown in the magnified portion of a). For clarity the baseline of each curve in b) has been shifted to separate the curves.

that the retardance is decreasing (see section 5.4.3). Indeed the images taken at $\lambda = 2.00$ and 2.09 have first order birefringence colours implying retardances of $0 < \Gamma < 600$ nm.

Figure 7.7(a) show the sample at $\lambda = 2.04$ with the polariser at angles of 0°, 45° and 90° to the director. Each photograph has a common region which appears black, indicative of zero retardance, *i.e.* an effectively isotropic region. Figure 7.7(b) plots the transmitted intensity in the four locations marked in figure 7.7(a) as the crossed polarisers were rotated. For clarity the baselines of the curves have been shifted to vertically separate the curves. The transmission plots show a decreasing amplitude of intensity variation near the dark regions of the sample. This observation is consistent with a near-zero retardance in the 'black' regions of the sample.

As the extension is increased beyond λ_c, we see from the birefringence colours

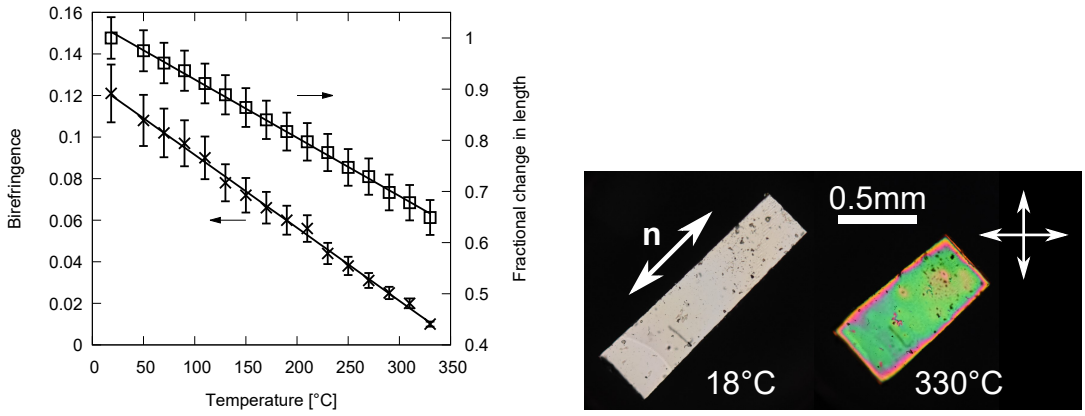

(a) (b)

Figure 7.8: a) Fractional length change and birefringence of LCE A as it is heated from 18° to 330°. For clarity errors have been enlarged by a factor of 5. b) Corresponding polarising microscopy images of the sample at 18° and 330°. The director orientation shown is common to both images. Photographs taken using a 10× objective.

of figure 7.6 that the retardance, and hence LC order parameter and step length anisotropy, increase.

7.4.4 Thermal testing

Figure 7.8 shows the fractional length change (relative to room temperature) and birefringence of the LCE as it is heated from 18°C to 330°C along with polarising microscopy images of the sample at 18°C and 330°C. Both the LCE fractional length change and the birefringence show effectively linear relationships with temperature and decrease by 1.13 % $^{\circ}C^{-1}$ and 3.5×10^{-2} $^{\circ}C^{-1}$ respectively. When a LCE sample reaches the isotropic phase, a reduction in the LC order parameter to zero, visible through a reduction in birefringence to zero, would be expected. [156, 94, 29] As we do not record a zero birefringence by 330°C, this zero birefringence state must either occur at a temperature greater than 330°C, or the presence of rod-like crosslinkers has removed the possibility of a zero birefringence state (isotropic phase) being attainable. [162] Heating the sample beyond

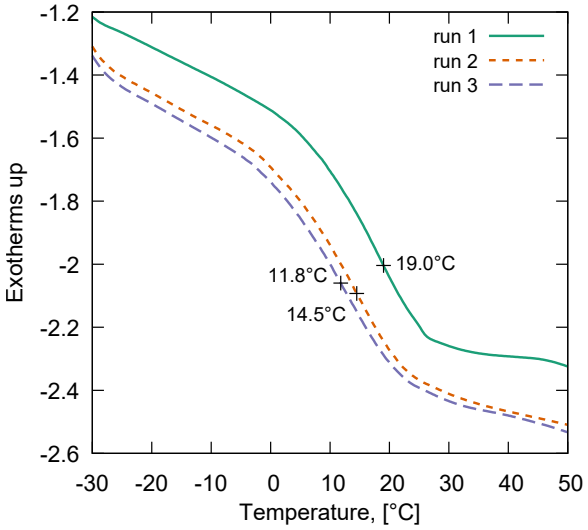

Figure 7.9: DSC curves of the glass transition of LCE A showing the effects of thermal degradation. Each run cycled a sample of LCE A between −40°C and 330°C at 20°C min^{-1}. After the first and second runs thermal degradation caused a shift in the glass transition temperature to lower temperatures.

330°C would not have made sense as our DSC results showed that by heating to 330°C, the LCE had begun to thermally degrade as seen through a slight change in the position of the inflection point of the glass transition (figure 7.9). Upon first heating to 330°C the inflection point decreased from 19°C to 14.5°C with a further decrease to 11.8°C after a second cycle to 330°C. As we did not heat the sample higher than 330°C in an attempt to observe the nematic to isotropic transition *via* the associated decline in sample birefringence to zero, we are left having to infer a reasonable value for the effective sample length in the isotropic phase in order to determine a value for r.

We start by establishing reasonable limits on the value T_{NI} and taking into consideration the effects of thermal degradation. The lowest temperature at which the isotropic phase could begin is 330°C. An upper limit for the start of the isotropic phase can be determined as 361°C, the point at which the extrapolated birefringence in figure 7.8(a) reaches zero. For the purposes of calculating r, we therefore take the nematic to isotropic transition temperature (T_{NI}) as the mid-

point between 330 and 361°C and use an uncertainty of ±15°C to reflect this range, hence T_{NI}= 345 ± 15°C. Thermal degradation of the LCE in this experiment would also cause further errors in this temperature. However, its effects were taken as acceptably small for the following reasons. Firstly, in the thermal degradation tests performed using DSC, the shift in the glass transition inflection point by 7.2°C occurred only after the sample had been maintained at over 200°C (an approximate temperature above which one may expect thermal changes to begin) for 45 minutes. By comparison, the sample tested for the data shown in figure 7.8 was tested on a microscopy hotstage and was maintained at over 200°C for less than 15 minutes. Any thermal degradation effects are therefore small by comparison. Secondly, the data for both curves shown in figure 7.8(a) show no apparent change in gradient at any point and therefore it is unlikely that any significant changes are occurring in the material on the time-scale of the experiments. Bearing the above in mind, we can safely assume that the thermal effects would have resulted in a maximum additional error of 10°C for T_{NI}. Combining the two uncertainties gives a final value of T_{NI}= 345 ± 20°C.

Since the birefringence and the step length anisotropy, r, are both related to the LC order parameter we can predict that if $\Delta n = 0$ at 345 ± 20°C, then similarly $r = 1$ at that temperature. A linear fit to the fractional change in sample length extrapolated to 345°C gives the fractional change between 18°C and 345°C, $L_{18}/L_{ISO} = \lambda_m = 1.56 \pm 0.06$. By using equation 4.21 and fully propagating the errors, we arrive at a final value of $r = \lambda_m^3 = 3.8 \pm 0.5$.

7.5 Discussion

At a first glance, the results presented above have produced two similar values for r and one significantly larger with the total range of values spanning an order of magnitude. Previous reports by several researchers have found relatively good agreement between several methods for calculating r. For instance Clarke *et. al.* found agreement between values of r calculated from thermal tests, the position of the SSE plateau and neutron scattering data for a range of polysiloxane-based

LCEs. [29] Further, Mitchell, Roberts and co-workers found agreement in the values of r calculated from MFT theory and Wide Angle X-ray Scattering (WAXS) experiments. [111, 132] However, here we have found significant disagreement, the reasons for which are explored in the following discussion.

First let us consider figures 7.4(b) and 7.5 together. The load curve in figure 7.4(b) has the characteristics of SSE. According to the SSE theory, such a load curve requires a gradual and continuous director rotation between λ_1 and λ_2. [169] However, as we see from figure 7.5, the director rotation for our LCE is consistent with a MFT occurring close to the boundary between regions II and III of the load curve. We know of no other reports of the load curve for an LCE displaying a MFT. The similarity in the appearance of the load curve to load curves of samples known to display SSE is highly significant as in recent years a load curve of such a shape is taken as being indicative of SSE. [169, 29, 166] We therefore suggest that the shape of the load curve cannot solely be used to determine either the mode of deformation or key parameters of LCEs such as r. Instead one must also consider how the director reorients with mechanical deformation.

Since the form of the director orientation curve (figure 7.5) suggests the deformation mode of this LCE is a MFT and not SSE, the value of $r = 3.2 \pm 0.4$ calculated from equation 4.40 must be discarded. This is despite its similarity to the value of $r = 3.8 \pm 0.5$ deduced from thermal tests.

In their experiments Mitchell et al. found a critical extension $\lambda_c = 1.13$. Applying equations 4.27 and 4.28 to their data gives in a narrow range of values of r, $1.4 < r < 1.6$ which is in agreement with the value they found from neutron scattering experiments. [111] However, in our work the comparatively large critical extension ratio of $\lambda_c = 2.1$, coupled with the form of equations 4.27 and 4.28 means a large range of values for r has been calculated which does little to provide a precise or accurate value for r. From this result alone it is therefore difficult for us to comment on the validity of this model when applied to the present LCE.

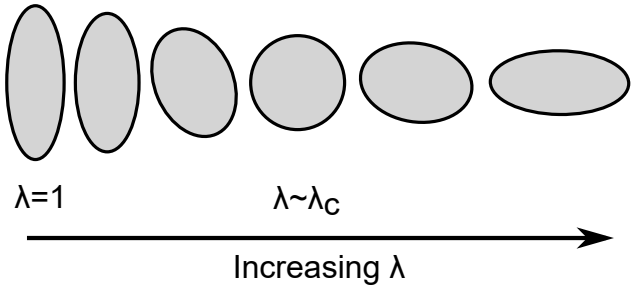

Figure 7.10: Diagram of the deduced evolution of the polymer conformation in the plane of the sample initially oriented at 89°

The observations in figures 7.6 and 7.7(a) of regions of near-zero retardance when the sample is extended close to λ_c is particularly interesting. As the sample began with a thickness of 99 μm the thickness must have remained ∼tens of microns thick at all stages of the extension. Therefore, the observation of a near zero retardance around λ_c corresponds to LCE going through a state of near-zero birefringence and hence of near-zero LC ordering within the image plane. Observations by Finkelmann *et. al.* can in part account for this behaviour. In their work they showed that if director rotation is prohibited when a LCE strained perpendicular to the director, then both the liquid crystal order and step length tensors will have to some degree become biaxial. [47] In our samples, the mechanical introduction of biaxiality has resulted in an effective lowering of the order parameter within the image plane and hence is responsible for the observation of a retardance which decreases to zero. Given the intimate link between LC order and the shape of the polymer conformation, the state of zero LC ordering within the image plane similarly translates to a near-circular polymer conformation within the image plane (as illustrated in figure 7.10). While we note that the above results provide no insight into the degree LC ordering in the plane perpendicular to the stress axis, it is reasonable to expect that throughout the deformation the sample will have become thinner through the sample extension (this deduction is verified in the following chapter). As a result the polymer conformation will have contracted in the direction perpendicular to the image plane. By the time $\lambda \sim \lambda_c$, where "black regions" are observed in figures 7.6 and 7.7(a), the polymer conformation would have become oblate.

The above observations must mean that at λ_c the sample has a negative LC order parameter (NOP) for the following reason: At λ_c, there is zero correlation and hence zero ordering between the LC molecules within the image plane (hence observation of zero retardance). Despite this, the thinning of the polymer conformation perpendicular to the image plane with strain will have confined the long axes of the LC molecules to the image plane. The symmetry of this arrangement of LC molecules corresponds to a NOP. [1] This state of ordering is physically unachievable for the majority of LC systems and is therefore rarely reported. Moreover we will see in the following chapter how this observation of a NOP has even greater significance as it coincides with the emergence of a new material property for LCEs - "auxeticity". Therefore further analysis and discussion of the negative order parameter state is reserved for the following chapter.

The implications of the above discussions taken together with the director orientation data from figure 7.5 indicates that neither theories of SSE or MFTs are completely appropriate for describing the deformation of the present LCE. Both theories assume a constant LC order parameter and hence constant value for r. As a result, equations 4.40, 4.27 and 4.28 cannot be reliably applied to the deformation of this LCE and our calculated values of $9.3 < r < 30$ must (for now) also be disregarded. The evident deformation of the polymer conformation does however demonstrate that the deformation process is not as discontinuous as figure 7.5 would suggest but instead behaves as shown in figure 7.10.

The question of a changing order parameter during the mechanical deformation of an LCE was explored by Mitchell, Roberts and co-workers. In one paper they saw a decrease in the LC order parameter, but concluded that the sample was spatially inhomogeneous near λ_c and the measurement of a reduced order parameter was an artefact of their WAXS measurements averaging over domains of different director orientation. When a pinhole was used to measure the order parameter over a smaller area, the decrease in the order parameter was only 10%. [132] In two other papers they reported neutron scattering and WAXS data which showed an unambiguous decrease in the nematic order parameter and therefore a decrease in the polymer conformation anisotropy between $\lambda = 0$ and

$\lambda = \lambda_c$. [111, 133] However, in both cases the calculation of r using equation 4.28 was sufficiently close to values obtained from direct measurements of r from neutron scattering data that the authors concluded that the MFT theory accurately described their results. A later paper from the same group does describe the MFT process as involving a change of r with a spherical polymer conformation being adopted at the MFT (no mention of the LC order parameter was made). [76] This is a similar conclusion to ours except the authors had not considered the effects of the LCE film thinning in the "thickness" direction during the deformation. As argued above this thinning must lead to an oblate polymer and would not allow a spherical polymer conformation to occur.

From our observations we would suggest that the deformation of the polymer conformation and reduction of the LC order parameter has a lower energy cost compared to the sharp director rotation described by a MFT. This process would give the same director reorientation appearance as an MFT but involves a change in r and the LC order parameter with deformation. As such, theory must take into account the changing order parameter.

The above discussion leads to us discounting values of r calculated for this material from optomechanical testing as the underlying theory assumes a constant order parameter. We are therefore left with $r = 3.8 \pm 0.5$ as the most reliable value. We can perhaps say that this value is reasonable since the physical process involved and theory behind it is comparatively simple compared to that describing the mechanical behaviour of LCEs, albeit we have still had to make assumptions in order to calculate this value.

Table 7.1 (overleaf) compares our value of $r = 3.8 \pm 0.5$ to values measured for other LCEs either reported or calculated by us using equations 4.28 or 4.21 from data contained within existing literature. The last column of table 7.1 gives details of how the mesogenic groups of each LCE are incorporated into the polymer backbone (see figure 2.9 on page 31 for schematic representations). LCE A consists of solely acrylate monomers and the LC-backbone coupling is entirely side chain end on. From table 3 we see that the value of $r = 3.8 \pm 0.5$ for our material

Table 7.1: Step length anisotropies, r, taken from the literature for various other LCEs

Reference	r	LC-backbone coupling type	Additional information
LCE A	3.8	Side chain, end-on	From thermal testing and equation 4.21
Mitchell (1993)[111]	1.3 and 1.4	Side chain, end-on	Values respectively from neutron scattering and mechanical test and equation 4.28
Tamashima (2016)[154]	~ 2.0	Side chain, end-on	From thermal testing and equation 4.21
Brömmel (2012)[22]	< 2.25	Side chain, end-on	Book chapter. Values based on SANS from refs. [118] and [119]
Brömmel (2012)[22]	< 25	Side chain, side-on	Book chapter. Values based on SANS from refs. [118] and [119]
Tajbakhsh (2001)[152]	~ 43	Majority main chain, some side chain	From thermal testing and equation 4.21
D'Allest (1988)[31]	≤ 60	Main chain	From SANS on a main-chain LC polymer

is comparable to the upper range of values seen for similar materials (first three rows of table 7.1). Of particular interest is the value of $r = 2.0$ calculated from data from Tamashima et al. (2016) as this is for the LCE described by Urayama et al. (2005) which contains the same primary monofunctional mesogenic group, A6OCB. [22, 154] Comparatively, values for r from side-on, side chain and main chain LCEs are far greater (≥ 25) as would be expected given their stronger LC-backbone coupling.

7.6 Conclusion

Although the aim of this chapter was to perform a basic mechanical characterisation of LCE A in order to assess its suitability for continued study in this thesis, the results go much further and have significant implications for the wider LCE field.

Considering first how the results relate to the aims of this thesis, we note two things:

- LCE A shows mechanical anisotropy in terms of its moduli, non-linearity and strain-at-failure. Together, with the thermo-mechanical actuation seen, these results mean that LCE A is indeed a Liquid Crystal Elastomer with significant levels of anisotropy which justifies further study toward the aims of this thesis.

- The moduli displayed have ∼MPa magnitudes. Given the fact that the crystalline lens itself has a modulus of 10 Pa – 100 kPa, LCE A would not ultimately be suitable for use in a final device. [73, 171]

On balance, as LCEs with ∼kPa moduli have been reported in the past, we do not believe the second of these points rules out the eventual feasibility of the proposed device as it seems realistic an appropriate material can be developed. In terms of our work, LCE A is still a facile material to synthesise and work with. Therefore in this thesis we can make significant progress using LCE A to demonstrate how the mechanical anisotropy of LCEs can be utilized to program

the deformations in AIOL and similar complex devices.

Turning to the implications of the results of this chapter to the wider LCE field; the key findings of our work are that:

- A characteristic load curve shape such as is shown in figure 7.4(b) on page 117 is not necessarily indicative of semi-soft elasticity as is currently accepted by the majority of the field.
- One cannot assume in a theoretical model of LCE deformation that the LC order parameter and r remains constant.
- It is possible to obtain a NOP state through mechanical deformation of a LCE.

While the theories of Warner, Terentjev and co-workers have described many observations of LCEs with great success, our data suggest that the story is not yet complete. Indeed our results from simultaneous mechanical and opto-mechanical tests have shown for the first time behaviours which are incompatible with both theories of SSE and MFTs, though these currently offer the best theoretical description of LCEs. A theoretical model for this new category, that explains why the material here shows a SSE-like load curve but has an apparent MFT-like director re-orientation, may also be answer the question of why some materials show SSE and others show MFT-like behaviour.

Our results also highlight the importance of measuring both the LC order and tensile properties simultaneously when characterising an LCE. If we had only tested the tensile load characteristics of LCE A, we would incorrectly concluded that the behaviour conformed to that described by SSE and would have calculated an inaccurate value of r.

We finish by noting that although the results of this chapter have led us to conclude that $r = 3.8$, results from chapters 8 and 10 will calculate several values of $r \sim 9$ therefore casting doubt on the conclusion of this chapter. Thus this conclusion will be revisited in the coming chapters.

Chapter 8

Coincident negative Poisson's ratio and negative LC order parameter

8.1 Introduction

In the previous chapter we sought to identify a category for LCE A based on the mechanical behaviour observed response to stresses applied perpendicular to the director. In this chapter we now begin to turn to the geometrical changes of LCE A. We restrict ourselves here to consider stresses applied perpendicular to the director as we report and investigate in detail a new mechanical phenomena of LCEs — negative Poisson's ratio or "auxeticity". Such behaviour has in the past been predicted for nematic LCEs by Warner and Terentjev and for smectic C LCEs by Brown and Adams but either case has never been observed experimentally. [169, 24]

The theoretical speculations of W&T for the strains at which auxeticity may occur in a nematic LCE are an extension of their theory of MFTs and offers another independent calculation of r which agrees with 9.3, the lower bound of r deduced from MFT theory in the previous chapter.

We see that the emergence of auxeticity coincides with the NOP state reported in the previous chapter. Thus in this chapter we study the NOP state in greater

detail in an attempt to understand extent the two curious behaviours of NOP and auxeticity are linked. Interestingly by applying W&T theory to the NOP state, under the assumption any change in the nematic free energy is negligible, we are able to deduce another independent calculate of r which again agrees well with the previously deduced value of 9.3. The significance and implications of these results is discussed in detail.

Beyond being an academic curiosity, our observation of auxetic behaviour in LCE A has much wider potential impact for applications of LCEs and materials science. This is because the auxeticity of LCE A must be an inherent material property as, unlike all existing synthetic auxetic materials, LCE A has zero porosity. Thus LCE A is the first example of a "synthetic molecular auxetic" — something which has been a long-standing goal for the auxetics community. [41, 40, 70, 4, 110] This chapter starts with an introduction to Poisson's ratio and a brief review of auxeticity. From this, the significance of the results presented in this chapter can be understood.

The research of this chapter was performed by myself with the exceptions of the acquisition of Scanning Electron Microscope (SEM) and and Atomic Force Microscope (AFM) images (shown in figure 8.4) which were acquired by Mr. Stuart Micklethwaite (Leeds) and Dr. Simon Connell (Leeds) respectively.

8.2 Poisson's ratio and "auxeticity"

Poisson's ratio, denoted by ν, is an elastic constant of materials defined by the negative ratio of the strains perpendicular and parallel to an applied stress. For isotropic and volume conserving (bulk modulus, $K = \infty$) materials, Poisson's ratio is equal to 0.5. In such materials a deformation of λ applied parallel to the stress axis will be accompanied by a contraction by a factor of $1/\sqrt{\lambda}$ along each of the transverse axes (previously illustrated in figure 4.2 on page 53). If an isotropic material instead has a finite bulk modulus then Poisson's ratio can take values of between $-1 < \nu < 0.5$. [41, 98] A typical isotropic rubber material has a Poisson's ratio of 0.499, a result of their bulk modulus, which is typically

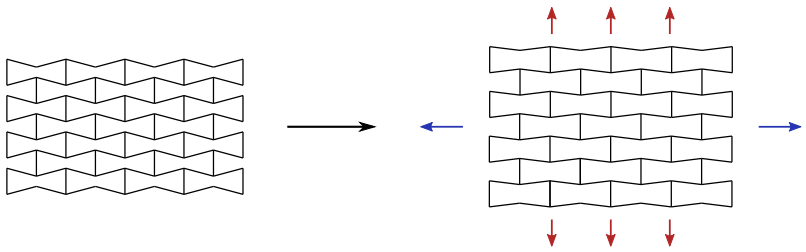

Figure 8.1: Simplistic model of a 2D auxetic structure based on a re-entract honeycomb geometry. Stresses applied in either of the principal directions cause a lateral expansion hence giving a material with this structure a negative Poisson's ratio.

around ∼GPa, being several orders of magnitude greater than their shear modulus. [55] Rubbers are therefore frequently assumed to be incompressible and volume conserving. [79, 114] In the case of anisotropic materials, Poisson's ratio is theoretically unbounded even for volume conserving materials. [41, 98] Such materials also have six Poisson's ratios depending on the axis along which the stress is applied and the transverse axis which the strain is measured along. In general, for a stress applied along the i^{th} axis

$$\nu_{ij} = -\frac{\epsilon_j}{\epsilon_i}, \tag{8.1}$$

where ϵ_i and ϵ_j are the strains along the i^{th} and the transverse j^{th} axis respectively.

"Auxetic" materials have negative Poisson's ratios meaning they counter-intuitively expand rather than contract in directions perpendicular to an applied stretch. [41, 63] Possibly the most simple illustration of an auxetic structure is the "2D re-entrant honeycomb" structure shown in figure 8.1. In this system a strain in a one direction causes the unfolding of the collapsed "cells" leading to a transverse expansion and thus a negative Poisson's ratio. Similar structures can be replicated in 3D geometries to give 3D auxetic materials which expand in both transverse directions in response to an applied stress. [80]

8. COINCIDENT NEGATIVE POISSON'S RATIO AND NEGATIVE LC ORDER PARAMETER

The use of a porous geometry in auxetic materials is a common feature of materials with proven negative Poisson's ratios. Crucially it is the porous geometries of existing materials that give rise to the auxeticity as opposed to the specific properties of the constituent material(s) which in fact have positive Poisson's ratio. [40, 140]

The porosity of existing auxetics causes two practical limitations. Firstly, porosity significantly weakens the material compared to its bulk form. Secondly the porous geometry must to engineered either by complex material processing or by use of additive manufacturing techniques. [40, 100, 80, 70, 128, 30]

Despite the above limitations, auxetics have been the subject of a vast body of research as they are expected to have several enhanced physical properties over conventional materials such as indentation resistance, fracture toughness, shear resistance and energy absorption. [4, 80]

A long-standing goal for the auxetics community has been the development of "synthetic molecular auxetic" materials that inherently have negative Poisson's ratios as their bulk material property. [41, 40, 70, 4, 110] Such materials would avoid porosity-weakening and their very existence would imply chemical tuneability *via* variations in the molecular composition or chemical structures. [41, 128, 69] Over the years several synthetic materials have been proposed and simulated to display molecular auxeticity, however in practice the materials have either been too difficult to synthesise or have not been measured to have a negative Poisson's ratio. [100, 70, 128] Arguably the most promising class of synthetic materials for displaying molecular auxeticity are LC polymers (LCPs) and LCEs. It has been suggested that in these systems an applied strain will cause a rotation of the mesogenic rods to a direction perpendicular to the polymer backbone (and hence applied strain) causing an increase in the inter-chain separation manifested on a macroscopic scale as a negative Poisson's ratio. [69] Polymeric molecular auxetics such as these are particularly attractive as they could readily be tuned, using copolymers composed of various combinations of LC and non-LC monomers. Simulations of several LCPs by Aldred *et. al.* predicted the success of such an

approach for a main chain LCP. [5] Experiments by Griffin and co-workers on polydomain LCPs and LCEs measured an increase in inter-chain separation via X-ray diffraction. [70, 69, 71, 131] However, crucially in all cases their materials always displayed positive Poisson's ratios hence the auxeticity of their materials remained unconfirmed.

8.3 Theory

8.3.1 Strain-dependent Poisson's ratio

The definition of Poisson's ratio given in equation given in equation 8.1 is valid only in the limit of strains tending toward zero. At strains greater than zero the fact that the sample has changed length from its unstrained state must be taken into account. In this chapter we observe Poisson's ratio to change with strain and auxetic behaviour to emerge at a finite strain. We can derive an expression for the strain-dependent Poisson's ratio by following and the method used by Caddock *et. al.* and Smith *et. al.* [25, 148]

For a sample of original length L_0 deformed along the i^{th} axis from L to $L' = L + \delta L$ (where δL is small), the instantaneous strain, ϵ_i is given by

$$\epsilon_i = \frac{L' - L}{L} = \frac{{}^{L'}/_{L_0} - {}^{L}/_{L_0}}{{}^{L}/_{L_0}} = \frac{\delta\lambda_i}{\lambda_i}, \tag{8.2}$$

which in the differential limit gives

$$\epsilon_i = \frac{d\lambda_i}{\lambda_i} = d\ln\lambda_i, \tag{8.3}$$

where λ_i is the component of the deformation gradient tensor along the i^{th} axis and $\delta\lambda_i$ is a small change in λ_i. Thus the strain dependent Poisson's ratio is given by

$$\nu_{ij} = -\frac{d\ln\lambda_j}{d\ln\lambda_i}. \tag{8.4}$$

One can easily verify equation 8.4 by considering the case for an isotropic and incompressible elastomer for which $\lambda_j = \lambda_i^{-1/2}$ which gives $\nu = 0.5$ as expected.

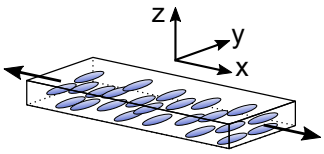

Figure 8.2: Illustration of coordinate geometry used in this chapter. For all samples, the director existed within the xy plane at an angle of $89 \pm 1°$ to the applied stress (x) axis.

8.3.2 Application of W&T theory to the state of negative order parameter

In this chapter we will see that the emergence of auxetic behaviour matches speculations made by W&T and also coincides with the NOP state encountered in the previous chapter. Therefore we here apply the Gaussian theory developed by W&T to the NOP state to see to what extent the theory can also account for the observed NOP.

As was done in chapter 4 we minimise of the elastic energy given by the trace formula. We use the same geometry as we have done in previous chapters which for reference is shown again in figure 8.2. As we begin with the director along the y axis, the initial step length tensor is given by $\underline{\underline{\mathbf{l}}}_{\mathbf{0}} = \mathrm{Diag}(l^0_\perp, l^0_\parallel, l^0_\perp)$. As in chapter 4, we use assume a shear-less deformation gradient tensor, $\underline{\underline{\lambda}} = \mathrm{Diag}(\lambda_x, \lambda_y, \lambda_z)$.

If we recall from section 7.5 that the appearance of black birefringence colours in the NOP state means that in the xy plane, the sample appears to be isotropic. Therefore in this state the step length tensor, $\underline{\underline{\mathbf{l}}}$, will have components of equal magnitude along x and y axes. Thus, for the deformed state the step length tensor must be given by $\underline{\underline{\mathbf{l}}}' = \mathrm{Diag}(l'_\perp, l'_\perp, l'_\parallel)$, which has principal axes parallel with those of $\underline{\underline{\mathbf{l}}}_{\mathbf{0}}$. It is important to note here that we have not set any constrains on the magnitude of $r' = {}^{l_\parallel}/_{l_\perp}$ with respect to unity. By inserting the expressions for $\underline{\underline{\mathbf{l}}}_{\mathbf{0}}$ and $\underline{\underline{\mathbf{l}}}'$ into the trace formula (equation 4.16), we arrive at the elastic free energy in the negative order parameter state

$$F_{el} = \frac{\mu}{2}\left(\lambda_x^2 \frac{l_\perp^0}{l'_\perp} + \lambda_y^2 \frac{l_\parallel^0}{l'_\perp} + \lambda_z^2 \frac{l_\perp^0}{l'_\parallel}\right), \tag{8.5}$$

where we have neglected the ln() term as we are setting the values of $\underline{\underline{\mathbf{l}}}_{\mathbf{0}}$ and $\underline{\underline{\mathbf{l}}}$ based on observations — thus the ln() term is automatically at a value which minimises F_{el}. Applying our constrain of volume conservation, $\lambda_z = {}^1/_{\lambda_x\lambda_y}$ and minimising with respect to λ_y gives

$$\lambda_y^2 = \frac{1}{\lambda_x\sqrt{r_0 r'}} \text{ and } F_{el} \propto \lambda_x^2 + \frac{2}{\lambda_x}\sqrt{\frac{r_0}{r'}}, \tag{8.6}$$

where $r_0 = {}^{l_\parallel^0}/_{l_\perp^0}$.

Minimising this with respect to λ_x gives the following relationships:

$$\lambda_x^6 = \frac{r_0}{r'} \text{ and } \lambda_y^6 = \frac{1}{r' r_0^2}, \tag{8.7}$$

which can be rearranged to

$$r_0 = \left(\frac{\lambda_x}{\lambda_y}\right)^2 \text{ and } r' = \frac{1}{\lambda_x^4 \lambda_y^2}. \tag{8.8}$$

Therefore values for the step length anisotropy in the unstrained and NOP state can be calculated from the measured deformations corresponding to the NOP state. Using the value of r_0 calculated from equation 8.8 we will be able to assess the applicability of the Gaussian theory to the mechanical phenomena of LCE A.

8.4 Experimental details

In this section we detail the modifications to the mechanical testing techniques described in chapters 5 which were needed to study the auxeticity of LCE A in this chapter. We also detail the relevant experimental details of the two additional techniques of Scanning Electron Microscopy and Atomic Force Microscopy used in this chapter to probe the porosity of LCE A down to molecular length scales.

Table 8.1: For each test the: parameters used, critical strain ϵ_x at the emergence of auxetic behaviour and Poisson's ratio at the maximum extension.

Test	Extension speed [%×L_0 min^{-1}]	Temperature [±2°C]	$\epsilon_c = \epsilon_x$ at emergence of auxeticity	Poisson's ratio at maximum extension
I	16	28	0.99	-0.34
II	7.5	28	0.78	-0.51
III	1.0	24	0.80	-0.52
IV	0.71	23	0.80	-0.80

LCE preparation. Samples of LCE A were prepared as described in chapter 6 with thickness of 100 ± 5 μm. Strips of dimensions $\sim 2 \times 20$ mm were cut with the nematic director at $89 \pm 1°$ to the film long axis (figure 8.2).

Scanning Electron Microscopy (SEM). (Performed by Mr. Micklthwaite) A section of the yz plane was exposed by freeze-fracturing a LCE sample. Prior to studying *via* SEM, the exposed faces were coated with a ~ 15 nm conductive carbon layer using a Quorum Q150T E high vacuum evaporative carbon coater. A high resolution Hitatchi SU8230 SEM was used to image the expose cross-sections from molecular to micron length scales. The single-pixel resolution in the highest magnification image in figure 8.4(a) on page 141 is 1 nm.

Atomic Force Microscopy (AFM). yz cross-sectional samples were prepared by encasing samples of LCE within a two-part epoxy glue and then freeze-fracturing by snapping off the exposed LCE. AFM images were acquired (by Dr. Connell) using a Bruker Dimension FastScan-Bio, using Bruker FastScan A probes with nominal tip radii of 5 nm, in air tapping mode at a frequency of 1.4 MHz. Images were acquired at a line rate of approximately 4 Hz at 1024 pixel resolution, then processed with a simple low order line flattening in Bruker Nanoscope Analysis v1.9 (performed by Dr. Connell).

Mechanical testing. Samples were mechanically tested using MESSE by applying successive extensions in discrete 0.5 mm steps between which the sample was allowed to stress relax. The frequency of the steps used for each particular sample dictated the overall "extension speed" which is characterised by the percentage of the original sample length by which the sample was extended per minute. Table 8.1 gives the extension speeds and temperatures used for each of the four configurations investigated here.

Three samples were tested under the test **I** parameters. The first imaged the xy plane of the sample using transmitted white light to enable the measurements of strains along x and y. Strains along x were determined using *trackpy* as described in chapters 5 and 7. Strains along y were determined as described in section 5.5.2. Using the conservation of volume the strain along the z axis was also determined.

The second test under parameter **I** viewed the edge of the sample in the xz axes such that the strain along z could be directly measured. The light source was moved such that the edge focused upon was viewed *via* reflected light. As the sample thickness (dimension along z) was only ~ 100 μm thick, the lens magnification was increased by a factor of 13 (from 0.7× to 9×). The camera resolution in this mode was 3 μm. This resolution was sufficient to precisely measure the change in thickness directly — allowing confirmation of the constant volume assumption validity. From photographs taken, the thickness was determined by a modified version of the width measuring *python* script. For each strain step the script first measured the average apparent brightness of the film from a window over the film edge and subtracted a background brightness measured from a window of the photograph where there was no film (figure 8.3 overleaf). The top and bottom edges of the film were then taken to be located at the first pixel from the upper and lower edges of the photograph respectively which had brightnesses of at least 40% of the difference in brightness previously calculated. The difference in pixel locations gave the pixel thickness. As the film appears tilted in the photographs (seen in figure 8.3) the thickness was measured in each single pixel column individually. The median value and median absolute deviation of

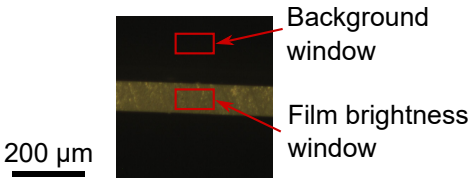

Figure 8.3: Example image of the sample tested under parameters **I** (table 8.1) and viewed *via* the xz plane with reflected light. A 9× lens magnification was used for this photograph.

these measurements were then taken as the sample thickness and error respectively and from which the strain ϵ_z was directly determined. The strain ϵ_x could not be determined from these photographs *via trackpy* and so instead had to be measured manually from the relative positions of identifiable features, measured using ImageJ.

The third test under parameters **I** imaged the xy plane of the sample *via* polarising microscopy such that the state of order could be determined. Again measuring the strain ϵ_x had to be performed manually from this set of images.

For tests performed under parameters **II-IV** (detailed in table 8.1), the samples were photographed in the xy plane *via* white light with the strains determined as described for the corresponding test from test **I**. The data from test **IV** is the data from the 89° sample studied in the previous chapter with the extension speed based on a typical time of 8 minutes between successive extensions.

8.5 Results

8.5.1 LCE geometry and porosity

As with all samples of LCE A used in this thesis, the samples used in this chapter were high quality monodomains like those shown in figures 6.3(a) and 6.4(a). When investigating auxetic materials it is important to know what (if any) structure is driving the auxetic response. The high uniformity of the polarising microscopy images of LCE A shown in figure 6.4(a) along with the transparency of

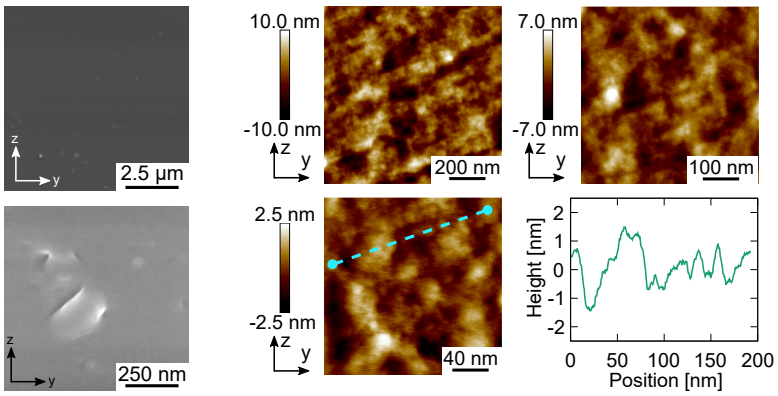

(a) (b)

Figure 8.4: a) SEM micrographs and b) AFM height maps showing the LCE microstructure across molecular to microscopic length scales. Height profile plotted is drawn on the highest resolution AFM image.

LCE A shown in figure 6.3(a) demonstrate, through the lack of light scattering, that there is no porous structure present down to approximately the wavelength of visible light ($\sim$ 400 nm). Cross-sections of LCE A imaged *via* SEM and AFM allow for the nano- and micro-structure of the material to be assessed. The SEM images shown in figure 8.4(a) reveal a homogeneous and largely featureless structure confirming that the material has no porosity on length scales between tens of nanometres and micrometers. Images shown in figure 8.4(b) acquired *via* AFM, which is more sensitive to topographical features than SEM, shows a complex picture of structure on length scales from molecular to several hundred nanometres. Two features are clear from the highest magnification AFM image and corresponding profile map: an extremely fine structure on the scale of a few nanometres; and a larger, slow undulation on the scale of $\sim$ 10 nm with an amplitude of $\sim$ 2 nm (comparable to the length of a mesogenic molecule). [86] Neither of these structures indicate the presence of material porosity on nanometre length scales. Thus from figure 8.4 we conclude that LCE A has zero detectable porosity. While such a result should be expected for a LCE, it was important to confirm the lack of porosity given the importance of porous geometries to the behaviour of previous auxetics. Moreover, there was a possibility of porosity in LCE A as

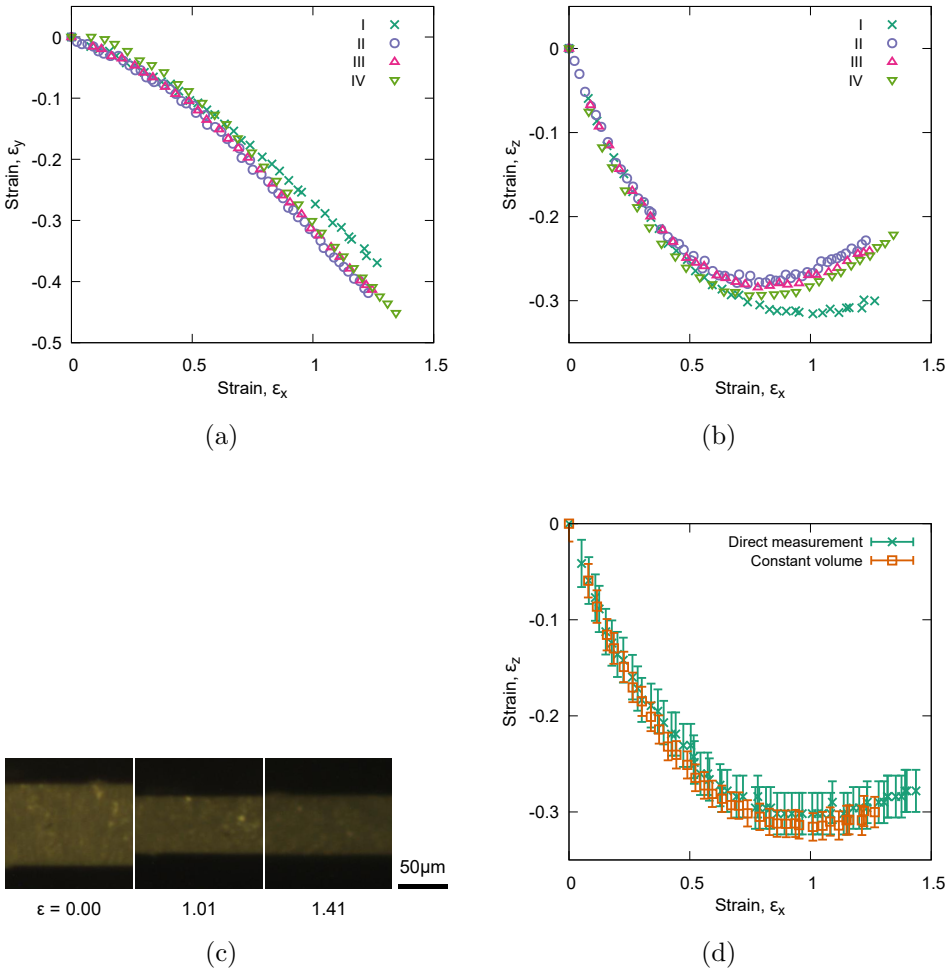

Figure 8.5: a) and b), Strains ϵ_y and ϵ_z, respectively, measured in response to the imposed strains ϵ_x. The data in b) is calculated using strains measured in the xy plane and the constant volume assumption. c) Images of the xz plane of the sample under test **I** parameters at strains corresponding to the unstrained sample, sample at the critical strain $\epsilon_x = \epsilon_c$ and at the maximum strain (9× lens magnification used). d) Comparison of $\epsilon_x - \epsilon_z$ strain curves for samples tested under parameter **I**, calculated *via* a constant volume assumption (using strains measured in the xy plane) and direct measurement of the strains in the xz plane.

its synthesis procedure (detailed in section 5.2.2) involved a post-polymerisation washing step in which the non-reactive 6OCB component, corresponding to $\sim$ 50% of molecules present, was removed. We believe no pores are present as the components of monomer mixtures are completely miscible in the monomer state. Further as the final LCE contains covalently bonded mesogenic groups, no phase separation of the 6OCB occurs during polymerisation.

8.5.2 Geometrical deformations and auxeticity

In contrast to the previous chapter, mechanical results presented in this chapter are presented and discussed in terms of strains, ϵ_i, as opposed to deformations, λ_i, as is typical for research in the auxetics field.

Figure 8.5(a) and 8.5(b) show, respectively, for each test parameter the transverse strains ϵ_y and ϵ_z (all from measurements in the xy place) in response to the imposed strain ϵ_x. While the strains ϵ_y all monotonically decrease, indicating conventional behaviour, the strains ϵ_z all show an initial decrease followed by an increase after a critical strain ϵ_x we denote as ϵ_c. The regions where the strains ϵ_z increase are indicative of auxetic behaviour.

Figure 8.5(c) shows photographs of the xz plane of the sample at several strain steps under test conditions **I**. In sequence the strain steps correspond to: zero strain, at ϵ_c and, at the maximum strain before failure. While it is clear the sample grows thinner between the strains corresponding to the first to second images shown, the increase in thickness beyond ϵ_c is more difficult to see by eye. However, figure 8.5(d) shows that, after analysing the images as described in section 8.4, the increase in thickness is clearly measurable and agrees with measurements made *via* the constant volume assumption. Moreover, the excellent agreement between the two datasets is consistent with the LCE deforming at constant volume and hence at constant density. This result, which is to be expected for non-porous elastomers, validates the method of determining the strains ϵ_z *via* deformations in the xy plane under a constant volume assumption and more importantly, removes the possibility of the observations of auxeticity being caused by wrinkling

effects.

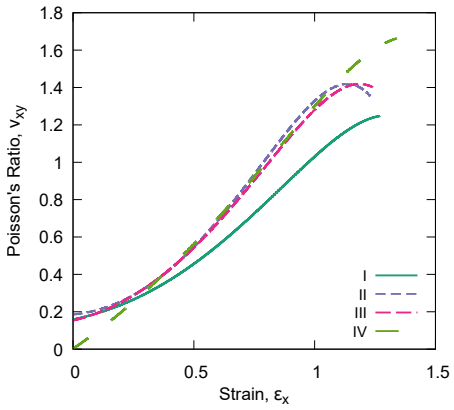

(a)

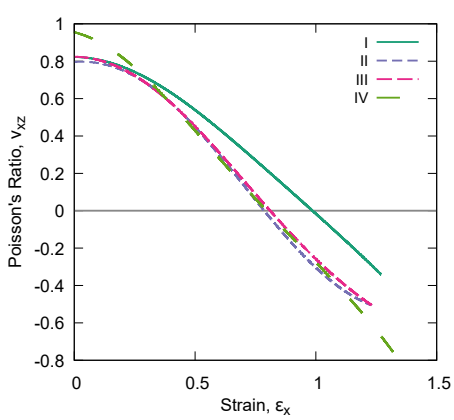

(b)

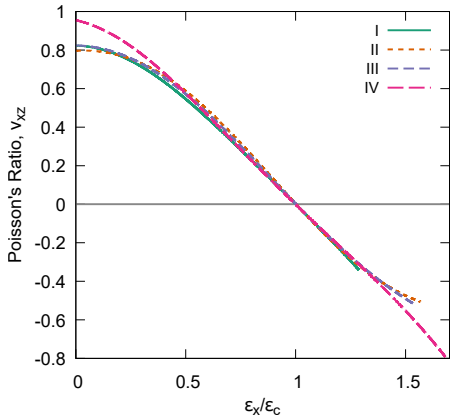

(c)

Figure 8.6: Poisson's ratio a) ν_{xy} measured from data in figure 8.5(a) and b) ν_{xz} measured from data in figure 8.5(b) calculated using equation 8.4. c) ν_{xz} replotted for teach test relative to the strain $\epsilon_x = \epsilon_c$.

Figure 8.6(a) shows the Poisson's ratio ν_{xy} determined by fitting a fourth order polynomial to each dataset from figure 8.5(a) (modified to be in terms of λ_x and λ_y) and inserting into equation 8.4. In each case ν_{xy} initially began close to zero before increasing with strain.

Figure 8.6(b) shows for each test the strain-dependent Poissons ratios, ν_{xz}, calculated in the same manner as ν_{xy}. The curves show that ν_{xz} initially begins close to 1 before monotonically decreasing with strain and entering the auxetic regime at a critical strain, $\epsilon_x = \epsilon_c$, beyond which ν_{xz} becomes negative. ϵ_c depends on the sample temperature and extension speed (table 8.1), a phenomenon attributed to the temperature sensitivity of LCEs and the different testing conditions allowing varying levels of stress relaxation between successive extensions. [156] A minimum value of $\nu_{xz} = -0.8$ was recorded in test **IV** which was strained by the largest factor (~ 1.7) above ϵ_c. If however the strains ϵ_x are normalised with respect to ϵ_c *for each test*, then we see that the magnitude of the auxetic response is in fact largely identical for each test (figure 8.6(c)).

The anisotropy between ν_{xy} and ν_{xz} is to be expected for two reasons. Firstly, monodomain LCEs are well known to have inherent mechanical anisotropy — as indeed we have already confirmed for LCE A in chapter 7. [169, 90, 130, 166] Secondly, simultaneous volume conservation and Poisson's ratio isotropy is only possible in the specific case of $\nu_{xy} = \nu_{xz} = 0.5$, for which there is no auxetic behaviour. [98]

After mechanical testing the films were allows to relax overnight before their thickness and birefringence remeasured. In all cases the films returned (within error) to their original thickness and birefringence demonstrating the elastic nature of the auxetic response.

8.5.3 State of negative order parameter

Figure 8.7 (overleaf) shows polarising microscopy images of the LCE deformed under test conditions **I**. The progression of birefringence colours here is very similar to those seen in chapter 7 however here the difference between each photo is much more striking with the sample appearing comparatively homogeneous. This could be a result of the particular sample having a more even thickness or

Figure 8.7: Polarising microscopy textures at each strain step of test **I**

a result of the film being loaded into the actuators in a perfectly flat manner.

8.6 Analysis and discussion

The applicability of W&T theory to the observations of auxeticity and the NOP state can be assessed through the consistency of multiple, independently calculated values of the initial step length anisotropy, r_0, and by comparing them to values calculated in the previous chapter.

When discussing the MFT transition in their book, Warner and Terentjev speculate that an auxetic response may be observed to begin at a deformation given by

$$(\lambda_x, \lambda_z) = (r_0^{1/3}, r_0^{-1/6}), \tag{8.9}$$

where the $\lambda_i (= \epsilon_i + 1)$. [169] This deformation $\lambda_x = r_0^{1/3}$ is the same lower bound for the deformation at which the director reorientation occurs in the theory of MTFs. Considering data for test **I** from figure 8.5(b) (for which corresponding

polarising microscopy images are shown in figure 8.7), two consistent values of $r_0 = 8.0 \pm 0.7$ and $r_0 = 9.3 \pm 1.6$ can be calculated from the critical strains $\epsilon_x = 1.00 \pm 0.06$ and $\epsilon_z = -0.31 \pm 0.02$ respectively. The latter of these values is independent from the previously calculated values of r.

From figure 8.7 we see that for test **I**, the state of negative order parameter occurs at $\lambda_x = 2.15 \pm 0.05$. Using the data from figure 8.5(b) we find the corresponding value of $\lambda_y = 0.67 \pm 0.05$. Inserting these values in to equation 8.8 we find $r_0 = 10.3 \pm 1.6$ and $r' = 0.103 \pm 0.015$, the former being consistent with both values calculated above. The calculation of $r' < 1$ at the state of zero retardance corresponds to the system adopting a uniaxial oblate polymer conformation, a result to be expected for a state of NOP given the shared symmetry between the LC order parameter and the step length tensors. [169, 119]

The fact that the independently determined values of r calculated here remarkably agree both with one another and the value determined from the theory of MFT from chapter 7 is encouraging but also quite puzzling. On one hand the agreement implies that a theoretical understanding of the auxetic and negative order parameter phenomena could be achieved using the basic Gaussian theory of W&T. However, on the other hand, we had quite reasonably concluded in the previous chapter that the Gaussian theory could not be applied as it neglects the effect of the changing LC order parameter and results in a value of $r \sim 9$ which is unlikely as it is several times greater than any other reported value for a side chain end-on LCE. We are left with one of two possibilities; first, that the value of r for LCE A is as large as ~ 9, which would truly be an unprecedented result; or second, that one can avoid having to take into direct consideration the possibility of a changing order parameter in W&T theory by instead increasing the value of r from its actual value when applying the theory. To know which possibility is correct would require further studies which directly measure either r, for instance *via* neutron scattering, or the LC order parameter in the unstrained state, for instance *via* polarised Raman spectroscopy, IR dichroism or XRD, from which r can be inferred from an inverted equation 4.46 [58, 93, 32]

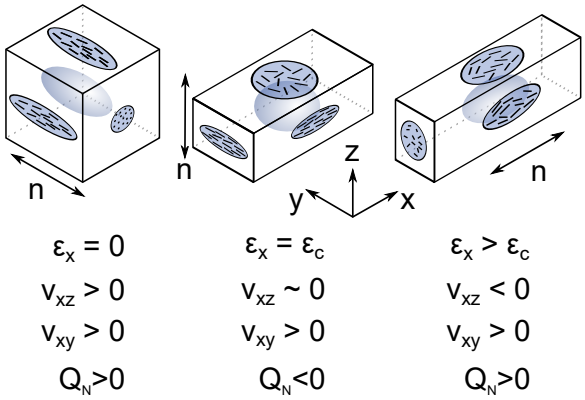

Figure 8.8: Model of the deformation described by: the relationships between the sample geometry (outline box), polymer conformation shape (enclosed ellipsoidal shapes) and the liquid crystal order parameter (denoted as Q_N) projected on each plane (rod arrangements). At the critical strain, ϵ_c, the symmetry of the LC ordering corresponds to a negative order parameter with the director lying parallel to the z axis.

$$Q_b = \frac{r-1}{r+2}. \tag{8.10}$$

Here we insert our determined values of r_0 and r' into equation 8.10 to calculate values of $Q_b^0 = 0.74 \pm 0.03$ and $Q_b' = -0.41 \pm 0.01$ respectively. According to Finkelmann *et. al.*, for side chain LCEs the backbone order parameter is proportional, by a positive constant, to the nematic LC order parameter, Q_N. While we do not know what this constant would be for LCE A, the fact that this relationship exists is encouraging as it gives a positive value for the order parameter in the unstrained state, as one would expect, and its gives a negative value for the state which we have been, until now, inferring as having a NOP from geometrical arguments. This is particularly significant as in the theory developed leading to equation 8.8 we did not constraint the magnitude of r' with respect to unity.

In figure 8.8 we bring together our results to illustrate the deduced relationships between: the macroscopic deformations; the polymer conformation shape; and the LC ordering with projections onto the xy, yz and zx planes. The highly non-linear mechanical behaviour of LCE is known to be intimately dependent on

the microstructure of the polymer conformation. [169] The depiction in figure 8.8 therefore suggests that it is highly likely that the oblateness of the polymer conformation close ϵ_c is driving the auxeticity observed.

8.7 Conclusion

The results of this chapter are particularly significant for the fields of LCEs and auxetic materials as until now, auxeticity has never been seen in a LCE and, as the material is non-porous, the auxeticity is an inherent material property and not the consequence of a porous geometry. Moreover, as the emergence of auxeticity coincides with the state of negative order parameter it appears likely that the two phenomena are linked. Since all previous examples of synthetic auxetics have relied on a porous geometry, LCE A can therefore be described as the first example of a "synthetic molecular auxetic" — a long-standing goal for the auxetics community. This observation is even more significant as LC polymers and LCEs have arguably been considered as the most promising type of synthetic material for displaying molecular auxeticity, but a negative Poisson's ratio has never previously been measured in systems studies. [169, 4, 69, 5, 71, 131] Our mechanical tests have shown a maximum magnitude of negative Poisson's ratio of -0.8, which is larger than most values seen in naturally occurring molecular auxetics such as iron pyrite ($\nu = -0.14$), α-cristobalite ($\nu \sim -0.5$), and cubic metals (broad range of negative ν *calculated* between $-0.8 \leq \nu \leq 0$). [101, 178, 14] Moreover, the trend of a monotonically decreasing Poisson's ratio, ν_{xz}, implies that if the sample were not to break when it did, then the Poisson's ratio would likely have continued to decrease below -0.8.

While a detailed theoretical understanding of the auxetic and negative order parameter states is beyond the scope of this thesis, we have performed an initial theoretical study to assess to what extent the Gaussian theory developed by W&T might be capable of describing the observed phenomena. We found that while several consistent values of r could be determined from the auxetic and negative order parameter states, these did not agree with value of r of 3.8 ± 0.5 which

we concluded was most accurate in the previous chapter. The consistency of values does however make us believe the Gaussian theory would still be a valid theoretical starting point from which to understand the observed phenomena in greater detail.

While the preliminary results presented in this chapter are very exciting, there are open questions which must be investigated before the auxeticity could be used in practical devices. Firstly, to what extent can the auxeticity be tuned in terms of the magnitude of the negative Poisson's ratio and the critical strain required before the auxeticity begins? More specifically, can the auxeticity be tuned to start from zero strain? Secondly, does this first example of a synthetic molecular auxetic have similar enhanced mechanical properties such a tear resistance and shock absorbance as porosity-based auxetics which makes them attractive for device applications?

Based on the results of this chapter we believe the auxeticity could be tuned in two ways. The apparent dependency of the critical strains along x and z axis on the value of r_0 implies that by modifying of the chemistry of the LCE to increase the value of r_0, it may be possible to change the magnitude of the auxetic response. This could be achieved by introducing main chain mesogenic units in LCE A. Additionally, the coincidence of the NOP state with the emergence of the auxetic behaviour leads us to believe that the auxeticity is likely to be driven by the oblate polymer conformation. Thus if a LCE prepared with a oblate polymer conformation in the unstrained state, then it may have an auxetic response from zero strain. Such a material could be produced using side chain LC mesogens that orient perpendicular to the polymer backbone or through using a LCE with a two-step synthesis procedure whereby the mechanical alignment is introduced using a biaxial or radial mechanical field. [169, 22]

In terms of the aims of this thesis, one might see the auxetic phenomena being useful for generating complex and lens-like geometries, especially since to the best of our knowledge, the present material is also the first example of a transparent auxetic. In one embodiment, a molecular auxetic could expand laterally when deformed by the ciliary body in a manner which would result in a lens-like

geometry. However, we believe such a deformation mode is likely to be unsuccessful, certainly using LCE A, as given the radial force distribution, a reduction in material density would be required to allow simultaneous expansion within and perpendicular to the deformation place. As we have seen that LCE A deforms at constant volume, this proposed mode of operation would be impossible. Despite this, we are optimistic for the potential of LCE auxeticity in application to other mechanical and opto-mechanical devices. In such devices the auxetic behaviour could be further augmented by the photopatterning of the director in LCE films or by the inclusion of azo-benzene groups which could offer photo-switchable auxeticity. [81, 37, 164, 179]

We finish this chapter by noting that the results of this chapter have opened up a new area of research for LCEs which could lead to the realisation of many of the proposed auxetic-based devices. To make progress in this field it will be important to understand the expected mechanical properties of auxetic LCEs from a theoretical point of view. However, clearly developments in theory will need to be informed by additional experimental data as currently a very limited amount of data is available.

8. COINCIDENT NEGATIVE POISSON'S RATIO AND NEGATIVE LC ORDER PARAMETER

Chapter 9

Interlude

Until now we have been performing relatively standard experimentation and characterisation to develop a new LCE which we can work with and to characterise its basic behaviour. Though simplistic, the depth of detail provided by the characterisation conducted in chapters 7 and 8 has revealed several new and unexpected mechanical phenomena of LCEs. While these discoveries were beyond the outset scope of this thesis, they are important and complementary to the aims of this thesis.

The discoveries of chapter 7 of new mechanical behaviour not conforming to either theories of SSE or MFT, but displaying aspects of both, shows us that much experimental and theoretical work still needs to be performed on LCEs to fully understand their physics. Clearly this additional understanding will also have great importance to the pursuit of mechano-LCE devices.

The discovery of molecular auxeticity in chapter 8 adds further weight to the need for additional basic characterisation of LCEs but also goes further by opening up a whole new field of study for LCEs and auxetics which could be the first stepping stones toward the realisation of molecular auxetics technologies. We are particularly excited by the prospects offered by combining auxeticity with the additional functionalities of LCEs.

While the work performed thus far has significant implications for the field of LCEs it is merely a foundation to the work pursuing of the aims of this thesis. The remaining chapters of this thesis go beyond the standard characterisation of LCEs and make strides in understanding the physics and identifying the challenges of non-trivial deformations of LCEs — ultimately working towards the design of prototype a LCE-based AIOL.

Chapter 10 considers the tensile optomechanical behaviour of LCE A in response to stresses applied at arbitrary angles relative to the director and develops an empirical model which describes much of the deformation behaviour of LCE A. Chapter 11 then applies this model in a study of the complex geometrical and mechanical deformation behaviour of a LCE prepared with a complex director profile. The results inform how complex shape changes can be programmed *via* director patterning. Chapter 12 considers radial or deformations of the "isotropic LCE" (LCE B) and provides an insight into the additional challenges which arise in equibiaxial deformation geometries — like that present in the eye.

What is learnt form chapters 10, 11 and 12 is used in the penultimate chapter to design a prototype AIOL device and to identify remaining research challenges which must be overcome before such as device could be successfully developed. Finally, the conclusion considers the key findings of this thesis together with recent advances from the wider field of LCEs to assess the prospects and feasibility of the proposed AIOL and other mechano-LCE devices. A suggested programme for further research to follow on from the work of this thesis is also provided.

Chapter 10

Empirical equations toward modelled deformations

10.1 Introduction

In this chapter we build upon the basic characterisation performed in chapters 7 and 8 by studying the tensile behaviour of LCE A when stressed at arbitrary angles relative to the director. In the context of this thesis this is important as we have proposed to use spatially patterned mechanical properties to control the mechanical shape deformations of an AIOL. Thus a complete picture of the angular dependence of the tensile mechanical behaviour is required to assess whether LCE A does have the required mechanical behaviour for the proposed mode of deformation and further whether the mechanical behaviour can be described by a model which can be used to design the device. The content of this chapter is also important to the wider field of LCEs as, until now, the tensile mechanical study of LCEs has almost exclusively focused on stresses applied either parallel or perpendicular to the director. Moreover, the few studies that have been performed at generic angles relative to the director have only considered either the director rotation behaviour or the stress-strain behaviour but not both. [90, 76, 166] To provide context for the results of this chapter these papers are briefly reviewed here.

Kundler *et. al* used X-ray diffraction to compare, for a side chain polysiloxane LCE, the director rotation behaviour for samples stressed at a range of angles between 56° and 90° to the director. For initial director angles greater than $\sim 70°$, stripe domains (see section 2.5.4) were observed, while for angles less than $\sim 70°$ the director across the entire film rotated with a single sense of rotation. For their 90° sample director rotation began above a threshold strain, behaviour consistent with semi-soft elasticity.

Hirschmann *et. al* studied the director rotation for the acrylate-based LCE developed and studied by Mitchell and co-workers. [76, 33] They found for three samples with initial director angles of 89°, 80° and 67°, a director rotation behaviour that could be accurately described by the MFT model of Bladon, Warner and Terentjev. [16]

Lastly, Ware *et. al.* recently reported stress-strain data for their acrylate-amine LCE stressed at (30°, 45° and 60°) as well as parallel or perpendicular to the director. [166] When stressed perpendicular to the director, the load curve showed the characteristic initial "step" and plateau of semi-soft elasticity. For angles less than 90° the step height increased and plateau became a linear region with a larger gradient recorded for angles closer to 0°. In general the initial modulus increased for direct angles closer to the stress axis with the 0° curve being an exception as its modulus appeared to less than of the 30° sample. Aside from the report of the semi-soft elastic-like director rotation of the 90° sample, no other details of the director rotation were reported.

From the above brief review, together with the literature review of section 2.5, it is clear that a complete picture of the mechanical behaviour for stresses at an arbitrary angle to the director of any given LCE is yet to be reported. In this chapter such a characterisation is performed on LCE A. While the results qualitatively appear as would be expect for any LCE (*i.e.* anisotropy is observed), these results cannot be taken as representative of LCEs in general because, as discussed in section 2.5, the mechanical properties of a given LCE is significantly

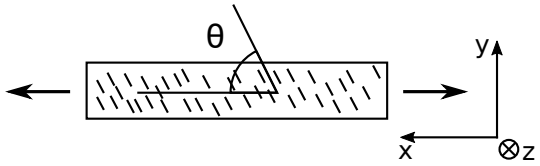

Figure 10.1: Illustration of geometries and coordinate set used in this chapter. The director angles are measured with respect to the applied stress (x) axis.

impacted by its chemical composition and its preparation route.

From chapter 7 we know the mechanical response will involve anisotropic elasticity, director rotations and a changing nematic order parameter. A theoretical model describing the complete mechanical behaviour of LCEs is highly desirable designing and simulating mechano-LCE devices. However, a general theoretical description involving all of the previously mentioned parameters for arbitrary stresses applied to LCEs is yet to be developed — perhaps because there are too many variables to account for. In section 10.3.1 we attempt to account for initial moduli of each sample measured to predictions from two simplified theoretical models. The failures of these models highlights the fact that a theoretical model is likely to be too complex to develop and implement. Consequently, we instead pursue an empirical model and compare its predictions to our experimental results. The successes and limitations of this model are discussed. We conclude that the model is sufficiently accurate for simplistic predictions of the LCE A's behaviour in response to generic uniaxial deformations.

10.2 Results

The materials used in this chapter were produced as described in chapter 6 with a range of different director angles relative to the length of the films. The geometry and coordinate system used in this chapter are illustrated in figure 10.1. Optomechanical testing methods used here were previously described in chapter 7. The results from stresses at 2° and 89° discussed in chapter 7 are reproduced here and are further analysed.

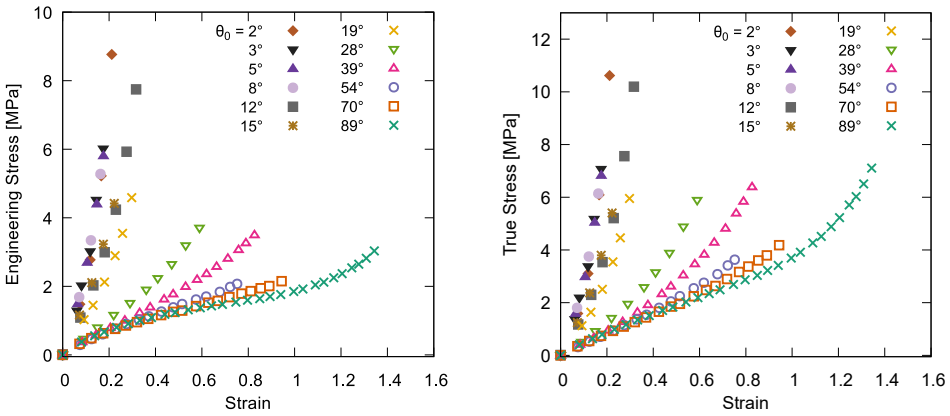

(a) (b)

Figure 10.2: a) Engineering and b) True stress as a function of strain for samples of various initial director angle strained until failure.

The results of the optomechanical tests are presented in this section with comparisons, where appropriate, made with the results of the existing literature. The majority of the analysis and discussion relevant to the aims of this chapter is reserved section 10.3 below.

Figure 10.2 shows the tensile load curves for the various samples of LCE prepared with a variety of different initial director angles. As intuitively expected from the results of chapter 7 we see that the greater the angle between the initial director orientation and the applied stress, the softer the elastic response (lower elastic modulus) and the greater the maximum sustainable strain before failure. These results are qualitatively similar to those reported by Ware *et. al.* although any initial "steps" in the load curve reported here are comparatively much smaller features.

Typically engineering stresses are reported for the mechanical behaviour of materials. However, for samples undergoing large strains the true stress provides a more accurate picture of the actual stress within the material as it takes into account the changing cross-sectional area of the sample. As the LCE under in-

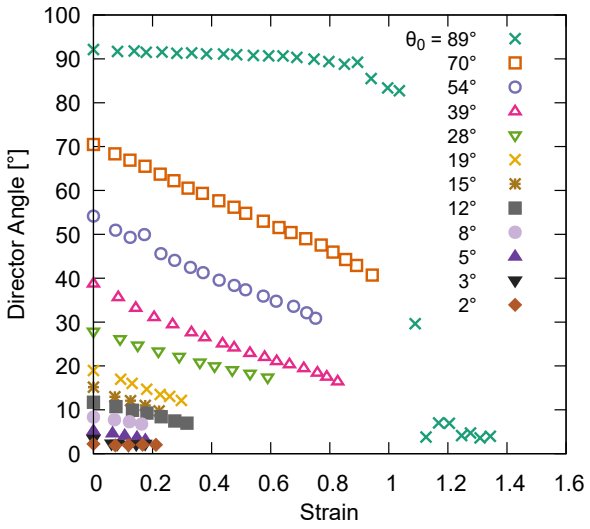

Figure 10.3: Traces of the director angle throughout tensile load tests shown in figure 10.2.

vestigation is known to deform at constant volume (see section 8.5), the product of the diagonal values of the deformation gradient tensor, *i.e.* $\lambda_x \times \lambda_y \times \lambda_z$, must equal unity at all strain steps. Therefore the true stress can be calculated by multiplying by the engineering stress by the deformation $\lambda_x (= \epsilon_x + 1)$ at each strain step. The result of this is plotted in figure 10.2(b).

The engineering stress curves shown in figure 10.2(a) show that the closer the initial director angle is to the stress axis, the greater the load the material can support as they show greater engineering stresses at failure. However, figure 10.2(b) shows that at the point of sample failure, the stress *actually present* within the 89° sample (7.2 MPa) is greatest of all of the samples excluding the 2° and 12° (10.6 and 10.2 MPa respectively).

During mechanical testing all samples with initial angles $\geq 12°$ were seen to fail at the clamps. This could be explained by director rotation at the clamps causing stress concentrations toward one edge of the film which in turn cause failure. Consequently, the failure point recorded for samples with initial angles above 12° may actually be premature failure points which would mean the maximum

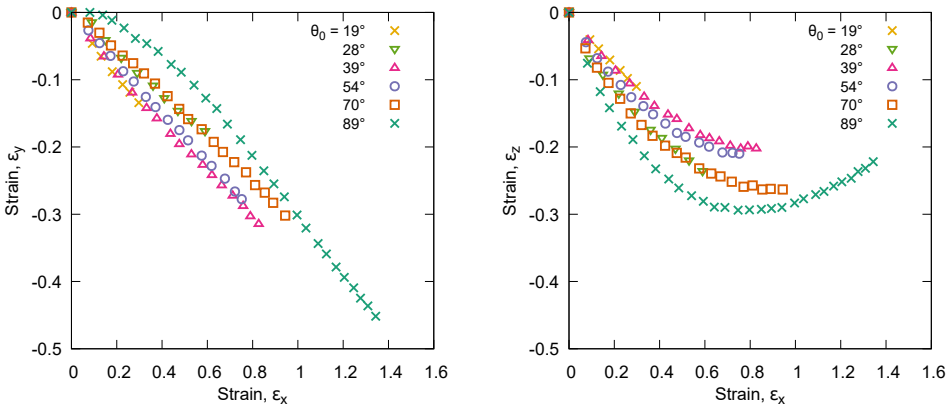

(a) (b)

Figure 10.4: Transverse strains along the a) y axis and b) z axes for samples with initial angles $\geq 19°$ according to the coordinate system illustrated by figure 10.1.

stresses recorded are underestimates of the actual maximum stresses sustainable for the central portion of each film.

Figure 10.3 shows the evolution of the director orientation with imposed strain. In all cases the director rotates with strain to align closer to the stress axis as would be expected. The form of director rotation for the 70° sample appears similar to that reported by Hirschmann *et. al.* for a sample initially oriented at 67°. [76] This agreement is consistent with the apparent MFT behaviour also seen in both materials (discussed in chapter 7).

Figure 10.4 plots the transverse strains along y and z axes for samples with initial director angles $\geq 19°$. Data for samples $\leq 19°$ have not been plotted for clarity and because the behaviour is largely similar to a linear isotropic response. Each sample shows anisotropy between the strain responses in each transverse dimension. The strains along y are largely linear while strains along z tend toward a plateau indicating a decrease in the strain dependent Poisson's ratio toward $\nu_{xz} \sim 0$. Based on the similarities with the 89° curve (discussed in chapter 8) it may be that these samples would also have entered an auxetic regime if they had

not failed when they did.

10.3 Analysis and discussion

We have seen from figure 10.4 that the appearance of the load curves significantly differs between engineering and true stress representations. As we would like to be able to compare the behaviour seen in the various curves against one another regardless of strain, it makes most sense to study the true stress load curves where the changing sample cross-section is taken into account and hence the strain dependency is, to a first approximation, removed. Thus in this section we have chosen to consider the true stress behaviour of the material.

10.3.1 Elastic modulus

Fitting functions for calculation of the elastic moduli

The elastic modulus is calculated from the derivative of the tensile load curves at zero strain and therefore can be calculated from a curves fitted to each load curve. The 89° load curve shown in figure 10.2(b) has the form of a "S" (sigmoidal) curve reflected in the line $y = x$, *i.e.* an inverse sigmoidal shape:

$$\sigma = A \times \log\left(\frac{1 + c\epsilon}{1 - d\epsilon}\right). \tag{10.1}$$

The form of equation 10.1 has been constrained to pass through the origin as a load curve must. For lower initial director angles, the curves have a positive second derivative (continually increasing gradient). At a first glance these shapes appears exponential in form, however they also resemble the shape of an inverse sigmoidal function which has been translated along its curve. Thus the function given in equation 10.1 represents a pragmatic choice function to fit to the load curve data of figure 10.2(b). It is important to explicitly note that there is no theoretical basis for our function choice.

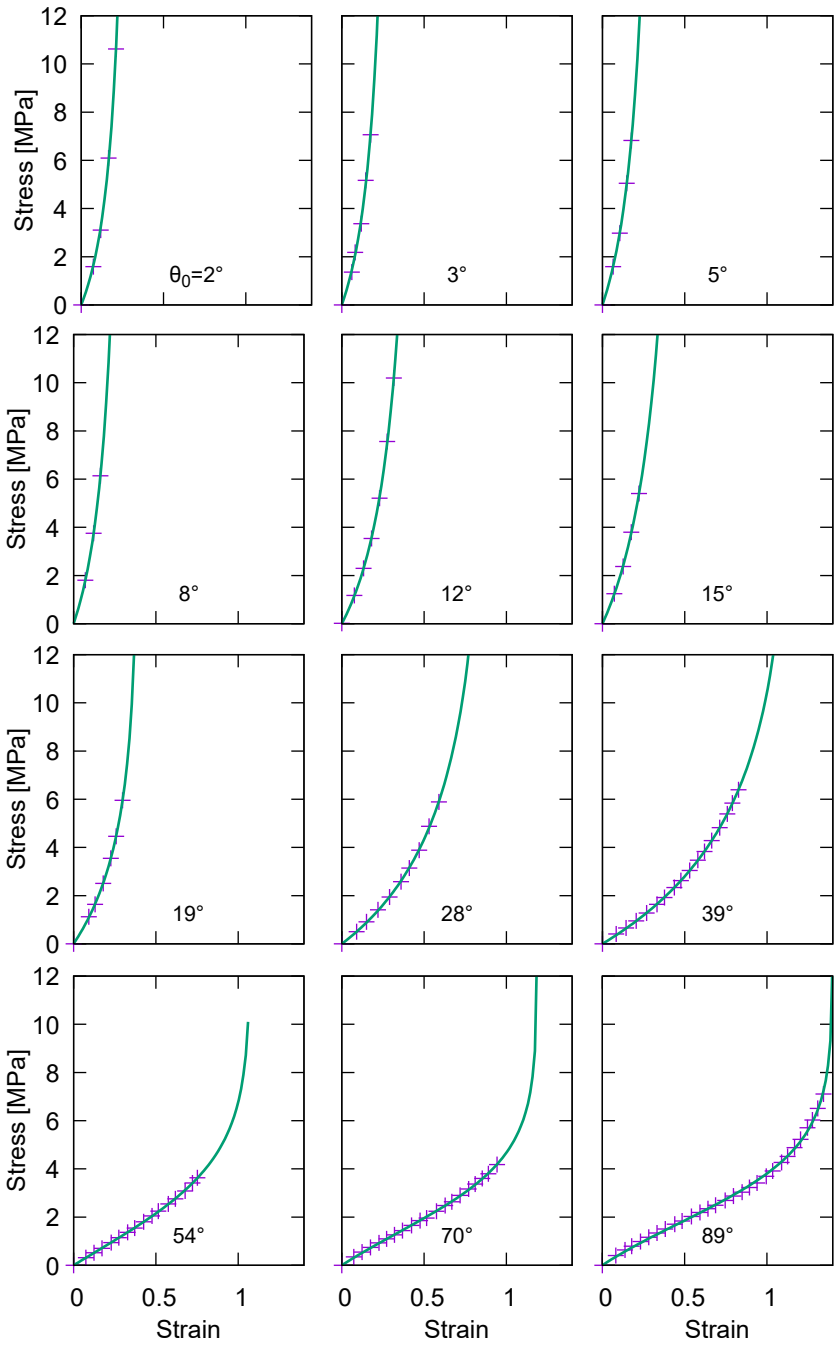

Figure 10.5: True stress load curves from figure 10.2(b) individually replicated and fitted with an inverse sigmoidal function shown in equation 10.1. The resultant fitting parameters are shown in table 10.1. For $\theta = 2$–$8°$ there are notable few data points which have been fitted against. The initial moduli values given in table 10.1 below take this into consideration.

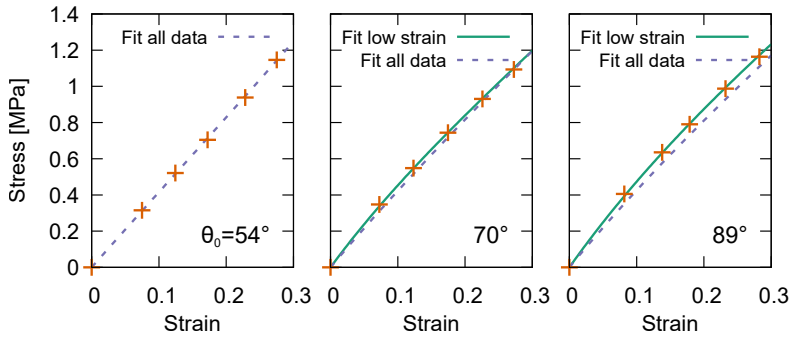

Figure 10.6: Low strain magnified views of the (a) $\theta_0 = 54°$, (b) 70° and (c) 89° load curve data and fits from figure 10.5. For the $\theta_0 = 70°$ and 89° samples additional curves are shown for fits performed on the low strain data points.

Table 10.1: Parameters and moduli from fitting equation 10.1 to true stress load curves from figure 10.5. Errors on moduli were manually deduced assessing lines plotted against the low strain data. ‡Fits performed on low strain data points.

Initial director angle [°]	Function fitting parameters A	c	d	Initial elastic modulus [MPa]
2	182	-3.06	3.15	17 ± 2
3	138	-2.90	3.04	20 ± 2
5	135	-2.64	2.80	20 ± 2
8	78.8	-2.73	2.98	20 ± 2
12	80.5	-1.81	1.97	13 ± 1
15	41.6	-1.54	1.91	15 ± 1
19	4.23	-0.13	2.57	10 ± 1
28	6.86	-0.38	1.13	5.2 ± 0.7
39	5.48	-0.11	0.87	4.1 ± 0.6
54	1.95	1.23	0.93	4.2 ± 0.1
70	1.60	1.92	0.84	4.4 ± 0.7
70‡	1.02	3.86	1.11	5.1 ± 0.2
89	1.59	2.14	0.71	4.5 ± 0.8
89‡	1.34	3.20	0.73	5.3 ± 0.2

Figure 10.5 replicates the load curves from figure 10.2(b) and shows that a fitted inverse sigmoidal function of the form shown in equation 10.1 (where parameters A, c and d are free parameters) describes the overall shape of the load curves extremely well. In order to accurately determine the initial elastic moduli for each sample we must ensure the curves of figure 10.5 fit well to the low strain data for each load curve. Figure 10.6 shows magnified sections of the 54°, 70° and 89° samples and shows that the functions fitted to the whole datasets of the 70° and 89° samples slightly miss the data points for low strain. Additional curves shown are fitted to the low strain data points, from which more accurate values of the moduli can be calculated. For samples with initial director angles $\leq 54°$, the fits performed to the whole data accurately fit the low strain data, an example of which is given in figure 10.6(a). Table 10.1 shows the resultant fitting parameters for each curve including the low strain fits for the 70° and 89° samples. Taking the derivative of equation 10.1 gives the strain dependency of the true modulus, E,

$$E(\epsilon) = \frac{d\sigma}{d\epsilon} = \frac{A \times (c+d)}{(1+c\epsilon)(1-d\epsilon)}, \tag{10.2}$$

where ϵ is the imposed strain along the x axis. The last column of table 10.1 shows the initial values of elastic moduli calculated using equation 10.2 for $\epsilon = 0$. For the 70° and 89° curves the differences in moduli between fits for the low strain data and the entire load curves is clear and demonstrates the care required in fitting such non-linear curves for determining the elastic modulus.

The relative differences between the calculated moduli for each sample are discussed below after we attempt to develop simple models by which to compare these results against. We do however note that the initial modulus values for the 89° and 2° samples calculated here (5.3 ± 0.2 and 17 ± 2 MPa respectively) differ to the values calculated in chapter 7 (4.0 ± 0.2 and 23 ± 2 MPa respectively). This difference should not be surprising as the values from chapter 7 were calculated from linear fits to low strain data which do not accurately reflect the shape of the load curves whereas the inverse sigmoidal fits used here do.

Developing simple models for initial moduli expectations

"Typical anisotropic property" model. The simplest model for how the initial modulus, $E(\theta_0)$, may be expected to vary with initial director angle, θ_0, between the stress axis and the director orientation can be found from a general form of the angular dependence of properties in anisotropic media. This model is used for the angular dependence of properties such as refractive index and dielectric constant for anisotropic materials and was detailed for the former in section 5.4. Adapting equation 5.1 gives

$$\left(\frac{1}{E(\theta_0)}\right)^2 = \left(\frac{\cos\theta_0}{E_\parallel}\right)^2 + \left(\frac{\sin\theta_0}{E_\perp}\right)^2, \tag{10.3}$$

where $E_\parallel$ and $E_\perp$ are the moduli experimentally measured for stresses applied parallel and perpendicular to the director respectively.

Gaussian theory. The above model is highly simplistic and does not take into account the elasticity of the system. One would anticipate a better model could be derived from the Gaussian theory developed by W&T even with the assumptions of zero director rotation and a constant LC order parameter. Gaussian theory has been used to determine stresses applied parallel and perpendicular to the director and calculates both moduli to be 3μ — the value for a isotropic elastomer. [169] This equality of moduli for stresses applied parallel and perpendicular to the director is well known to be inaccurate, however corrections to made to include non-Gaussian chains and a non-constant order parameter significantly complicate the theory. [105, 47, 126] To the best of our knowledge the simplest form of the Gaussian theory has not been used to predict the variation of the elastic modulus for stresses applied at generic angles to director.

We start from the trace formula (equation 4.16) and neglect the ln() term which has no λ_x or λ_y dependency as this will disappear as we differentiate to find the stress and modulus,

$$F = \frac{\mu}{2}\,\mathrm{Tr}\,[\underline{\underline{\mathbf{l}}}_{\mathbf{0}} \cdot \underline{\underline{\boldsymbol{\lambda}}}^{\top} \cdot \underline{\underline{\mathbf{l}}}^{-\mathbf{1}} \cdot \underline{\underline{\boldsymbol{\lambda}}}]. \tag{10.4}$$

10. EMPIRICAL EQUATIONS TOWARD MODELLED DEFORMATIONS

The step length tensor, $\underline{\underline{\mathbf{l}}}_{\mathbf{0}}$, to be used here has the same uniaxial form as used previously but takes a rotated form with respect to the system axes.

$$\underline{\underline{\mathbf{l}}}_{\mathbf{0}} = \begin{pmatrix} \cos\theta_0 & -\sin\theta_0 & \\ \sin\theta_0 & \cos\theta_0 & \\ & & 1 \end{pmatrix} \begin{pmatrix} l_\parallel & & \\ & l_\perp & \\ & & l_\perp \end{pmatrix} \begin{pmatrix} \cos\theta_0 & \sin\theta_0 & \\ -\sin\theta_0 & \cos\theta_0 & \\ & & 1 \end{pmatrix}. \tag{10.5}$$

Multiplying this through and finding the inverse gives

$$\underline{\underline{\mathbf{l}}}_{\mathbf{0}} = \begin{pmatrix} \alpha & \beta & \\ \beta & \gamma & \\ & & l_\perp \end{pmatrix}, \tag{10.6}$$

where

$$\alpha = l_\parallel \cos^2\theta_0 + l_\perp \sin^2\theta_0, \tag{10.7}$$

$$\gamma = l_\parallel \sin^2\theta_0 + l_\perp \cos^2\theta_0, \tag{10.8}$$

$$\text{and} \quad \beta = (l_\parallel - l_\perp)\sin\theta_0\cos\theta_0 = \Delta l \sin\theta_0\cos\theta_0. \tag{10.9}$$

As we are concerned with the initial elastic modulus (modulus at zero strain), we make the simplifying assumption that $\underline{\underline{\mathbf{l}}} = \underline{\underline{\mathbf{l}}}_{\mathbf{0}}$ — *i.e.* no director rotation and a constant nematic order parameter. Therefore $\underline{\underline{\mathbf{l}}}^{-\mathbf{1}}$ is given by

$$\underline{\underline{\mathbf{l}}}^{-\mathbf{1}} = \frac{1}{\delta}\begin{pmatrix} \gamma & -\beta & \\ -\beta & \alpha & \\ & & {}^{\delta}/_{l_\perp} \end{pmatrix}, \tag{10.10}$$

where

$$\delta = l_\parallel l_\perp. \tag{10.11}$$

For the deformation gradient tensor we assume deformations occur along the principal axes with conservation of volume and (again for simplicity) we also assume no shear terms:

$$\underline{\underline{\boldsymbol{\lambda}}} = \underline{\underline{\boldsymbol{\lambda}}}^{\top} = \begin{pmatrix} \lambda_x & & \\ & \lambda_y & \\ & & \frac{1}{\lambda_x\lambda_y} \end{pmatrix}. \tag{10.12}$$

Evaluating $\underline{\underline{\mathbf{l}}}_{\mathbf{0}} \cdot \underline{\underline{\boldsymbol{\lambda}}}^{\top} \cdot \underline{\underline{\mathbf{l}}}^{-\mathbf{1}} \cdot \underline{\underline{\boldsymbol{\lambda}}}$ gives:

$$\frac{1}{\delta}\begin{pmatrix} \alpha\gamma\lambda_x^2 - \beta^2\lambda_x\lambda_y & \alpha\beta\lambda_y(\lambda_y - \lambda_x) & \\ \gamma\beta\lambda_x(\lambda_x - \lambda_y) & \alpha\gamma\lambda_y^2 - \beta^2\lambda_x\lambda_y & \\ & & \frac{\delta}{\lambda_x^2\lambda_y^2} \end{pmatrix}. \tag{10.13}$$

Thus from equation 10.4 the free energy is given by:

$$F = \frac{\mu}{2\delta}\left[\alpha\gamma(\lambda_x^2 + \lambda_y^2) - 2\beta^2\lambda_x\lambda_y + \frac{\delta}{\lambda_x^2\lambda_y^2}\right], \tag{10.14}$$

which can be rewritten in the following simpler form:

$$F = \frac{\mu}{2}\left[\lambda_x^2 + \lambda_y^2 + \frac{1}{\lambda_x^2\lambda_y^2} + \eta(\lambda_x - \lambda_y)^2\right], \tag{10.15}$$

$$\text{where} \quad \eta = \frac{\Delta l^2 \sin^2(2\theta_0)}{4 l_\parallel l_\perp}, \tag{10.16}$$

$$= \frac{(r-1)^2}{4r}\sin^2(2\theta_0). \tag{10.17}$$

In the parentheses of equation 10.15 there are three terms. The $\sin(2\theta_0)$ dependency of the third term equals zero for $\theta_0 = 0$ or $90°$ (stresses applied parallel and perpendicular to the director) giving the trace formula isotropic forms as expected by basic W&T theory. [105] For other values of θ_0 between $0°$ and $90°$ the third term raises the free energy of the system, although this will only be valid when calculating the initial material modulus as equation 10.15 is only valid for λ_x and λ_y tending tending to unity.

In order to determine the modulus from equation 10.15 we must first eliminate λ_y by minimising equation 10.15 with respect to λ_y. Doing this gives:

$$2\lambda_y - \frac{2}{\lambda_x^2\lambda_y^3} - 2\eta(\lambda_x - \lambda_y) = 0, \tag{10.18}$$

which can be rearranged to

$$(1+\eta)\lambda_x^2\lambda_y^4 - \eta\lambda_x^3\lambda_y^3 - 1 = 0. \tag{10.19}$$

Although equation 10.19 cannot easily be rearranged to give λ_y in terms of λ_x and η, it will still be of use below for determining the elastic modulus from

equation 10.15.

By differentiating equation 10.15 twice with respect to λ_x (bearing in mind the λ_x dependency of λ_y) we can find the elastic modulus. The first differentiation gives the stress

$$\sigma = \frac{dF}{d\lambda_x} = \frac{\mu}{2}\left(2\lambda_x + 2\lambda_y\lambda_y' - \frac{2}{\lambda_x^3\lambda_y^2} - \frac{2}{\lambda_x^2\lambda_y^3}\lambda_y' + 2\eta\left(\lambda_x - \lambda_y - \lambda_x\lambda_y' + \lambda_y\lambda_y'\right)\right), \tag{10.20}$$

where λ_y' is the derivative of λ_y with respect to λ_x — which we can find from equation 10.19. Differentiating equation 10.20 again with respect to λ_x gives the modulus.

$$E = \frac{\mu}{2}\left[2 + 2(\lambda_y')^2 + 2\left(\lambda_y - \frac{1}{\lambda_x^2\lambda_y^3}\right)\lambda_y'' + \frac{6}{\lambda_x^2\lambda_y^2}\left(\frac{1}{\lambda_x^2} + \left(\frac{\lambda_y'}{\lambda_y}\right)^2\right) + \left(\frac{2}{\lambda_x\lambda_y}\right)^3\lambda_y' + 2\eta\left(1 - 2\lambda_y' - (\lambda_x - \lambda_y)\lambda_y'' + (\lambda_y')^2\right)\right], \tag{10.21}$$

where λ_y'' is the second derivative of λ_y with respect to λ_x. Equation 10.21 is only valid in the limit of $\lambda_x = \lambda_y = 1$ where the original assumptions of no director rotation and no change in the nematic order parameter are valid. Thus equation 10.21 simplifies to

$$E = \mu\left[4\left(1 + (\lambda_y')^2 + \lambda_y'\right) + \eta(\lambda_y' - 1)^2\right], \tag{10.22}$$

$$= \mu\left[(4 + \eta)(\lambda_y' - 1)^2 + 12\lambda_y'\right]. \tag{10.23}$$

Our final result can be obtained by returning to equation 10.19, differentiating it with respect to λ_x and using the condition $\lambda_x = \lambda_y = 1$. This result can be used to remove λ_y' from equation 10.22

$$2\lambda_x\lambda_y^3(1 + \eta)(\lambda_y + 2\lambda_x\lambda_y') - 3\eta\lambda_x^2\lambda_y^2(\lambda_y + \lambda_x\lambda_y') = 0, \tag{10.24}$$

$$2(1 + \eta)(1 + 2\lambda_y') - 3\eta(1 + \lambda_y') = 0. \tag{10.25}$$

Which rearranges to give

$$\lambda'_y = \frac{\eta - 2}{\eta + 4}. \tag{10.26}$$

Inserting this into equation 10.22 and rearranging gives our final result

$$E(\theta_0) = 12\mu \left(\frac{1+\eta}{4+\eta} \right), \text{where} \quad \eta = \frac{(r-1)^2}{4r} \sin^2(2\theta_0). \tag{10.27}$$

The $2\theta_0$ periodicity of this equation means the elastic moduli at 0° and 90° are both equal to 3μ and the $\sin^2$ dependency means the equation is symmetric about $\theta_0 = 90°$. Both of these features were expected of this final result as it means the final result agrees with expectations of the Gaussian theory and that it has the correct symmetries for degenerate orientations of the director.

Comparing measured elastic moduli to predictions from simple models

Figure 10.7 (overleaf) shows the elastic moduli from the last column of table 10.1, normalised with respect to (*i.e.* divided by) the value recorded for the 89° sample. For the 70° and 89° sample the moduli from fits to the low strain data points are used as their fits were more accurate. The expected anisotropy is seen by the fact that the modulus for the 2° sample is about 3.2 times that of the 89° sample. However, the variation of the modulus for intermediate angles has two surprising features. The first is the fact that as the initial director angle is increased above 2°, the elastic modulus also appears to undergo a slight increase, whereas a decrease would be physically intuitive. The second surprise is almost the opposite of the first surprise — as the director angle is rotated from 89° toward the stress axis, the elastic modulus *decreases* instead of the physically intuitive increase. Our findings appear to some extent to be consistent with the load curves reported by Ware *et. al.* which show that the maximum modulus of their LCE was not seen for stresses applied parallel to the director. However, the authors did not comment on this result.

Also plotted in figure 10.7 are the predicted variations of the initial elastic modulus according to the two models described above. The first of the plotted models (solid line) is the "typical anisotropic property" model from equation 10.3

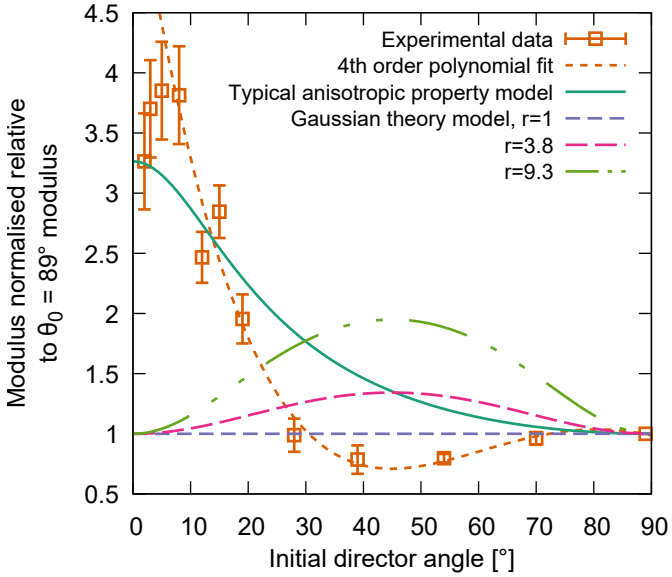

Figure 10.7: The initial elastic moduli of the LCEs from table 10.1 relative to (normalised with respect to) the value for $\theta_0 = 89°$. For the $\theta_0 = 70°$ and 89° samples moduli are from low strain fits. Solid line plots the model from equation 10.3. The last three curves from the legend plot the form of the moduli given by equation 10.27 for several key values of r. The minimum of the 4^{th} order polynomial fit is $\theta = 44.7°$.

but normalised with respect to the moduli recorded for the 89° sample — that is $E_\parallel = {}^{E_2}/_{E_{89}} = 3.2$ and $E_\perp = 1$. While this model does not account for the two surprising features of the experiment data described above, it does broadly agree with the observation of greater initial moduli for angles closer 0°.

Three curves generated from the Gaussian model have been plotted for values of r of 1, 3.8 and 9.3. For this model the moduli have all been normalised with respect to the isotropic rubber modulus 3μ. $r = 1$ corresponds to the case of an isotropic rubber and is shown to confirm that the model derived shows a constant normalised modulus of unity as it should do. The other two values were calculated for LCE A in chapter 7 from thermal testing ($r = 3.8$) and from applying the MFT model to the director reorientation of the 89° sample ($r = 9.3$). We can see that the model derived agrees in part with the experimental data by the fact that the modulus increases as the initial director angle is increased

from 0°. However, the rate of increase of the modulus is underestimated. Beyond this similarity the curves significantly disagree with the experimental data. For instance models predict the elastic modulus to be symmetrical about a maximum at $\theta_0 = 45°$, whereas the experimental data has a minimum at 44.7° (found from the fitted polynomial) and is far from symmetric about this point. While we knew that the Gaussian model would not show the expected differences between the moduli for stresses parallel and perpendicular to the director, it is surprising that it shows such disagreements with almost all aspects of the experimental data.

While the models presented significantly differ from the experimental results, the data and aspects that agree may be helpful for informing theoretical developments which can account for the variation in moduli observed.

The above analysis of the initial elastic moduli highlights the fact that despite the successes of the W&T theory at explaining the variety of mechanical behaviours of LCEs, many areas still remain open for investigation and explanation. As we evidently cannot account for the initial moduli observed for each material (never mind the following non-linearities) we believe an empirical approach to predicting the mechanical behaviours observed may be an easier tool to develop and may be still be useful for designing the target AIOL device.

10.3.2 Director rotation behaviour

In the previous section we were able to fit all the load curve data quite accurately with a single function. Achieving a similar result for the strain dependence of the director orientation will allow us to relate the elastic moduli for each curve to the director angle. In chapter 7 we deduced that the deformation mode of LCE A is better described by the W&T model of a MFT as opposed to the model of SSE, thus it is sensible to first consider the predictions of director rotation made in the MFT model. Bladon *et. al.* derived the following equation for describing the director orientation, θ, (relative to the stress axis) based on the initial director angle relative to the stress axis (θ_0) and the applied deformation, λ_x, [16]

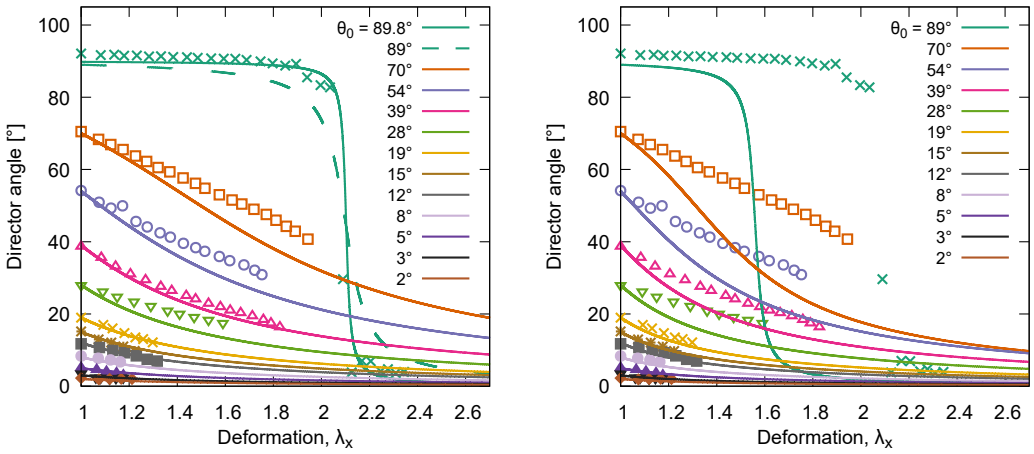

(a) (b)

Figure 10.8: Director orientation curves plotted against the deformation, $\lambda_x = \epsilon_x + 1$, parallel to the stress axis. Points correspond to experimentally measured points. Calculated curves are generated using equation 10.28 and $\lambda_c = r^{1/3}$ with a) $r = 9.3$ and b) $r = 3.8$ — key values of r deduced in chapter 7. For b) two calculated curves are shown for the near-perpendicular case.

$$\tan(2\theta) = \frac{2 \times (\lambda_c^3 - 1) \times \lambda_x^{3/2} \times \sin(2\theta_0)}{(\lambda_c^3 + 1)(\lambda_x^3 - 1) + (\lambda_c^3 - 1)(\lambda_x^3 + 1)\cos(2\theta_0)}, \tag{10.28}$$

where λ_c is the critical deformation for director reorientation in the MFT model. As described in chapter 4 the MFT model relates the critical strain for director reorientation to the step length anisotropy, r.

Figure 10.8 plots the model from equation 10.28 against the experimental data from figure 10.3. While it is clear from the experimental data for $\theta_0 = 89°$ shown in figure 10.3 that $\lambda_c = 2.1$ (model plots given in figure 10.8(a)), for comparison we also show in figure 10.8(b) curves generated by using the value of $r = 3.8$ — calculated from thermal tests in chapter 7. We also note here that equation 10.28 is once again based upon the assumption that the LC order parameter remains constant throughout the mechanical deformation.

From figure 10.8 we first consider the 89° data and associated curves. The curve for $r = 9.3$ agrees with the experimental data much more closely than that for $r = 3.8$. This result is not particularly surprising given that equation 10.28 was developed to account for the MFT-type behaviour. In figure 10.8(a) we have plotted curves for $\theta = 89°$ and 89.8° to show the sensitivity of the curve shape to angles close to 90°. Since the experimental error on the angular measurements is ±1°, we see that this sample may actually have been oriented closer to 90° than recorded.

Turning our attention to the rest of the data we also see that the rest of the curves of figure 10.8(a), agree very well with with the measurements, especially for smaller initial director angles. By comparison there is little agreement between the curves and data shown in figure 10.8(b) for samples with initial director angle $\geq 19°$.

Taking the director rotation behaviour of LCE A to be accurately described by equation 10.28 with $r = 9.3$ we can now link the elastic moduli to the director angle and remove the strain dependency.

10.3.3 The director-moduli relationship

By rearranging equation 10.28 to give the strain as a function of current and initial director angles and inserting this into equation 10.2 above, we can plot the elastic modulus against director angle for each experiment (figure 10.9 overleaf).

The most striking feature of figure 10.9 is that for the range of director angles between 15° and 70°, the plotted curves largely overlap with one another. This means that over this range of director angles, the elastic modulus of LCE A is predominantly dependent on the current director angle present and that strain dependencies are a secondary contribution which can be decoupled from the observed behaviour. In turn this implies that in the region of overlapping curves, imposed stresses only cause the polymer conformation (and hence step length tensor) to rotate and not be deformed, as deformations of the polymer conformation

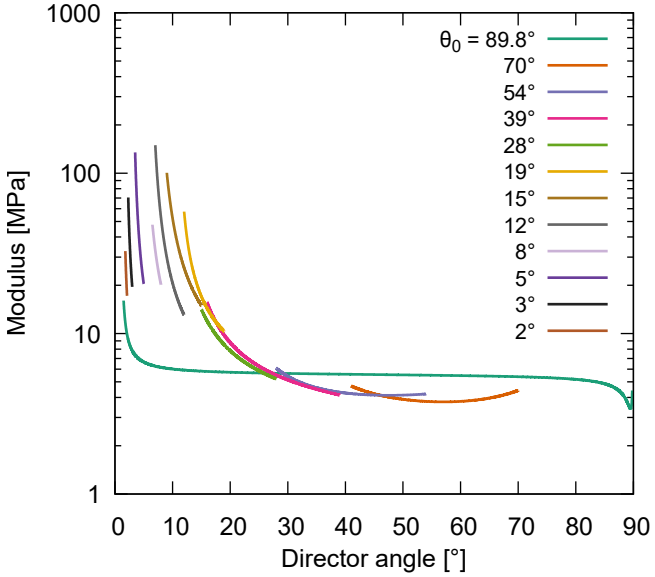

Figure 10.9: Curves of the elastic moduli of LCE A against the director angle. The function derived from equations 10.2 and 10.28 used to generate this data have only been plotted over the domain of director angles recorded experimentally (figure 10.3).

would change the step length anisotropy and hence the stress-strain behaviour. Moreover, as the polymer conformation shape and tensoral LC order parameter are intrinsically linked, we can conclude that the LC order parameter remains constant for deformations within this region of director angles.

The consequence of this result is that the nematic free energy should be constant for deformations of LCE A where the director angle is between 15° and 70° which vastly simplifies the complexity of the theory that would be required to describe the behaviour.

By comparison, for initial director angles less than 15°, the director rotates by much smaller amounts and the curves no longer overlap with one another. Therefore the deformation of the polymer conformation dominates the non-linear mechanical behaviour observed. The shape of the 89° curve is more difficult to interpret as the majority of the plateau-like region of the curve corresponds to a relatively small change in strain and so much of the behaviour is confined to

extremes of the curve. However, what is particularly interesting is that this curve finishes with a director angle of 1.5° and an elastic modulus similar to the starting elastic modulus of the 2° curve. Essentially this means that despite the 89° sample being strained by over 100% at the point at which the director emerges parallel to the stress axis, the continued mechanical behaviour is very similar to a unstrained LCE stressed parallel to the director.

10.4 Master curves, empirical equations and modelled deformations

Figure 10.9 showed us that for director angles between 15° and 70° the tensile load curves plotted in figure 10.5 had equal gradients at corresponding points of matching director angle. It is therefore reasonable that the curves should follow on continuously from one another if they are translated such that points of equal director orientation are matched. Thus it should be possible to create a "master load curve" for generic uniaxial deformations within this region of director angles — from which generic deformations of LCE A could be predicted solely from the initial director angle and the applied stress.

In order to match the positions of the true stress load curves based on director orientation, the horizontal "translation" strains of each curve must first by identified. To this end, a "master director curve" for the director orientation-strain curves was first created. A linear function as opposed to equation 10.28 was fitted to each curve as over the range of director angles seen, the curves appear sufficiently linear. Moreover, the linear function is much simpler than equation 10.28 and is therefore far easier to work with. As there are a range of overlapping director angles between the curves, the midway of overlapping angles was chosen as the angle on which to base the strain translation of each curve. This was done for the 54° and 70° curves by taking the average of the last recorded angle of the 70° curve (40.7°) and the first recorded angle of the 54° curve (which by definition is 54°) and finding the strains corresponding to this average angle (47.4°) for both

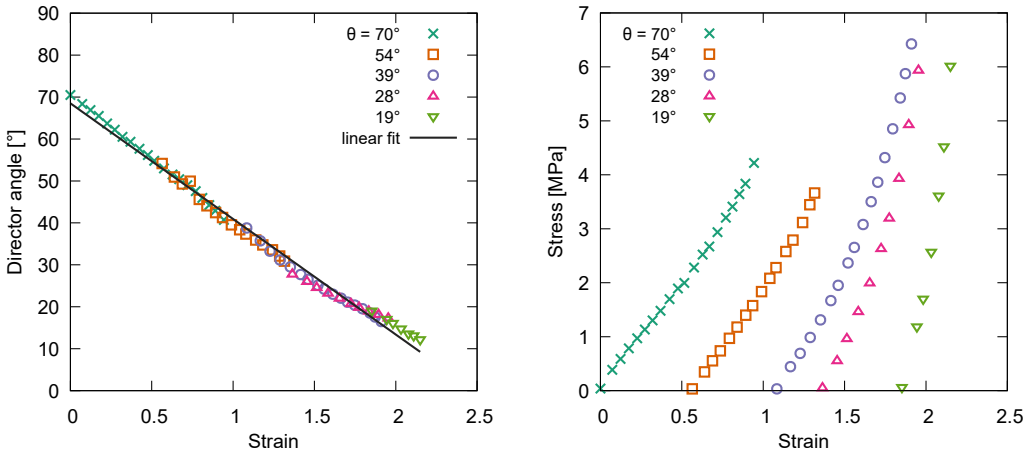

(a) (b)

Figure 10.10: a) Master director curve formed by translating individual curves to overlap with on another. b) The true stress load curves translated by the same amounts to position where they are expected to have matching gradients (elastic moduli).

of the fitted curves. The difference between the two determined strains gives the horizontal translation strain by which the 54° director orientation and load curve needed to be translated along the strain axis.
Translation strains calculated between subsequent pairs of director orientation-strain curved were summed to previously calculated translation strains in order to give the total translations required for each load curve. Figure 10.10(a) shows the final master director curve following the translation of the director orientation curves of figure 10.3. A linear curve fitted to this master director curve has the form

$$\theta = 68.5 - 27.6 \times \epsilon\,. \tag{10.29}$$

Figure 10.10(b) shows the corresponding result of translating true stress load curves of figure 10.2(b).

According to figure 10.9, the translations applied to the load curves in fig-

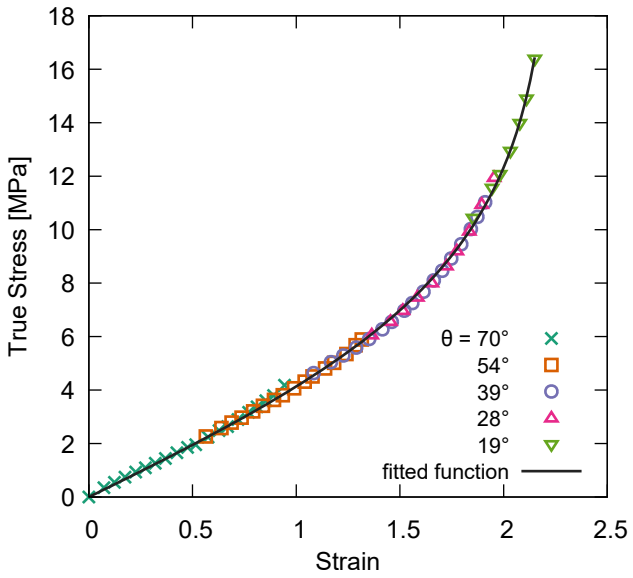

Figure 10.11: Master curve from which generic deformations of LCE A with director angles between 15° and 70° can be deduced.

ure 10.10(b) should now mean that for any given strain where two curves overlap, the gradients of each load curve should be equal. Therefore, by translating the load curves along the stress axis to the point where they meet, they should have equal gradients and the curves should follow on continuously from one another resulting in the final "master load curve". In a similar manner to the process used above to translate curves along the strain axis, translation stresses were calculated using the fitted inverse sigmoidal functions and the matching strains for pairs of director orientation-strain curves. The difference of the stresses calculated from the matching strains gives the relative stress translation of neighbouring load curves. Sequential summing of these stresses gives the total vertical translation of each load curve required to create the master load curve. Figure 10.11 plots the final master load curve generated by translating the load curves shown in figure 10.10(b).

Figure 10.11 shows that the the director-modulus plot of figure 10.9 correctly predicted the existence of a master load curve describing the tensile behaviour of LCE A for director angles of between 15°–70° relative to the stress axis. The

gradients between the curves match exceptionally well with the result being a single seamless curve. Portions of this master load curve could be used to plot the expected load curve for LCE A stressed at an arbitrary angle between 15° and 70° to the director.

10.4.1 An empirical model?

Given that we have two continuous curves linking the evolution of the director orientation and the stress within LCE A to imposed strains, we now look to develop an empirical model from which the behaviour of LCE A under arbitrary uniaxial deformations can be predicted.

We have already seen above in figure 10.10(a) that the master director curve is be well-fitted to by the linear function described by equation 10.29. The overall shape of director-modulus superposition curve is similar to the inverse sigmoidal form of the original load curves shown in figure 10.2(b). Fitting the master load curve with an inverse sigmoidal function results in the following function

$$\sigma = 4.39 \times \log\left(\frac{1 + 0.426\epsilon}{1 - 0.444\epsilon}\right). \tag{10.30}$$

For clarity, we proceed with the forms of the master load curve equations with the numerical constant replaced by symbols:

$$\sigma = A \times \log\left(\frac{1 + c\epsilon}{1 - d\epsilon}\right), \tag{10.31}$$

$$\theta = \alpha - \beta\epsilon. \tag{10.32}$$

If we are to specify a particular initial director angle, θ_i, between 15° and 70°, we can rearrange equation 10.32 to identify the starting strain, ϵ_i, of the master load curve.

$$\epsilon_i = \frac{\alpha - \theta_i}{\beta}. \tag{10.33}$$

This strain can be fed into equation 10.31 to determine the"zero" stress level, σ_i, from the master load curve.

If a graph of the master load curve was now plotted with the origin placed at (ϵ_i,σ_i) the resultant curve in the positive quadrant would correspond to the expected tensile load curve of a sample of LCE A prepared with a director of θ_i.

A *true* stress of Σ_T applied to this sample will take us to the final stress, σ_f

$$\sigma_f = \sigma_i + \Sigma_T, \tag{10.34}$$

on the master load curve. Inserting equation 10.31 gives

$$\sigma_f = A \times \log\left(\frac{1 + c\epsilon_i}{1 - d\epsilon_i}\right) + \Sigma_T, \tag{10.35}$$

where ϵ_i is given by equation 10.33.

To find the final strain on the master load curve we can insert this final stress into the inverted form of equation 10.31

$$\epsilon_f = \frac{\exp(\sigma_f/A) - 1}{d \times \exp(\sigma_f/A) + c}. \tag{10.36}$$

Finally by inserting equation 10.35 into equation 10.36 and using equation 10.33 the final strain, $\Delta\epsilon$, can be determined using

$$\Delta\epsilon = \epsilon_f - \epsilon_i. \tag{10.37}$$

Given the linear relationship of the collapsed director-strain curve in figure 10.10(a) we can also relate the amount of director rotation, $\Delta\theta$, to the strain determined through equation 10.37

$$\Delta\theta = \beta \times \epsilon. \tag{10.38}$$

The ease with which the above relationships have been derived has been down to the simple forms of the master director and load curve equations which are readily inverted.

10.4.2 Testing the model

Tensile load curves can be generated from the model by rearranging equation 10.35 to, for instance, calculate the engineering stress, Σ_E based on the initial director angle and an imposed strain $\Delta\epsilon$

$$\Sigma_E = \frac{1}{1+\Delta\epsilon}\left[\sigma_f - A \times \log\left(\frac{1+c\epsilon_i}{1-d\epsilon_i}\right)\right], \tag{10.39}$$

$$\text{where } \sigma_f = A \times \log\left(\frac{1+c(\epsilon_i+\Delta\epsilon)}{1-d(\epsilon_i+\Delta\epsilon)}\right), \tag{10.40}$$

where ϵ_i is calculated from equation 10.33 using the initial director angle θ_i.

Figure 10.12(a) uses equation 10.39 to generate expected load curves for the samples of LCE A with initial director angles between 15° and 70° which were experimentally measured. For comparison the original data is also plotted. The remarkable agreement between the model and the experimental data proves the accuracy of the model and demonstrates its potential for predicting the deformation behaviour for LCEs with more complex director geometries.

In figure 10.12(b) we show how the equations of the model can be used to generate alternative representations of the deformation behaviour of LCE A. Here the curves show the expected strain changes with initial director angle for various true stresses applied. This representation could be useful for designing a device if the target true stress for a system is known and a target strain is required. The correct director angle can then be found by generating the relevant curve. Moreover, as equation 10.38 shows the director rotation is proportional to the strain of the sample, the final director angle can also easily be extracted from figure 10.12(b) *via* the right hand axes. As one would have expected, figure 10.12(b) shows that larger director rotations can be obtained by applying larger stresses and by increasing the initial angle between the director and the stress axis.

The presented form of the model is, however, not without limitations. If one aims to design a device based on a stress which can be applied, then it will be the

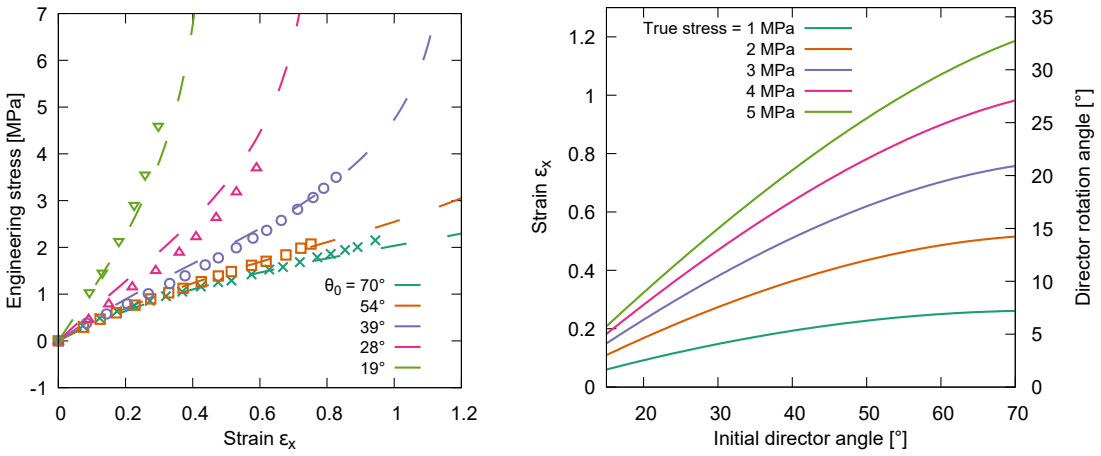

(a) (b)

Figure 10.12: a) Verification of the accuracy of the model developed by regenerating load curves for the original mechanical responses and comparing them to the experimentally measured data. b) Alternative representation of the empirical model which would be useful for predicting deformations and the director response based on applied true stresses and initial director angles.

engineering stress that would be known as opposed to the *true* stress. Equivalent versions of the equations used to generate figure 10.12(b) cannot be derived analytically as this would require inverting equation 10.39 to have the strain, $\Delta\epsilon$ as a function of Σ_E and θ_i which is impossible. Instead the modified version of equation 10.39 would need to be solved numerically. This would be achievable through a computational model based on these equations.

10.4.3 Extending the model to geometry changes

Another important aspect required for the design of the AIOL is being able to predict the geometrical changes that will result from an applied stress. The transverse strains of the 15°–70° (replotted in figure 10.13 overleaf) samples show different forms, however to a first approximation we can describe them by a single linear curve that is constrained to pass through the origin. Fitting to the curves

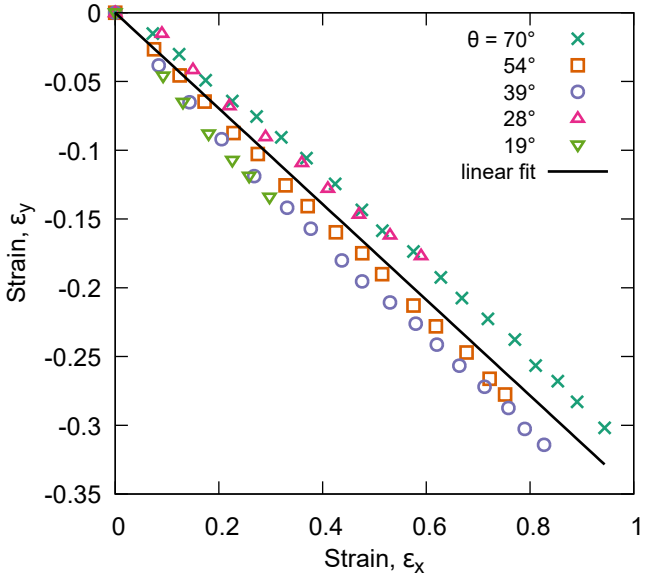

Figure 10.13: Transverse strains along y for the $19 - 70°$ samples replotted from figure 10.4(a) along with a linear fitted line which, to a first approximation, each of the curves follows.

gives:

$$\epsilon_y = -0.35 \times \epsilon_x \,. \tag{10.41}$$

Using this alongside equation 10.37 we can attempt to predict the transverse strain along y in response to an applied true stress. Predicted deformations are plotted in figure 10.14(a) against the original data. Figure 10.14(b) shows similar plots for deformations along z predicted *via*

$$\epsilon_z = \frac{1}{(\epsilon_x + 1)(\epsilon_y + 1)} - 1, \tag{10.42}$$

which makes use of the fact that LCE A deforms at constant volume.

While the predictions of figure 10.14 are comparatively worse than the level of agreement between the predicted longitudinal strain with stress shown in figure 10.12(a), they still offer a reasonably good model which could still be useful for a first prediction of the complete geometry changes of LCE A under deformation. The predictions here appear to have been affected by the assumption

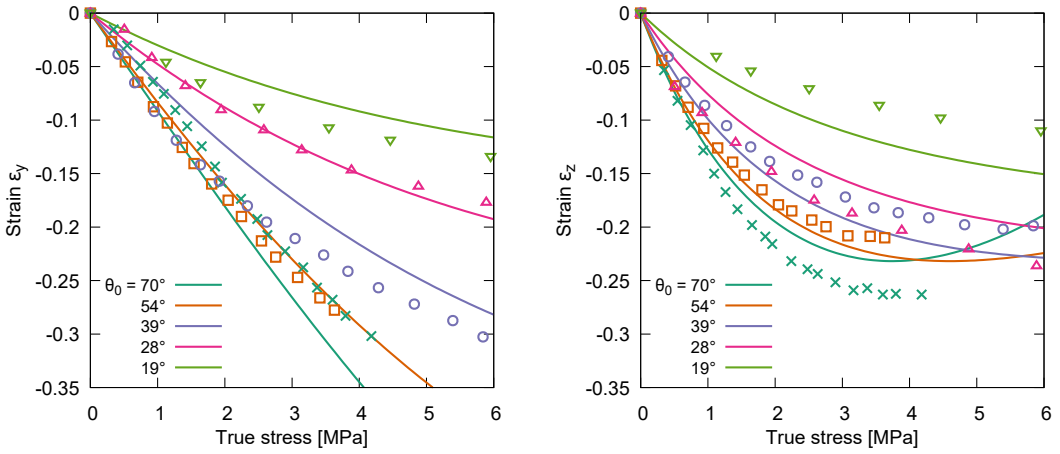

Figure 10.14: Predictions for the transverse strains along the a) y and b) z axes compared against experimentally measured strains.

that the original deformations along the y axis with strain could be approximated by the linear function. Evidently the additional complexities of the $\epsilon_y - \epsilon_x$ relationship would need to be taken into account for accurate prediction of complete geometrical changes.

Interestingly the curves shown in figure 10.14(b) suggest that the 54° and 70° samples would have displayed auxeticity had they not failed when they did. The auxeticity for LCE A stressed perpendicular to the director was discussed in chapter 8, however the results here suggest that the auxetic response of the LCE could also be tuned by controlling the angle between the applied stress and the director. Theoretically, the predictions of auxeticity by W&T apply to stresses applied perpendicular to director — stresses at other angles remain uninvestigated.

10.5 Conclusion

In this chapter we have seen that the mechanical richness of LCEs extends yet further when we consider stresses applied at angles other than the well studied cases of parallel or perpendicular to the director. By using the bespoke equipment developed in thesis we have been able to probe the mechanical response in these new geometries with a far greater level of detail than has previously been reported. The complexity of the results again demonstrates the importance of studying both the director orientation and the tensile mechanical properties of LCE simultaneously. If we had not taken this approach in this work then it would not have been possible to develop the empirical model for the deformation behaviour of LCE A.

In terms of the fundamental physical properties of LCE A we have once again been able to discuss what the value of the step length anisotropy is for LCE A. We have seen that the director rotation behaviour agrees well with the theoretical model of Bladon *et. al.* when the value of $r = 9.3$ is used. By comparison, using $r = 3.8$ gave curves which vastly differed from the recorded behaviour. [16] In this chapter we have seen that the assumption of a constant order parameter may be valid under certain circumstances by the fact that the moduli-director curves of figure 10.9 overlap with one another remarkably well over the range of director angles between 15° and 70°. However, the mechanical behaviour of LCE A is still clearly highly complex as the attempted description of the initial elastic moduli for each sample *via* simple theoretical models was decidedly unsuccessful. We anticipate that the mechanical behaviours of other LCEs stressed at arbitrary angles will show similar levels of complexity but which may be quite different to the complexity seen here for LCE A.

In this chapter we have also learned a great deal relevant to the design of the target AIOL. Most importantly we have seen that the modulus, non-linearity and geometry changes of LCE A are widely tuneable *via* the orientation of the director relative to the stress axis. From this we conclude that LCE A shows a promising level of controllable mechanical properties for application to complex mechanical

devices such as the target LCE AIOL. Additionally the biggest and most striking range of moduli variations occurs for initial director angles between $\sim 5°$ and $\sim 45°$. Consequently the greatest in contrast in strains and deformations could be achieved using director angles within this range, a useful consideration for designing patterned director geometries. The development of a fairly accurate empirical model has been the greatest success of this chapter. Given the evident complexity of LCE A and the difficulties facing the bottom-up development of theory to describe the mechanical behaviours seen, the model offers a route by which devices could be designed now, especially if the model can be integrated into computational simulations.

10. EMPIRICAL EQUATIONS TOWARD MODELLED DEFORMATIONS

Chapter 11

Toward programmed complex mechanical deformations of LCEs

11.1 Introduction

In the introductory chapters of this thesis we identified the use of programmed deformations as a route for realising functional "mechano-LCE" devices such as the target AIOL device. Our conclusion was based upon the evident mechanical anisotropy of LCEs which can be spatially programmed through techniques such as photoalignment.

In this chapter we seek to study in detail the deformation behaviour of a complexly-aligned film of LCE A using the powerful equipment and methods already developed in this thesis. Of particular interest is understanding how complex geometries can be mechanically induced and further, what we can deduce about the stress distribution in the film through application of the empirical model derived in the previous chapter. The results of this chapter will inform the design of the AIOL prototype in chapter 13.

In 2012 de Haan *et. al.* made the first report of LC networks prepared with complex director geometries. The authors polymerised their LC monomer resin within cells constructed using substrates encoded with complex alignment geometries *via* photoalignment. [37] In the years since, there has been a wealth of

research into the development of alignment methods capable of patterning director geometries with increased fidelity and resolution. [164, 175, 180] In all but one of the reported cases the ultimate aim was to produce LCEs with novel shape actuations.

Only two reports of the mechanical behaviour of a complex-aligned LCE film have been published to date. The first, published by Ware *et. al.* in 2016, showed that complex director geometries could generate complex mechanical deformations. However, the paper did not consider in detail how the complex geometries were generated and how the director profile evolved during the deformation. The second, published by Godman *et. al.* in 2017, was primarily focused on reporting a new LCE chemistry. [60] The authors briefly discussed how a narrow film of LCE patterned in discrete blocks with director orientations between 90° and 0° relative to the stress axis would preferentially undergo deformations in the regions of greater initial director inclination (as one should expect). [60] Like Ware *et. al.*, the rotation of the polymer conformation in each region was not monitored. However, as little mechanical data was presented (compared to that of Ware *et. al.*), it is difficult to further study the complex deformation repored by Godman *et. al.* [166, 60]

Here, using our own results as a guide, we analyse in greater depth the deformation seen by Ware *et. al.* in order to develop a greater understanding of how complex geometries can be mechanically generated in mechano-LCE devices.

11.2 Sample preparation and experimental methods

The simplest way to produce a film of LCE with a complex director alignment is to prepare a cell (as described in chapter 5) with substrates rubbed in a circular geometry as illustrated in figure 11.1. The resultant LCE polymerised in such a cell will have a director profile of concentric rings centred on a +1 defect.

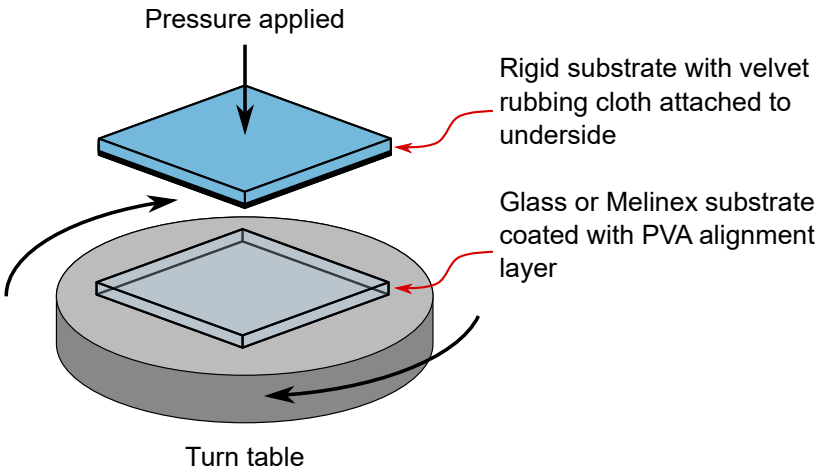

Figure 11.1: Illustration of how a director pattern of concentric circles can be achieved by rubbing the cell substrates mounted on a rotating platform (for instance a spin coater rotating at low speeds).

By carefully choosing an appropriate cut of the polymerised LCE, a film with a complex alignment can be prepared (figure 11.2 overleaf). This chosen geometry offers regions where the director orientation varies in both the x and y directions which allows us to probe a complete spectrum of mechanical behaviours using a single sample.

Figure 11.3 (overleaf) shows a polarising microscopy image of a complete film of LCE A prepared in a circularly aligned cell prior to cutting of the final strip. The appearance of the dark "brushes" forming a "Maltese cross" pattern shows the director profile has formed concentric rings about a +1 defect as expected. As it was difficult to perfectly align the cell substrates with one another, there was an offset of ~ 100 μm between the rubbing centres of each substrates. However, the effects of this are negligible as this distance was sufficiently small compared to the perpendicular distance from the centre at which the film was cut (~ 1 mm). Therefore any difference in director angle between the top and bottom substrates, and hence any twist in the nematic director throughout the film thickness, is negligible.

It is also evident from figure 11.3 that the prepared film of LCE is not a flat

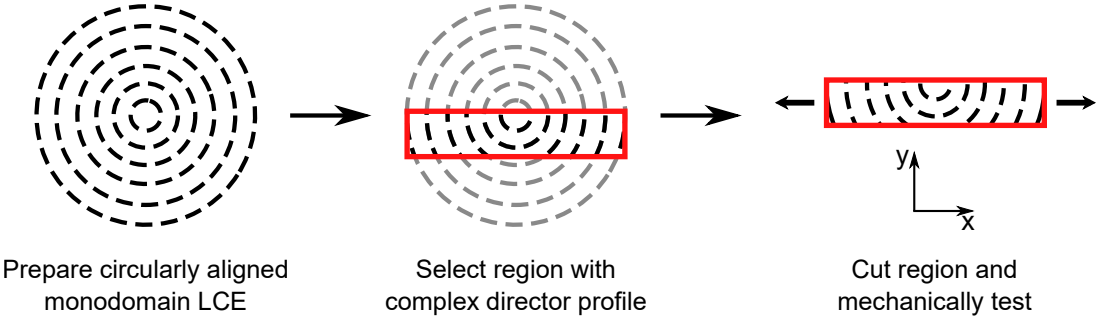

Figure 11.2: Films of complex alignment can be easily prepared by cutting a strip from the circularly aligned LCE away from the central +1 defect. If the cut included the defect then the director orientation would largely be close to $\sim 90°$ across the whole film.

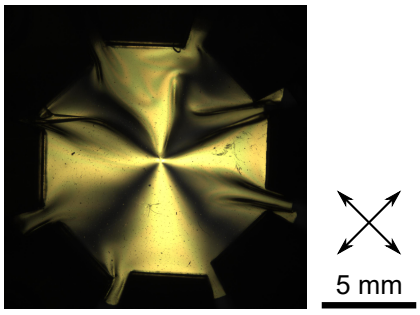

Figure 11.3: Polarising microscopy photograph of the polymerised film following de-swelling. The "Maltese cross" appearance confirms the intended director profile has been achieved, however the sample has adopted a saddle-splay geometry due to anisotropic de-swelling (figure 11.4).

sheet of material. This is a consequence of the film anisotropically de-swelling when 6OCB was removed from the polymerised (flat) LCE film during the washing step (described in chapter 6). Upon removal of 6OCB, the film contracts by a greater degree in directions perpendicular to the director compared to directions parallel to the director. Thus for a given circular path centred on the +1 defect, the radius, ρ, contracts by a greater factor than the circumference, c, such that in the final film geometry $c > 2\pi\rho$ — indicative of negative curvature. This geometrical change is illustrated in figure 11.4 which shows the final film adopts a saddle-splay geometry as opposed to a cone or spherical-cap geometry.

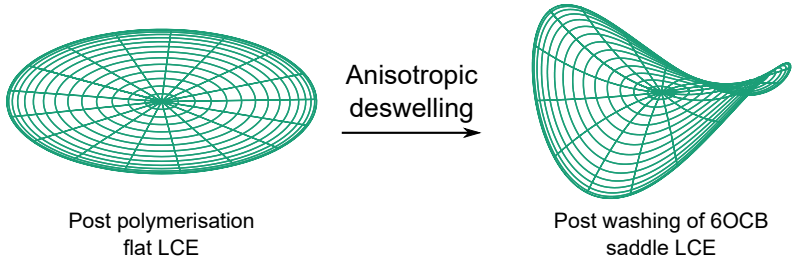

Figure 11.4: Illustration of the consequence of the anisotropic de-swelling of the LCE film caused by the washing process. A greater contraction perpendicular to the director compared to parallel results in the generation of a saddle-splay film geometry apparent in figure 11.3.

As with previous samples of LCE A mechanically tested, a strip of film approximately 2 mm wide was cut from the sample. Care was taken to ensure the saddle-like film was flattened without creases prior to cutting this sample. Despite this care, the cut strip had a slightly warped natural shape, however this was flattened out upon application of the first strain step of mechanical testing. For simplicity in the analysis of this chapter we assume any effects of the slight warping of the film to be negligible but in the conclusion we do consider its possible implications.

For consistency, the testing procedure used in this chapter was identical to to chapters 7 and 10 — *i.e.* the film (maintained at $23 \pm 2°C$) was extended in 0.5 mm steps. Between strain steps the sample was allowed to stress relax for two minutes before photographs of the sample under polarising microscopy and white light illumination were taken.

11.3 Results and discussion

In this section the raw results are first presented with a brief discussion of some intuitively deduced behaviours before subsequent analysis steps and deeper discussions exploring the deformation behaviour in greater detail.

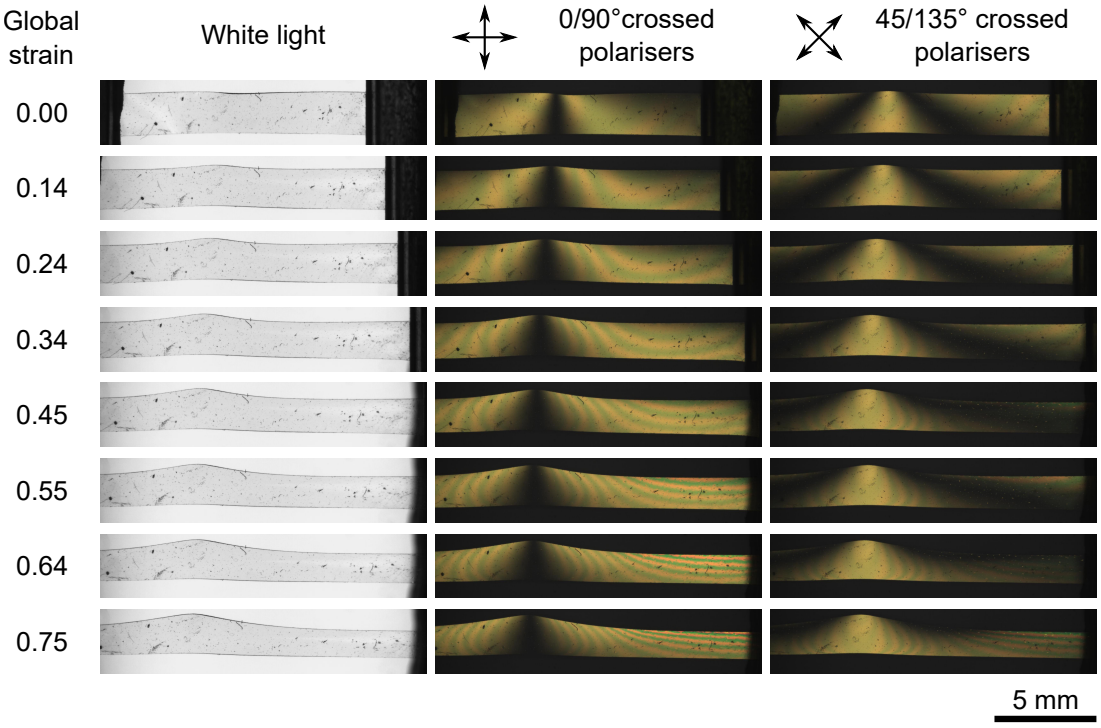

Figure 11.5: Selected photographs of the sample at every other stage of the deformation. The sample clamps are clearly visible in the top left image and disappear out of view as the strain is increased.

11.3.1 Images of sample deformation

The sample was extended by 14 steps from its unstrained state before the film tore at one of the sample clamps. Figure 11.5 shows selected photographs of the sample at every other strain step. The first column of images show the sample as seen *via* white light illumination. From these photographs it is plain to see that the sample deforms inhomogeneously as certain regions show greater thinning along their widths more than other regions. The region which has deformed the least (herein referred to as the "prominence region") must correspond to the stiffest part of the film and thus other film regions were preferentially deformed. Overall the film shape morphs from a rectangular shape to a much more complex shape where the lower edge (as shown in the photographs) remains relatively straight while the top edge instead adopts a highly curved profile.

The observed shape change seen in the white light photographs can be readily explained by considering the second columns of photographs of figure 11.5 where the sample is viewed *via* crossed polarisers oriented at 0/90° with respect to the applied stress axis. In these photographs we see that prominence region appears black which, by considering the illustration of the director profile in figure 11.2, corresponds to the director lying close to parallel to the applied stress axis. This director orientation within the region of least deformation makes sense based on the results of the previous chapter which showed that LCE A has its stiffest response when stresses are applied close to parallel to the director. We also see from the 0/90° crossed polarising photographs that the size of the region appearing black increases with applied strain. This means that as the strain is being increased, the director within the prominence region is rotating toward the stress axis. This inferred behaviour is again consistent with the director rotation behaviour observed in the previous chapter. Lastly, from the 0/90° photographs we see the birefringence colours change with strain. The change is most pronounced in the right-hand portion of the sample where an increase in the saturation of the birefringence colours is evident. A similar behaviour was observed in chapters 7 and 8 for the samples strained close to perpendicular to the director and is indicative of a reduction of the retardance, $\Gamma = \Delta n \times d$ where Δn is the sample birefringence and d the sample thickness. Based on the deductions from chapters 7 and 8 that these observations corresponded to a reduction in the LC order parameter within the plane of the film, we would assume a similar process is occurring in the right-hand portion of the present sample. However, this would need to be confirmed by direct measurement of the LC order parameter in the present sample as the progression of the birefringence colours is by comparison far less extreme than that seen in the samples studied in chapters 7 and 8.

The last column of photographs from figure 11.5 again shows the sample viewed *via* polarising microscopy, but now with the polariser and analyser oriented at 45/135° relative to the stress axis. The black brushes correspond to regions of the sample with director angles aligned parallel with either the polariser or the analyser. By considering the top photo from the 45/135° column together with the director profile illustration shown in figure 11.2, it is evident

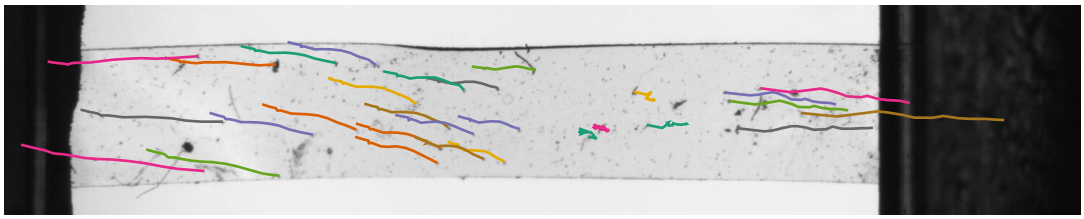

(a)

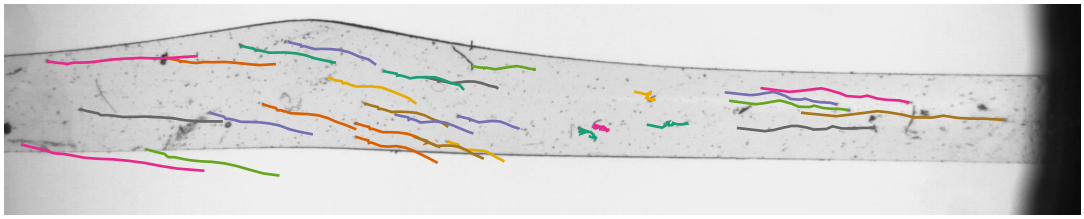

(b)

Figure 11.6: Trajectories of each tracked particle overlaid onto photographs of the film in (a) the unstrained, and (b) the maximally strained states.

that in sample regions between the observed brushes and the sample clamps, the director must be inclined at angles greater than 45° to the stress axis. As the strain is increased the brushes rotate away from the prominence region indicating the director is rotating toward the stress axis. By the final strain step the brushes have rotated almost off the top edge of the film thus the director across the film is expected to be $\leq 45°$ to the stress axis.

The above intuitive predictions of the director behaviour will be useful in assessing the accuracy of further analysis later in this chapter.

11.3.2 Particle tracking

In order to analyse the deformation behaviour of this film, it is important to be able to assess the distribution in localised strain across the sample. We have already seen section 7.2.1.1 that this is readily done using *trackpy*. As the sample under consideration has variations in the initial director orientation in both

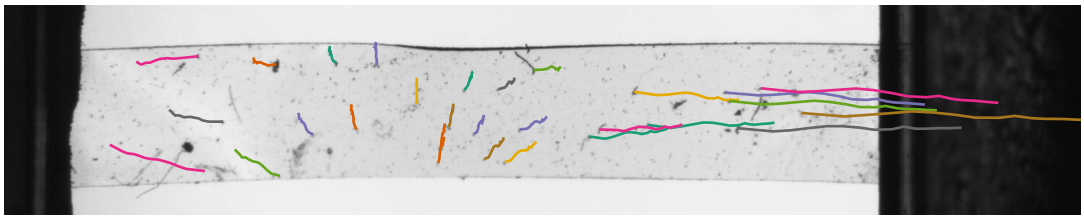

(a)

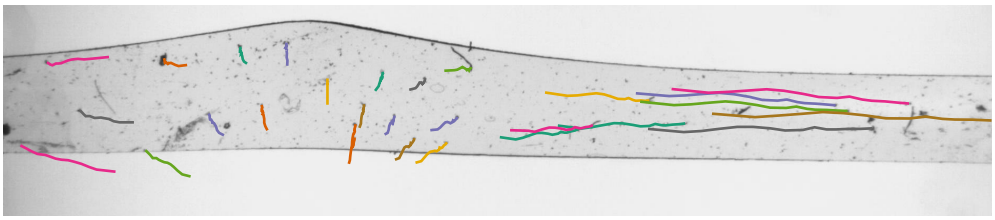

(b)

Figure 11.7: Figure 11.6 replotted with the origin of the trajectories translated to the centre of the prominence region. This replotting reveals in greater detail how the film deforms in the prominence region.

x and y directions, it was important to have many tracked particles spread out across the entire film. Therefore particle trajectories were measured in two separate runs of *trackpy* which tracked particles of different sizes, supplemented by additional particles manually tracked using ImageJ. Occasionally corrections had to be made (using ImageJ) to the errors in trajectories determined by *trackpy*. Figure 11.6 shows the trajectories of all the particles tracked overlaid onto the images of the film in the unstrained and maximally states.

The prominence region of the film shows the most interesting shape evolution with strain. However, from figure 11.6 it is difficult to interpret the deformation behaviour in this region as it moves relative to the camera position. To better understand how the film is deforming in the prominence region, figure 11.7 replots the trajectories and photographs shown in figure 11.6 relative to the centre of the prominence region. This replotting shows clearly how in the prominence

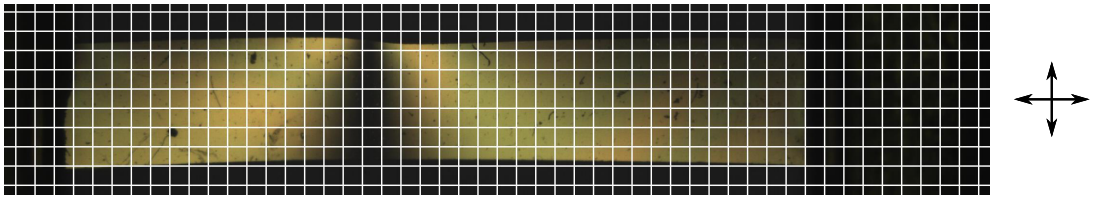

Figure 11.8: 40 × 40 px grid overlaid onto a polarising microscopy image of the film in the unstrained state. For each frame the director orientation was measured at each vertex of the grid.

region of the film there is a large transverse displacement which indicates the region is undergoing a significant shear. To either side of the prominence region the particles have divergent and bending trajectories implying these regions are undergoing both shears and body rotations. Comparatively, on the far right hand side of the film the particles are moving in comparatively uniform and parallel manner and so in this region the film is primarily undergoing a linear strain with minimal shear. Herein, the far right region of the film will be referred to as the "uniform" region to reflect the deduced deformation behaviour.

11.3.3 Spatial mapping of the director

In the section above we used the appearance of the sample *via* selected polarising microscopy images to infer the director microstructure of the film and how this evolves with strain. From this we were able to deduce an outline of the overall deformation behaviour of the film. By relating localised strains (deduced from the above tracked particles) to the local director orientation we will be able to understand the deformation behaviour in greater qualitative detail and further apply the model of the previous chapter.

To achieve this we used the director monitoring python scripts used in previous chapters (detailed in section 5.5.2) but modified to measure the director across the entirety of the film at each strain step. Figure 11.8 shows a 40 × 40 pixel (px) grid overlaid onto the 0/90° photo of the unstrained sample. For each strain step, the director orientation was measured at each grid vertex using 19×19

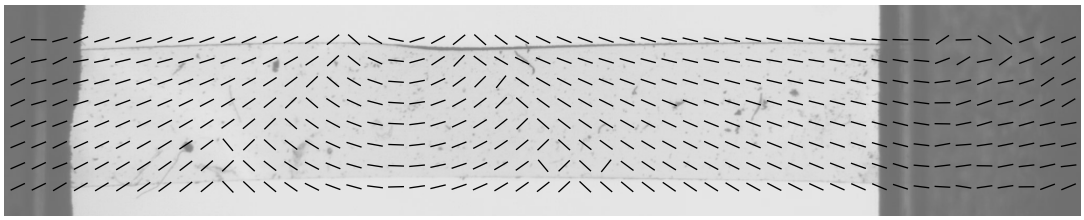

(a)

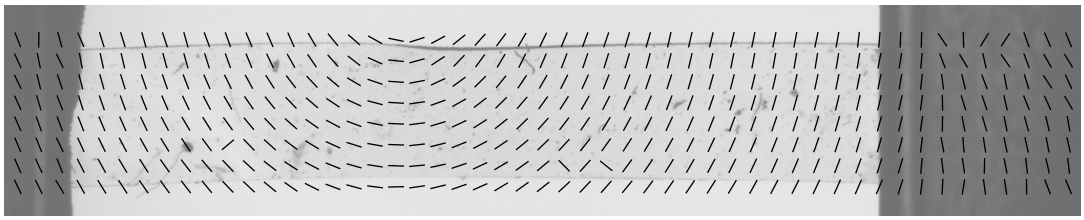

(b)

Figure 11.9: a) Quiver plot showing, for the unstrained state, the result of fitting the director orientation to polarising microscopy transmitted intensities measured at each grid point. The degeneracy of the director orientation leads to numerous discontinuities in the measured director profile which are corrected in (b). However, in (b) several anomalous points are still visible. Figure 11.10 shows the fully process data.

px measurement windows.

We recall equation 5.3 which is fitted to transmitted intensities in order to measure the local director angle

$$I = I_0 \sin^2\left(\frac{b\pi \times (\theta - c)}{180}\right) + d. \qquad \text{(5.3 revisited)}$$

From our observations we knew that the director orientation varied across the film, however the precise distribution was initially unknown. Therefore in each fit of equation 5.3, a starting director angle value of $c = 1°$ was used. The range of possible fitted director values was constrained to between $-95°$ and $+95°$, while the frequency parameter, b, was restricted to take values of between 1.97 and 2.03

with $b = 2.00$ being the theoretically expected value.

Figure 11.9(a) shows a quiver plot of the fitted director orientations for the unstrained and maximally strained states overlaid on top of the corresponding sample photograph. The small lines illustrate the local orientation of the liquid crystal director at each grid vertex as determined by the fitting. Considering the result of the fitting for the unstrained step, several issues are apparent. Firstly, on each row of figure 11.9(a) there are at least two discontinuities in the apparent director angle. Similar discontinuities are seen for the fits at other strain steps. These discontinuities are a result of the degeneracy in possible values for the fitting parameter c within the range of $\pm 95°$, with the wrong one frequently being chosen. From our preliminary analysis of the polarising microscopy photographs in section 11.3.1, we can see that the angles fitted in the prominence region are correct. Therefore the fitted orientations away from the prominence region need to be rotated by 90°. Additionally, numerous isolated points in figure 11.9(a) show anomalous director orientations which need correcting. Lastly, many grid vertices existed beyond the boundary of the film and so corresponding data points should be disregarded.

Before the fitted data could be analysed, processing was required to correct the above issues. The degeneracy related errors were corrected *via* a *python* script which added or subtracted 90° from the incorrect fitted angles, blocks of which were identified by differences in adjacent director angles exceeding 50° on a given row. Figure 11.9(b) shows, for the unstrained sample, how this first level of correction resulted in a director profile which more closely matches what was expected from the initial deductions made in section 11.3.1. The anomalous orientations still seen in figure 11.9(b) were corrected by setting their value based on the average of adjacent points from either the same column or row as the anomalous point. Lastly, data from grid vertices outside of the film boundary at each strain step were removed.

Figure 11.10 shows the final director mappings for every second strain step of the LCE after processing the fitted data. The heat map representation was

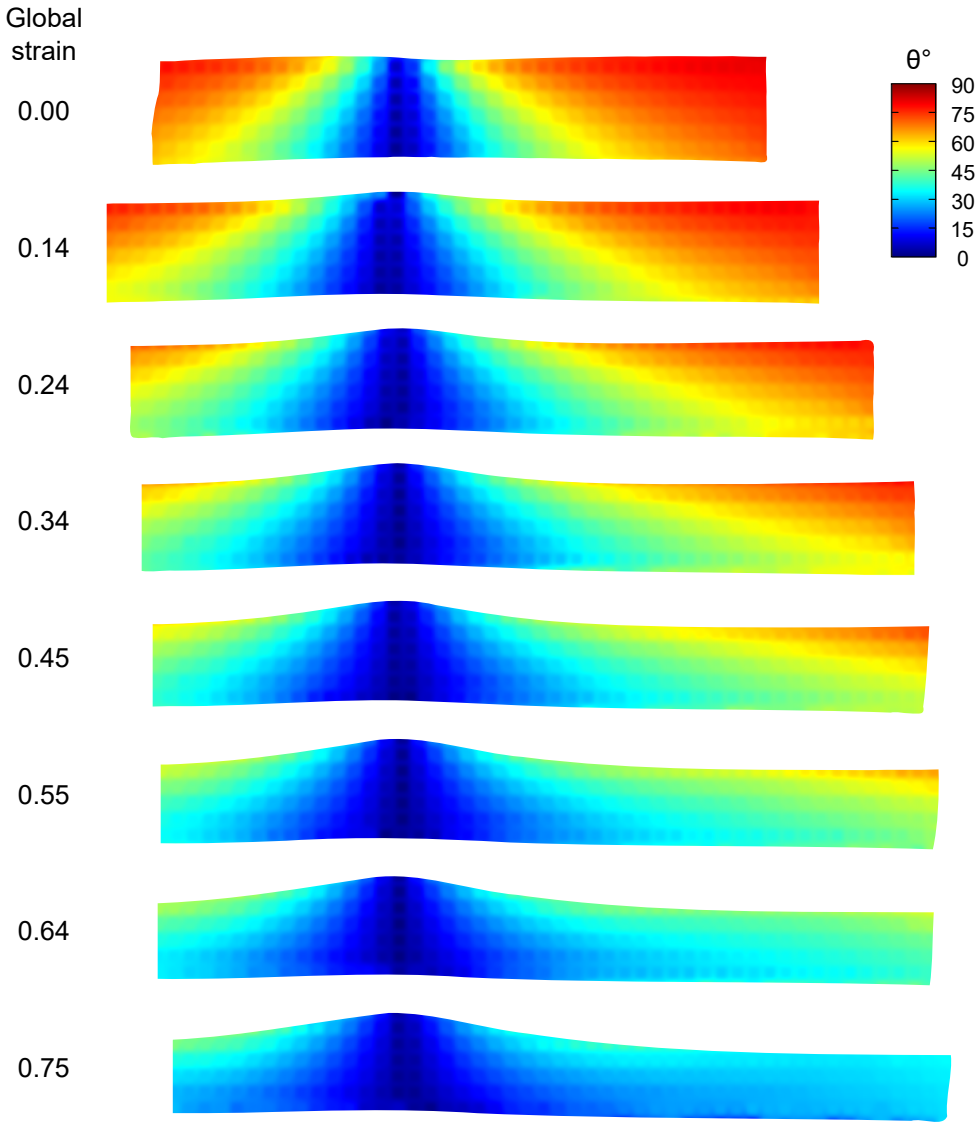

Figure 11.10: The final director profiles shown for every other strain step after all processing to remove degeneracy-related discontinuities and anomalous points. The heat map representation clearly shows the range of director angles across the entirety of the film and how the director profile evolves with strain.

chosen such that the magnitude of the director rotation with strain across the whole extent of the film could be clearly seen. The figure also verifies the predictions of director orientation and rotation made in section 11.3.1. Most notably, we see that the prominence region has a director angle closest to parallel to the

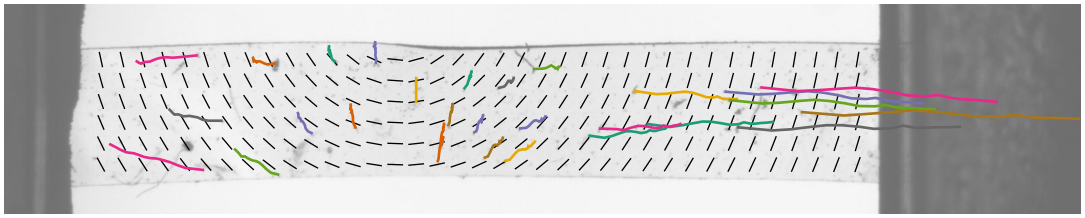

Figure 11.11: Tracked particle trajectories and quiver plot of initial director orientations overlaid on top of a photograph of the unstrained film.

applied strain axis and that the uniform region initially has director angles greater than 45° which rotate with strain to become $< 45°$ at the maximal strain step.

One of the most important aims of this chapter is to understand how to program complex shape deformations. By considering the above heat maps together with the particle trajectories shown in figure 11.7, we can see how the evolved shape profile was driven by the initial complex director profile.

The heat maps of figure 11.10 show that to the left of the prominence region the director rotates anticlockwise while to the right it rotates clockwise. At the centre of the prominence region there is zero director rotation as the director is already lying parallel to the applied stress axis. By replotting the particle trajectories from figure 11.7(a) over the director orientation map for the unstrained film (figure 11.11), we see that the result of these opposite senses of rotation is the transverse movement of the prominence region along the y axis. By comparison, in the uniform region, where there is only a single sense of director rotation, the particles show minimal shear and predominantly deform *via* a linear strain parallel to the applied strain axis.

In their investigations into the mechanical deformations of director-patterned LCEs, Ware *et. al.* were able to generate similar transverse distortions. When a strip of LCE a patterned as shown in figure 11.12 was stretched, the film developed a zig-zag like shape. Although Ware *et. al.* did not monitor the director orientation with strain, they deduced a similar reorientation process as being responsible for the shears observed.

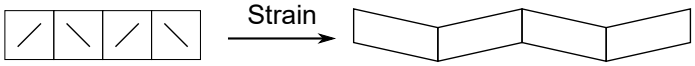

Figure 11.12: Illustration of the complex deformation behaviour for a director-patterned LCE reported by Ware *et. al.* [166] At present, the samples studied by Ware *et. al.* are the only other report of LCEs mechanically evolving complex shape profiles. The example shown here is the only sample of Ware *et. al.*'s which is feasible to comparing our results against.

By comparing the shape changes observed by Ware *et. al.* with the present system we can learn a great deal about how curvatures and shapes can be controlled and generated *via* patterning of the director. Firstly, the shape generated here has a comparatively smooth and curved profile across its length. By comparison the film of Ware *et. al.* has straight edges which turn sharply. It seems plausible that this difference is driven by the smooth and continuous director profile of the present LCE compared to the domains of alternating director orientation studied by Ware *et. al.* Secondly, the width of the Ware *et. al.* LCE appears to remain uniform across the entire longitudinal extent of the film whereas in our LCE the width varies significantly. This difference is easily attributable to the fact that in the Ware *et. al.* LCE, domains of 45/135° director orientation are essentially degenerate in terms of their stiffness and response. By comparison in our LCE, the director angle varies from 0° to $\sim 80°$ thus the deformation stiffness and response also vary spatially.

More interesting is the fact that the shape profiles for the top and bottom edges of our LCE differ significantly where as in Ware *et. al.*'s system the top and bottom edges show identical profiles. We attribute this to the fact that in our LCE, the director angle across a given width varies by typically $\sim 15°$ whereas in Ware *et. al.*'s LCE, the director is constant across any given width. Therefore while in Ware *et. al.*'s LCE, the entirety of a given film width has the same ability or "power" to generate transverse strains, in our LCE the power to generate transverse strains varies across a given width — resulting in different profiles for the top and bottom edges. Moreover, the degree to which these shape profiles differ‘’ changes along the length of our LCE. The most dramatic shape profile

difference is seen in the prominence region while the uniform region shows almost identical shape profiles. We note that although the variation in director angle across any given film width (aside from the centre of the prominence region) is typically $\sim 15°$ (figure 11.10), the typical variation in $\sin\theta$ across the film width in prominence and uniform regions differs significantly. In the prominence region ($\Delta \sin\theta \sim \sin 30 - \sin 15 \approx 0.24$) which is more than twice of that in the uniform region ($\Delta \sin\theta \sim \sin 75 - \sin 60 \approx 0.10$). We deduce that the extent of the difference between the top and bottom edge shape profiles is related to the variation in the sine of the director angle across a film width.

In chapter 13 the relationships deduced above, which link the initial director profiles and shapes generated, are used to develop predictions of novel director geometries and their deformations. These in turn are used to design a LCE devices expected to behave as a mechanically deformable lens for the target AIOL device. In the following section we now perform a deeper analysis of the results presented in this section to understand the localised deformation behaviour of the film and apply the empirical model deduced in chapter 10 to develop predictions for the stress distribution within the film in its maximally strained state.

11.4 Analysis and discussion

11.4.1 Lagrangian frame director rotations

While the above director heat maps clearly show the distribution of director angles across the whole film at each strain step, they cannot be used to map and quantify the degree of director rotation as each measurement location is fixed with respect to the camera. In order to map the director rotation across the film it is necessary to instead measure the director angle at points in the Lagrangian frame, that is, at points fixed with respect to the sample. The particles tracked above for mapping the sample deformation exist fixed with respect to the Lagrangian frame and hence can be used to provide coordinates from which to measure the director angle at each strain step.

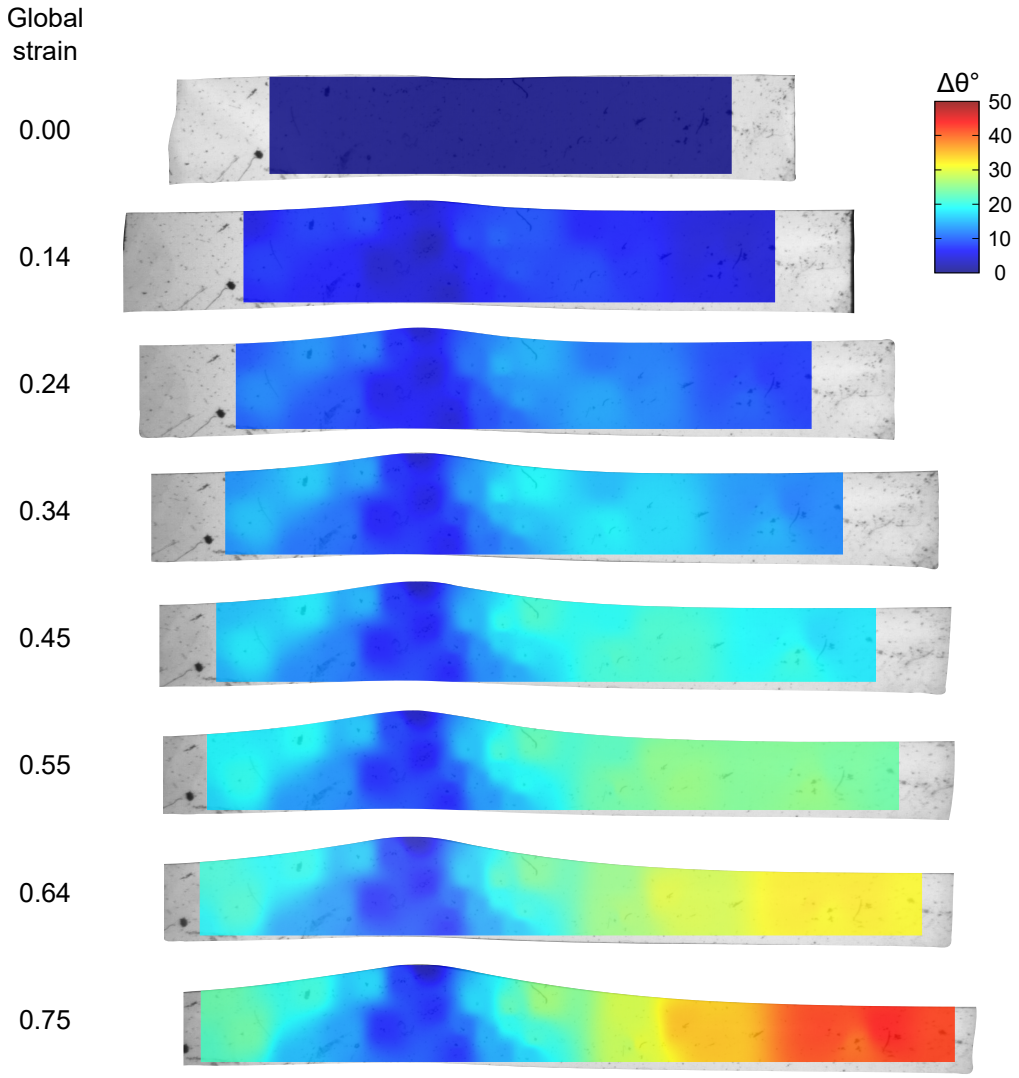

Figure 11.13: Interpolated heat maps of the magnitude of director reorientation. The strain of the film has been taken into account by measuring the director orientation at the location of tracked particles at each strain step. The heat maps are therefore in the Lagrangian frame.

By repeating the measurements of transmitted intensity with crossed polariser angle (for each particle at each strain step) and fitting for director angle, the director rotation can be mapped. Accurate director angles were determined by using the localised orientations deduced in figure 11.10 as a look-up table for the starting values of the fitted c parameter of equation 5.3. For each determined

director angle in each frame, subtracting the director angle from the first frame gives the director rotation at each particle site.

Figure 11.13 (previous page) shows, for every other strain step, heat maps for the director rotation interpolated from the measured director rotations. By comparing with the director orientation map for the unstrained LCE shown in figure 11.10, it is clear that the greater the initial director angle, the greater the magnitude of director rotation by the final strain step. However, we interestingly see from the third and fourth heat maps of figure 11.13 that initially the greatest director rotation occurs for regions which have director angles of approximately 45°. This is perhaps to be expected as in figure 10.7 on page 170 we saw that LCE A displays the lowest initial modulus when stressed at $\sim 45°$ to the director. Thus it is realistic that this region should initially undergo the greatest director rotation.

11.4.2 Mechanical behaviour and model testing

The second aim of this chapter is to apply the empirical model derived in the previous chapter to the sample tested here and determine how the model can be used to predict the stress distribution and generated shape changes for mechano-LCE devices.

11.4.2.1 Global load curve

Figure 11.14 plots the overall sample strain, measured using the separation distance between sample clamps, against applied engineering stress. True stress is not plotted as the complexity of the director geometry and film deformation renders it meaningless for the global deformation. The engineering stress reported in figure 11.14 is based on the force measured by the load cell and the initial sample cross-sectional area. The cross-sectional area was calculated from the average sample thickness (measured using a micrometer of 1 μm accuracy) and the width of the sample measured from the photograph of the sample in the unstrained state. The measurements of the sample thickness varied across the length of the sample thus an average value of 79 ± 5 μm was used. Measurements

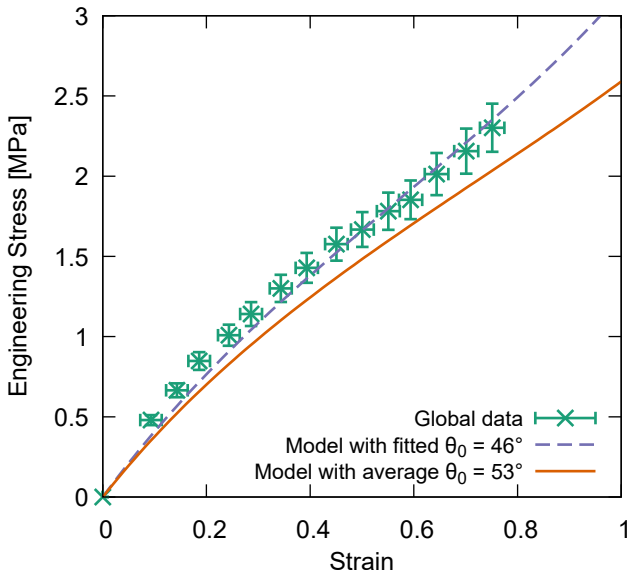

Figure 11.14: Engineering tensile load curve of the sample based on the strain measured by the separation distance between the sample clamps. The curves are plots of the model derived in chapter 10 (equation 10.39). The solid line uses an initial director angle based on the average director angle of the sample in the unstrained state while the dashed line has been fitted to the data *via* the initial director angle.

of the film widths from 5 locations evenly spread out across the unstrained film's length produced a range of values between 244 and 263 px wide. The lower of these values is anomalously low and is a result of the slight warping of the film in the unstrained state (evidenced by the "thicker" appearance of the top edge of the film halfway between the actuators — seen most clearly in figure 11.6(a) on page 194) giving the appearance of the sample being thinner in the middle region of the photograph. We therefore neglected this lower value of film width in the calculation of the average film width. The remaining measurements of the sample width spanned the range of 255–263 px and so sample width was taken to be 259 ± 4 px which is equivalent to 2.00 ± 0.03 mm.

Given the sample has a highly complex director profile, one might assume that attempting learning anything from the global load curve to be a fruitless endeavour. However, the solid line of figure 11.14 plots equation 10.39 of the empirical

model derived in chapter 10 using an initial director angle of 53°, which is the average value of the director angles measured across the unstrained film from figure 11.10. The curve is remarkably similar to the experimental data, despite the fact that the director profile across the present sample is highly complex. Consequently, it appears that crude approximations of the overall film's behaviour can be made from considering the average director angle across a film of LCE A. In device considerations this would be useful when constraints on the engineering stress or overall strain possible are known. The dashed plot in figure 11.14 shows the empirical model fitted to the data *via* the director angle as a free parameter. The resultant fitted angle of $\theta = 46°$ represents the best approximation of the film's behaviour when modelled as a film of constant director orientation.

Perhaps the most interesting conclusion to draw from figure 11.14 is that the introduction of a complex director profile has not changed the overall apparent nature of the LCE's mechanical behaviour. This is further supported by the fact the the present sample's maximum strain of ~ 0.8 is similar to the maximum strains seen in chapter 10 for samples with initial director angles of $\sim 45°$ (figure 10.2 on page 158).

11.4.2.2 Localised mechanical behaviour and load curves

The prediction of the global load curve from the average director angle of the film was surprisingly successful. However, in order to understand the film's deformation in greater detail we must consider the localised behaviour of the film. Localised load curves can be generated by measuring strains between pairs of tracked particles. Figure 11.15 on page 209 on pages 208 and 209 (spread across two pages for clarity) shows load curves from 12 such particle pairs (labelled **A1**–**H2**) distributed across the length and width of the film, along with corresponding load curves curves generated from the model as described below. In this section true stresses have been plotted as we are interested in the localised material response.

In generating these plots several several we had to carefully consider how to analyse and interpret the experimental data and make some assumptions. These are described as follows:

- The film has a spatially varying director profile in two dimensions. Ideally the localised strains should be measured using points close enough to each other such that the director could be taken as constant over the distance between points. However, doing so would give large errors in the measured strains and true stresses. Thus, particle separations were chosen to balance director uniformity with acceptably low errors.

- We assume the behaviour shown in each load curve pertains to a characteristic point located at the mid-point between the relevant tracked particles. Thus the sample thickness (see below) and director angle at the characteristic point were respectively used to calculate the true stress and to generate model load curves (central curve plotted within the shaded regions of each graph plotted in figure 11.15) for comparison. Herein this central curve is referred to as the "characteristic curve". The director angle at each characteristic point was measured using the same procedure used to measure the director angle at the particle positions (described in section 11.4.1).

- In calculating the initial cross-sectional areas for determination of stress, we must take into account the varying the film thickness noted in the preceding section. On the left hand side, centre and right hand side of the film the measured thickness was 74, 77 and 84 μm respectively. Based on this, the film thickness with longitudinal position, x, was assumed to linearly vary from 74 to 84 μm with a ± 3 μm error.

- In calculating the stress from the load cell reading at each extension step, we first calculated the engineering stress by dividing the force by the initial cross-sectional area (using a width of 2.00 ± 0.03 mm as determined in the preceding section). As in section 10.2, true stresses were calculated by multiplying engineering stresses by the longitudinal deformation ($\lambda_x = \epsilon_x + 1$) at each strain step. While this methodology is identical to that used in chapter 10, it assumes that the force distribution is spread equally across any given cross-sectional area. This assumption was appropriate in chapter 10 as the director angle was uniform across the sample. However, here we know this assumption to be, in general, false. Nevertheless, as

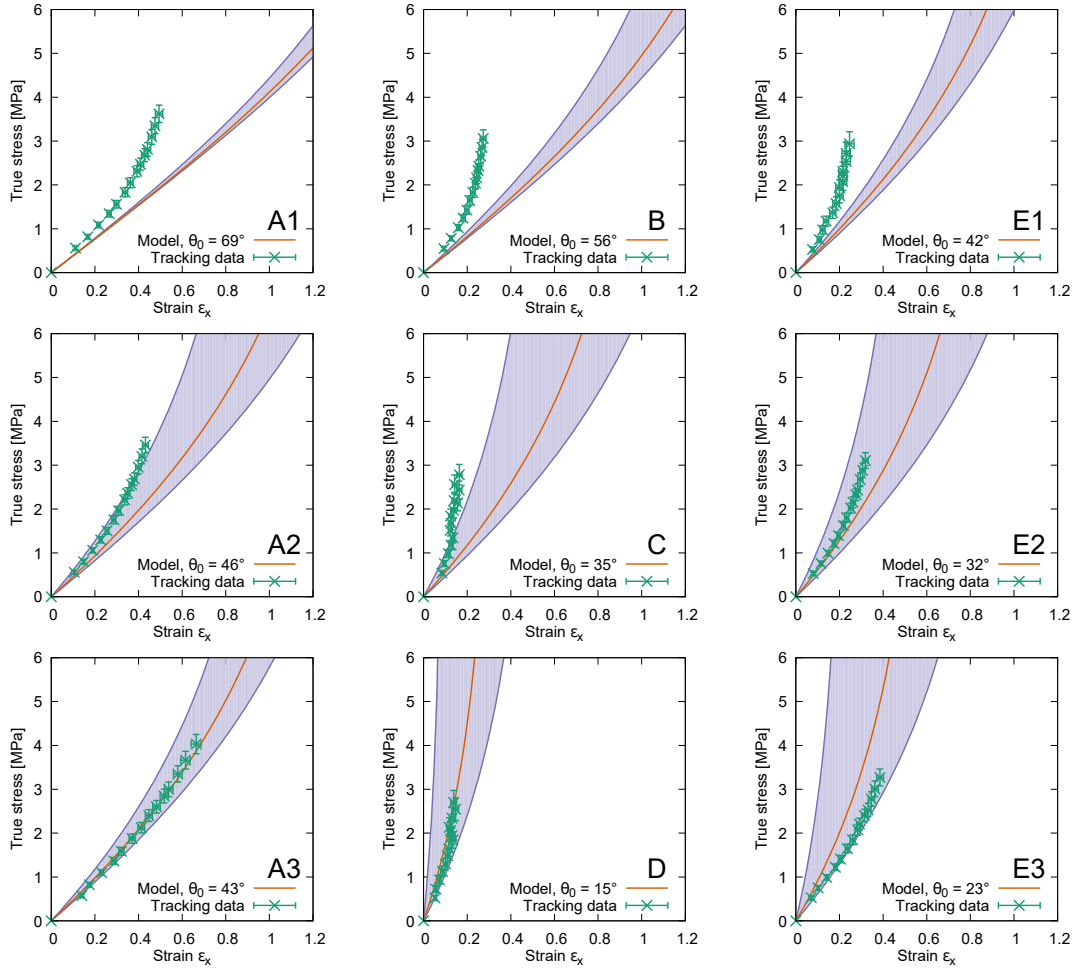

[figure caption on opposite page]

we do not know how the stress distribution within the film, we start our analysis of the localised tensile response under this assumption.

In the analysis and discussion that follows it will be important to bear in mind the above considerations and assumptions.

Alongside the data and characteristic curves plotted in figure 11.15, additional model curves are also shown which are generated using the initial director angles at the initial particle locations from each pair of particles. The shaded region bounded by these two curves represents the region in which one might expect to find the measured load curve should the last of the above assumptions (uniform

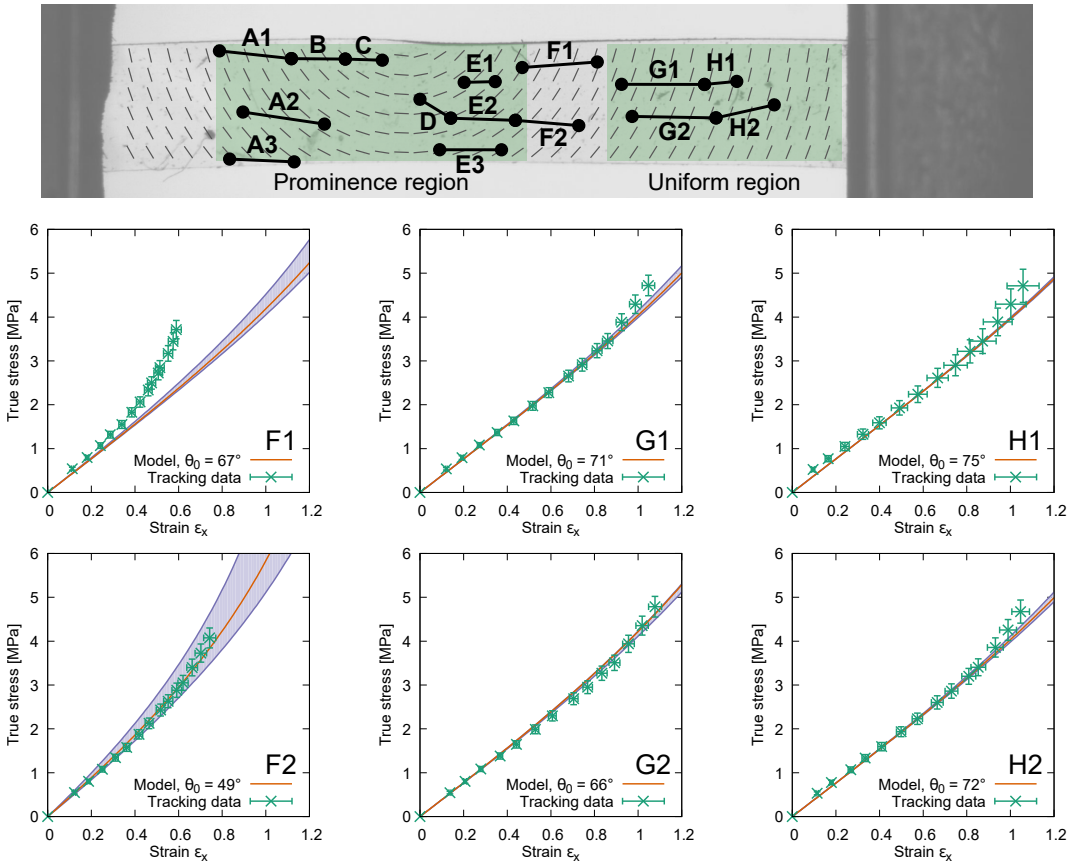

Figure 11.15: (Including graphs on opposite page) Localised load curves generated using local strains measured by the change in relative separation of tracked particles marked on the photograph. True stress tensile load curves have been generated using the model with initial director angles from: each particle used for tracking (curves bounding shaded regions), and the initial point mid-way between the tracked particles (the "characteristic" point).

force distribution) hold for a particular pair of particles. Further, if the measured data agrees with the characteristic curve, then the assumption that the director angle at the characteristic point is representative of the deformation between the tracked particles also holds.

Of the tracked pairs, those that span the width of the film at a given longitudinal position are particularly interesting as they can be used to see how the variations in director orientation across a width impacts the mechanical response. As such, groups of particle pairs which span single longitudinal position are iden-

tified by the same initial character *e.g.* **A1-3** and **F1&2**.

On a first look at the load curves plotted in figure 11.15 we see that for many locations there is close agreement between the measured data and characteristic load curves. In particular, the data from the uniform region of the film (containing locations **G1&2** and **F1&2**) show both a narrow shaded region and excellent agreement between the data and characteristic curves. Thus in uniform region the assumptions made above hold true.

By comparison, in the prominence region the data and model only agree for locations closer to the bottom edge of the film. We believe that the main reason for this is that the above assumption of a constant force distribution across the film width is far from valid for this region.

These observations can be rationalised by considering table 11.1 which gives — for the prominence and uniform regions in the unstrained and maximally strained states — the average and spread of director orientations and a characteristic range of initial elastic moduli. The spread of director angles in each region is quantified by the standard deviation of the angles measured within each region. The range of initial elastic moduli is then calculated, using the empirical model equations 10.31 and 10.32, from the upper and lower limits of the spread of director orientations determined for each region and each strain state. In the following discussion it is useful to recall figure 10.9 on page 174.

Consider first the values from the uniform region. The initial average director angle (71°) is highly inclined to the stress axis and has a low standard deviation. Through application of the model these values translate to a very narrow range of initial elastic moduli across the uniform region. From figure 10.9 this is evident because the expected modulus for director angles between $\sim 40°$ and $\sim 70°$ is always ~ 4 MPa. By the final strain state, the average director angle in the uniform region has decreased to 31°. From the model, the expected range of moduli should increase, however the magnitude of the increase is countered by a decrease in the standard deviation of angles within the uniform region. Together

Table 11.1: A study of the inhomogeneity of the prominence and uniform regions based of the spread of director angles in each region and the spread of expected moduli according to equations 10.2 and 10.29. *Value calculated with $\theta = 10°$ which is below the lower limit of 15° for which the model was deduced to be accurate for.

	Prominence region		Uniform region	
Strain state	Average director angle $\theta°$±s.d.	Model modulus range [MPa]	Average director angle $\theta°$±s.d.	Model modulus range [MPa]
Unstrained	41 ± 20	3.9–9.3	71 ± 6	3.8–3.9
Maximally strained	23 ± 13	5.32–14.9*	31 ± 4	5.5–7.0

these results show that in the uniform region, the film is indeed behaving similarly to a film of uniform director orientation. This explains the close agreement between the measured data and the characteristic model for particle pairs in the uniform region and why all of the above assumptions hold true for the uniform region.

By comparison, in the unstrained and maximally strained states of the prominence region, the coupling of comparatively lower average director angles and significantly larger standard deviations results in a much broader range of moduli present. While in table 11.1 we have applied the model to a director angle of $23 - 13 = 10°$, which is below the lower value of 15° for which the model was deemed accurate in chapter 10, the above analysis does show that the force distribution across film cross-sections in the prominence region will be far from uniform. Therefore the behaviour of the prominence region is clearly inhomogeneous. These observations explain the disagreements between the data and characteristic models for locations in the prominence region and show that the assumption of a constant force distribution across a given film cross-section is not valid for this region. This important deduction is used in the following section.

11.4.3 Predicting the stress distribution

The analysis of the previous section succinctly illustrates how calculating the stress distribution throughout inhomogeneous materials is a difficult problem without some initial idea of the material's local response to an applied stress. However, in order to design the functioning of mechano-LCE devices it will be important to be able to accurately predict the stress distribution within, and deformation behaviour of devices. This problem is common to the stress-strain analysis of systems that cannot be analytically solved and instead require numerical methods such as Finite Element Analysis (FEA). Nonetheless, despite the complexity of the present system, we have an opportunity to apply the model derived in chapter 10 to gain, what can at least be taken as, a first approximation of the stress distribution within the material. This is possible as the local director orientation within the material provides an additional piece of information to the localised strain, allowing a deeper insight into the localised behaviour which is impossible for most materials.

The analysis performed in this chapter is therefore reminiscent of "photoelasticity" a technique, revisited in the following chapter, which can determine the stress distribution within isotropic and transparent materials, such as plastics, *via* the stress-induced optical retardance. [123] Ultimately a FEA model will be required for the design of devices made from LCE A. However, this will require data from many additional mechanical tests probing the anisotropic shear and biaxial deformation modes of LCE A.

In this section we consider the stress distribution in the maximally strained state using the localised strains and director orientations relative to the unstrained state. First, we make intuitive predictions of how the stress is expected to be distributed throughout the film before describing two methods for generating predictions of the stress distribution using the empirical model. In section 11.4.3.4 the stress distribution predictions from each method are plotted and are compared against one another and against the intuitively deduced stress distribution.

11.4.3.1 Prediction *via* intuition

We deduce several simple predictions of how the stress is distributed across the sample by considering the director orientations shown in figure 11.10 on page 199:

- Throughout the entire deformation, the centre of the prominence region has a director orientation which lies parallel to the applied stress axis across the entire width of the film. Therefore across this film cross-section, the material should behave as though it has a single elastic modulus. To a first approximation (*i.e.* neglecting any couplings which may affect how the stress propagates through the film) this should mean that the stress will be evenly distributed across the film width at the centre of the prominence region.

- To either side of the prominence region there are gradients in director orientation across the film width. At the bottom edge, the director lies close to parallel to the stress axis. As we look higher up the film (as seen in the photographs/director maps) the inclination of the director relative to the stress axis increases. Considering figure 10.9 on page 174, this should (in the prominence region) mean that the modulus is greatest at the lower edge of the film and should monotonically decrease as we move toward the top edge of the film. Therefore, the stress should be concentrated toward the bottom edge of the film where it is stiffest. This deduction is supported by the characteristic curves for locations sets **A1-3** and **E1-3** shown in figure 11.15 on pages 208 and 209. For a given strain the sets of characteristic curves predict a greater stress at the lower edge of the film. Therefore the experimental data plotted, in most cases, incorrectly predicts the stress at each location.

- We have already seen several times that the uniform region behaves similarly to a film of uniform director angle. Therefore we expect the stress to be uniform across this region.

11.4.3.2 Prediction A: *via* θ_0 and strain

Equation 10.39 gave the engineering stress as a function of the initial director angle and strain. Thus the true stress, Σ_T, can instead be determined by multiplying equation 10.39 by the deformation λ_x:

$$\Sigma_T = \sigma_f - A \times \log\left(\frac{1 + c\epsilon_i}{1 - d\epsilon_i}\right), \tag{11.1}$$

$$\text{where } \sigma_f = A \times \log\left(\frac{1 + c(\epsilon_i + \Delta\epsilon)}{1 - d(\epsilon_i + \Delta\epsilon)}\right), \tag{11.2}$$

$$\text{and } \epsilon_i = \frac{\alpha - \theta_i}{\beta}. \tag{11.3}$$

In the above equations $\Delta\epsilon$ is the local strain, θ_i is the initial director angle and A, c, d, α and β are fitted constants from the empirical model (see section 10.4.1).

By inserting the strains and initial director angle measured from each particle pair location of figure 11.15 into equation 11.1 we can calculate expected stresses at each location.

11.4.3.3 Prediction B: *via* θ_0 and $\Delta\theta$

In section 10.4.1, we also saw that the strain-induced director rotation $\Delta\theta$ and applied strain ϵ are directly proportional to one another:

$$\epsilon = 0.0362 \times |\Delta\theta|. \tag{11.4}$$

Thus the strain, $\Delta\epsilon$ in equation 11.1 can be replaced by $\Delta\theta$ using equation 11.4. This method should have several advantages over the method behind Prediction A described previously. Firstly, this method enables the strain to be inferred at a point, thus measurements over finite distances are not required. Moreover, localised stresses can be determined from the director response at each tracked particle which therefore offers over twice as many data points as the method used to generate Prediction A above. Additionally, as the strain is determined from a single point, and not over a region of varying director angle, fewer

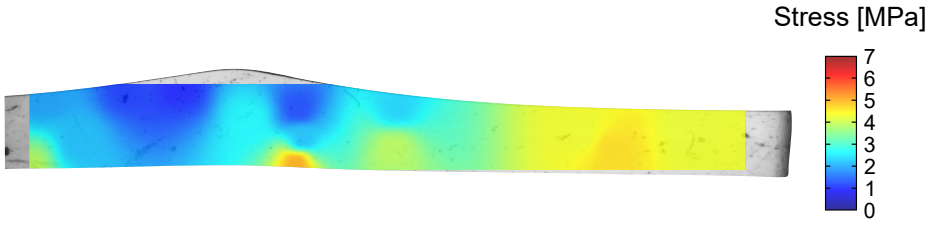

(a)

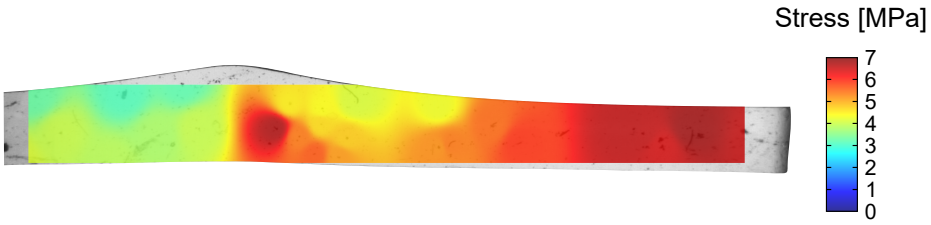

(b)

Figure 11.16: Predictions of the stress distribution across the film in the maximally strained state calculated using the model. a) uses the strains and initial director orientations measured from pairs of tracked particles shown in figure 11.15 and equation 11.1. b) uses the initial director angle and magnitude of director rotation from each tracked particle and equations 11.1 and 11.4.

assumptions are required about the effective director angle over the measured region as discussed in section 11.4.2.2.

11.4.3.4 Comparing Predictions A and B

Figure 11.16(a) and 11.16(b) show, for the final strain step, interpolated heat maps of the calculated stresses generated using the above predictions A and B (herein referred to as "map A" and "map B").

Both stress maps generally show distributions which agree with the predicted stress distribution. That is, the stress is uniform across the width at the centre of the prominence region and for adjacent regions, the stress is at its greatest at the lower film edge. Additionally the stresses shown in the uniform region are uniform

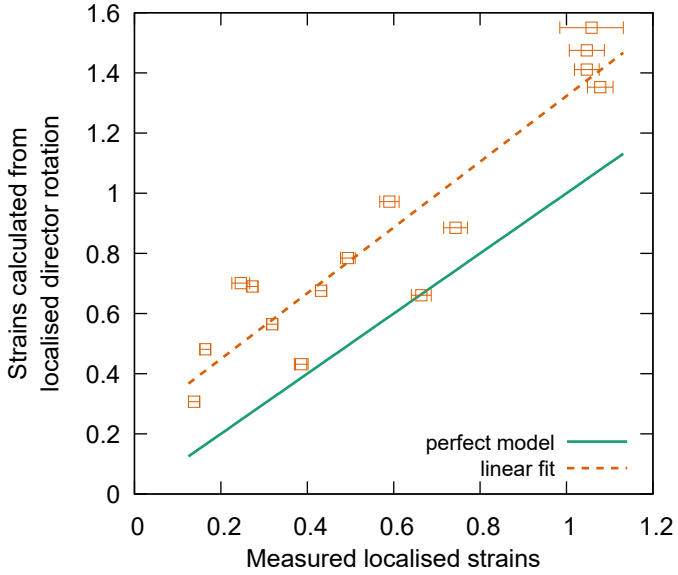

Figure 11.17: A comparison of the strains measured between particle pairs in figure 11.15 and the predicted strains from the initial and change in director orientation at the characteristic point from each pair of particles.

as expected. Aside from these similarities, the heat maps show several differences.

Most strikingly, map A predicts stresses that are lower in magnitude that those predicted in map B. Here we believe map A is more accurate as the stresses shown in the uniform region (~ 4.5 MPa) agree with the data in figure 11.15 — which we deduced were accurate. The stresses shown in map B (~ 7 MPa) are therefore likely to be over-predictions. Having said this, the range and distribution of stresses in map B still appear to be valid.

From figure 11.17 we can see why map B over-predicts the stresses. The figure plots the strains predicted from the director rotation at the characteristic points of each particle pair against the strain directly measured from the separation particle pairs. The fact that all data points lie above the solid line, $(y = x)$, means that equation 11.4 has over-predicted the strains, which in turn results in an over-prediction of the localised stresses. The dashed line shown in figure 11.17 has been fitted to the data. As the gradient of this line (1.1) is close to the perfect

gradient of 1, the strains predicted by equation 11.4 are on average offset from the actual strains. The discrepancy is quite surprising as equation 11.4 is based off a director rotation behaviour that was consistently seen in the samples tested chapter 10 which gave the strong and clear "master director curve" relationship shown in figure 10.10(a) on page 176. It is possible that this discrepancy was caused by the smooth variation in director orientation across the film giving rise to an enhanced director rotation behaviour not seen the deformation of the uniformly aligned sampled in chapter 10. This argument is supported by our earlier observation in section 11.3.1 of regions of the present film undergoing body rotations. Clearly the director re-orientation processes in complexly aligned films have additional complexities over those seen in uniformly aligned films.

Map B also predicts stresses of significantly greater magnitude on the right hand side of the prominence centre compared to the left hand side. If the stresses were to be integrated over cross-sections either side of the prominence region then they would appear to give an imbalance of forces — impossible as the film is stationary and not accelerating toward one of the sample clamps. This error could be corrected, and indeed the accuracy of both methods improved, by applying a constraint that the integral of stresses across any given film cross-section must equal the applied force measured by the load cell. This would also be helpful in accurately predicting the stresses in regions where the director either starts or finishes with an angle of $\leq 15°$ for which the model cannot be accurately applied.

Despite the above analysis indicating that the stress distribution in map A is more accurate than that shown in map B, it would be advantageous to be able to use an improved version of the second method as map B clearly has a greater resolution than map A — a result expected since in the second method, every tracked particle could be used to generate a localised stress prediction.

11.5 Conclusion

In this chapter we have studied the deformation behaviour of a single film of LCE A with a complex director profile and have learned a great deal about how com-

plex geometries can be mechanically generated and how stresses are distributed throughout such materials. While it is evident that numerical methods will need to be employed for the design of real devices, an encouraging result of this chapter is that intuitive predictions of how materials prepared with complex director geometries will respond to applied stresses appear to be reasonably accurate. Perhaps the most surprising result of this chapter is that the global load curve of the sample studied appeared similar to a model load curve where the initial director angle was equal to the average angle from across the whole film. If this relationship can be shown to hold for a variety of films with complex director profiles, then this would be a useful tool for the design of devices.

Our results have also shown signs of additional complexities, such as body rotations, over those already seen in this thesis. We propose that such additional complexities may be the reason why the relationship between strain and director rotation seen in chapter 10 has not held here. Unfortunately, the exact cause of these new behaviours and discrepancies are cannot be precisely defined as we cannot fully account for the effects of the slight warping of the film, caused by anisotropic de-swelling, and effects of the varying film thickness. More experiments on samples with a variety of different director geometries, created for instance using photoalignment techniques, are thus required in order to more fully understand mechanical-shape generation in LCEs and further to test out the hypotheses set out section 11.3.3.

In these suggested future tests it would be advantageous to use a different LCE which is not affected by anisotropic de-swelling, although this would require repeating the work of chapter 10 for that material. Despite the inconvenience of the anisotropic de-swelling on the particular work of this chapter, the process could actually be a useful tool that one could employ for creating devices which have surfaces of positive or negative curvature in their "natural" (*i.e* unstrained and ambient temperature) states.

To summarise, in this chapter we have, for the first time, carefully performed an in-depth analysis of the mechanical behaviour of a LCE prepared with a com-

plex director geometry. The wealth of information learnt will be central to the hypothesised shape deformations and LCE-AIOL concept described in chapter 13. Evidently, however, many more tests of complexly aligned LCEs need to be performed using the powerful techniques developed in this thesis in order to develop a full understanding of the mechanical behaviour of complexly-aligned LCEs.

11. TOWARD PROGRAMMED COMPLEX MECHANICAL DEFORMATIONS OF LCES

Chapter 12

Preliminary study of radial deformations of LCE B

12.1 Introduction

In the previous chapter we highlighted the fact that in order to create FEA simulations of mechano-LCE devices, information will be required about the biaxial stress response of the LCE to be used. Such studies would require the development or use of additional mechanical testing apparatus capable of applying sophisticated biaxial stresses. However, we can gain a first insight into the new challenges and complexities introduced by radial stress environments (*i.e.* a circularly-symmetric stress) applied to LCEs using minor additions to the equipment already developed and LCE B — the "isotropic LCE" developed in chapter 6.

In this chapter we subject samples of LCE B to linear and radial mechanical tests and compare the results. We observe stress-induced birefringence, a phenomenon known as "photoelasticity" and compare the magnitude of the response to that seen in common isotropic polymeric materials and in the side chain polysiloxane LCEs studied by the Finkelmann group. We also apply theory from isotropic and nematic rubber elasticity (W&T theory) to our results and see that both theories appear to correctly describe the observed phenomena. Moreover, using nematic rubber elasticity we are able to deduce the mechanically induced

ordering of LCE B in both the linear and radial tests.

The vast majority of the theory required for this chapter has already been described in chapters 4 and 8 and is referred to where appropriate. Here we only need to briefly introduce the concept of photoelasticity as many of the results of this chapter relate to the photoelastic response of LCE B. Photoelastic experiments performed on isotropic materials have long shown that the stress-induced birefringence of a material is proportional to the applied true stress. [134, 59] The constant of proportionality is called the stress-optic coefficient , C. The photoelastic response of a material is therefore summarised by the "stress-optic law,

$$\Delta n = C \times \Delta\sigma_T, \tag{12.1}$$

where $\Delta\sigma_T$ is in difference in true stresses along the principal axes (assuming only 2D stresses).

12.2 Experimental methods

12.2.1 Linear testing

As LCE B is isotropic in its unstrained state, the method we use here to study the evolution of the microscopic ordering differs to that used in previous chapters for LCE A. We do not need to determine the director orientation with strain as we can deduced from simple symmetry arguments that one of the principal axes of the induced anisotropic state will emerge parallel to the applied stress axis. This allows us to instead focus on quantitative assessment of the apparent induced LC ordering by measuring the optical retardance with strain using a Berek compensator (method described in section 7.2.2). For this test we therefore mount MESSE on the Leica polarising optical microscope shown figure 7.3(a) on page 114 and measure the induced retardance at each strain step. A preliminary test confirmed that the fast axis of the mechanically induced optical retardance of LCE B lay parallel to the stress axis. Recalling the method described in section 7.2.2, this meant that for measuring the optical retardance in the present

test, the stress axis had to be oriented at 90° to the fast axis of the Berek compensator's rutile crystal.

In this test we were particularly interested in the initial emergence of birefringence for comparison to the behaviours of other materials. Therefore we wanted to extend the sample in smaller strain steps compared to those we have used in previous chapters. However, as we could not reduce the incremental step size of the actuators below 0.5 mm (the step size used in all tests of previous chapters), we instead prepared a sample with greater a initial length (~ 35 mm) than previously used. Each strain step was therefore $\sim 1.5\%$ relative to the initial sample length compared to the typical value of $\sim 3\%$ which was used when investigating LCE A. Samples of LCE B were synthesised according to the procedure given in section 5.2.2, from which strips were cut with 2 mm widths (the same nominal widths used in previous chapters). The average thickness of the cut strip was measured to be 109 ± 5 μm.

The mechanical test was performed with the sample held at 28 ± 2°C and the film was viewed using a 4× microscope objective which provided a sufficiently wide field of view for observing the entirety of the film width throughout the mechanical test. At each strain step:

- Photographs of the sample were taken while viewed *via* white light and crossed polarisers oriented at 45/135° to the stress axis.
- The retardance was measured as described in section 7.2.2.
- A load cell reading was taken.

As with experiments performed in chapters 7, 10 and 11, the sample was allowed to stress relax for 2 minutes before measurements were taken. Data were collected over 15 strain steps before the sample broke.

Because we viewed the sample *via* a 4× objective as opposed to the camera and lens system used previously, the displacement of the tracked "particles" between successive photographs was too great for tracking using *trackpy*. Therefore the

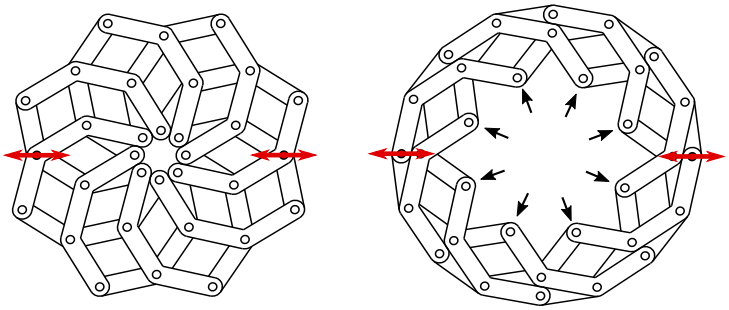

(a)

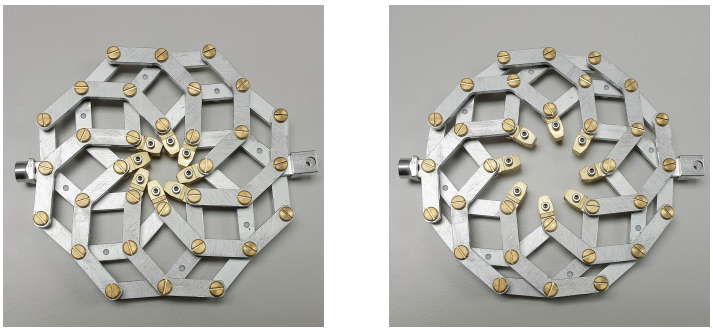

(b)

Figure 12.1: a) CAD diagram and b) photographs of the radial adapter used to apply an radial stress to a film of LCE B. [35, 103, 77]

strains parallel and perpendicular to the stress axis (ϵ_x and ϵ_y respectively) were measured manually using ImageJ. The change in sample thickness with strain (used for determining the birefringence from the retardance) was calculated from ϵ_x and ϵ_y using the constant volume assumption as before.

12.2.2 Radial testing

A radial strain adapter, illustrated in figure 12.1, was used to convert the linear strain of the actuators into an radial strain. [35, 103, 77] For this experiment, MESSE was returned to the stage as shown in figure 5.5 on page 83 such that the full extent of the film deformation could be recorded using the wide-field camera and lens system (configuration used in all previous experimental chapters).

A 82 ± 5 μm thick film of LCE B was prepared with dimensions of 15×15 mm and cut into an octagonal shape for loading into the radial strain adapter. The film, again held at 28°C, was radially stretched by increasing the separation of the *linear* actuators in steps of 0.5 mm. Two strain steps were performed before the sample failed. The strain of the sample was measured *via trackpy* as previously described. Before the first, and between each strain step the sample was allowed to relax for 2 minutes before photographs of the sample were taken using white light illumination and crossed polarisers oriented at 0/90° and 45/135° to the horizontal camera axis. Given that the force required to actuate the radial adapter was unknown, the load cell was replaced by a metal bar to prevent over-stressing and damaging the load cell. Consequently, no tensile load data is reported for the radial test of LCE B.

12.3 Results and discussion

All the results are first presented with some basic analysis in this section before deeper analysis and discussion in the following section.

In the following results, several one-parameter functions are fitted to experimental data. Errors attributed with each value were manually determined by varying the value of the parameter about the fitted value in order to assess the range of values which give curves which lie acceptably within the errors of the associated data.

12.3.1 Linear testing

Figure 12.2(a) (overleaf) shows the engineering stress tensile load curve for LCE B. The fitted curve shown has the form derived in section 4.2 for the load curve of an isotropic material

$$\sigma_x = \mu \left(\lambda_x - \frac{1}{\lambda_x^2} \right), \qquad \text{(4.14 revisited)}$$

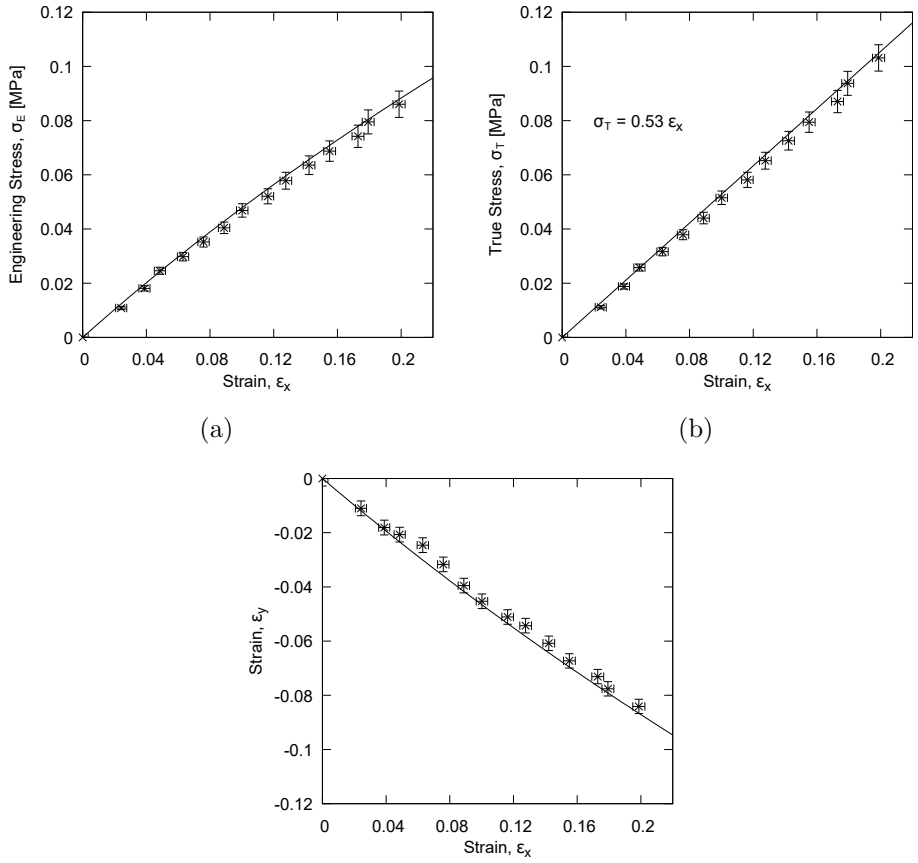

Figure 12.2: a) Engineering stress tensile load curve for a linear deformation applied to LCE B. Curve shown has the expected form for an isotropic rubber. b) Corresponding true stress tensile load curve fitted with a linear curve of gradient 0.53 ± 0.03. c) Measured strains (ϵ_x) and (ϵ_y) in response to the stress applied along the x axis. Curve shown plots the expected relationship for an isotropic material.

where μ is the shear modulus (fitted parameter) and $\lambda_x (= \epsilon_x + 1)$ is the deformation. The fitting gives a shear modulus of 0.17 ± 0.01 MPa, hence an elastic modulus (assuming incompressibility) of $E = 3\mu = 0.51 \pm 0.03$ MPa. The excellent agreement between the single parameter fitted function and the plotted data indicates that LCE B behaves isotropically.

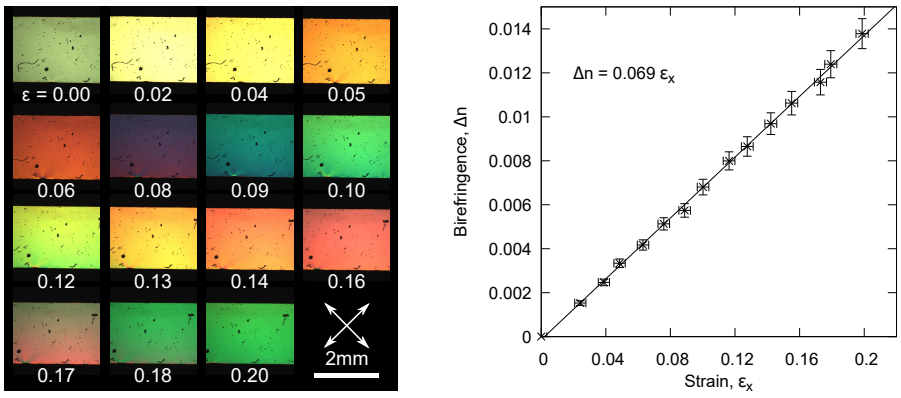

(a) (b)

Figure 12.3: a) Polarising microscopy photographs at each strain step of the linear mechanical test of material B (4× objective lens used). b) The induced birefringence and applied strain are proportional to one another with a proportionality constant of 0.069 ± 0.004.

Given the agreement between the fitted curve and data in figure 12.2(a), it is implicit that the true stress tensile load curve, shown in figure 12.2(b), would similarly agree with equation 4.14 multiplied by λ_x. We however show in figure 12.2(b) that the true stress load curve is remarkably linear over the region of strains considered and is well described by $\sigma_T = (0.53 \pm 0.03)\epsilon_x$. The gradient of this curve is consistent with the elastic modulus, E, calculated above.

Figure 12.2(c) plots, against one another, the x and y strains measured from the photographs of the samples at each strain step. The curve shown plots the expected form for the relationship between ϵ_x and ϵ_y for an incompressible and isotropic material, *i.e.* $\lambda_y = {}^1/\lambda_x^2$ where $\lambda_i = \epsilon_i + 1$. Again, the excellent agreement between the curve and the data indicates that mechanically, LCE B behaves isotropically. Moreover, the agreement also shows the assumption of incompressibility holds sufficiently well for LCE B.

Figure 12.3(a) shows polarising microscopy photographs taken at each strain step of the mechanical test and demonstrates the photoelastic response of LCE

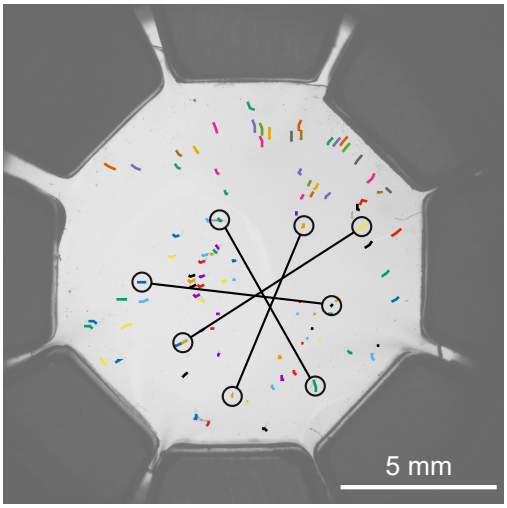

Figure 12.4: Trajectories of tracked particles for the radial deformation of LCE B overlaid on top of a photograph of the unstrained sample.

B. In section 6.3.2 we saw that LCE B was optically isotropic when unstrained and so consistently appeared black when rotated between crossed polarisers. Here the "unstrained" state displays a small degree of unavoidable optical anisotropy caused by the slight strain required to hold the sample flat in the initial state. Although a definite birefringence colour is seen in the unstrained state, the birefringence induced by any the slight strain was measured as effectively zero, seen by the fact the first data point of figure 12.3(b) lies above the origin. The non-black appearance of the sample in the unstrained state is a combined result of the extremely large photoelastic response of LCE B (discussed below) coupled with the thickness of the sample which amplifies appearance of the induced birefringence. The progression of the photoelastic birefringence colours seen in figure 12.3(a) matches the progression of colours seen in a Michel-Levy chart. The colour seen in the last photograph corresponds to an optical retardance of 1370 nm — a second order birefringence colour. Figure 12.3(b) plots the mechanically induced birefringence, Δn, against applied strain and shows a strongly linear relationship with a fitted proportionality constant of 0.069 ± 0.004.

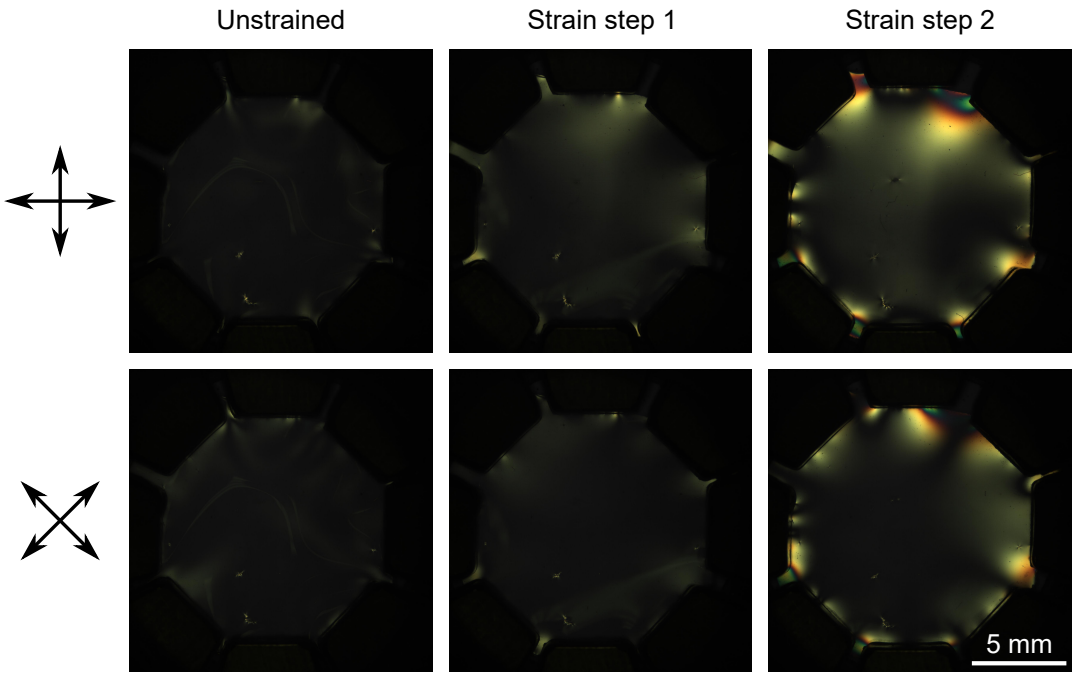

Figure 12.5: Polarising microscopy photographs of the radially deformed sample of LCE B at each stage of the experiment. In section 12.4.2 we show that a negative LC order parameter evolves with radial strain.

12.3.2 Radial testing

Figure 12.4 shows the tracked particle trajectories overlaid onto a white light photograph of the unstrained film. From the trajectories the apparent centre of the deformation appears to be offset from the central point between the sample clamps, a result likely to have been caused by imperfect loading of the film onto the radial adapter. Pairs of particles are highlighted on figure 12.4 between which strains of 0.10, 0.05, 0.09 and 0.07 were calculated. From these we deduce an average radial strain of 0.08 ± 0.02.

The polarising microscopy photographs of figure 12.5 show the sample at each of the strain steps with the polariser and analyser in 0/90° and 45/135° configurations. In each photograph, the main body of the sample appears almost completely isotropic with only a slight birefringence colour appearing in the photographs at strain steps 1 and 2. From the average radial strain of 0.08 ± 0.02 we

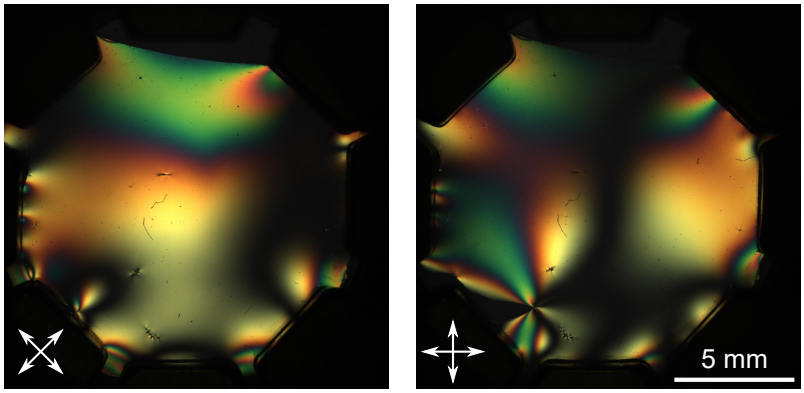

Figure 12.6: Polarising microscopy photographs of the sample as it fails.

can calculate (under the constant volume assumption) that after the second strain step, the strain along the thickness (z) axis is $\epsilon_z = -0.14 \pm 0.03$. Therefore the final sample thickness will have reduced from 82 ± 5 μm to 70 ± 5 μm. Using the fitted curve from figure 12.3(b) we can calculate a value for the expected retardance of the sample *if the response of the radial sample were identical to sample linearly tested above*. By considering a Michel-Levy chart we can see that the calculated value of 380 ± 100 nm, corresponds to colours within the low retardance colour sequence of yellow—orange—purple. Despite the large error on the calculated retardance (caused by the large uncertainty in the average radial strain), the grey birefringence colour seen in the third strain step images of figure 12.5 clearly corresponds to a induced retardance below the range of retardances calculated. This is as to be expected as in an ideal radial strain test of an isotropic material, the material would be isotropically deformed, *i.e.* $\Delta\sigma_T = \Delta n = 0$ in equation 12.1, and so no anisotropy within the plane of the deformation would occur. The slight birefringence seen in figure 12.5 is therefore a consequence of the sample and experimental arrangement being slightly imperfect.

The above argument is also confirmed by considering the appearance of the sample as it slips from the clamps and begins to tear (figure 12.6). During this phase the radial nature of the applied stress is lost resulting in the emergence of first and second order birefringence colours.

Table 12.1: A comparison of stress-optic coefficients for LCE B, the Finkelmann side chain polysiloxane LCE and a range of common elastomeric materials.

Material	Stress-optic coeff., C, [Brewsters]	Comment	Ref(s).
LCE B	1.3×10^5	Acrylate "isotropic" LCE	n/a
Polysiloxane side chain LCEs	$\pm 10^3$–10^5	Early Finkelmann LCEs stressed in isotropic phase	[59, 143, 66]
Polybutadiene	3000	Synthetic rubber	[106, 134]
Polyisobutylene	3300	Synthetic rubber	[134, 13]
Natural rubber	2200		[113]
PDMS (silicone)	200	Common base polymer for elastomers	[106]
Polycarbonate	3500 (typical)	Common thermoplastic polymer	[106]
Polyethylene	2000	Common thermoplastic polymer	[106]

12.4 Analysis and further discussion

12.4.1 Photoelasticity of LCE B

For the uniaxial test presented here, there is only a single stress applied and so equation 12.1 reduces to $\Delta n = C \times \sigma_T$. This proportionality relationship evidently holds for LCE B given the linearity of the true stress-strain and birefringence-strain graphs shown in figures 12.2(b) and 12.3(b) respectively. From the linear fit gradients of these graphs, we calculate a value for the stress-optic constant of $C = (1.3 \pm 0.1) \times 10^5$ Brewsters (1 Brewster = 10^{-12} Pa^{-1}). This is an extraordinary large value for the stress-optical coefficient and is ~ 50 times larger than then highest values typically seen in isotropic plastics and (non-LC) elastomers as shown in table 12.1. The side chain polysiloxane-based LCEs of the Finkelmann group have been reported, when stressed above their respective T_{NI}s, to have stress-optical coefficients of similar magnitude to LCE B — spanning $\pm 10^3$–10^5 Brewsters. The $\pm$ sign in the quoted values reflects the fact that Finkelmann

materials with an odd-length spacer group had stress induced *negative* birefringences. The stress-optical coefficients of all of the Finkelmann LCEs had strong temperature dependences with the value having their largest magnitudes ($\sim 10^5$ Brewsters) at temperatures just above the respective T_{NI} of each material (values for T_{NI} varied between 11°C and 57°C). On heating any of the Finkelmann materials by $\sim$ 20°C above its T_{NI}, the stress-optical coefficient was typically reduced by an order of magnitude. [59, 143, 66] It would therefore be interesting to study the temperature dependence of LCE B's stress-optical coefficient as although LCE B contains mesogenic units, it does not exhibit a nematic phase and hence does not have a T_{NI}.

12.4.2 Mechanically induced ordering

To investigate the degree of stress-induced ordering within LCE B we can apply the Gaussian theory of Warner and Terentjev in a similar manner as was done in chapter 8. For the present system, which is initially isotropic and is stressed along the x axis, the initial and final step length anisotropies are given by $\underline{\underline{\mathbf{l}}}_{\mathbf{0}} = \underline{\underline{\boldsymbol{\delta}}}$ and $\underline{\underline{\mathbf{l}}}' = \mathrm{Diag}(l_\parallel, l_\perp, l_\perp)$. It is easy to show that by inserting these into the trace formula (equation 4.16) and minimising, that the step length anisotropy is given by [47]

$$r = \lambda_x^3 = (\epsilon_x + 1)^3. \tag{12.2}$$

Further by inserting this into equation 4.3 we find the backbone order parameter, Q_B to be [47]

$$Q_B = \frac{(\epsilon_x + 1)^3 - 1}{(\epsilon_x + 1)^3 + 2} \approx \epsilon_x, \tag{12.3}$$

where the approximation is valid for low strains of $\epsilon_x \lesssim 0.2$. Thus over the range of linear strains applied to LCE B, the backbone order parameter is approximately equal to the applied strain. As for a side chain LCE the nematic and backbone order parameters, (Q_N and Q_B), are proportional, equation 12.3 also means that strains applied to LCE B induce a non-zero Q_N and hence a nematic phase within LCE B. [47, 169] Moreover, as we saw above that $\Delta n \propto \epsilon_x$

(figure 12.3(b)), we therefore also have the result that for LCE B the induced birefringence is proportional to the nematic order parameter, a result which intuitively makes sense. It remains to be seen as to whether this relationship holds above a strain of 0.2.

Turning to the radial test of LCE B we take two (entirely equivalent) approaches the calculation of the backbone order parameter under the assumption that the slight optical anisotropy seen in figure 12.5 is negligible (*i.e.* $\Delta\sigma_T = 0$). Values calculated below relate to the second strain step of the experiment.

Firstly, we can use the fact that a biaxial extension in the xy plane is equivalent to a uniaxial compression along the z axis. In section 12.3.2 we calculated that in the second strain step, $\epsilon_z = -0.14 \pm 0.03$. Therefore using equation 12.2, $r' = 0.63 \pm 0.07$ and using equation 12.3, $Q_B = -0.14 \pm 0.03$.

Alternatively, we can take equation 8.8 from chapter 8 and insert $r_0 = 1$ and $\lambda_x = \lambda_y = 1.08 \pm 0.02$ to find $r' = 0.63 \pm 0.07$ and hence the same value of Q_B. Given the nematic order parameter, $Q_N \propto Q_B$, the radial strained system must be in a state of negative LC order parameter (see section 2.2.2.2). If we assume that the strain dependency of the birefringence shown in figure 12.3(b) can be validly extrapolated to compressive strains, we can deduce that at the second radial strain step the sample will have a birefringence of -0.010 ± 0.002. The presence of a negative birefringence could be confirmed using conoscopy and a half wave plate retarder.

By considering the above observations and results together we can see that an observation of negative birefringence in an isotropic system containing (calamitic) mesogenic groups translates to a state of negative LC ordering. Thus, when the Finkelmann group observed negative stress-optic coefficients, they were also observing a mechanically induced state of negative LC ordering, although this was not recognised at the time.

12.5 Conclusion

While in this chapter we have considered an "isotropic LCE" as opposed to a true nematic LCE, the relative simplicity of LCE B has allowed us an insight into a challenge which will be faced when considering nematic LCEs when biaxial stressed. From the stress-optic law (equation 12.1), we see that the magnitude of the optomechanical response is altered by the presence of two dimensional stresses. It is intuitive that a analogous effect will occur when aligned LCEs (of complex or trivial director geometries) are biaxially stressed. For instance we anticipate that the director rotation response for a biaxial stress geometry will differ to that seen in uniaxial deformations. In turn this means any models, like that developed in chapter 10, derived for nematic LCEs would need to be expanded to account for biaxial phenomena before they could be used for predicting biaxial deformations and stress distributions of aligned LCE devices.

Our analysis of the linear mechanical behaviour of LCE B has also shown the stress-strain response and $\epsilon_x - \epsilon_y$ relationship conform to the behaviour expected for a typical rubber. Perhaps in conflict, we also argued that the deduced proportionalities between the induced birefringence and backbone and nematic order parameters conform to the behaviour expected of a LCE. While it is likely that some may argue that a "paranematic" state is induced in LCE B as opposed to true nematic phase, we believe these results together means that LCE B is equally well described as being an isotropic rubber or as a nematic LCE. Given that anisotropy will be induced when mechanically deforming conventional isotropic polymeric materials we pose the question of whether W&T theory might be usefully applied to the physical properties (for instance dielectric anisotropy) of conventional rubbers under stress.

Chapter 13

Hypothesised complex shape generations and LCE-AIOL concepts

13.1 Introduction

The previous chapters have demonstrated that LCEs have programmable mechanical properties and can undergo controlled shape changes. These results indicate that LCEs show promise for the development of a mechanically switchable lens. However clearly much more research is needed into the behaviour of LCEs stretched in biaxial geometries such that FEA-type models of devices can be created. Despite this, between chapters 10 and 12 we have learnt a sufficient amount about how LCEs behave mechanically in order to be able to develop new hypotheses for how patterned LCEs may respond to uniaxial and radial mechanical forces.

In this chapter we draw upon what we have learnt so far to make intuitive predictions of how complex mechanically-induced shapes can be created from a variety of patterned LCEs. In section 13.2 we first make predictions of how patterned films of LCEs, similar to those presented by Ware *et. al.* and by ourselves in chapter 11, deform under uniaxial stresses. Section 13.3 extends our predictions to radial deformations of patterned circular disks of LCE. In section 13.4

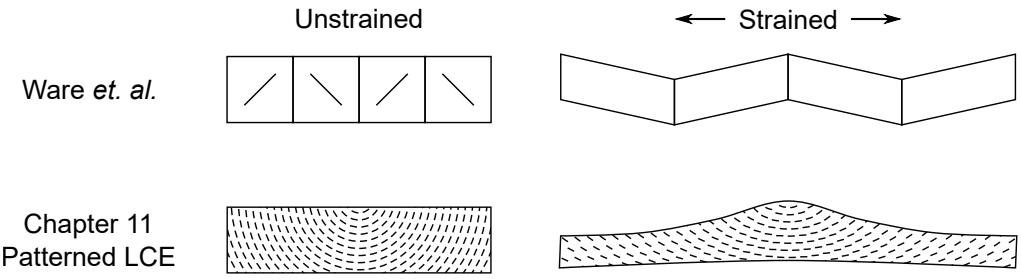

Figure 13.1: Known mechanically-generated complex shapes for patterned LCEs described by Ware *et. al.* and ourselves in chapter 11. In section 11.3.3 we deduced the molecular re-orientations which drive the shape changes observed. In this chapter we use these known deformations to hypothesise additional complex deformations.

we put together our deductions from sections 13.2 and 13.3 with the results of chapter 10 in order to develop LCE-AIOL concepts and discuss how they would operate within the eye.

Before we proceed it is important to reiterate that the purpose of this chapter is to show that the initial motivation for this thesis — the use of LCEs for a functional AIOL — was justified. Following the results chapters of this thesis we are now in a position to suggest a potential geometry and mode of operation for a LCE-AIOL, however we accept that we do not attempt to prove that the proposed device works in practice. This chapter essentially uses the expertise developed so far to explore innovative concepts which should be investigated in future work. If the hypotheses made in sections 13.2 and 13.3 could be proved to be correct, then this would give additional confidence for continued pursuit of the LCE-AIOL concepts proposed in section 13.4.

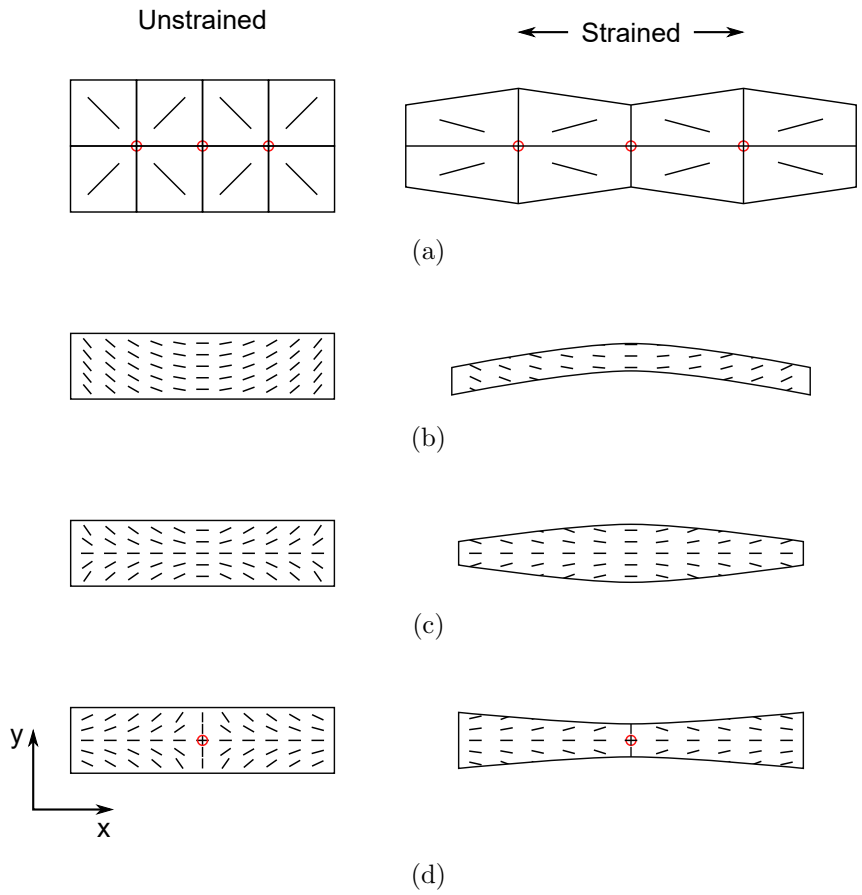

Figure 13.2: Four examples of hypothesised complex shape deformations based on the known behaviours shown in figure 13.1. In a) and d) the red circles signify LC defects.

13.2 Shape generation through uniaxial deformations of LCE strips

Before we make any new hypotheses, we re-illustrate in figure 13.1 the deformation behaviour of the patterned LCEs reported by Ware *et. al.* and ourselves from chapter 11. Using these deformations, along with the discussion of section 11.3.3 we hypothesise the deformations shown in figure 13.2. The director profiles shown in figures 13.2(a) and 13.2(d) include liquid crystal defects (highlighted by red cir-

cles). As no experiments performed to date have studied the mechanical response of a defect embedded within a LCE, these predicted deformations are a little more speculative than deformations shown for geometries which do not include defects.

Figure 13.2(a) is an extension of the deformation reported by Ware *et. al.* where we propose that by making the film symmetric about its central x axis, the evolved shape becomes symmetric about the same axis. [166] The deformation about the outermost defects is smaller than the deformation at the central defect which, in the context of the Ware *et. al.* paper, would make such locations ideal for the placement of fragile components if such a film was used as a substrate for flexible electronics. [166] The symmetry of the director patterning also makes it reasonable to suggest that such regions would undergo the least deformation if the sample were strains along the y axis instead.

The director geometry of figure 13.2(b) shows similarities to both director geometries to Ware *et. al.*'s LCE and our own from chapter 11 — *i.e.* the director angle is constant across any given y cross-section, however there is a smooth variation of the director angle in the x direction. Based on the findings of chapter 11 we hypothesise that the evolved shape profiles of each edge would be smooth and identical in shape.

The hypothesised deformations of figures 13.2(c) and figure 13.2(d) are particularly interesting as the evolved profiles have shapes similar to cross-sections of biconvex (figure 13.2(c)) and biconcave (figure 13.2(d)) lenses. However, again, as the geometry shown in figure 13.2(d) includes a "-1" defect, the predicted deformation is more speculative than that shown in figure 13.2(c). [104]

13.3 Deformation behaviour of radially deformed LCE films

We now turn to discuss the radial deformation behaviour of films of LCE with directors patterned within the film plane (figures 13.3 and 13.4 overleaf). We consider these cases here as such geometries have already been created using photoalignment techniques, however no mechanical tests have been known to be performed on such samples. [37, 108, 164, 163] Moreover, the deformation geometry is similar to the stresses imposed by the ciliary body of the eye onto the crystalline lens/an AIOL and so discussing the expected behaviours here will help inform how a LCE-AIOL should be designed. What will become apparent is that although LCEs with the below director fields can already be readily produced (and therefore may be attractive to explore for a AIOL device), such geometries may actually not in practice behave any different to an isotropic material subjected to a biaxial stress.

In the below discussions we consider applied radial strains and the resultant stress distributions and director responses. Considering applied *strains* as opposed to applied *stresses* better reflects how experiments would be performed in reality. In all cases we assume that the initially 2D (Euclidean) sheets of material remain Euclidean with deformation and therefore the strains along the radial (ρ) and tangential (θ) axes must be equal. We start by noting that for an isotropic material, the stresses in ρ and θ directions will also be equal and thus the stress distribution within the plane of the deformation will be isotropic (as should be expected).

The simplest cases to first consider are shown in figure 13.3. Given that in both cases the director lies at either 0° or 90° to the radial (ρ) and tangential (θ) axes, we assume from the results of chapter 7 that in both cases no director rotation would occur. For the geometry shown in figure 13.3(a) it seems plausible from the well known elastic anisotropy of LCEs and the moduli shown in figure 10.7 on page 170 that the stiffness along the ρ axis will be greater than the stress along the θ axis. [93, 47] Thus the induced radial stress $\sigma_{\rho}^{(a)}$ should be

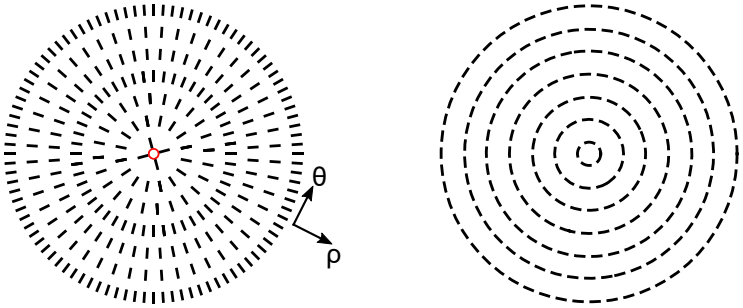

(a) (b)

Figure 13.3: a) Radial and b) axial director fields are the simplest circularly symmetric LCEs which we can consider the radial deformation behaviour of. The axes shown reflect the circular coordinate system centred on each director pattern. We hypothesise that the response to a radial strain for both systems would be identical although the anisotropic stress distributions would differ.

greater than the induced tangential stress $\sigma_\theta^{(a)}$ and therefore the stress distribution at any given point would be anisotropic. Similarly, for the case shown in figure 13.3(b) the stresses ($\sigma_\rho^{(b)}$ and $\sigma_\theta^{(b)}$) will be anisotropic however should be switched compared to the case shown in figure 13.3(a) — *i.e.* $\sigma_\rho^{(b)} = \sigma_\theta^{(a)}$ and $\sigma_\theta^{(b)} = \sigma_\rho^{(a)}$.

Deducing the behaviour for the intermediate case of the director inclined at a constant angle to the radial axis (*i.e.* director trajectories forming logarithmic spirals as highlighted in figure 13.4) is more complicated as there is the potential for director rotations to occur which may cause internal body rotations like those hypothesised by figure 13.4. [167]

However, if we consider the case of the director being inclined at 45° to the radial axis, then the material response along ρ and θ axes must be equal by symmetry and so no director rotation could occur. Based on this deduction, we propose an alternative hypothesis that the mechanical response of films patterned with director profiles forming logarithmic spirals (which includes the patterns shown in figure 13.3) would be spatially uniform (*i.e.* spatially uniform in "stiffness")

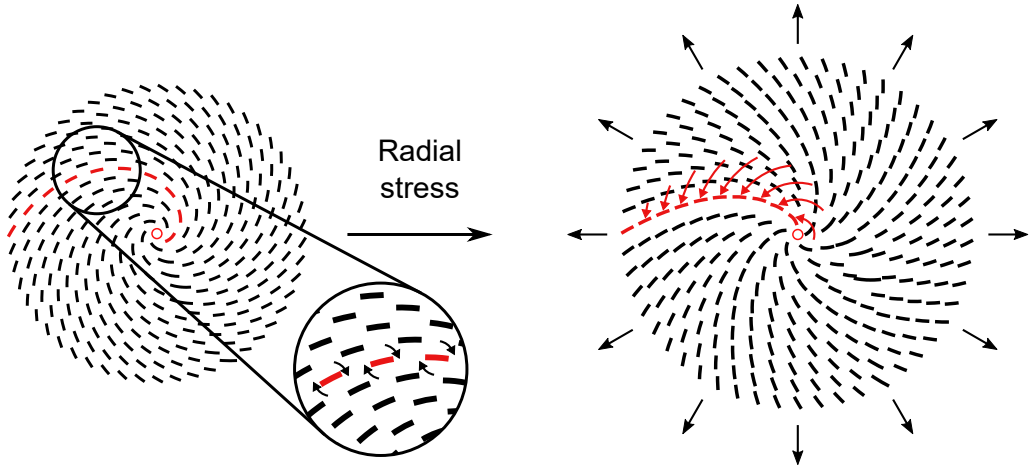

Figure 13.4: The director fields shown in figure 13.3 can be generalised to fields described by logarithmic spirals. We hypothesise that in response to a radial strain the behaviour would either be similar to the cases shown in figure 13.3 or, as hypothesised here, localised director rotations may cause an internal body rotation. [167]

and independent of the angle of the logarithmic spiral. If true, then this argument could be extended to any radially strained LCE with a circularly symmetric director profile which always lies within the plane of the film. Thus in order to induce complex deformations, the effective anisotropy (and hence effective stiffness) must spatially vary. For a LCE, we propose this would mean spatially varying the "pre-tilt" (the inclination angle of the director relative to the plane of the film surfaces) of the director throughout the film. This idea is explored in the following section in our proposal of LCE-AIOL concepts.

13.4 AIOL design concept

13.4.0.1 Overview of lens operation

We now present our concept for a LCE-based AIOL and discuss how such a lens would operate and how it could be potentially be manufactured. The design has been created bearing in mind the numerous challenges which still must be overcome before such a device could be produced.

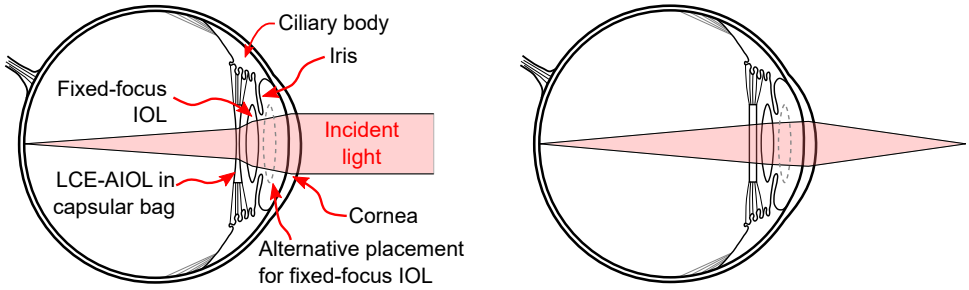

(a) (b)

Figure 13.5: Proposed mode for how a LCE-AIOL system could function. The LCE-AIOL in the capsular bag would have a optical power of between a) -4 and b) 0 D (controlled by the ciliary body) while the fixed focus positive powered lens placed in either the posterior or anterior chamber would give the overall optical system the correct magnitude of optical power to restore emmeotropic vision.

Figure 13.5 illustrates the overall lens concept. A two-lens solution is proposed. The anterior lens is a fixed-focus IOL with sufficient optical power to enable the patient to focus on near-by objects at a functional distance ($\sim$ 25 cm) from the eye. The posterior lens would be the LCE-AIOL which would be implanted into the capsular bag and would restore the accommodative ability to the eye. In its undeformed state (where the ciliary body is contracted) the LCE-AIOL would have flat surfaces with zero optical power, thus enabling focusing at near distance *via* the cornea and fixed-focus IOL. In its deformed state (ciliary body relaxed), the LCE-AIOL would be deformed into a shape with a negative optical power. This negative optical power would act against the power of the fixed-focus IOL and cornea in order to allow focusing at distant objects.

The fixed-focus IOL could potentially be placed in one of two positions: either in the posterior chamber (placement of solid-line lens in figure 13.5) or in the anterior chamber (placement of dashed-line in figure 13.5). Both locations are currently used for IOL placement when the capsular bag is not sufficiently strong

to support a IOL following phacoemulsification (removal of the crystalline lens nucleus and cortex — discussed in section 2.1.5). [42] The power of the fixed focus lens would be chosen as appropriate to correct a individual's eyesight (which may be emmeotropic, myopic or hyperopic) for near vision. This would mean that the LCE-AIOL implanted into each patient could be identical as all patient-specific tuning would be performed using the fixed-focus IOL. Not only would this reduce the challenges of developing the LCE-AIOL to the development of a single design, but it would also help the manufacturability of the lenses.

13.4.0.2 Lens optics

We describe here one embodiment of the combined LCE-AIOL, fixed-focus IOL system. The aim is to outline a simple enough system that has the potential to be functional but which could also be realistically demonstrated *via* a proof of principle within the next few years.

For an emmeotropic patient, the total power of the cornea and fixed-focus lens would need to be ~ 54 D in order to focus on an object placed ~ 25 cm from the eye. With the cornea being ~ 44 D, this would leave the fixed-focus IOL needing to be, in this case, 10 D. [117] Such optical powers are readily achievable with current IOLs and could for instance be achieved using a biconvex lens of refractive index 1.55 and equal surface radii of curvatures of 44 mm (calculated using equation A.8, a refractive index of 1.33 for the aqueous humour and neglecting the thickness of the lens).

To allow distance vision the entire optical system should have an optical power of ~ 50 D, thus the AIOL should adopt a power of -4 D in the distance vision state. Using a lens refractive index of 1.5 (a typical ordinary refractive index, n_o, for a liquid crystal) a lens could take the form of a biconcave lens of equal surface radii of curvature of 85 mm. [96, 97] Alternatively, and more ideally as discussed below, the lens could have a plano-concave shape with the concave surface having a radius of curvature of 42.5 mm. In the former case, the effect of the lens

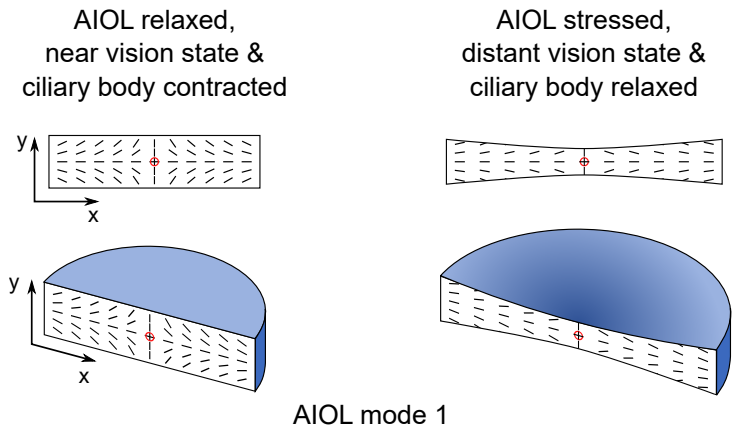

(a)

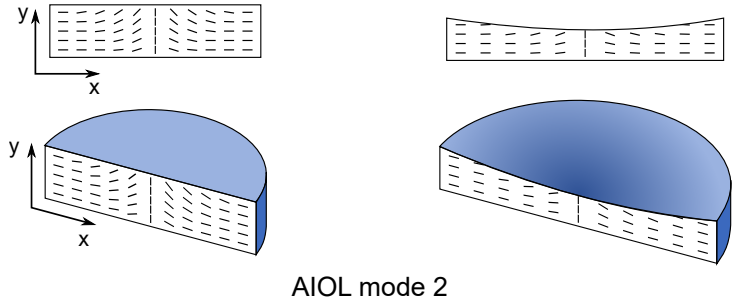

(b)

Figure 13.6: Concept director fields and operations for the LCE-AIOL lens. Neglecting any potential gradient index effects of the LC units, both lenses have a power of 0 D in their relaxed states which becomes negative with deformation. In a) the lens would have a biconcave shape when deformed while in b) the lens would have a plano-concave shape.

thickness is small while in the latter case it is irrelevant (seen from equation A.8).

Given the circular symmetry of the system we can create initial designs of the types of director profiles required by considering the deformations of films like those shown in section 13.2. Figure 13.6 shows two hypothesised director geometries and deformation modes for the LCE AIOL. The director profiles in both designs varies across the lens cross-sections and are symmetric about the

central axis of the lens. By patterning the director "pre-tilt" throughout the film thickness, the devices should effectively have a spatially patterned stiffness thus enabling complex, lens-like deformations.

The first AIOL mode shown in figure 13.6(a) considers taking the previous director field shown in figure 13.2(d) (which we hypothesised would undergo a lens-like deformation) and creates a lens design by revolving the design about its mid-point. Compared to the deformation hypothesised in figure 13.2(d), the deformation in this radial deformation geometry should be even more extreme as the thickness of the film must decrease sufficiently to enable the radial extension. Although this design is quite intuitive in its proposed operation we have two concerns about its practicality. Firstly, the lens would contain a defect (indicated by the red ring) at its centre — the mechanical behaviour for which is unknown and which would also likely affect the optics of the lens. Secondly, in the central plane of the lens the director lies entirely within the plane of the radial stress. Based on the discussion of section 13.3 this plane of the lens would do nothing to aid the patterning of the stiffness in order to promote deformation in the central lens region for forming the biconcave shape proposed.

The second proposed deformation mode seeks to overcome the hypothesised disadvantages of the first mode by proposing a plano-concave arrangement of the lens in the deformed state. This essentially means the lens would only need the director profile from one half of the first mode and thus the presence of a defect can be avoided (figure 13.6(b)). Moreover, the central region could be designed to have a pre-tilt across its entire width to help promote preferential deformation of the central region. Considering the director angle-elastic moduli dependency shown in figure 10.7 on page 170, the pre-tilt in the central region should be between $\sim 20°$ and $45°$ from the bottom to top surface to maximise the softness and deformation of the lens in this region. We have however shown in figure 13.6(b) that the central axis of the proposed lens would have a director pre-tilt of $90°$. This is a necessity to maintain the circular symmetry of the lens.

The hypothesised deformation mode of figure 13.6(b) is our preferred mode for future investigation. However, without performing a much deeper study of the proposed deformation it is difficult to assess the ultimate feasibility of this design as a LCE-AIOL given the strain constraints of the eye. However, if the demonstrated concepts could be experimentally verified in lab-based prototype devices then this would help deduce the concept's feasibility and also the design of improved concepts.

13.4.0.3 Proof of principle fabrication methods

Initial proof of principle devices to explore the lens concept shown in figure 13.6(b) could be made in a geometries of ~ 100 μm thick using photoalignment techniques to prepare cell substrates with the appropriate director profiles. de Haan *et. al.* demonstrated the facile photo-patterning of substrates with circularly symmetric director profiles using a photo-mask and a rotating stage. [37] This technique could be coupled with the pre-tilt control of between 0° and 40° offered by the photoalignment technique described by Sakamoto *et. al.* in order to spatially pattern cell substrates as appropriate. [138] The lensing response of the device could then be tested using the radial adapter described in chapter 12.

Moreover, while devices as thicker than ~ 150 μm could not be produced using patterned cell substrates, they could instead be produced using carefully controlled magnetic fields. Schuhladen *et. al.* showed that ~ 300 μm thick films of LCE monomer precursor can be aligned in complex geometries using a shaped magnetic field prior to photopolymerisation of the final LCE. [146] The hyperbolic hedgehog director profile of figure 13.6(a) resembles the arrangement of magnetic field lines for two magnets placed with like poles placed opposing and close to one another. If the shape of sufficiently strong magnets was tuned to give the correct magnetic field shape then it may be possible to create devices with either designs of figure 13.6.

Although 3D printing techniques have been recently developed, they do not currently appear to have sufficient resolution to print devices with the correct

director profile. [7, 87] Additionally, they currently have only been reported to offer patterned director profiles within the plane of each layer and the interfaces between filament interfaces appear to scatter light which would not be ideal for an optical device. [7, 87]

13.4.1 Conclusion

In this chapter we have hypothesised the mechanical behaviour of a variety of patterned LCEs in uniaxial and radial testing geometries. Experimentally testing the geometries shown would inform the prospects of mechano-LCE devices. As was highlighted at several points in this chapter, the mechanical response of a LC defect is completely unknown. Therefore future mechanical tests into defects of a variety of strengths would be interesting to explore.

We also proposed an initial concept for a LCE-AIOL which should be experimentally testable within the next few years. While in this thesis we have demonstrated that films of patterned LCEs can generate complex shapes when mechanically deformed, testing of the suggested proof-of-principle lens devices would be the next biggest milestone in the development of a LCE-AIOL device.

We finish by noting that the mechanically switchable lens concepts discussed in this chapter could also see use outside of AIOLs in technological devices such as smartphones or cameras. Such devices could prove a simpler first step for development as there would be fewer constraints on the lens geometry and biocompatibility which have made it difficult here to fully detail a LCE-AIOL lens concept.

Chapter 14

Conclusion

In this thesis we were motivated by presbyopia and cataracts — conditions affecting the ageing eye — to explore and develop the prospects of mechanical-based LCE devices. Specifically our vision has been the development of a truly functional LCE-AIOL which could restore a youthful magnitude of accommodation to presbyopes and those suffering from cataracts.

The results of this thesis have shown that the development of LCE-AIOL is, on a physical level, a feasible goal which should be the subject of continued research and development. The achievements which support this conclusion are as follows:

- We have demonstrated a range of acrylate-based LCEs with sub-room glass transition temperatures synthesised from commercially available starting materials. In particular LCE A had a T_g of 14.0 ± 1.0°C and a high step length anisotropy, r, which after discussing a range of calculated values appears be as great as $r = 9$. This is a truly unprecedented value of r for an acrylate LCE. However, the fact that we could calculate a range of values for r, of between 3.2 – 30.0, using various (plausible) theoretical models highlights the need for further convergence between experiments and theory.
- Secondly, our in-depth characterisation of LCE A discussed in chapter 10, led to the development of an empirical model which describes the general

uniaxial deformation behaviour of LCE A with a remarkable level of accuracy — something we saw was likely to be an infeasible goal using theory alone. We anticipate that the use of such empirical models could be useful tools for the design and development of proof-of-principle mechano-LCE devices. Moreover, such models could feed into the development of a full FEA model to simulate more complex and realistic mechano-LCE devices, including the LCE-AIOL concept.

- Perhaps the most significant parts of this thesis which leads us to believe LCE-AIOLs remain a realistic prospect, were the results and discussion of chapter 11. Here we showed that complex-shape deformations of LCEs can be programmed *via* spatial control of the director. Through deducing the factors affecting the evolved shapes, we were able to devise in chapter 13 realistic hypotheses of how further complex shapes could be generated and how a LCE-AIOL could be designed and it would operate. These designs should the be main research focus for the continued pursuit of the LCE-AIOL technology.

In the chapter 1 we highlighted the fact complete development of a new AIOL technology would require numerous levels of development beyond development of a mechanically switchable lens. We therefore propose that a more practical and low-risk route to the realisation of a LCE-AIOL would be to pursue an intermediary technology such as a mechanically switchable lens for camera or smartphone devices. Such devices would avoid the challenges of implantation of a device into the eye and the need for clinical trials.

One of the major aims of this thesis identified in chapter 2 was the development of new acrylate-based LCEs. The materials developed required the inclusion of 6OCB (the non-reactive LC group) in the LCE monomer precursors in order to achieve the correct phase behaviours and for the creation of high quality alignment of the LCE A monomer mixture. While the need to include 6OCB led to the undesirable effect of anisotropic de-swelling (see chapter 11), the fact that it has been even possible to create acrylate LCEs with the reported physical properties challenges the commonly-held view that acrylates LCEs are by default: brittle

at room temperature and have low anisotropies. We believe that further work could realistically develop new acrylate LCEs which do not need non-reactive LC groups to achieve the correct phase behaviour for the monomer mixture. We would argue that such materials could be the most simple and attractive LCE for general-purpose research with the potential to accelerate development of mechano-LCE devices. We also note that for the specific goal of developing a LCE-AIOL, one could use the vast array of LC and non-LC acrylate monomers in order to develop a high LC order, low birefringence material in order to minimise the dual-focusing effects of a birefringent lens.

Our ability to develop the empirical model describing general uniaxial deformations of LCE A was only possible because of the depth of the mechanical characterisation performed. We believe that such a model has never been developed before as no other studies have reported such a comprehensive study of a single LCE's mechanical anisotropy and non-linearity. A key and surprising result of this chapter was that the full range of elastic modulus anisotropy for LCE A is accessible for stresses applied at angles between $\sim 5°$ and $45°$ to the director. Knowledge of this range should simplify the design of devices and also provides a redundancy in behaviours for angles $\lesssim 5°$ and $> 45°$ which could be a useful tool when designing around specific geometric constraints of devices. It will be interesting to see if similar empirical models can be developed for LCEs of different chemistries and also if the approach taken can be extended to describe biaxial deformations of LCEs.

In chapter 11 we demonstrated application of the empirical model to study the localised deformation behaviour of a LCE patterned with a complex director geometry. We surprisingly found that the deformation behaviour of the patterned film appeared to be well described by the expected deformation behaviour of a uniformly aligned film of director angle equal to the average director of the patterned film. If this relationship can be validated for more complexly-aligned samples, then this could be a powerful tool for the design of mechano-LCE devices. Additionally, our use of the empirical model allowed us to generate intuitively correct predictions of the stress distribution within the deformed sample which

again could be useful for the design of mechano-LCE devices.

The work of this thesis has also seen significant steps forward in the understanding of the fundamental physical behaviours of LCEs. In chapter 7 we observed a new deformation mode for a LCE stressed perpendicular to the director — *i.e.* a deformation of the polymer conformation and LC order parameter through a state of negative order. We propose that this new deformation mode be termed an "order parameter deformation" (OPD) mode. Perhaps most significantly, we saw that this new behaviour shows hallmarks of both "mechanical Fréedericksz" transitions (MFT) and semi-soft elasticity (SSE). Alternatively, one may say that our observations actually open the possibility that MFTs, SSE and OPD deformation modes may be closely linked phenomena and not entirely distinct behaviours.

A key concluding point to reiterate from chapter 7 is that it is extremely important to monitor the director (and hence polymer conformation) response of LCEs throughout mechanical tests. If we had not observed the polarising microscopy textures of mechanically tested samples in chapter 7, we would probably have incorrectly concluded, from the shape of the tensile load curve, that LCE A undergoes only a SSE-like behaviour when stressed perpendicular to the director.

Our observation of new physics continued in chapter 8 where we discovered molecular auxeticity (negative Poisson's ratio behaviour) in LCE A. Such a behaviour has been a long-standing goal for the auxetics community as auxetics are known to have enhanced physical properties over conventional materials, however existing auxetics have been limited by their necessary engineered porosity causing material weakness. [40] Our discovery opens a new door for the study of, and potential applications of LCEs. The discussion of chapter 8 used the theory of LCEs developed by Warner and Terenjev to identify ways in which the auxetic nature of LCEs could be further investigated in order to: increase the magnitude of the negative Poisson's ratio beyond the maximum value of -0.8 that we have measured so far; and to tune the auxetic response to start from zero strain. While

a molecular understanding of why the auxetic behaviour occurs is currently unknown, we were able to deduce an insight from the polarising microscopy textures of deformed samples. We saw that the auxetic response appeared to be intimately tied to the presence of the negative LC and polymer backbone order parameters. For one sample we deduced that near the critical strain for the emergence of auxeticity, the backbone order parameter had a value of -0.41 ± 0.01.

Critical to the achievements of this thesis has been the development of the bespoke mechanical testing apparatus (MESSE) and analysis methods detailed in chapter 5. Together, this equipment and these methods have enabled us to study the mechanical properties and microscopic response of LCEs subjected to deformations. We feel that going forward this equipment could play a key role in not only further understanding the physics of the new phenomena discovered in chapters 7 and 8, but also for studying in greater detail the existing unknowns of LCEs, namely:

- What factors govern which deformation mode (out of MFT, SSE and OPD) a given LCE will display when stressed perpendicular to the director?
- What factors in addition to geometry govern the appearance of stripe domains?

We propose that these tests would involve the mechanical testing (using MESSE) of a range of LCEs of a variety of chemistries and various geometries, at a variety of temperatures relative to T_g and (if appropriate) T_{NI}, and also at a variety of strain rates. A tantalising prospect would be if one could make a given LCE display any of the deformation modes through controlling the sample geometry and testing parameters.

With the current experimental arrangement of MESSE, which makes each test labour intensive, it may not be realistically achievable to perform the suggested body of work. However, by upgrading MESSE to include motorized polarisers and a second camera, mechanical tests could be completely automated — thus making the proposed investigations feasible. If these upgrades were to be made,

then we would also advise replacing the actuators with units capable of smaller incremental step sizes and a greater range of extension speeds in order to further enhance the range of tests possible.

While the simplicity and efficiency of MESSE was central to the quantity and variety of work we were able to report in this thesis, we did have to accept not being able to directly measure and quantify the LC order parameter, Q_N, during deformations. We were left to deduce approximate values for Q_N based on calculated values of the step length anisotropy, r. Thus future work should also consider quantitative measurements of Q_N with deformation such that the exact relationships between Q_N and r for LCE A can be determined. Techniques such as polarised Raman spectroscopy, IR dichroism and X-ray diffraction could be employed for this purpose. [58, 93, 132] However, we suggest that during these tests the samples should also be photographed *via* crossed polarisers such that one is confident of the deformation mode of the LCE. Tests measuring the strain-dependency of Q_N will also help in the development of a more complete picture of the molecular behaviour driving the auxetic response of LCE A. As the discovery of the auxetic behaviour could, with time, prove be the single most important finding of this thesis, we suggest that experiments to determine the strain dependency of Q_N should be performed as a matter of priority.

To summarise, this thesis has advanced several aspects of research surrounding LCEs. We have:

- Taken important steps supporting the development of novel mechano-LCE devices for treating conditions of the ageing eye.
- Demonstrated new LCEs which have challenged the community's thoughts on what is possible with solely acrylate-based starting materials.
- Discovered new physics for the mechanical behaviours of LCEs.
- Developed powerful new testing equipment and analysis methods which enabled us to discover new physical behaviours of LCEs.

The exciting results of our work have perhaps created more questions for future research than were answered. However, we take this as a positive result as it demonstrates the continued richness of LCEs and further increases the prospects of real-world applications of LCEs.

Appendix A

Lens optics

A lens focuses the light from an object to form an image. Figure A.1 shows a typical simplified ray diagram illustrating the action of a lens. The object and image distances (u and v respectively) are linked by the equation

$$\frac{1}{f} = \frac{1}{u} + \frac{1}{v}, \tag{A.1}$$

where f is known as the focal length of the lens and is related to the radii of curvature of each lens surface (R_1 and R_2), the thickness of the lens, t, and the refractive indices of (in general) the media either side of the lens (n_1 and n_2) and the lens itself (n_L). While the focal length of a lens describes how strong its focusing effect is, the "power", given by the reciprocal of the focal length (in metres), is typically used to quantify the strength of lenses. [72] The unit of optical power is the dioptre, D. The radii of curvature for a lens can be either positive or negative depending on which way the surface is curved. The convention for assigning a sign to a radius of curvature of each lens surface is best demonstrated by the illustrations of figure A.2. [72]

Deriving the dependency of a lens' focal length on the above factors can easily be done using Ray Transfer Matrices (RTMs). In the paraxial limit (*i.e.* small angles θ between light rays and the optic axis) the effect of optical elements on the position and angle of light rays can be described a RTM, M [72]

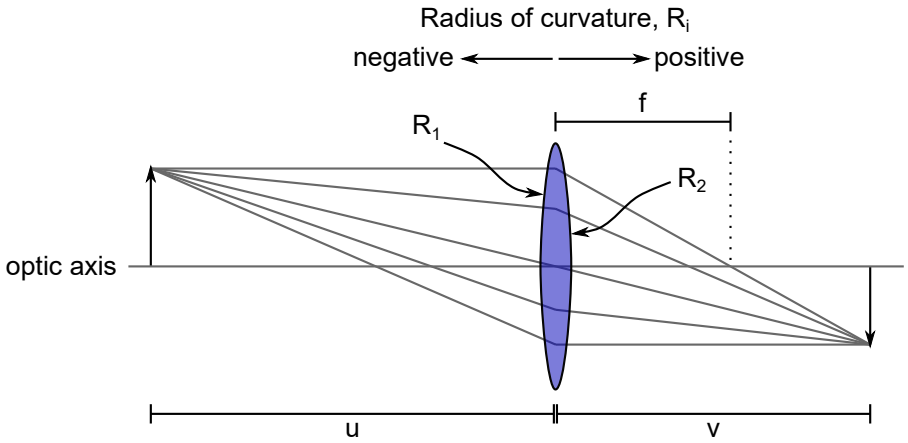

Figure A.1: Simplified diagram of the operation of a lens producing an image a distance v behind the lens of an object placed a distance u in front of the lens. The lens has a focal length f and has spherical-cap surfaces of radii R_1 and R_2.

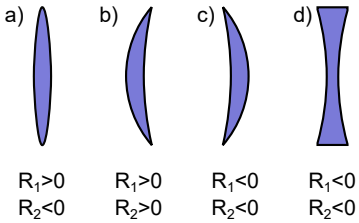

Figure A.2: Illustration of the convention for assigning signs to a lens' radii of curvature.

$$\begin{pmatrix} x' \\ n'\theta' \end{pmatrix} = M \begin{pmatrix} x \\ n\theta \end{pmatrix} = \begin{pmatrix} A & B \\ C & D \end{pmatrix} \begin{pmatrix} x \\ n\theta \end{pmatrix}, \tag{A.2}$$

where x and x' are the initial and final transverse distances of the ray from the optic axis, θ and θ' are the initial and final angles of the ray relative to the optic axis and n and n' are the initial and final refractive indices experienced by the ray. Figure A.3 provides a diagrammatic representation of these aspects of equation A.2.

RTMs describing: the progression of a ray through a length of space, t between refractive elements (M_A); and the effect of a *single* spherical refracting surface of radius R (*i.e.* on face of a lens) (M_B), are given by [61]

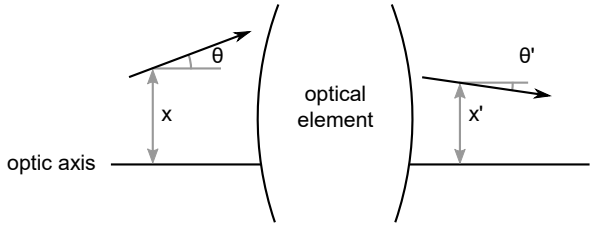

Figure A.3: Diagram of how the effects of optical elements are viewed using ray transfer matrices (RTMs). The element "transfers" the ray from an initial height and inclination of x and θ to and final height and inclination of x' and θ.

$$M_A = \begin{pmatrix} 1 & {}^{t}/_{n} \\ 0 & 1 \end{pmatrix} \quad \text{and} \quad M_B = \begin{pmatrix} 1 & 0 \\ -{}^{1}/_{f} & 1 \end{pmatrix} = \begin{pmatrix} 1 & 0 \\ -(\frac{n'-n}{R}) & 1 \end{pmatrix}, \tag{A.3}$$

where n in M_A is the refractive index of the media through which the ray is propagating and n and n' in M_B are the initial and final environment refractive indices experienced by the ray passing through the lensing surface.

A single RTM, M_T describing the effect of a sequence of optical components can be found by multiplying the RTMs of the individual optical components *in sequence* [72]

$$M_T = M_1 M_2 M_3 ... \ , \tag{A.4}$$

where $\{M_i\}$ are the RTMs of each optical component.

The RTM for a lens of refractive index n_L, thickness t and surface curvatures R_1 and R_2, placed at the interface between media of refractive indices n_1 and n_2 can therefore be found *via*

$$M_{lens} = \begin{pmatrix} 1 & 0 \\ -(\frac{n_2-n_L}{R_2}) & 1 \end{pmatrix} \begin{pmatrix} 1 & {}^{t}/_{n_L} \\ 0 & 1 \end{pmatrix} \begin{pmatrix} 1 & 0 \\ -(\frac{n_L-n_1}{R_1}) & 1 \end{pmatrix}, \tag{A.5}$$

$$= \begin{pmatrix} 1-\left(\frac{n_L-n_1}{n_L}\frac{t}{R_1}\right) & \frac{t}{n_L} \\ -\frac{1}{f_L} & 1-\left(\frac{n_2-n_L}{n_L}\frac{t}{R_2}\right) \end{pmatrix}, \tag{A.6}$$

where f_L is the focal length of the lens

$$\frac{1}{f_L} = \frac{n_L - n_1}{R_1} - \frac{n_L - n_2}{R_2} + \frac{(n_L - n_2)(n_L - n_1)}{n_L}\frac{t}{R_1 R_2}. \tag{A.7}$$

In the simplifying case of a lens placed entirely in a medium of refractive index $n_m (= n_1 = n_2)$, equation A.7 simplifies to the "lensmakers's equation"

$$\frac{1}{f_L} = (n_L - n_m)\left(\frac{1}{R_1} - \frac{1}{R_2} + \frac{(n_L - n_m)}{n_l}\frac{t}{R_1 R_2}\right). \tag{A.8}$$

Equation A.8 has a strong dependence on the difference in refractive indices between the lens and surrounding media and the curvature of each lens surface. The lens thickness, t, also effects the lens' power, however this term is often neglected under the thin lens approximation as frequently the lens thickness is small compared to both the surface radii of curvature.

From the form of equation A.8 is is clear that a lens of shape shown in figure A.2a will always have a positive optical power, while a lens of shape shown in figure A.2d will always have a negative optical power. Lenses of shapes shown in figures A.2b and A.2c can have either positive or negative optical powers depending on the relative size of R_1 and R_2.

Using RTMs we can also deduce the RTM, M_T, and hence overall focal length, f_T of a system of two lenses of focal lengths f_1 and f_2, separated by a distance, d:

$$M_T = \begin{pmatrix} 1 & 0 \\ -1/f_2 & 1 \end{pmatrix}\begin{pmatrix} 1 & \frac{d}{n_m} \\ 0 & 1 \end{pmatrix}\begin{pmatrix} 1 & 0 \\ -1/f_1 & 1 \end{pmatrix} = \begin{pmatrix} 1 - d/n_m f_1 & \frac{d}{n_m} \\ -1/f_T & 1 - d/n_m f_2 \end{pmatrix}, \tag{A.9}$$

where

$$\frac{1}{f_T} = \frac{1}{f_1} + \frac{1}{f_2} - \frac{d}{f_1 f_2}. \tag{A.10}$$

Similar to the thickness of a lens, the distance between two lenses often has a negligible effect on the overall power of a compound lens as typically the focal lengths of both lenses is much greater than the separation distance between them.

Appendix B

Derivation of the trace formula

Here we outline the derivation of W&T's trace formula which describes the deformation behaviour of LCEs. [169] The derivation follows a modification of classical rubber elasticity which was outlined in section 4.2.

The random walk for a nematic polymer is anisotropic which means that the magnitude of each step length depends on the direction of the step. Along the three principle axes we, in general, will have step lengths of l_1, l_2 and l_3. This anisotropy in step lengths can therefore be encapsulated by an effective step length tensor, $\underline{\underline{\mathbf{l}}}$, which in the diagonal frame is given by $\mathrm{Diag}(l_1, l_2, l_3)$. The variance of the end-to-end vector for such a polymer chain is therefore given by

$$\langle \vec{R}^2 \rangle = N\bar{l}^2 = L\bar{l} = \frac{L}{3}(l_1 + l_2 + l_3), \tag{B.1}$$

where $\bar{l}$ is the average step length (given that essentially a third of the steps will be taken along each principle direction) and L is the contour length of the polymer chain. If our coordinate system is aligned with the principle axes of $\underline{\underline{\mathbf{l}}}$, then the variance of $\vec{R}$ along each axis would be given by

$$\langle \vec{R}_i^2 \rangle = \frac{Ll_i}{3}. \tag{B.2}$$

More generally for any orientation of $\underline{\underline{\mathbf{l}}}$ with respect to the coordinate system we have

$$\langle \vec{R}_i \vec{R}_j \rangle = \frac{L}{3} l_{ij}, \tag{B.3}$$

where l_{ij} is the ij^{th} component of $\underline{\underline{\mathbf{l}}}$. For simplicity, we proceed by considering the diagonal frame of $\underline{\underline{\mathbf{l}}}$ and generalise to any orientation of $\underline{\underline{\mathbf{l}}}$.

Using equation B.2, we can see that the probability distribution function for the random walk along the i^{th} axis will be given by

$$p(R_i) = \left(\frac{3}{2\pi l_i L}\right)^{1/2} \exp\left(-\frac{3R_i^2}{2Ll_i}\right), \tag{B.4}$$

which means the total probability distribution function for a nematic chain with end-to-end vector of $\vec{R}$ is

$$p(\vec{R}) = p(R_x)p(R_y)p(R_z) = \left[\left(\frac{3}{2\pi L}\right)^3 \frac{1}{l_1 l_2 l_3}\right]^{1/2} \exp\left[-\frac{3}{2L}\left(\frac{R_x^2}{l_1} + \frac{R_y^2}{l_2} + \frac{R_z^2}{l_3}\right)\right]. \tag{B.5}$$

Generalising this gives

$$p(\vec{R}) = \left[\left(\frac{3}{2\pi L}\right)^3 \frac{1}{\mathrm{Det}(\underline{\underline{\mathbf{l}}})}\right]^{1/2} \exp\left(-\frac{3}{2L}\vec{R} \cdot \underline{\underline{\mathbf{l}}}^{-\mathbf{1}} \cdot \vec{R}\right). \tag{B.6}$$

The free energy of a single strand, f_s, of the polymer network is therefore

$$f_s = \frac{3k_B T}{2L}\vec{R} \cdot \underline{\underline{\mathbf{l}}}^{-\mathbf{1}} \cdot \vec{R} + \frac{k_B T}{2} \ln\left(\frac{\mathrm{Det}(\underline{\underline{\mathbf{l}}})}{A}\right), \tag{B.7}$$

where A is a constant.

As in section 4.2, an affine deformation of $\underline{\underline{\lambda}}$ applied to the strand results in a free energy of

$$f_s' = \frac{3k_B T}{2L}\vec{R} \cdot \underline{\underline{\lambda}}^{\mathrm{T}} \cdot \underline{\underline{\mathbf{l}}}^{-\mathbf{1}} \cdot \underline{\underline{\lambda}} \cdot \vec{R} + \frac{k_B T}{2} \ln\left(\frac{\mathrm{Det}(\underline{\underline{\mathbf{l}}})}{a}\right). \tag{B.8}$$

Following section 4.2, the total elastic free energy density is given by

$$F_{el} = \frac{3n_s k_B T}{2L}\langle R_i \lambda_{ik} l_{kl}^{-1} \lambda_{lj} R_j \rangle + \frac{n_s k_B T}{2} \ln\left(\frac{\mathrm{Det}(\underline{\underline{\mathbf{l}}})}{a}\right). \tag{B.9}$$

Again, the averaging is only performed over $\langle R_i R_j \rangle$ and so we can use equation B.3 to give the result

$$F_{el} = \frac{n_s k_B T}{2} l_{ij}^{0} \lambda_{ik} l_{kl}^{-1} \lambda_{lj} + \frac{n_s k_B T}{2} \ln\left(\frac{\mathrm{Det}(\underline{\underline{\mathbf{l}}})}{a}\right), \tag{B.10}$$

$$= \frac{\mu}{2} \mathrm{Tr}\left(\underline{\underline{\mathbf{l}}}^{\mathbf{0}} \cdot \underline{\underline{\lambda}}^{\mathrm{T}} \cdot \underline{\underline{\mathbf{l}}}^{-\mathbf{1}} \cdot \underline{\underline{\lambda}}\right) + \frac{\mu}{2} \ln\left(\frac{\mathrm{Det}(\underline{\underline{\mathbf{l}}})}{a}\right), \tag{B.11}$$

where $\underline{\underline{\mathbf{l}}}^{\mathbf{0}}$ (l_{ij}^{0} in index notation) is the step length tensor of the network in the undeformed state, $\underline{\underline{\mathbf{l}}}^{-\mathbf{1}}$ is the inverse step length tensor in the deformed state and we have replaced $n_s k_B T$ with the shear modulus μ. If no deformation is applied to the system (*i.e.* $\lambda_{ij} = \delta_{ij}$) then $\underline{\underline{\mathbf{l}}} = \underline{\underline{\mathbf{l}}}^{\mathbf{0}}$ and

$$F_{el} = \frac{3\mu}{2} + \frac{\mu}{2} \ln\left(\frac{\mathrm{Det}(\underline{\underline{\mathbf{l}}}^{\mathbf{0}})}{a}\right). \tag{B.12}$$

We are free to set as F_{el} to whatever value we like. Choosing $F_{el} = {}^{3\mu}/_{2}$ seems sensible as it keeps the free energy density for the undeformed nematic elastomer the same as the free energy of an undeformed isotropic rubber. Our choice means that

$$a = \mathrm{Det}(\underline{\underline{\mathbf{l}}}^{\mathbf{0}}). \tag{B.13}$$

Inserting this into equation B.11 gives our final result — the trace formula

$$F_{el} = \frac{\mu}{2}\left[\mathrm{Tr}\left(\underline{\underline{\mathbf{l}}}^{\mathbf{0}} \cdot \underline{\underline{\lambda}}^{\mathrm{T}} \cdot \underline{\underline{\mathbf{l}}}^{-\mathbf{1}} \cdot \underline{\underline{\lambda}}\right) + \ln\left(\frac{\mathrm{Det}(\underline{\underline{\mathbf{l}}})}{\mathrm{Det}(\underline{\underline{\mathbf{l}}}^{\mathbf{0}})}\right)\right]. \tag{B.14}$$

Notes and references

[1] (2017) Negative order parameters in LCEs were first reported independently by Lagerwall et al. and Mistry et al. at the 2017 European Liquid Crystals conference in Moscow. 110, 126

[2] Agrawal, A., Adetiba, O., Kim, H., Chen, H., Jacot, J.G. & Verduzco, R. (2015). Stimuli-responsive liquid crystal elastomers for dynamic cell culture. *Journal of Materials Research*, **30**, 453–462. 38, 39

[3] Ahir, S.V., Tajbakhsh, A.R. & Terentjev, E.M. (2006). Self-assembled shape-memory fibers of triblock liquid-crystal polymers. *Advanced Functional Materials*, **16**, 556–560. 2, 33

[4] Alderson, A. & Alderson, K.L. (2007). Auxetic materials. *Proceedings of the Institution of Mechanical Engineers, Part G: Journal of Aerospace Engineering*, **221**, 565–575. 132, 134, 149

[5] Aldred, P. & Moratti, S.C. (2005). Dynamic simulations of potentially auxetic liquid-crystalline polymers incorporating swivelling mesogens. *Molecular Simulation*, **31**, 883–886. 135, 149

[6] Alió, J.L., Alió del Barrio, J.L. & Vega-Estrada, A. (2017). Accommodative intraocular lenses: where are we and where we are going. *Eye and Vision*, **4**, 16. 3, 4, 5, 16, 17

[7] Ambulo, C.P., Burroughs, J.J., Boothby, J.M., Kim, H., Shankar, M.R. & Ware, T.H. (2017). Four-dimensional Printing of Liquid Crystal Elastomers. *ACS Applied Materials and Interfaces*, **9**, 37332–37339. 41, 45, 247

[8] Amigó-Melchior, A. & Finkelmann, H. (2002). A concept for bifocal contact- or intraocular lenses: liquid single crystal hydrogels (LSCH). *Polymers for Advanced Technologies*, **13**, 363–369. 15, 39

[9] Andley, U.P. (2008). The lens epithelium: focus on the expression and function of the alpha-crystallin chaperones. *The international journal of biochemistry & cell biology*, **40**, 317–23. 10

[10] Asbell, P.A., Dualan, I., Mindel, J., Brocks, D., Ahmad, M. & Epstein, S. (2005). Age-related cataract. *The Lancet*, **365**, 599–609. 3, 13, 14

[11] Atchison, D.A. (1995). Accommodation and presbyopia. *Ophthalmic and Physiological Optics*, **15**, 255–272. 13

[12] Bailey, J., Kaur, S., Morgan, P.B., Gleeson, H.F., Clamp, J.H. & Jones, J.C. (2017). Design considerations for liquid crystal contact lenses. 15

[13] Balasubramanian, V., Bush, K., Smoukov, S., Venerus, D.C. & Schieber, J.D. (2005). Measurements of flow-induced anisotropic thermal conduction in a polyisobutylene melt following step shear flow. *Macromolecules*, **38**, 6210–6215. 231

[14] Baughman, R.H., Shacklette, J.M., Zakhidov, A.A. & Stafström, S. (1998). Negative Poisson's ratios as a common feature of cubic metals. *Nature*, **392**, 362–365. 149

[15] Bladon, P., Terentjev, E.M. & Warner, M. (1993). Transitions and instabilities in liquid crystal elastomers. *Physical Review E*, **47**, R3838–R3840. 59, 116

[16] Bladon, P., Terentjev, E. & Warner, M. (1994). Deformation induced orientational transitions in liquid crystals elastomer. *J. Phys. II France*, **4**, 75–91. 156, 171, 184

[17] Bradley, A., Nam, J., Xu, R., Harman, L. & Thibos, L. (2014). Impact of contact lens zone geometry and ocular optics on bifocal retinal image quality. *Ophthalmic & physiological optics : the journal of the British College of Ophthalmic Opticians (Optometrists)*, **34**, 331–45. 14

[18] Brehmer, M. & Jeu, W.D. (2012). *Liquid Crystal Elastomers: Materials and Applications*, vol. 250 of *Advances in Polymer Science*. Springer Berlin Heidelberg, Berlin, Heidelberg. 2

[19] Brehmer, M. & Zentel, R. (2006). Liquid Crystalline ElastomersCharacterization as Networks. *Molecular Crystals and Liquid Crystals Science and Technology. Section A. Molecular Crystals and Liquid Crystals*, **243**, 353–376. 40

[20] Broer, D.J. & Heynderickx, I. (1990). Three Dimensionally Ordered Polymer Networks with a Helicoidal Structure. *Macromolecules*, **23**, 2474–2477. 40

[21] Broer, D.J., Lub, J. & Mol, G.N. (1995). Wide-band reflective polarizers from cholesteric polymer networks with a pitch gradient. *Nature*, **378**, 467–469. 40

[22] Brömmel, F., Kramer, D. & Finkelmann, H. (2012). Preparation of Liquid Crystalline Elastomers. *Advances in Polymer Science*, **250**, 1–48. 25, 32, 38, 39, 43, 93, 128, 129, 150

[23] Brostow, W., Chiu, R., Kalogeras, I.M. & Vassilikou-Dova, A. (2008). Prediction of glass transition temperatures: Binary blends and copolymers. *Materials Letters*, **62**, 3152–3155. 96

[24] Brown, A.W. & Adams, J.M. (2012). Negative Poisson's ratio and semisoft elasticity of smectic-C liquid-crystal elastomers. *Physical Review E - Statistical, Nonlinear, and Soft Matter Physics*, **85**, 1–13. 131

[25] Caddock, B.D. & Evans, K.E. (1989). Microporous materials with negative Poisson's ratios. I. Microstructure and mechanical properties. *Journal of Physics D: Applied Physics*, **22**, 1877–1882. 135

[26] Charman, W.N. (2008). The eye in focus: Accommodation and presbyopia. *Clinical and Experimental Optometry*, **91**, 207–225. 3, 10, 11, 12

[27] Charman, W.N. (2014). Developments in the correction of presbyopia I: spectacle and contact lenses. *Ophthalmic and Physiological Optics*, **34**, 8–29. 12

[28] Chow, T.S. (1980). Molecular Interpretation of the Glass Transition Temperature of Polymer-Diluent Systems. *Macromolecules*, **13**, 362–364. 94

[29] Clarke, S.M., Tajbakhsh, A.R., Terentjev, E.M., Remillat, C., Tomlinson, G.R. & House, J.R. (2001). Soft elasticity and mechanical damping in liquid crystalline elastomers. *Journal of Applied Physics*, **89**, 6530–6535. 35, 121, 124

[30] Critchley, R., Corni, I., Wharton, J.A., Walsh, F.C., Wood, R.J.K. & Stokes, K.R. (2013). A review of the manufacture, mechanical properties and potential applications of auxetic foams. *Physica Status Solidi (B)*, **250**, 1963–1982. 134

[31] D'Allest, J.F., Maïssa, P., ten Bosch, A., Sixou, P., Blumstein, A., Blumstein, R., Teixeira, J. & Noirez, L. (1988). Experimental Evidence of Chain Extension at the Transition Temperature of a Nematic Polymer. *Physical Review Letters*, **61**, 2562–2565. 31, 128

[32] Davidson, P., Petermann, D. & Levelut, A.M. (1995). The Measurement of the Nematic Order Parameter by X-ray Scattering Reconsidered. *Journal de Physique II*, **5**, 113–131. 147

[33] Davis, F. & Mitchell, G. (1996). Liquid crystal elastomers: controlled crosslinking in the liquid crystal phase. *Polymer*, **37**, 1345–1351. 156

[34] De Castro, A., Siedlecki, D., Borja, D., Uhlhorn, S., Parel, J.M., Manns, F. & Marcos, S. (2011). Age-dependent variation of the gradient index profile in human crystalline lenses. *Journal of Modern Optics*, **58**, 1781–1787. 12

[35] De Focatiis, D. & Kelly, S. (2016). An adaptor, a modified stress testing device and a method of performing a multi-axial stress test. xxiii, 224

[36] de Gennes, P.G. & Prost, J. (1995). *The Physics of Liquid Crystals*. Clarendon Press, Oxford. 24

[37] de Haan, L.T., Sánchez-Somolinos, C., Bastiaansen, C.M.W., Schenning, A.P.H.J. & Broer, D.J. (2012). Engineering of Complex Order and the Macroscopic Deformation of Liquid Crystal Polymer Networks. *Angewandte Chemie International Edition*, **51**, 12469–12472. 40, 151, 187, 239, 246

[38] Donnio, B., Wermter, H. & Finkelmann, H. (2000). A Simple and Versatile Synthetic Route for the Preparation of Main-Chain, Liquid-Crystalline Elastomers. *Macromolecules*, **33**, 7724–7729. 39, 73

[39] Efron, N., ed. (2002). *Contact lens practice*. Buttweworth Heinemann, Oxford, 1st edn. 14

[40] Evans, K.E. & Alderson, A. (2000). Auxetic Materials: Functional Materials and Structures from Lateral Thinking! *Advanced Materials*, **12**, 617–628. 132, 134, 252

[41] Evans, K.E., Nkansah, M.A., Hutchinson, I.J. & Rogers, S.C. (1991). Molecular network design. *Nature*, **353**, 124. 132, 133, 134

[42] Evereklioglu, C., Er, H., Bekir, N.A., Borazan, M. & Zorlu, F. (2003). Comparison of secondary implantation of flexible open-loop anterior chamber and scleral-fixated posterior chamber intraocular lenses. *Journal of Cataract & Refractive Surgery*, **29**, 301–308. 243

[43] Finkelmann, H. (1981). Investigations on liquid crystalline polysiloxanes 3. Liquid crystalline elastomersa new type of liquid crystalline material. *Makromol. Chem.*, **2**, 317–322. 39

[44] Finkelmann, H. (1987). Liquid Crystalline Polymers. *Angewandte Chemie International Edition in English*, **26**, 816–824. 39

[45] Finkelmann, H., Kaufhold, W., Noirez, L., ten Bosch, A. & Sixou, P. (1994). Chain conformation in nematic elastomers. *Journal de Physique II*, **4**, 1363–1373. 39

[46] Finkelmann, H., Kundler, I., Terentjev, E.M. & Warner, M. (1997). Critical Stripe-Domain Instability of Nematic Elastomers. *Journal de Physique II*, **7**, 1059–1069. 39

[47] Finkelmann, H., Greve, A. & Warner, M. (2001). The elastic anisotropy of nematic elastomers. *European Physical Journal E*, **5**, 281–293. 34, 39, 65, 125, 165, 232, 239

[48] Fisher, R.F. (1977). The force of contraction of the human ciliary muscle during accommodation. *J. Physiol.*, **270**, 51–74. 13

[49] Forrester, J.V., Dick, A.D., McMenamin, P.G., Roberts, F. & Pearlman, E. (2015). *The Eye: Basic Sciences in Practice*. Elsevier Health Sciences UK. 8, 9, 10, 11

[50] Gabbott, P., ed. (2008). *Principles and Applications of Thermal Analysis*. Blackwell Publishing Ltd, Oxford, UK. 72, 73

[51] Gao, Y., Mori, T., Manning, S., Zhao, Y., Nielsen, A.D., Neshat, A., Sharma, A., Mahnen, C.J., Everson, H.R., Crotty, S., Clements, R.J., Malcuit, C. & Hegmann, E. (2016). Biocompatible 3D Liquid Crystal Elastomer Cell Scaffolds and Foams with Primary and Secondary Porous Architecture. *ACS Macro Letters*, **5**, 4–9. 38

[52] Geary, J.M., Goodby, J.W., Kmetz, A.R. & Patel, J.S. (1987). The mechanism of polymer alignment of liquidcrystal materials. *Journal of Applied Physics*, **62**, 4100–4108. 69

[53] Gelebart, A.H., Jan Mulder, D., Varga, M., Konya, A., Vantomme, G., Meijer, E.W., Selinger, R.L.B. & Broer, D.J. (2017). Making waves in a photoactive polymer film. *Nature*, **546**, 632–636. 40

[54] Gent, A. (2005). Science and Technology of Rubber. In J.E. Mark, B. Erman & F.R. Eirich, eds., *Science and Technology of Rubber*, chap. 1, 1–27, Academic Press, London, 2nd edn. 54

[55] Gent, A.N. (2012). Elasticity. In *Engineering with Rubber*, chap. 3, 37–60, Carl Hanser Verlag GmbH & Co. KG, München, 3rd edn. 24, 25, 27, 133

[56] Glasser, A. (2008). Restoration of accommodation: Surgical options for correction of presbyopia. *Clinical and Experimental Optometry*, **91**, 279–295. 4, 12

[57] Glasser, A. & Campbell, M.C. (1998). Presbyopia and the optical changes in the human crystalline lens with age. *Vision Research*, **38**, 209–229. 11

[58] Gleeson, H.F., Southern, C.D., Brimicombe, P.D., Goodby, J.W. & Görtz, V. (2010). Optical measurements of orientational order in uniaxial and biaxial nematic liquid crystals. *Liquid Crystals*, **37**, 949–959. 28, 147, 254

[59] Gleim, W. & Finkelmann, H. (1987). Thermoelastic and photoelastic properties of crosslinked liquid-crystalline side chain polymers. *Die Makromolekulare Chemie*, **188**, 1489–1500. 222, 231, 232

[60] Godman, N.P., Kowalski, B.A., Auguste, A.D., Koerner, H. & White, T.J. (2017). Synthesis of Elastomeric Liquid Crystalline Polymer Networks via Chain Transfer. *ACS Macro Letters*, **6**, 1290–1295. 35, 188

[61] Goodman, D.S. (2010). *Handbook of Optics, Third Edition Volume I: Geometrical and Physical Optics, Polarized Light, Components and Instruments(Set)*. McGraw-Hill, Inc., New York, NY, USA, 3rd edn. 258

[62] Gray, G.W. (1962). *Molecular Structure and the Properties of Liquid Crystals*. Academic Press, London, 1st edn. 21, 22

[63] Greaves, G.N., Greer, A.L., Lakes, R.S. & Rouxel, T. (2011). Poisson's ratio and modern materials. *Nature materials*, **10**, 823–837. 133

[64] Haloi, D.J., Roy, S. & Singha, N.K. (2009). Copper catalyzed atom transfer radical copolymerization of glycidyl methacrylate and 2-ethylhexyl acrylate. *Journal of Polymer Science Part A: Polymer Chemistry*, **47**, 6526–6533. 97

[65] Hamed, G.R. (2102). Materials and Compounds. In *Engineering with Rubber*, chap. 2, 11–36, Carl Hanser Verlag GmbH & Co. KG, München, 3rd edn. 25

[66] Hammerschmidt, K. & Finkelmann, H. (1989). Stressoptical and thermomechanical measurements on liquid crystalline elastomers. *Die Makromolekulare*, **1101**, 1089–1101. 231, 232

[67] Hardouin, F., Mery, S., Achard, M.F., Noirez, L. & Keller, P. (1991). Evidence for a jacketed nematic polymer. *Journal de Physique II*, **1**, 511–520. 32

[68] Hardouin, F., Leroux, N., Mery, S., Noirez, L. (1992). Small angle neutron scattering experiments on "side-on fixed" liquid crystal polysiloxanes. *Journal de Physique. II*, **2**, 271–278. 32

[69] He, C., Liu, P. & Griffin, A.C. (1998). Toward Negative Poisson Ratio Polymers through Molecular Design. *Macromolecules*, **31**, 3145–3147. 134, 135, 149

[70] He, C., Liu, P., Griffin, A.C., Smith, C.W. & Evans, K.E. (2005). Morphology and Deformation Behaviour of a Liquid Crystalline Polymer Containing Laterally Attached Pentaphenyl Rods. *Macromolecular Chemistry and Physics*, **206**, 233–239. 132, 134, 135

[71] He, C., Liu, P., McMullan, P.J. & Griffin, A.C. (2005). Toward molecular auxetics: Main chain liquid crystalline polymers consisting of laterally attached para-quaterphenyls. *physica status solidi (B)*, **242**, 576–584. 135, 149

[72] Hecht, E. (2002). *Optics*. Addison-Wesley. 4, 9, 257, 259

[73] Heys, K., Cram, S. & Truscott, R. (2004). Massive increase in the stiffness of the human lens nucleus with age: the basis for presbyopia? *Molecular Vision*, **10**, 956–963. 10, 129

[74] Higaki, H., Takigawa, T. & Urayama, K. (2013). Nonuniform and Uniform Deformations of Stretched Nematic Elastomers. *Macromolecules*, **46**, 5223–5231. 36, 40, 81, 82, 93, 94, 105

[75] Hikmet, R.A.M., Lub, J. & Broer, D.J. (1991). Anisotropic networks formed by photopolymerization of liquid-crystalline molecules. *Advanced Materials*, **3**, 392–394. 40

[76] Hirschmann, H., Roberts, P., Davis, F., Guo, W., Hasson, C. & Mitchell, G. (2001). Liquid crystalline elastomers: the relationship between macroscopic behaviour and the level of backbone anisotropy. *Polymer*, **42**, 7063–7071. 35, 36, 40, 81, 127, 155, 156, 160

[77] Hoberman, C. (1991). Radial expansion/retraction truss structures. xxiii, 224

[78] Höhne, G.W.H., Hemminger, W.F. & Flammersheim, H.J. (2003). *Differential Scanning Calorimetry*. Springer Berlin Heidelberg, Berlin, Heidelberg. 72, 73

[79] Horgan, C.O. & Murphy, J.G. (2007). Constitutive Models for Almost Incompressible Isotropic Elastic Rubber-like Materials. *Journal of Elasticity*, **87**, 133–146. 133

[80] Huang, C. & Chen, L. (2016). Negative Poisson's Ratio in Modern Functional Materials. *Advanced Materials*, **28**, 8079–8096. 133, 134

[81] Ikeda, T., Mamiya, J.I. & Yu, Y. (2007). Photomechanics of liquid-crystalline elastomers and other polymers. *Angewandte Chemie - International Edition*, **46**, 506–528. 151

[82] Jones, C.E., Atchison, D.A. & Pope, J.M. (2007). Changes in lens dimensions and refractive index with age and accommodation. *Optometry and Vision Science*, **84**, 990–995. 12

[83] Katritzky, A.R., Rachwal, P., Law, K.W., Karelson, M. & Lobanov, V.S. (1996). Prediction of Polymer Glass Transition Temperatures Using a General Quantitative StructureProperty Relationship Treatment. *Journal of Chemical Information and Computer Sciences*, **36**, 879–884. 96

[84] Kaufman, P.L., Levin, L.A., Adler, F.H. & Alm, A. (2011). *Adler's Physiology of the Eye*. Elsevier Health Sciences. 10

[85] Keller, P., Carvalho, B., Cotton, J., Lambert, M., Moussa, F. & Pépy, G. (1985). Side chain mesomorphic polymers : studies of labelled backbones by neutron scattering. *J. Phys. Lett.*, **46**, 1065–1071. 32

[86] Kočevar, K. & Muševič, I. (2001). Forces in the isotropic phase of a confined nematic liquid crystal 5CB. *Physical Review E*, **64**, 051711. 141

[87] Kotikian, A., Truby, R.L., Boley, J.W., White, T.J. & Lewis, J.A. (2018). 3D Printing of Liquid Crystal Elastomeric Actuators with Spatially Programed Nematic Order. *Advanced Materials*, 1706164. 41, 45, 247

[88] Krag, S., Olsen, T. & Andreassen, T.T. (1997). Biomechanical characteristics of the human anterior lens capsule in relation to age. *Investigative ophthalmology & visual science*, **38**, 357–63. 12

[89] Kularatne, R.S., Kim, H., Boothby, J.M. & Ware, T.H. (2017). Liquid crystal elastomer actuators: Synthesis, alignment, and applications. *Journal of Polymer Science Part B: Polymer Physics*, **55**, 395–411. 38

[90] Kundler, I. & Finkelmann, H. (1995). Strain-induced director reorientation in nematic liquid single crystal elastomers. *Macromolecular Rapid Communications*, **16**, 679–686. 35, 36, 39, 57, 60, 81, 145, 155

[91] Kundler, I. & Finkelmann, H. (1998). Director reorientation via stripe-domains in nematic elastomers: influence of cross-link density, anisotropy of the network and smectic clusters. *Macromolecular Chemistry and Physics*, **199**, 677–686. 35, 39, 41, 42, 60

[92] Kundler, I., Nishikawa, E. & Finkelmann, H. (1997). Nematic and smectic liquid single crystal elastomers: Influence of external stress parallel and perpendicular to the director. *Macromol. Symp.*, **117**, 11–19. 34

[93] Küpfer, J. & Finkelmann, H. (1991). Nematic liquid single crystal elastomers. *Die Makromolekulare Chemie, Rapid Communications*, **12**, 717–726. 30, 34, 35, 36, 39, 45, 60, 80, 147, 239, 254

[94] Küpfer, J. & Finkelmann, H. (1994). Liquid crystal elastomers: Influence of the orientational distribution of the crosslinks on the phase behaviour and reorientation processes. *Macromolecular Chemistry and Physics*, **195**, 1353–1367. 35, 36, 45, 60, 80, 81, 121

[95] Lecommandoux, S., Noirez, L., Richard, H., Achard, M.F., Strazielle, C. & Hardouin, F. (1996). Effect of the Spacer and Aliphatic Tail Length on the Conformation of "Side-on Fixed" Liquid Crystal Polyacrylates: "SANS" Experiments. *Journal de Physique II*, **6**, 225–234. 32

[96] Li, J., Gauza, S. & Wu, S.T. (2004). Temperature effect on liquid crystal refractive indices. *Journal of Applied Physics*, **96**, 19–24. 243

[97] Li, J., Wen, C.H., Gauza, S., Lu, R. & Wu, S.T. (2005). Refractive Indices of Liquid Crystals for Display Applications. *Journal of Display Technology*, **1**, 51–61. 243

[98] Lim, T.C. (2015). *Auxetic Materials and Structures*. Engineering Materials, Springer Singapore, Singapore. 132, 133, 145

[99] Linebarger, E.J., Hardten, D.R., Shah, G.K. & Lindstrom, R.L. (1999). Phacoemulsification and Modern Cataract Surgery. *Survey of Ophthalmology*, **44**, 123–147. 14

[100] Liu, Y. & Hu, H. (2010). A review on auxetic structures and polymeric materials. *Scientific Research and Essays*, **5**, 1052–1063. 134

[101] Love, A.E.H. (1892). *A Treatise on the Mathematical Theory of Elasticity*, vol. 1. Cambridge University Press, Cambridge. 149

[102] Luckhurst, G.R. & Zannoni, C. (1977). Why is the Maier-Saupe theory of nematic liquid crystals so successful? [6]. *Nature*, **267**, 412–414. 23

[103] Luo, Y., Mao, D. & You, Z. (2007). On a type of radially retractable plate structures. *International Journal of Solids and Structures*, **44**, 3452–3467. xxiii, 224

[104] Lydon, J.E., Gleeson, H. & Jull, E.I. (2017). The identification of the sign and strength of disclinations in the schlieren (nucleated domain) texture of the nematic phase, by optical microscopy. *Liquid Crystals*, **44**, 1775–1786. 238

[105] Mao, Y., Warner, M., Terentjev, E.M. & Ball, R.C. (1998). Finite extensibility effects in nematic elastomers. *The Journal of Chemical Physics*, **108**, 8743–8748. 34, 66, 165, 167

[106] Mark, J.E. (2007). *Physical Properties of Polymers Handbook*. Springer New York, New York, NY. 231

[107] Mark, J.E., Ngai, K., Graessley, W., Mandelkern, L., Samulski, E., Koenig, J. & Wignall, G. (2003). *Physical Properties of Polymers*. Cambridge University Press, Cambridge, 3rd edn. 24

[108] McConney, M.E., Martinez, A., Tondiglia, V.P., Lee, K.M., Langley, D., Smalyukh, I.I. & White, T.J. (2013). Topography from Topology: Photoinduced Surface Features Generated in Liquid Crystal Polymer Networks. *Advanced Materials*, **25**, 5880–5885. 239

[109] Milton, H.E., Morgan, P.B., Clamp, J.H. & Gleeson, H.F. (2014). Electronic liquid crystal contact lenses for the correction of presbyopia. *Optics express*, **22**, 8035–8040. 15

[110] Mir, M., Ali, M.N., Sami, J. & Ansari, U. (2014). Review of Mechanics and Applications of Auxetic Structures. *Advances in Materials Science and Engineering*, **2014**, Article ID 753496, 1–17. 132, 134

[111] Mitchell, G., Davis, F. & Guo, W. (1993). Strain-induced transitions in liquid-crystal elastomers. *Physical Review Letters*, **71**, 2947–2950. 36, 40, 57, 60, 119, 124, 127, 128

[112] Mkrtchyan, V.P., Gasparyan, L.G., Dadalyan, T.K., Balyan, M.K. & Kuyumchyan, A.V. (2014). Measurement of the refractive index of nematic liquid crystals 5CB by means of x-ray interferometry. In C. Morawe, A.M. Khounsary & S. Goto, eds., *Proceedings of SPIE*, vol. 9207, 920714. 21

[113] Mott, P.H. & Roland, C.M. (1996). Elasticity of natural rubber networks. *Macromolecules*, **29**, 6941–6945. 231

[114] Mott, P.H.Ã., Dorgan, J.R. & Roland, C.M. (2008). The bulk modulus and Poisson's ratio of incompressible" materials. *Journal of sound and vibration*, **312**, 572–575. 133

[115] Mottram, N.J. & Newton, C.J.P. (2014). Introduction to Q-tensor theory. 22, 23

[116] Moussa, F., Cotton, J., Hardouin, F., Keller, P., Lambert, M., Pépy, G., Mauzac, M. & Richard, H. (1987). Conformational anisotropy of liquid crystalline side chain polymers : a small angle neutron scattering study. *J. Phys.*, **48**, 1079–1083. 32

[117] Mutti, D.O., Mitchell, G.L., Sinnott, L.T., Jones-Jordan, L.A., Moeschberger, M.L., Cotter, S.A., Kleinstein, R.N., Manny, R.E., Twelker, J.D. & Zadnik, K. (2012). Corneal and Crystalline Lens Dimensions Before and After Myopia Onset. *Optometry and Vision Science*, **89**, 251–262. 8, 243

[118] Noirez, L., Cotton, J.P., Hardouin, F., Keller, P., Moussa, F., Pepy, G. & Strazielle, C. (1988). Backbone conformation of a mesogenic side-chain polyacrylate. *Macromolecules*, **21**, 2889–2891. 128

[119] Noirez, L., Keller, P. & Cotton, J.P. (1995). On the structure and the chain conformation of side-chain liquid crystal polymers. *Liquid Crystals*, **18**, 129–148. 128, 147

[120] Olmsted, P.D. (1994). Rotational invariance and Goldstone modes in nematic elastomers and gels. *Journal de Physique II*, **4**, 2215–2230. 60

[121] Pakula, T. & Zentel, R. (1991). Mechanical behaviour of liquidcrystalline polymers and their networks. *Die Makromolekulare Chemie*, **192**, 2401–2410. 40

[122] Pardue, M.T. & Sivak, J.G. (2000). Age-related changes in human ciliary muscle. *Optometry and vision science : official publication of the American Academy of Optometry*, **77**, 204–210. 4, 13

[123] Patterson, E.A. (2002). Digital Photoelasticity: Principles, Practice and Potential. *Strain*, **38**, 27–39. 212

[124] Pei, Z., Yang, Y., Chen, Q., Terentjev, E.M., Wei, Y. & Ji, Y. (2014). Mouldable liquid-crystalline elastomer actuators with exchangeable covalent bonds. *Nature materials*, **13**, 36–41. 33

[125] Pepose, J.S., Burke, J.S. & Qazi, M.A. (2017). Accommodating Intraocular Lenses. *Asia-Pacific Journal of Ophthalmology*, **6**, 1–8. 4, 17, 18

[126] Pereira, G.G. & Warner, M. (2001). Mechanical and order rigidity of nematic elastomers. *European Physical Journal E*, **5**, 295–307. 34, 165

[127] Pierscionek, B.K. (1990). Presbyopia - effect of refractive index. *Clinical and Experimental Optometry*, **73**, 23–30. 12

[128] Pour, N., Itzhaki, L., Hoz, B., Altus, E., Basch, H. & Hoz, S. (2006). Auxetics at the Molecular Level: A Negative Poisson's Ratio in Molecular Rods. *Angewandte Chemie International Edition*, **45**, 5981–5983. 134

[129] Rajagopalan, A. (2006). Visual performance of subjects wearing presbyopic contact lenses. *Optometry & Vision*. 14

[130] Ren, W., McMullan, P.J. & Griffin, A.C. (2008). Poisson's ratio of monodomain liquid crystalline elastomers. *Macromolecular Chemistry and Physics*, **209**, 1896–1899. 145

[131] Ren, W., McMullan, P.J. & Griffin, A.C. (2009). Stress-strain behavior in main chain liquid crystalline elastomers: effect of crosslinking density and transverse rod incorporation on Poisson's ratio. *physica status solidi (b)*, **246**, 2124–2130. 135, 149

[132] Roberts, P.M., Mitchell, G.R. & Davis, F.J. (1997). A Single Director Switching Mode for Monodomain Liquid Crystal Elastomers. *Journal de Physique II*, **7**, 1337–1351. 36, 40, 57, 82, 119, 124, 126, 254

[133] Roberts, P.M.S., Mitchell, G.R., Davis, F.J. & Pople, J.A. (1997). Mechanical Switching and Soft Elasticity in Liquid Crystal Elastomers. *Molecular Crystals and Liquid Crystals Science and Technology. Section A. Molecular Crystals and Liquid Crystals*, **299**, 181–186. 36, 40, 82, 119, 127

[134] Roland, C.M. (2011). *Viscoelastic Behavior of Rubbery Materials*. Oxford University Press, Oxford, 1st edn. 24, 25, 53, 222, 231

[135] Roorda, A. (2002). Human visual systemImage formation. *Encyclopedia of Imaging Science and Technology*, **161**, 539–557. 11

[136] Saed, M.O., Torbati, A.H., Starr, C.A., Visvanathan, R., Clark, N.A. & Yakacki, C.M. (2016). Thiol-acrylate main-chain liquid-crystalline elastomers with tunable thermomechanical properties and actu-

ation strain. *Journal of Polymer Science Part B: Polymer Physics*, **55**, 157–168. 42

[137] Saed, M.O., Volpe, R.H., Traugutt, N.A., Visvanathan, R., Clark, N.A. & Yakacki, C.M. (2017). High strain actuation liquid crystal elastomers via modulation of mesophase structure. *Soft Matter*, **13**, 7537–7547. 42

[138] Sakamoto, K., Usami, K. & Miki, K. (2014). Photoalignment efficiency enhancement of polyimide alignment layers by alkyl-amine vapor treatment. *Applied Physics Express*, **7**. 246

[139] Sato, Y., Sato, K. & Uchida, T. (1992). Relationship between Rubbing Strength and Surface Anchoring of Nematic Liquid Crystal. *Japanese Journal of Applied Physics*, **31**, L579–L581. 69

[140] Saxena, K.K., Das, R. & Calius, E.P. (2016). Three Decades of Auxetics Research Materials with Negative Poisson's Ratio: A Review. *Advanced Engineering Materials*, **18**, 1847–1870. 134

[141] Sayegh, F.N. (1996). The correlation of corneal refractive power, axial length, and the refractive power of the emmetropizing intraocular lens in cataractous eyes. *German journal of ophthalmology*, **5**, 328–31. 8

[142] Schätzle, J. & Finkelmann, H. (1987). State of Order in Liquid Crystalline Elastomers. *Molecular Crystals and Liquid Crystals*, **142**, 85–100. 81

[143] Schätzle, J., Kaufhold, W. & Finkelmann, H. (1989). Nematic elastomers: The influence of external mechanical stress on the liquid-crystalline phase behavior. *Die Makromolekulare Chemie*, **190**, 3269–3284. 231, 232

[144] Schindelin, J., Arganda-Carreras, I., Frise, E., Kaynig, V., Longair, M., Pietzsch, T., Preibisch, S., Rueden, C., Saalfeld, S., Schmid, B., Tinevez, J.Y., White, D.J., Hartenstein, V., Eliceiri, K., Tomancak, P. & Cardona, A. (2012). Fiji: an open-source platform for biological-image analysis. *Nature Methods*, **9**, 676–682. 90, 113

[145] Schindelin, J., Rueden, C.T., Hiner, M.C. & Eliceiri, K.W. (2015). The ImageJ ecosystem: An open platform for biomedical image analysis. *Molecular Reproduction and Development*, **82**, 518–529. 90, 113

[146] Schuhladen, S., Preller, F., Rix, R., Petsch, S., Zentel, R. & Zappe, H. (2014). Iris-Like Tunable Aperture Employing Liquid-Crystal Elastomers. *Advanced Materials*, **26**, 7247–7251. 30, 40, 246

[147] Sharma, A., Neshat, A., Mahnen, C.J., Nielsen, A.D., Snyder, J., Stankovich, T.L., Daum, B.G., LaSpina, E.M., Beltrano, G., Gao, Y., Li, S., Park, B.W., Clements, R.J., Freeman, E.J., Malcuit, C., McDonough, J.A., Korley, L.T.J., Hegmann, T. & Hegmann, E. (2015). Biocompatible, Biodegradable and Porous Liquid Crystal Elastomer Scaffolds for Spatial Cell Cultures. *Macromolecular Bioscience*, **15**, 200–214. 38

[148] Smith, C.W., Wootton, R.J. & Evans, K.E. (1999). Interpretation of Experimental Data for Poisson's Ratio of Highly Nonlinear Materials. *Experimental Mechanics*, **39**, 356–362. 135

[149] Snell, R.S. & Lemp, M.A. (1997). *Clinical Anatomy of the Eye*. Wiley. 9, 11

[150] Spector, A. (1995). Oxidative stress-induced cataract: mechanism of action. *FASEB J*, **9**, 1173–1182. 13

[151] Stannarius, R., Eremin, A., Harth, K., Morys, M., DeMiglio, A., Ohm, C. & Zentel, R. (2012). Mechanical and optical properties of continuously spun fibres of a main-chain smectic A elastomer. *Soft Matter*, **8**, 1858–1864. 33

[152] Tajbakhsh, A. & Terentjev, E. (2001). Spontaneous thermal expansion of nematic elastomers. *The European Physical Journal E*, **6**, 181–188. 128

[153] Talroze, R.V., Zubarev, E.R., Kuptsov, S.A., Merekalov, A.S., Yuranova, T.I., Plate', N.A. & Finkelmann, H. (1999). Liquid crystal acrylate-based networks: Polymer backbone-LC order interaction. *Reactive and Functional Polymers*, **41**, 1–11. 57, 81, 82

[154] Tamashima, K., Takigawa, T. & Urayama, K. (2016). Effects of Mechanical Constraint on Director Configuration of Monodomain Nematic Elastomers under Temperature Variation. *Nihon Reoroji Gakkaishi*, **44**, 17–27. 33, 128, 129

[155] Teraoka, I. (2002). *Polymer Solutions: An Introduction to Physical Properties*. John Wiley & Sons. 25

[156] Thomsen, D.L., Keller, P., Naciri, J., Pink, R., Jeon, H., Shenoy, D. & Ratna, B.R. (2001). Liquid crystal elastomers with mechanical properties of a muscle. *Macromolecules*, **34**, 5868–5875. 33, 40, 93, 94, 121, 145

[157] Urayama, K., Arai, Y.O. & Takigawa, T. (2005). Volume Phase Transition of Monodomain Nematic Polymer Networks in Isotropic Solvents Accompanied by Anisotropic Shape Variation. *Macromolecules*, **38**, 3469–3474. 30, 32, 40, 93, 94

[158] Urayama, K., Honda, S. & Takigawa, T. (2005). Electrooptical Effects with Anisotropic Deformation in Nematic Gels. *Macromolecules*, **38**, 3574–3576. 40

[159] Urayama, K., Mashita, R., Kobayashi, I. & Takigawa, T. (2007). Stretching-Induced Director Rotation in Thin Films of Liquid Crystal Elastomers with Homeotropic Alignment. *Macromolecules*, **40**, 7665–7670. 35, 40, 57, 94, 100

[160] Urayama, K., Kohmon, E., Kojima, M. & Takigawa, T. (2009). PolydomainMonodomain Transition of Randomly Disordered Nematic Elastomers with Different Cross-Linking Histories. *Macromolecules*, **42**, 4084–4089. 40, 95, 96, 100

[161] Verwey, G.C. & Warner, M. (1997). Compositional fluctuations and semisoftness in nematic elastomers. *Macromolecules*, **30**, 4189–4195. 62

[162] Verwey, G.C. & Warner, M. (1997). Nematic elastomers cross-linked by rigid rod linkers. *Macromolecules*, **30**, 4196–4204. 33, 62, 121

[163] Ware, T.H. & White, T.J. (2015). Programmed liquid crystal elastomers with tunable actuation strain. *Polym. Chem.*, **6**, 4835–4844. 36, 41, 239

[164] Ware, T.H., McConney, M.E., Wie, J.J., Tondiglia, V.P. & White, T.J. (2015). Voxelated liquid crystal elastomers. *Science*, **347**, 982–984. 2, 5, 30, 32, 41, 42, 43, 107, 151, 188, 239

[165] Ware, T.H., Perry, Z.P., Middleton, C.M., Iacono, S.T. & White, T.J. (2015). Programmable Liquid Crystal Elastomers Prepared by ThiolEne Photopolymerization. *ACS Macro Letters*, **4**, 942–946. 33, 36

[166] Ware, T.H., Biggins, J.S., Shick, A.F., Warner, M. & White, T.J. (2016). Localized soft elasticity in liquid crystal elastomers. *Nature Communications*, **7**, 10781. xxii, 34, 35, 36, 41, 124, 145, 155, 156, 188, 201, 238

[167] Warner, M. (????). Private conversation. xxv, 240, 241

[168] Warner, M. (1999). New elastic behaviour arising from the unusual constitutive relation of nematic solids. *Journal of the Mechanics and Physics of Solids*, **47**, 1355–1377. 33

[169] Warner, M. & Terentjev, E.M. (2013). *Liquid Crystal Elastomers*. Clarendon Press, Oxford. xiv, 2, 5, 25, 27, 28, 29, 31, 32, 33, 34, 35, 38, 49, 50, 59, 62, 65, 66, 93, 115, 116, 118, 124, 131, 145, 146, 147, 149, 150, 165, 232, 261

[170] Warner, M., Bladon, P. & Terentjev, E.M. (1994). "Soft elasticity" - deformation without resistance in liquid crystal elastomers. *Journal de Physique II*, **4**, 93–102. 2

[171] Weeber, H.A., Eckert, G., Pechhold, W. & van der Heijde, R.G.L. (2007). Stiffness gradient in the crystalline lens. *Graefe's Archive for Clinical and Experimental Ophthalmology*, **245**, 1357–1366. 10, 129

[172] Wermter, H. & Finkelmann, H. (2001). Liquid crystalline elastomers as artificial muscles. *e-Polymers*, **1**, 111–123. 33

[173] White, T.J. & Broer, D.J. (2015). Programmable and adaptive mechanics with liquid crystal polymer networks and elastomers. *Nature Materials*, **14**, 1087–1098. 2

[174] Wood, L.A. (1958). Glass transition temperatures of copolymers. *Journal of Polymer Science*, **28**, 319–330. 96

[175] Xia, Y., Cedillo-Servin, G., Kamien, R.D. & Yang, S. (2016). Guided Folding of Nematic Liquid Crystal Elastomer Sheets into 3D via Patterned 1D Microchannels. *Advanced Materials*, **28**, 9637–9643. 188

[176] Yakacki, C.M., Saed, M., Nair, D.P., Gong, T., Reed, S.M. & Bowman, C.N. (2015). Tailorable and programmable liquid-crystalline elastomers using a two-stage thiolacrylate reaction. *RSC Adv.*, **5**, 18997–19001. 30, 38, 42, 107

[177] Yamada, M., Kondo, M., Mamiya, J.i., Yu, Y., Kinoshita, M., Barrett, C.J. & Ikeda, T. (2008). Photomobile Polymer Materials: Towards Light-Driven Plastic Motors. *Angewandte Chemie International Edition*, **47**, 4986–4988. 32

[178] Yeganeh-Haeri, A., Weidner, D.J. & Parise, J.B. (1992). Elasticity of α-Cristobalite: A Silicon Dioxide with a Negative Poisson's Ratio. *Science*, **257**, 650–652. 149

[179] Yu, Y., Nakano, M. & Ikeda, T. (2003). Directed bending of a polymer film by light. *Nature*, **425**, 145–145. 151

[180] Zeng, H., Wani, O.M., Wasylczyk, P., Kaczmarek, R. & Priimagi, A. (2017). Self-Regulating Iris Based on Light-Actuated Liquid Crystal Elastomer. *Advanced Materials*, **29**, 1701814. 94, 188

[181] Zentel, R. (1989). Liquid Crystalline Elastomers. *Advanced Materials*, **1**, 321–329. 40

[182] Zentel, R. & Wu, J. (1986). Rheological properties of liquidcrystalline sidegroup polymers in the isotropic, nematic, and smectic states. *Die Makromolekulare Chemie*, **187**, 1727–1736. 40

[183] Zubarev, E.R., Kuptsov, S.a., Yuranova, T.I., Talroze, R.V. & Finkelmann, H. (1999). Monodomain liquid crystalline networks: reorientation mechanism from uniform to stripe domains. *Liquid Crystals*, **26**, 1531–1540. 35, 40, 81, 82, 93